

Deep Learning For Track Finding and the Reconstruction of Excited Hyperons in Proton Induced Reactions

DISSERTATION

zur

Erlangung des Grades eines
„Doktors der Naturwissenschaften“

an der Fakultät für Physik und Astronomie
der Ruhr-Universität Bochum

von

Waleed Ahmed Mohammed Esmail

aus

Kairo, Ägypten

Bochum (2021)

1. Gutachter: Prof. Dr. James Ritman ¹

2. Gutachter: Prof. Dr. Ulrich Wiedner ²

Datum der Disputation:

¹ Forschungszentrum Jülich, Ruhr-Universität Bochum

² Ruhr-Universität Bochum

ZUSAMMENFASSUNG

Ein leistungsfähiges Werkzeug zum Studium der starken Wechselwirkung bei kleinen Energien ist die Untersuchung der Produktion und des Zerfalls von Hyperonen. Daher konzentriert sich diese Dissertation auf drei Themen der Hyperonenphysik.

Der erste Teil präsentiert einen Track-Finding-Algorithmus für den Forward-Tracker des zukünftigen PANDA-Experiments unter Verwendung modernster neuronaler Graphennetze. Der Nachweis vorwärts gerichteter Teilchen spielt eine bedeutende Rolle bei der Rekonstruktion und Analyse des Grundzustands sowie angeregter Hyperonen (z.B. Σ^0 , $\Sigma(1385)$, $\Lambda(1405)$ and $\Lambda(1520)$). Als Eingabe für das Netzwerk dient ein Bild des Forward-Trackers, wobei die Detektortreffer die Knoten und alle möglichen Verbindungen zwischen zwei Treffern in benachbarten Schichten des Detektors die Kanten sind. Das Netzwerk wurde als binärer Klassifikator trainiert, um zwischen korrekten und fehlerhaften Kanten zu unterscheiden. Auf Grundlage der Netzwerkausgabe wurde ein Clustering-Algorithmus implementiert, der die zusammengehörigen Graphenpunkte durch eine Tiefensuche ermittelt. Die Güte des Netzwerks wurde auf Grundlage von Qualitätssicherungskriterien bewertet. Diese Kriterien sind die Reinheit, die Effizienz, und die sog. Geisterrate. Im Durchschnitt wurde eine Reinheit von $\approx 100\%$, eine Effizienz von $\approx 90\%$, sowie eine Geisterrate von weniger als 3% ermittelt. Da das neuronale Graphennetz darauf abzielte nur eine Projektion der Spur zu rekonstruieren, wurde ein zweiter Schritt implementiert, der diese Projektion als Startpunkt für die Rekonstruktion der gesamten Spur nutzt. Darüber hinaus liefert der Algorithmus einen Schätzwert für den Teilchenimpuls, wobei die berechnete relative Impulsauflösung 6.7% beträgt.

Der zweite Teil der Dissertation beschäftigt sich mit der Untersuchung des Produktionsmechanismus des Σ^0 Hyperons. Hierzu wird die exklusive Reaktion $p + p \rightarrow p + K^+ + \Sigma^0$ bei einer Strahl-Energie von 3.5 GeV gemessen mit dem HADES-Detektor verwendet. Das Tochterphoton $\Sigma^0 \rightarrow \Lambda\gamma$ (BR $\approx 100\%$) wurde dabei als fehlendes Teilchen behandelt, während das Tochterteilchen Λ über den Zerfallsmodus $\Lambda \rightarrow p\pi^-$ (BR $\approx 63.9\%$) nachgewiesen wurde. Dieser Nachweis erfolgte hierbei teilweise über die zentralen HADES-Detektoren, und teilweise über die Forward-Wall. Ein kinematischer Fit mit den zwei Nebenbedingungen, dass die Masse des Proton-Pion-Systems der Masse des Λ Baryon, sowie die fehlende Masse aller gemessenen Teilchen der Photonenmasse entsprechen, wurde durchgeführt. Insgesamt konnten 2613 Ereignisse rekonstruiert werden, davon 58% mittels des zentralen HADES-Detektors und 42% über die Forward-Wall. Des Weiteren wurde die Dynamik der Reaktion $p + p \rightarrow p + K^+ + \Sigma^0$

durch die Untersuchung der Winkelverteilungen im Schwerpunkts-, Gottfried-Jackson-, und Helizitäts-System studiert. Die verschiedenen Winkelverteilungen wurden mittels der Inversen der Detektor-Antwort-Matrix korrigiert. Diese Inverse wurde durch die SVD-Faktorisierungsmethode berechnet. Der Gesamtwirkungsquerschnitt der Σ^0 Produktion wurde durch die Integration der Ausbeute aus den verschiedenen Winkelverteilungen berechnet und ergibt sich zu $\sigma = 18.74 \pm 1.01(stat) \pm 1.71(syst) \mu b$. Die korrigierten CMS-Winkelverteilungen des Σ^0 und des Protons zeigen Anisotropien, wobei das erwartete Verhalten des Protons ausgeprägter ist, wenn der Produktionsprozess vom Pionen-Austausch dominiert wird. Die Winkelverteilung im $K^+\Sigma^0$ Gottfried-Jackson-System ist tendenziell asymmetrisch, was durch Nukleonenresonanzen, die in $K^+\Sigma^0$ zerfallen, hervorgerufen werden könnte. Darüber hinaus sind die Winkelverteilungen im Helizitäts-System nicht mit isotropen Verteilungen kompatibel. Dies ist ein Hinweis darauf, dass die Σ^0 Produktion zusätzlich zum reinen Phasenraum über resonante Kanäle verläuft. Um die experimentellen Winkelverteilungen besser beschreiben zu können, wurde eine Partialwellenanalyse im Zuge der BG-PWA durchgeführt. Die BG-PWA bestimmt den Beitrag verschiedener Partialwellen zur $pK^+\Sigma^0$ Produktion. Es wurden mehrere Anpassungen durchgeführt, wobei die Güte einer solchen Anpassung über den Wert der Log-Likelihood bestimmt wird. Eine Anpassung basiert hierbei auf einer Sammlung von Partialwellen, die im initialen Proton-Proton-System beitragen. Solch eine Sammlung nennt man häufig eine Lösung. Die beste Lösung in diesem Fall berücksichtigt die 2S_0 , 3P_0 , 3P_1 , 3P_2 , 1D_2 , sowie 3F_2 Partialwellen. Aufgrund der begrenzten Statistik war es jedoch nicht möglich, die genauen Beiträge der Nukleonen-Resonanzen zu bestimmen. Dennoch sind Nukleonen-Resonanzen mit einer Masse nahe $1.710 \text{ GeV}/c^2$ ($N^*(1710)$) und 1.900 ($N^*(1900)$ oder $\Delta^*(1710)$) mit Sicherheit für die Anpassung erforderlich.

Der letzte Teil der Arbeit präsentiert eine Machbarkeitsstudie zur Messung von radiativen Zerfällen angeregter Hyperonen mit dem verbesserten HADES-Aufbau und dem neuen Vorwärtsdetektor im Rahmen des FAIR-Phase-0-Programms. Auch hier wurde das Tochterteilchen Λ ($Y \rightarrow \Lambda\gamma$) teilweise im zentralen HADES-Detektor und teilweise im Vorwärts-Detektor nachgewiesen. Um die hauptsächliche Untergrund-Reaktion ($p + p \rightarrow p + K^+ + \Lambda + \pi^0$) zu unterdrücken, wurden zwei Schnitte auf fehlende Massen eingeführt. Zum Einen wird verlangt, dass die quadrierte fehlende Masse des primären Protons und des Kaons im Bereich ($1.6 < MM^2(p_p K^+) [GeV^2/c^4] < 2.6$) liegt. Zweitens muss die quadrierte fehlende Masse aller gemessenen Teilchen die Bedingung ($-0.04 < MM^2(p_p K^+ \Lambda) [GeV^2/c^4] < 0.01$) erfüllen. Als zusätzliche Variable wurde der Öffnungswinkel $OA(\Lambda\gamma)$ im Ruhesystem des Hyperons genutzt, dieser muss größer als 165° sein.

Die Rekonstruktionseffizienz ϵ dieses Kanals wurde für die verschiedenen Schnittkombinationen ermittelt und bewegt sich im Bereich von 0.0250 - 0.0193 %. Zusätzlich werden die erwartbaren Zählraten für die kommende Strahlzeit im Jahre 2022 abgeschätzt.

ABSTRACT

A powerful tool to study the strong interaction at low energies is the investigation of hyperon production and decay. Therefore, this thesis presents work focused on three topics related to hyperon physics.

The first part presents a track finding algorithm for the future \bar{P} ANDA experiment forward tracker using the state-of-art graph neural networks. The detection of forward emitted particles plays a significant role in the reconstruction and analysis of the ground state and excited hyperons (e.g., Σ^0 , $\Sigma(1385)$, $\Lambda(1405)$ and $\Lambda(1520)$). The network accepts an image of the forward tracker as an input, where the detector hits are the graph vertices, and all possible connections between two hits in adjacent layers are the graph edges. It was trained as a binary classifier to classify the graph edges. Guided by the network output, a clustering algorithm that traverses the output graph depth-wise was implemented in order to find the connected components. The performance of the network were evaluated based on quality assurance measurements, which are the purity, the efficiency, the ghost rate. On average, the purity was found to be $\approx 100\%$, the efficiency $\approx 90\%$ and the ghost ratio less than 3%. As the graph neural network was aimed to reconstruct only a 2D projection of a track, a second step was implemented that uses the projection as a seed to reconstruct the full 3D track. In addition, the algorithm also provides an estimated value for the particle momentum, where the calculated relative momentum resolution was found to be 6.7%.

The second part of the thesis presents a study of the production mechanism of the Σ^0 hyperon via the exclusive reaction $p + p \rightarrow p + K^+ + \Sigma^0$ at beam energy 3.5 GeV with the HADES detector setup. The daughter Lambda hyperon $\Sigma^0 \rightarrow \Lambda \gamma$ (BR $\approx 100\%$) was reconstructed via the decay mode $\Lambda \rightarrow p \pi^-$ (BR $\approx 63.9\%$) partly within the main HADES acceptance and partly within the forward wall acceptance. A kinematic refit was applied by constraining the secondary proton and the pion to the nominal Λ mass and the overall missing mass to the photon mass. In total, 2613 events were reconstructed 58% are within the main HADES acceptance and 42% within the forward wall acceptance. Furthermore, the dynamics of the reaction $p + p \rightarrow p + K^+ + \Sigma^0$ were investigated by studying the angular distributions in the CMS, Gottfried-Jackson and helicity frames. The different angular distributions has been corrected using the inverse of the detector response matrix calculated by the SVD factorization method. The total production cross section of the Σ^0 hyperon was obtained by integrating the yield for the different angular distributions and found to be $\sigma = 18.74 \pm 1.01(stat) \pm 1.71(syst) \mu b$. The corrected CMS

distributions of the Σ^0 and the proton show anisotropies, this is more pronounced in the case of the proton, which is the expected behavior if pion exchange dominates the Σ^0 production process. The angular distribution in the $K^+\Sigma^0$ Gottfried-Jackson frame tends to be asymmetric, which could be caused by the excitation of nucleon resonances decaying into the $K^+\Sigma^0$ channel. In addition, the helicity angular distributions are highly non-isotropic, which is a clear indication that there is a resonant component of the Σ^0 production. In order to provide a better description of the experimental angular distributions, a partial wave analysis using BG-PWA has been performed. The BG-PWA determines the contribution of different partial waves to the $pK^+\Sigma^0$ production. Multiple fits have been performed and the fit quality is determined by a log-likelihood value. The best solution was obtained by including the initial p+p waves 2S_0 , 3P_0 , 3P_1 , 3P_2 , 1D_2 and 3F_2 . However, due to the poor statistics, it was not possible to obtain an accurate determination of the relative contribution of each intermediate nucleon resonance to the overall final state. Nevertheless, nucleon resonances with mass around $1.710 \text{ GeV}/c^2$ ($N^*(1710)$) and $1.900 \text{ GeV}/c^2$ ($N^*(1900)$ or $\Delta^*(1900)$) are certainly required by the fit.

The last part of the thesis presents a feasibility study to investigate excited hyperons radiative decays using the upgraded HADES setup and the new forward detector as part of the FAIR Phase-0 physics program. The study focus on the exclusive reconstruction of the reaction ($p + p \rightarrow p + K^+ + Y$), where Y is any one of the lower-laying excited hyperon. Once again, the daughter Λ ($Y \rightarrow \Lambda\gamma$) was reconstructed partly within the main HADES acceptance and partly within the forward detector acceptance. In order to suppress the main background ($p + p \rightarrow p + K^+ + \Lambda + \pi^0$), two missing mass cuts have been introduced, (i) the squared missing mass of the primary proton and the kaon $1.6 < MM^2(p_p K^+) [\text{GeV}^2/c^4] < 2.6$ and (ii) the squared missing mass of all charged particles $-0.04 < MM^2(p_p K^+ \Lambda) [\text{GeV}^2/c^4] < 0.01$. An additional discriminating variable was introduced, which is the opening angle $OA(\gamma\Lambda)$ in the hyperon rest frame that is required to be greater than 165° .

The overall signal reconstruction efficiency ϵ was calculated and found to be in the range 0.0250 - 0.0193 % and the expected count rates for the upcoming 2022 proton beam time is presented.

CONTENTS

1	INTRODUCTION	1
1.1	The Standard Model	1
1.1.1	Leptons	2
1.1.2	Quarks	2
1.1.3	Gauge Bosons	3
1.2	Quantum Chromodynamics	5
1.2.1	High Energy Regime	6
1.2.2	Low Energy Regime	7
1.3	The Quark Model and the Strange Sector	8
1.3.1	Hyperons	10
1.4	Thesis Outline:	11
2	EXPERIMENTAL SETUP	13
2.1	HADES Detector Setup	13
2.1.1	The Target	14
2.1.2	START Detector	14
2.1.3	The RICH Detector	14
2.1.4	The Magnet	15
2.1.5	The MDC Detector	15
2.1.6	The META System	15
2.1.7	The Forward Wall	17
2.2	HADES Software Tools	17
2.2.1	Event Generator	17
2.2.2	HGeant	17
2.2.3	DST	18
2.3	Facility for Antiproton and Ion Research	18
2.4	The \bar{P} ANDA Detector Setup	18
2.4.1	Forward Tracking System	21
2.5	\bar{P} ANDA Software Tools	22
3	DEEP LEARNING BASED TRACK RECONSTRUCTION	25
3.1	Introduction	26
3.1.1	Artificial Neural Networks ANN	27
3.1.2	Related Work	30
3.1.3	Graph Neural Networks	31
3.2	Training Phase	33
3.3	Prediction Phase	37

3.4	Addition of the stereo hits	39
3.5	Momentum Estimation	44
3.6	Summary	46
4	Σ^0 PRODUCTION IN P+P COLLISIONS	47
4.1	Theoretical Background	48
4.1.1	Phase Space Considerations	48
4.1.2	Production Mechanisms	50
4.1.3	Reference Frames	52
4.2	Analysis Procedure	56
4.2.1	Simulations	56
4.2.2	Start Time t_0 Reconstruction	58
4.2.3	Particle Identification PID	62
4.2.4	The Λ Hyperon Reconstruction	67
4.3	Kinematic Refit	72
4.3.1	Theory	72
4.3.2	Quality of the kinematic refit	75
4.3.3	Kinematic refit applied to $p + p \rightarrow p + K^+ + \Sigma^0$	76
4.4	Results	79
4.4.1	Signal Extraction	79
4.4.2	Angular Distributions	80
4.4.3	Acceptance and Efficiency Correction	81
4.4.4	Absolute Normalization	88
4.4.5	Systematic Uncertainties	90
4.4.6	Angular Distributions Revisited	92
4.5	Partial Wave Analysis	97
4.5.1	Quantum Numbers of the Initial State	100
4.5.2	Quantum Numbers of the Final State	101
4.5.3	BG-PWA Analysis Method	102
4.5.4	PWA Systematics	107
4.5.5	Total production cross section	108
4.6	Investigation of the Y^* Resonance Region	111
4.7	Summary	113
5	FEASIBILITY STUDY FOR RADIATIVE DECAYS OF EXCITED HYPERONS	115
5.1	FAIR Phase-0 and the HADES Upgrade	115
5.1.1	FAIR Phase-0 Physics Program	115
5.1.2	HADES Upgrade	117
5.2	Physics Motivations	120
5.3	Signal Reconstruction Strategy	122
5.3.1	Particle Identification PID	125
5.3.2	The Λ Hyperon Reconstruction	128
5.3.3	Background Suppression	132

5.3.4	Photon Identification	134
5.4	Excited hyperon Y^* Yield	136
5.4.1	Kinematic Refit	137
5.5	Summary	141
6	CONCLUSIONS AND OUTLOOK	143
6.1	Deep Learning Based Track Reconstruction:	143
6.2	Σ^0 Production in p-p Collisions:	144
6.3	Feasibility Study for Radiative Decays of Excited Hyperons	146
	Appendices	149
A	PERFORMANCE PLOTS OF THE PID MODEL	151
A.1	Performance of the VAE for $p(3.5\text{GeV})p \rightarrow pK^+\Sigma^0$	151
A.2	Performance of the PID NN model for $p(4.5\text{GeV})p \rightarrow pK^+Y^*$	153
B	COVARIANCE MATRIX ESTIMATION	155
B.1	Covariance Matrix Estimation for $p + p \rightarrow p + K^+ + \Sigma^0$ Analysis	155
B.2	Covariance Matrix Estimation for $p + p \rightarrow p + K^+ + Y^*$ Feasibility Study:	155
C	PARTIAL WAVE ANALYSIS: BACKGROUND ESTIMATION	163

LIST OF FIGURES

Figure 1	A schematic depiction of the SM fermions and gauge bosons [101].	5
Figure 2	Summary of determinations of α_s as function of the energy scale.	7
Figure 3	(a) The meson octet. (b) The baryon octet.	9
Figure 4	The baryon decuplet [68].	9
Figure 5	Schematic cross sectional view of the HADES detector setup [16].	13
Figure 6	The future FAIR facility with different accelerators and experiments annotated [53].	19
Figure 7	The \bar{P} ANDA detector setup [1].	20
Figure 8	The \bar{P} ANDA Forward Tracking Stations, adapted from [114].	21
Figure 9	The $x - z$ projection of the FTS straw tubes.	22
Figure 10	The PandaRoot workflow illustrating the main steps of the physics analysis chain [19].	23
Figure 11	A comparison between the performance of traditional ML algorithms vs DL algorithms with increasing amounts of data [95].	27
Figure 12	A Perceptron. The weighted sum of the inputs is calculated and then an activation function (a <i>sigmoid</i> function in this case) is applied. [90]	28
Figure 13	The validation curve, a relationship between between model capacity, training score, and validation score [127].	30
Figure 14	An ANN (a) without dropout (b) with dropout [95].	30
Figure 15	(a) Convolution operation on Euclidean datatype (an image). (b) Convolution operation on non-Euclidean datatype (a graph).	33
Figure 16	(a) The number of tracks in one event and (b) the number of FTS hits in one event.	34
Figure 17	An example of an input graph to the GNN.	34
Figure 18	(a) Classification accuracy as function of the number of iterations for the training data-set and a hold-out data-set. (b) The ROC curve evaluated on the hold-out data-set.	35
Figure 19	(a) The GNN output for true and fake edges. (b) The edge efficiency and purity as function of the GNN output.	36
Figure 20	The output graph corresponding to the input graph shown in Fig. 17).	36

- Figure 21 The QA measurements as function of the GNN output. (b) The QA measurements as function of the momentum. 40
- Figure 22 The distance between the reconstructed hit position and the actual hit position for (a) FST1, FTS2, (b) FST3, FTS4 and (c) FST5 and FTS6. 42
- Figure 23 The distance between the skewed layer x measurements and the predicted x positions for true combinations (blue) and false combinations (red). The distance shown for stations (a) FTS1, FTS2, (b) FST3, FTS4 and (c) FST5 and FTS6. 42
- Figure 24 A drawing showing the geometrical interpretation of compatible hits based on the fitted $x - z$ projections [50]. 43
- Figure 25 The distance between the reconstructed hit position and the actual hit position for (a) FST1, FTS2, (b) FST3, FTS4 and (c) FST5 and FTS6. 44
- Figure 26 (a) The particle momentum is estimated from the kick that the particle receives in the magnetic field. (b) The relative momentum resolution. 45
- Figure 27 Feynman diagrams representing t-channel scattering in case of (a) kaon exchange, (b) pion exchange and (c) pion exchange with an intermediate resonance produced, which decays to a hyperon and a kaon. 50
- Figure 28 Angular distribution of final state protons in the center of mass frame measured at beam momentum 5 GeV/c for (a) $p + p \rightarrow p + K^+ + \Lambda$ and (b) $p + p \rightarrow p + K^+ + \Sigma^0$. 52
- Figure 29 Definitions of different reference frames (a) center of mass frame, (b) Gottfried-Jackson frame and (c) the helicity frame. 54
- Figure 30 An example of the phase space fit for (a) $p + p \rightarrow p + p + \pi^+ + \pi^-$ (b) $p + p \rightarrow p + K^+ + \Sigma^0$. Determined cross section at beam energy 3.5 GeV and 4.5 GeV are shown. 57
- Figure 31 The absolute difference between the reconstructed momentum and the generated momentum as a function of the reconstructed momentum for (a) protons p , (b) pions π^- and (c) kaons K^+ . 58
- Figure 32 $MM(pK^+)$ missing mass distribution of the sum of all simulated channels before and after the momentum correction. 59
- Figure 33 The RICH matching quality for everything (in black) and for matched rings (in red). 61
- Figure 34 The reduced velocity β as a function of momentum (a) before t_0 and (b) after t_0 reconstruction (under the condition $|t_0| < 1$ ns). 61
- Figure 35 The Energy loss dE/dx as a function of the momentum for all particle candidates. 62

- Figure 36 Input features for the VAE for protons (green) and pions (blue) and kaons (red). 64
- Figure 37 A schematic diagram of the VAE used for the purpose of the PID task. 65
- Figure 38 (a) The Confusion matrix. (b) The ROC graph for protons p (green), pions π^+ (blue) and kaons K^+ . 66
- Figure 39 The output probability of the network as applied to real data as function of the particle mass squared for (a) protons p , (b) pions π^+ and (c) kaons K^+ . 67
- Figure 40 The Λ hyperon decay topology. 68
- Figure 41 (a) The primary vertex transverse position as function of the longitudinal position. Accepted events are within $-65 < z[mm] < -5$ and $r[mm] < 5$ as indicated by the white dashed line. (b) The primary vertex distribution in the $x - y$ plane for events in the target region $-65 < z[mm] < -5$. 68
- Figure 42 (a) The DCA between the p , and π^- tracks. (b) The DCA between the π^- track and the primary vertex $d_{\pi,pvtx}$ as a function of the DCA between the p track and the primary vertex $d_{p,pvtx}$. (c) The DCA between the Λ track and the primary vertex. 69
- Figure 43 The missing mass squared distribution of $pp_{hades}\pi^-$. The data are shown as black dots, the violet histogram is the simulation of $pp \rightarrow pp\pi^+\pi^-$, the red one is $pp \rightarrow pK^+\Lambda$ and the blue one is $pp \rightarrow pK^+\Sigma^0$ simulation. 70
- Figure 44 The invariant mass spectrum of the p_{hades} and π^- . The peak was fit by a Gaussian distribution and the background was fit by a fourth order polynomial. 70
- Figure 45 (a) The missing mass squared distribution of $pK^+p_{wall}\pi^-$. (b) The missing mass squared distribution of $pp_{wall}\pi^-$. 71
- Figure 46 The invariant mass spectrum of the p_{wall} detected in the FWall and π^- detected in HADES. 71
- Figure 47 The χ^2 probability density function for different numbers of degrees of freedom. 75
- Figure 48 The χ^2 distribution of (a) the HADES data-set and (b) the FWall data-set. 77
- Figure 49 The p-value $P(\chi^2)$ of (a) the HADES data-set and (b) the FWall data-set. 78
- Figure 50 The missing mass distribution of pK^+ before and after the kinematic refit for the (a) HADES data-set and (b) the FWall data-set. 78
- Figure 51 The missing mass distribution of the primary proton and the kaon for the sum of the HADES and the FWall data-sets. 79

- Figure 52 The photon energy spectrum calculated in the rest frame of the Σ^0 hyperon. 80
- Figure 53 Angular distributions in experimental data and simulation. The first row shows the CMS angular distributions of the Σ^0 hyperon, the proton p and the kaon K^+ , the second row shows the distributions for the three G-J angles and the third row shows the distributions for the three helicity angles. 82
- Figure 54 (b) The response matrix of the two kinematical variables $\cos\theta_{\Sigma^0}^{cms}$ and $p_{\Sigma^0}^{cms}$ and (b) the purity matrix. 86
- Figure 55 Comparison between different correction methods. (b) The corrected $dN/d\cos\theta$ data distribution and (b) the bias to the Monte Carlo simulation. 87
- Figure 56 Differential cross section of the Σ^0 hyperon in the CMS frame. 89
- Figure 57 The distribution of the of the determined cross section for different values of the selection criteria in the analysis. 91
- Figure 58 The proton G-J angle in the $p\Sigma$ reference frame. 92
- Figure 59 Differential cross section of the Λ hyperon in the CMS frame. 93
- Figure 60 Angular distributions in the CMS frame for (a) the Σ^0 , (b) the proton p and (c) the kaon K^+ . 94
- Figure 61 Angular distributions in the G-J frames (a) G-J angle of the proton in the $p\Sigma$ frame, (b) G-J angle of the kaon in the $K^+\Sigma$ frame and (c) G-J angle of the kaon in the K^+p frame. 95
- Figure 62 Angular distributions in the helicity frames (a) the helicity angle between p, Σ in the $K^+\Sigma$ frame, (b) the helicity angle between p, K^+ in the $p\Sigma$ frame and (c) the helicity angle between K^+, Σ in the K^+p frame. 95
- Figure 63 Pluto simulations of Σ^0 resonant production. (a) The $K^+\Sigma^0$ invariant mass and (b) the $p\Sigma^0$ invariant mass. 96
- Figure 64 The contributions of phase space and resonance production of Σ^0 compared to the experimental data, the reduced χ^2 is stated for both invariant masses. (a) The $K^+\Sigma^0$ invariant mass distribution and (b) the $p\Sigma^0$ invariant mass distribution. 97
- Figure 65 Angular distributions in the helicity frames corrected by the incoherent sum of the phase space and the resonant production. (a) The helicity angle between p, Σ in the $K^+\Sigma$ frame, (b) the helicity angle between p, K^+ in the $p\Sigma$ frame and (c) the helicity angle between K^+, Σ in the K^+p frame. 98
- Figure 66 A comparison between the experimental data and the best PWA solution for (a) the $K^+\Sigma^0$ invariant mass, (b) the $p\Sigma^0$ invariant mass and (c) the K^+p invariant mass distributions. 105

- Figure 67 A comparison between the experimental data and the best PWA solution. The upper row shows the CMS angular distributions, the middle row shows the G-J angular distributions and the bottom row shows the helicity angular distributions. 106
- Figure 68 Invariant mass spectra corrected with the best PWA solution. (a) The $K^+\Sigma^0$ invariant mass, (b) the $p\Sigma^0$ invariant mass and (c) the K^+p invariant mass distributions. 107
- Figure 69 Angular distributions in experimental data corrected by the best PWA solution. The upper row shows the CMS angular distributions, middle row shows the G-J angular distributions and the bottom row shows the helicity angular distributions. 108
- Figure 70 The Dalitz plot, the black line marks the kinematic boundary. (a) Before efficiency and acceptance correction and (b) after the correction. 109
- Figure 71 Compilation of cross sections from different experiments. The calculated production cross section of $p + p \rightarrow p + K^+ + \Sigma^0$ is shown by the green square. 110
- Figure 72 The missing mass of pK^+ after a tighter cut on the missing mass squared of $p\Lambda$ ($MM^2(p\Lambda) > 0.4\text{GeV}^2/c^4$) for the HADES (solid line) and the FWall datasets (dashed line). 111
- Figure 73 The different missing mass spectra after the fit to the simulation, the reduced χ^2 value is stated for each spectrum, (a) $MM(pK^+\Lambda)$, (b) $MM(pK^+)$ and (c) $MM(pK^+\Lambda)$. 113
- Figure 74 Local p-value as function of the $MM(pK^+)$. Large p-value is an indication that the data is consistent with the assumed hypothesis, which in this case the null hypothesis H_0 . The red dashed lines indicate the confidence levels. 113
- Figure 75 (a) Front view of the EMC, dimensions measured in millimeters. (b) 3D arrangement of the EMC modules [119]. 118
- Figure 76 Schematic cross sectional view of the upgrade HADES detector setup including the EMC and the FD [9]. 119
- Figure 77 Radiative decays of the lower lying excited state hyperons. 121
- Figure 78 Topology of EM decay for the exclusive reaction $p + p \rightarrow p + K^+ + (Y^* \rightarrow \Lambda\gamma)$. 122
- Figure 79 The polar angle distributions of the final state particles at the generator level for the reaction $p + p \rightarrow p + K^+ + (Y^* \rightarrow \Lambda\gamma)$. 123
- Figure 80 The difference between the reconstructed momentum and the generated momentum as a function of the reconstructed momentum for (a) protons p , (b) protons detected in the FD p_{fd} (c) pions π^- and (d) kaons K^+ . 126
- Figure 81 Distributions of input features to the neural network used for the PID. 127

- Figure 82 (a) The Confusion matrix. (b) The ROC graph for protons p (green), pions π^+ (blue) and kaons K^+ . The inset shows values of the area under curve AUC for the three classes. 128
- Figure 83 The DCA between the proton and the kaon tracks for all combinations and the distribution of the smallest DCA value in a given event. 129
- Figure 84 (a) The primary vertex transverse position as function of the longitudinal position. (b) The projection on the z-axis. 129
- Figure 85 (a) The DCA distribution between the p , and π^- tracks, (b) The DCA distribution between the π^- track and the primary vertex $d(\pi^-, pvtx)$ as a function of the DCA between the p track and the primary vertex $d(p, pvtx)$ and (c) the pointing angle vector distribution. 130
- Figure 86 The invariant mass distribution M_{p,π^-} before and after the topological cuts. 130
- Figure 87 The FRPC *tof* spectra for different particle species. The cut value is indicated by the dashed line. 131
- Figure 88 (a) The DCA between the FD proton track and the π^- for all channels and (b) for signal events. The dashed line indicates the cut value. 131
- Figure 89 The invariant mass distribution M_{p_{FD},π^-} before and after the *tof* and DCA cuts. 132
- Figure 90 The squared missing mass $MM^2(p_p K^+)$ distribution in (a) linear and (b) logarithmic scale. 133
- Figure 91 The squared missing mass $MM^2(p_p K^+ \Lambda)$ distributions in (a) linear and (b) logarithmic scale. 133
- Figure 92 The velocity ($\beta = v/c$) spectrum for all photon candidates (black), photons with clusters that are geometrically uncorrelated with charged tracks (blue) and real photons (green). 134
- Figure 93 (a) The optimization of the photon energy cut and (b) the reconstructed photon energy for all clusters (black), photons with clusters that are geometrically uncorrelated with charged tracks (blue) and real photons (green). 135
- Figure 94 (a) The difference between the EMC cluster energy and the generated photon energy as a function of the cluster energy. (b) The $\Lambda\gamma$ invariant mass distribution of the resonances before (black) and after (blue) the energy correction. 135
- Figure 95 The $\Lambda\gamma$ invariant mass distribution after all cuts. 136
- Figure 96 (a) The opening angle between the Lambda and the photon $OA(\Lambda\gamma)$ in the hyperon rest frame and (b) The $\Lambda\gamma$ invariant mass distribution after the opening angle cut. 137

- Figure 97 The χ^2 distribution for (a) the photon hypothesis M_γ and (b) the pion hypothesis M_{π^0} . 139
- Figure 98 The p-value for (a) the photon hypothesis and (b) the pion hypothesis. 139
- Figure 99 The logarithm of the p-value for the photon hypothesis on the x -axis and for the pion hypothesis on the y -axis for (a) signal events and for (b) background events. 140
- Figure 100 The $\Lambda\gamma$ invariant mass distribution after applying the χ^2 cut (a) without the $OA(\Lambda\gamma)$ cut and (b) with the $OA(\Lambda\gamma)$ cut applied. 140
- Figure 101 The momentum as a function of the polar angle for the (a) π^+ , (b) p and (c) K^+ . 152
- Figure 102 The efficiency map for the (a) π^+ , (b) p and (c) K^+ . 152
- Figure 103 The purity map for the (a) π^+ , (b) p and (c) K^+ . 152
- Figure 104 The momentum as a function of the polar angle for the (a) π^+ , (b) p and (c) K^+ . 153
- Figure 105 The efficiency map for the (a) π^+ , (b) p and (c) K^+ . 153
- Figure 106 The purity map for the (a) π^+ , (b) p and (c) K^+ . 154
- Figure 107 The resolution plots of protons detected in the main HADES detector setup for (a) the absolute momentum inverse ($1/p$), (b) polar angle (θ) and (c) azimuthal angle (ϕ). 156
- Figure 108 The resolution plots of kaons for (a) the absolute momentum inverse ($1/p$), (b) polar angle (θ) and (c) azimuthal angle (ϕ). 156
- Figure 109 The resolution plots of pions for (a) the absolute momentum inverse ($1/p$), (b) polar angle (θ) and (c) azimuthal angle (ϕ). 156
- Figure 110 The pull distributions (see Eq. 29) of protons detected in the main HADES detector setup for (a) the absolute momentum inverse ($1/p$), (b) polar angle (θ) and (c) azimuthal angle (ϕ). 157
- Figure 111 The pull distributions (see Eq. 29) of kaons detected in the main HADES detector setup for (a) the absolute momentum inverse ($1/p$), (b) polar angle (θ) and (c) azimuthal angle (ϕ). 157
- Figure 112 The pull distributions (see Eq. 29) of pions for (a) the absolute momentum inverse ($1/p$), (b) polar angle (θ) and (c) azimuthal angle (ϕ). 157
- Figure 113 The pull distributions (see Eq. 29) of protons reconstructed in the forward wall detector setup for (a) the absolute momentum inverse ($1/p$), (b) polar angle (θ) and (c) azimuthal angle (ϕ). 158
- Figure 114 The resolution plots for the absolute momentum inverse ($1/p$) (a) of protons detected in the main HADES detector setup, (b) of protons detected in the FD, (c) kaons and (d) pions. 158

- Figure 115 The resolution plots for the polar angle (θ) (a) of protons detected in the main HADES detector setup, (b) of protons detected in the FD, (c) kaons and (d) pions. 158
- Figure 116 The resolution plots for the azimuthal angle (ϕ) (a) of protons detected in the main HADES detector setup, (b) of protons detected in the FD, (c) kaons and (d) pions. 159
- Figure 117 The resolution plots for the DCA between the track and the beam axis (R) (a) of protons detected in the main HADES detector setup, (b) of protons detected in the FD, (c) kaons and (d) pions. 159
- Figure 118 The resolution plots for the z -coordinate of the PCA between the track and the beam axis (z) (a) of protons detected in the main HADES detector setup, (b) of protons detected in the FD, (c) kaons and (d) pions. 159
- Figure 119 The pull distributions for the absolute momentum inverse ($1/p$) (a) of protons detected in the main HADES detector setup, (b) of protons detected in the FD, (c) kaons and (d) pions. 160
- Figure 120 The pull distributions for the polar angle (θ) (a) of protons detected in the main HADES detector setup, (b) of protons detected in the FD, (c) kaons and (d) pions. 160
- Figure 121 The pull distributions for the azimuthal angle (ϕ) (a) of protons detected in the main HADES detector setup, (b) of protons detected in the FD, (c) kaons and (d) pions. 160
- Figure 122 The pull distributions for the DCA between the track and the beam axis (R) (a) of protons detected in the main HADES detector setup, (b) of protons detected in the FD, (c) kaons and (d) pions. 161
- Figure 123 The pull distributions for the z -coordinate of the PCA between the track and the beam axis (z) (a) of protons detected in the main HADES detector setup, (b) of protons detected in the FD, (c) kaons and (d) pions. 161
- Figure 124 The missing mass distribution of the primary proton and the kaon for the sum of the HADES and the FWall data-sets. 164
- Figure 125 A comparison between the experimental data (black points) for which $1.090 < MM(pK^+)[GeV/c^2] < 1.150$ and the PWA solution (red histogram) listed in Tab. 17 for (a) the $K^+\Lambda$ invariant mass, (b) the $p\Lambda$ invariant mass and (c) the K^+p invariant mass distributions. 164

Figure 126 A comparison between the experimental data (black points) for which $1.090 < MM(pK^+)[GeV/c^2] < 1.150$ and the PWA solution (red histogram) listed in Tab. 17. The upper row shows the CMS angular distributions, the middle row shows the G-J angular distributions and the bottom row shows the helicity angular distributions. 165

LIST OF TABLES

Table 1	Production cross section of the simulated channels. 57
Table 2	Parameters of fit to the Monte Carlo bias for the different correction methods. 88
Table 3	The variation of different cuts used to evaluate the systematic uncertainty. 91
Table 4	A list of N^* and Δ^* resonances that might contribute to the $pK^+\Sigma^0$ reaction. 96
Table 5	Possible combinations of the initial state of two protons with $J^P = \frac{1}{2}^+$. 101
Table 6	Possible combinations of the non-resonant production of $pK^+\Sigma^0$ used in this study. 102
Table 7	Possible combinations of the proton and a nucleon resonance (N^* -p or Δ^* -p) to produce the final state $pK^+\Sigma^0$ out of a certain p-p initial state. 103
Table 8	Partial wave contributions to the total $pK^+\Sigma^0$ production. 104
Table 9	The best five PWA solutions. 109
Table 10	The extracted total production cross section from the different differential distributions. 110
Table 11	EM transition $Y^* \rightarrow \Lambda\gamma$ decay widths in keV. 122
Table 12	The acceptance of final state particles of signal events as calculated from the PLUTO output. 123
Table 13	Signal and background channels simulated with the corresponding estimated cross section and the weight factor. 125
Table 14	Contributions of the different background channels to the invariant mass spectrum $M_{\Lambda\gamma}$ presented in Fig. 95. 136
Table 15	Comparison between the four invariant mass spectra $M_{\Lambda\gamma}$ in terms of the signal significance (ss) and the signal reconstruction efficiency (ϵ %). 141
Table 16	Estimated count rates (events/day) for the EM decay of low lying excited state hyperons for the future beam time. 141
Table 17	Partial wave contributions to the total $pK^+\Lambda$ production. 163

INTRODUCTION

Particle physics tries to answer the ancient question “What is the world made of ?!”. The ancient Greeks were first to answer this question by describing nature in a systematic way. The Greek Philosopher Democritus (460 B.C.) proposed a model, which stated that matter consists of indivisible particles called atoms and a void. He stated that atoms are indestructible, unchangeable, infinite in number and various in size and shape, and perfectly solid.

It was only recently that individual atoms were discovered. In 1897, J.J. Thomson discovered the *electron* with his famous experiment on cathode rays. Since the atom as a whole is electrically neutral, Thomson suggested that electrons were suspended in heavy positively charged paste, like the plums in a pudding. Soon afterwards in 1911, Sir Rutherford proposed a different a model for the atom. Rutherford designed an experiment, in which a beam of alpha particles, emitted by a radioactive material are fired into a thin sheet of gold foil. He observed that most of the alpha particles pass through the sheet completely undeflected, but a few of them scatter at small angles. Rutherford concluded that the atoms have their positive charge concentrated in a tiny nucleus (10^{-5} smaller than the size of the atom) that contains almost all the mass of the atom, subsequently, the nucleus of the hydrogen was called the *proton*. The essential nature of the atomic nucleus was established by James Chadwick in 1932 with the discovery of the *neutron*, an electrically neutral twin to the proton. These three particles accounted for the structure of matter. But with the discovery of anti-particles, muons, pions, strange particles, neutrinos and a plethora of other particles, a whole new world was uncovered [68].

1.1 THE STANDARD MODEL

There are four known fundamental forces of nature, the gravitational force, the weak nuclear force, the electromagnetic force, and the strong nuclear force. The elementary particles interact with each other through one or more of these forces. However, gravity is

2 INTRODUCTION

too weak to play any significant role in elementary particle interactions. All interactions are non-contact forces, which means that a force carrier (or a mediator) act between elementary particles.

During the second half of the 20th century a theory emerged that described all the elementary particles and their interactions, except gravity, the theory has come to be called the *Standard Model of particle physics* (SM). The SM was formulated and developed by the joint effort of experimental and theoretical physicists, it postulates that the universe consists of three families of *fermions* (half integer spin particles) classified into *leptons* and *quarks*. This classification is according to the way the particles interact with each other. Quarks interact via the electromagnetic, weak and strong forces, while leptons interact via the electromagnetic and weak forces. For each fermion there exists an anti-fermion of the same mass and quantum numbers except for an opposite electric charge. The forces between fermions are mediated by particles known as *gauge bosons* (integer spin particles).

Quantum Field Theory QFT is the theoretical framework that describes the interactions between elementary particles, it combines the Lagrangian formalism from the classical field theory with the quantum mechanics and special relativity. Within the QFT framework, all the fundamental interactions derive from one general principle, the requirement of *local gauge invariance*, where the force between two particles is visualized as being due to the exchange of field quanta that are called gauge bosons.

1.1.1 Leptons

The group of leptons consist of the three charged leptons: the *electron* e^- , *muon* μ^- and *tau* τ^- and the electrically neutral leptons: the *electron neutrino* ν_e , *muon neutrino* ν_μ , *tau neutrino* ν_τ and their corresponding anti-particles. The charged leptons interact with each other via the electromagnetic and weak force, while neutrinos interact only via the weak forces.

1.1.2 Quarks

The group of quarks consist of the six different flavors, three of them carry a fractional positive charge $+\frac{1}{3}$ of the elementary charge (e): the *up* (u), *charm* (c), and *top* (t) and the other three carry a fractional negative charge $-\frac{2}{3}$: the *down* (d), the *strange* (s) and the *bottom* (b) and their corresponding anti-particles. The quarks interact with each other via the electromagnetic, weak and strong forces.

Both leptons and quarks are believed to be elementary that is have no internal structure and they are arranged in three generations in increasing order of mass. Apart from the mass differences, the physical properties in the three generations are the same in the sense that they possess the same fundamental interactions.

1.1.3 Gauge Bosons

Electromagnetic Interaction

The Quantum Electrodynamics QED is a QFT that explains the electromagnetic interaction at a fundamental level, where in this case the interaction is mediated by the exchange of *virtual photons* (γ). All particles that carry an electric charge feel the electromagnetic force. For each type of interaction, there is an associated *coupling strength* between the gauge boson and the fermion, which is a measure of the probability that the fermion emits or absorbs a gauge boson. For the electromagnetic force, it is the familiar fine structure constant:

$$\alpha = \frac{e^2}{4\pi\epsilon_0\hbar c} \approx \frac{1}{137},$$

where e is the electron charge, \hbar is the reduced Planck constant, ϵ_0 is the permittivity of vacuum and c is the speed of light.

Weak Interaction

The weak interaction occurs between all elementary fermions, and it is classified into charged or neutral interactions depending on whether the particle participating in the interaction suffers from a change of electric charge or not. The charged weak interaction, which is responsible for the nuclear β decay, is mediated by the charged *weak gauge bosons* W^\pm , while the neutral weak interaction is mediated by the Z boson. Due to the huge mass of the weak gauge bosons, the weak interaction has a small coupling strength $\alpha_w \approx 10^{-8}$ and it has an extremely short effective range (10^{-16} m) compared to the infinite range of the electromagnetic force.

In the SM, the electromagnetic and the weak interaction are low-energy manifestation of the *electroweak interaction*, which is introduced in the Glashow-Weinberg-Salam theory. The fermions that interact via the electroweak force carry a *weak hypercharge* Y_w that is

conserved during the interaction, the weak hypercharge is related to the *weak isospin* T and the electric charge Q via the Gell-Mann Nishijima formula:

$$Q = T_3 + \frac{1}{2}Y_w,$$

where T_3 is the third component of the weak isospin. The weak isospin of the weak gauge bosons is $T=1$, where the charged bosons W^\pm have $T_3 = \pm 1$ and the Z boson have $T_3 = 0$.

The Strong Interaction

The strong interaction binds quarks together to form *mesons* (quark anti-quark pair e.g. π, μ, \dots), *Baryons* (three quarks bound state, e.g. p, n, \dots) and *anti-Baryons* (three anti-quark bound state, e.g. $\bar{p}, \bar{\Lambda}, \dots$). Both baryons and mesons are categories of more general objects named *Hadrons*, where a hadron is composite particle made of two or more quarks. As a consequence of the Pauli exclusion principle, quarks are assigned a *color charge*, where a quark comes in one of three different colors, **red** r , **green** g and **blue** b . These colors have nothing to do with actual colors, they are just labels to distinguish different quarks. The *gluons* are the mediators of the strong interaction. There are eight of them predicted by the Quantum Chromodynamics QCD, which is a QFT theory that describes the strong interaction. QCD is discussed in more detail in the next section.

The Higgs Boson

The final building block of the SM is the *Higgs boson*, which was discovered in 2012 by the ATLAS and CMS collaborations independently [2, 38]. In the SM, particles acquire mass through a process known as *spontaneous electroweak symmetry breaking*. The idea is to suppose that the vacuum contains a scalar field known as the Higgs field, which has a non vanishing Vacuum Expectation Value (VEV) in the ground state. The result is that the field quanta (the gauge bosons) acquire mass when propagating through the Higgs field.

The properties of the elementary particles and the force carriers are depicted in Fig. 1, these properties along with physical observables are derived from the SM Lagrangian, which has to be invariant under Lorentz transformations, in addition it has to satisfy some *discrete symmetries*, which of particular importance in particle physics. These symmetries are the *charge conjugation* C , *parity* P and *time reversal* T . Because of the local gauge invariance principle, the SM Lagrangian has to be invariant under *local gauge*

symmetries. All of these symmetries are represented as elements of *Lie groups*. Therefore, the SM has a symmetry group $SU(3)_C \times SU(2)_L \times U(1)_Y$, where C stands for color, L means it only acts on the *left-handed* states and Y stands for hypercharge.

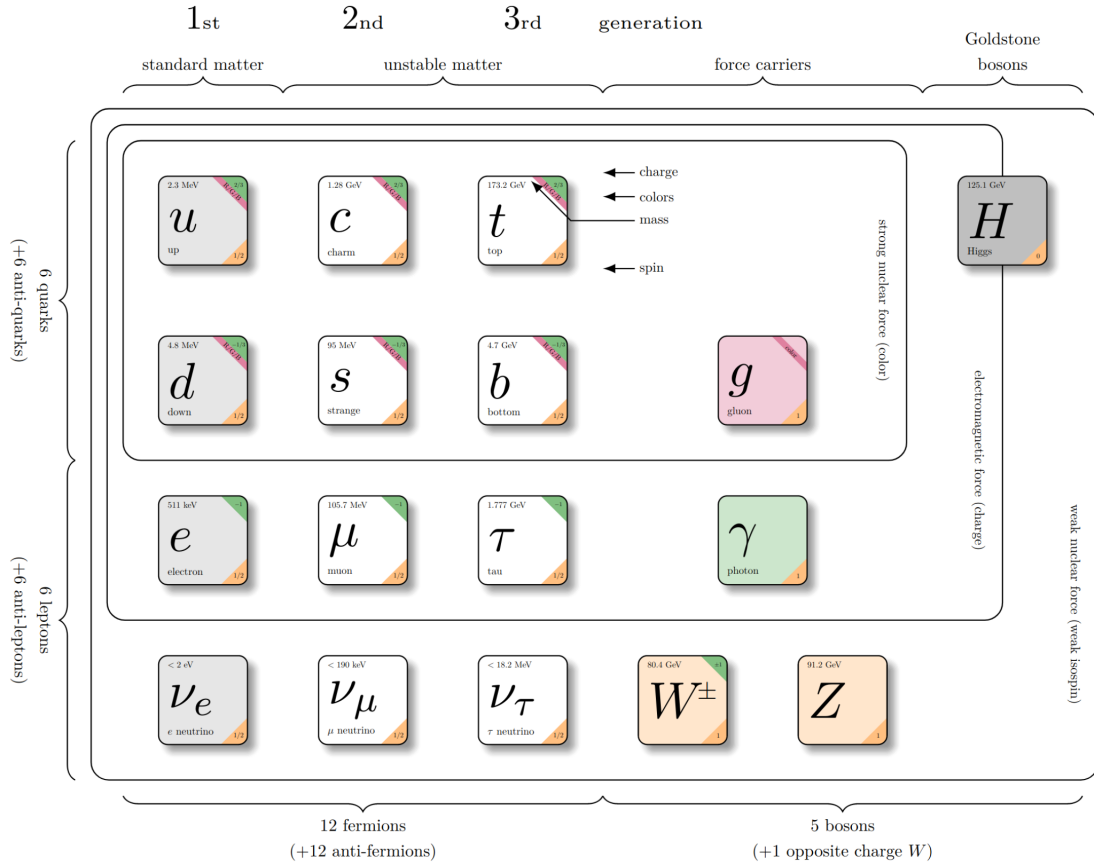


Figure 1: A schematic depiction of the SM fermions and gauge bosons [101].

1.2 QUANTUM CHROMODYNAMICS

The theory of strong interaction is the Quantum Chromodynamics QCD, the underlying symmetry associated with the QCD is the invariance under $SU(3)$ local phase transformation. Since the $SU(3)$ symmetry group has eight generators, there are eight gauge bosons (the *gluons*) and because the eight generators do not commute, QCD is a non-Abelian gauge theory, which gives rise to gluon-gluon *self interaction vertices*. The $SU(3)$ is an exact color symmetry, where the “color charge” r , g , and b are the labels of the orthogonal states in the $SU(3)$ color space. Only particles that carry a non-zero color charge feel the strong interaction. Therefore, only quarks interact via the strong force. However, experimentally “free” quarks have never seen directly. This is explained by the *color confinement* hypothesis, which states that colored particles are always confined to

color singlet states and no object with non-zero color charge can propagate as a free particle. The color confinement hypothesis places strong restrictions on possible hadronic states, where color singlet hadronic state is either in the form of mesons ($q\bar{q}$), baryons (qqq) or anti-baryons ($\bar{q}\bar{q}\bar{q}$). The existence of pentaquark states ($qqqq\bar{q}$) is in principle allowed by the color confinement hypothesis. In 2015, the LHCb collaboration announced the discovery of a new pentaquark particle $P_c(4312)^+$ with statistical significance of 7.3σ , however, the binding mechanism of the pentaquark is not yet clear if it is a pure hadronic state ($qqqq\bar{q}$) or a hadronic molecule ($q\bar{q}$)-(qqq) [3]. In addition, *tetraquark* states, which are exotic particles, have been reported by many experiments. In 2003, the Belle collaboration announced the discovery of the exotic meson $X(3872)$, which proposed to be a tetraquark state [42]. Since then, many of exotic states have been uncovered, most recently, the LHCb collaboration reported the discovery of exotic states with a quark content ($c\bar{c}u\bar{s}$) decaying to the $J/\psi K^+$ final state [4].

The coupling strength of the strong force α_s depends on the energy scale of the interaction as a result of the *vacuum polarization* phenomena. In terms of the squared four-momentum transfer q^2 , the QCD “running” coupling strength is expressed as [124]:

$$\alpha_s(q^2) = \frac{\alpha_s(\mu^2)}{1 + B\alpha_s(\mu^2)\ln(\frac{q^2}{\mu^2})}; \quad B = \frac{11N_c - 2N_f}{12\pi}, \quad (1)$$

where N_f is the effective number of quark flavors, N_c is the number colors defined at an energy scale μ . In a t-channel annihilation process both q^2 and μ^2 are negative and the coupling strength is often written as $\alpha(Q^2)$. Since $N_f = 6$ and $N_c = 3$, then B is greater than zero, hence, α_s decreases with increasing momentum transfer. This behavior is known as *asymptotic freedom*. Fig. 2 presents a summary of experimental determinations of the QCD running coupling strength at different energy scales. An average value was obtained at the Z boson mass $M_Z = 91.2 \text{ GeV}/c^2$, $\alpha_s(M_Z) = 0.1181 \pm 0.0011$.

The description of the strong interaction can be put into one of two categories depending on the energy regime:

1.2.1 High Energy Regime

High energy regime at $|q| > 100 \text{ GeV}$, the coupling strength is sufficiently small $\alpha_s \approx 0.1$ so that perturbation theory can be applied to predict different experimental observables, in this case the theory of strong interactions is referred as *perturbative QCD* (pQCD) and it provides very accurate predictions. This is the typical scale of modern high-energy

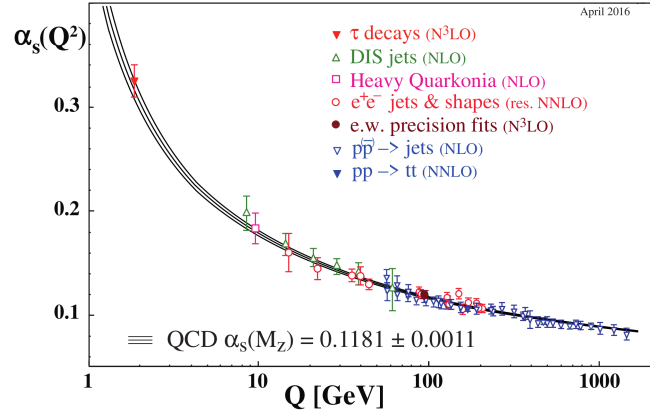


Figure 2: Summary of determinations of α_s as function of the energy scale. The determination is based on perturbative approaches [121].

collider experiments. In this regime, the quarks are the relevant degrees of freedom, the combination of quark anti-quark to form a meson results in a colored octet and colorless singlet, in this case the color wave function of mesons is [124]:

$$\psi(q\bar{q}) = \frac{1}{\sqrt{3}}(r\bar{r} + g\bar{g} + b\bar{b}),$$

while the combination of three quarks to form a baryon results in a colorless singlet [124]:

$$\psi(qqq) = \frac{1}{\sqrt{6}}(rgb - rbg + gbr - grb + brg - bgr).$$

1.2.2 Low Energy Regime

At small energies $|q| \sim 1$ GeV, the coupling strength is of $\mathcal{O}(1)$ and the perturbation theory is no longer applicable. In this case, the theory of strong interaction is referred as *non-perturbative QCD* (non-pQCD) and the understanding at this energy regime is still very poor. The transition between pQCD and non-pQCD is characterized by a critical energy scale given by [39]:

$$\Lambda_{QCD}^2 = \frac{\mu^2}{e^{1/B\alpha_s(\mu)}}; \quad B = \frac{1}{4\pi} \left(11 - \frac{2}{3}N_f\right).$$

At this energy scale the QCD coupling constant diverges to infinity, which is defined as the energy, below which the perturbation theory is inapplicable.

In this energy regime, the wavelength of the exchange particle is large compared to the radius of the interacting hadron and thus the interaction happens between hadrons not constituent quarks. Therefore, in the non-pQCD, the degrees of freedom are no longer quarks and gluons but hadrons themselves. Since the perturbation theory is not applicable, other methods were developed to describe the strong interaction. The Chiral Perturbation Theory χ PT [97] is one of those methods, where an effective Lagrangian is constructed using hadrons as the degrees of freedom. Another interesting and powerful tool is the Lattice QCD [70], which is a gauge theory formulated on a lattice of space-time points and solved through numerical calculations.

1.3 THE QUARK MODEL AND THE STRANGE SECTOR

During the period (1937-1961), many mesons and baryons were discovered, including muons (μ), pions (π) and strange particles (e.g., K , Λ , ...), they were referred collectively as the *particle zoo*. In 1961, Murray Gell-Mann proposed the *Eightfold Way* to arrange the particles of the zoo into geometrical patterns according to their *charge* and *strangeness* quantum numbers [68]. The *pseudoscalar mesons* ($J^P = 0^-$, where J is the total angular momentum and P is the parity) can be arranged into a hexagonal pattern called the *meson octet* (see Fig. 3a), where the particle charge (Q) lie along the diagonal of the octet and particles of the same strangeness (S) lie along the same row. Baryons, on the other hand, are arranged into the *baryon octet* ($J^P = \frac{1}{2}^+$) (Fig. 3b), contains the eight lightest baryons and the *baryon decuplet* ($J^P = \frac{3}{2}^+$) incorporating ten heavier baryons (Fig. 4). Once again, particles having the same strangeness lie on the same row and the diagonal elements represent the particle charge [68].

The *Eightfold Way* led to the discovery of the Ω^- baryon [25] in 1964, which was the last piece that completed the baryon decuplet. The discovery of Ω^- proved the success of the *Eightfold Way* and eventually led to formulating the *quark model* [63].

In the quark model, the hadron are composed of quarks, where a baryon is three quark state (qqq) and a meson is quark-anti-quark state ($q\bar{q}$) and all the *Eightfold Way* multiples emerge naturally.

Because the strong force Hamiltonian treats all quark flavors equally, the strong force must possess a flavors symmetry, for example, nothing would change if an up-quark is replace by a down-quark or vice versa. As a consequence of this up-down flavor symmetry, the proton (uud) and the neutron (udd) are manifestation of a single entity named the *nucleon*. This flavors symmetry can be extended to include the strange quark, however,

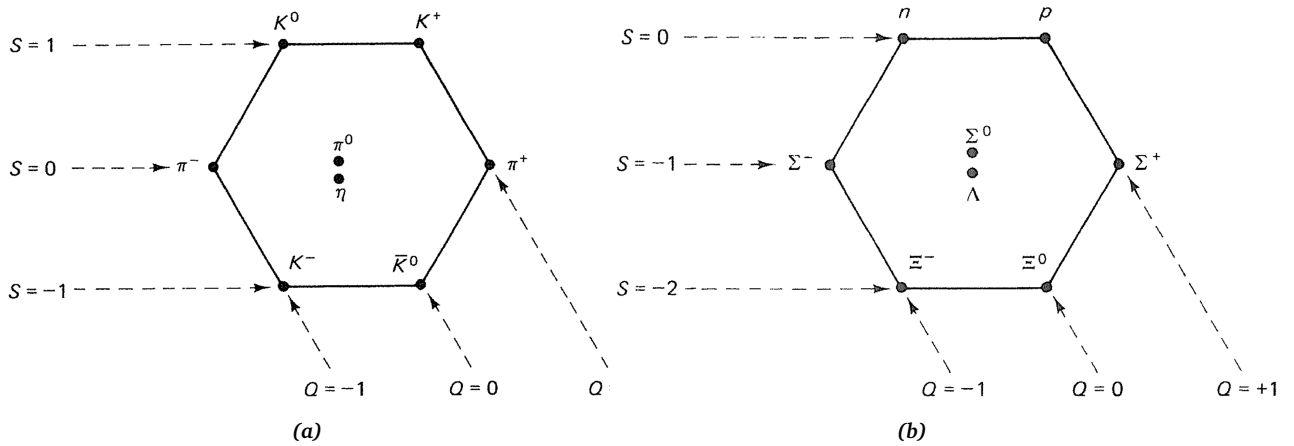


Figure 3: (a) The meson octet. (b) The baryon octet. Diagonal lines represent the particle charge (Q) and horizontal lines determine the strangeness (S) [68].

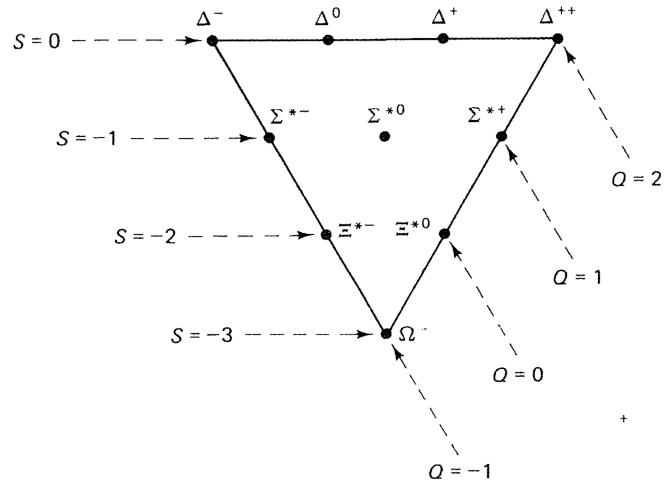


Figure 4: The baryon decuplet [68].

in this case the flavors symmetry is not exact since the strange quark mass ($M_{strange} \approx 96 \text{ MeV}/c^2$) is much larger than the up and down quark masses ($M_{up} \approx 2.2 \text{ MeV}/c^2$ and $M_{down} \approx 4.7 \text{ MeV}/c^2$). The mathematical group that describes the up-down-strange flavor symmetry is the $SU(3)$ symmetry group.

The total baryon wave function have to account for all possible degrees of freedom. Therefore, it is composed of several terms, the spatial term, the color term, the spin term and the flavor term and it can be written as:

$$\psi(qqq) = \phi(space)\eta(color)\phi(spin)\chi(flavors).$$

The overall wave function $\psi(qqq)$ is required to be antisymmetric, i.e. it must obey the Pauli exclusion principle since quarks are fermions. For ground state baryons ($L=0$), the space wave function is symmetric, since the exchange symmetry is given by (-1^L) . Therefore, for the total wave function to be antisymmetric, the combination $\phi(space)\eta(color)$ has to be antisymmetric and the combination $\phi(spin)\chi(flavors)$ has to be symmetric under interchange of any two quarks. The flavor wave function of the ground state baryons is obtained by combining three quarks in $SU(3)$ flavors symmetry:

$$3 \otimes 3 \otimes 3 = 10 \oplus 8 \oplus 8 \oplus 1,$$

which gives rise to a symmetric decuplet, two mixed symmetry octets and a totally antisymmetric singlet state. In the quark model, the ground state baryon masses are given by [124]:

$$M = m_1 + m_2 + m_3 + A \left(\frac{\langle S_1 \cdot S_2 \rangle}{m_1 m_2} + \frac{\langle S_1 \cdot S_3 \rangle}{m_1 m_3} + \frac{\langle S_2 \cdot S_3 \rangle}{m_2 m_3} \right), \quad (2)$$

where A is a parameter can be determined experimentally, S_1, S_2 and S_3 are the three quark spins and m_1, m_2 and m_3 are the *constituent* quark masses.

1.3.1 Hyperons

A hyperon is a baryon that contains one or more strange-quarks. Hyperons are of particular interest since the strange quark is heavier than the up/down quarks, where in this case the $SU(3)$ flavors symmetry is not exact. In most nucleon models, the strange quark appears as a sea quark, while the lighter up/down quarks appears as both valance and sea quarks [102]. Therefore, hyperons serves as a tool to investigate several phenomena. The scale of a hadronic reaction is influenced by the mass of the produced quarks, the strange quark mass $M_s \approx 96 \text{ MeV}/c^2$ is close to the confinement scale ($\Lambda_{QCD} = 100 - 300 \text{ MeV}$). Therefore, hyperon production provides a straightforward way to study the confinement domain of QCD. Furthermore, good understanding of the strangeness production mechanism is crucial for model calculations of heavy-ion collisions since strangeness enhancement is generally seen to be a signature for the formation of the quark-gluon plasma [93].

Hyperons decay via the strong, electromagnetic or weak interactions. However, weak hyperon decays violate parity and as a consequence the hyperon spin is experimentally accessible, i.e, if the hyperon is produced with some degree of polarization, this will

manifest in the angular distributions of the daughter particles. Therefore, hyperon weak decays serve as a tool for testing CP violation.

The quark model was remarkably successful in describing the ground state hyperon wave functions, however, it was less successful in the case of excited hyperons (Y). Therefore, various theoretical models have been proposed to better describe the hyperon wave function. A powerful tool to discriminate between different models is the electromagnetic decays of a decuplet hyperon to an octet hyperon ($Y \rightarrow \Lambda\gamma$, where Y is an excited hyperon) as different models predict different decay widths. In addition, the radiative decays provide an important milestone in the hyperon Dalitz decay studies ($Y \rightarrow \Lambda e^+ e^-$) that provide access to the electromagnetic transition form factors, which are an important tool to study the internal structure of hyperons [108].

1.4 THESIS OUTLINE:

This thesis focusses on the hyperon production and their radiative decays. Chapter 2 briefly describes the HADES and \overline{P} ANDA detector setups. Chapter 3 presents a deep learning algorithm proposed for the \overline{P} ANDA straw tube forward tracker, the detection of forward emitted particles is of particular importance for the reconstruction of ground state and excited hyperons. Chapter 4 presents an analysis of the production mechanism of the Σ^0 hyperon produced in p+p collision using the HADES detector setup. This analysis is the first step towards measuring the excited hyperon's radiative decays as the Σ^0 hyperon decays electromagnetically ($\Sigma^0 \rightarrow \Lambda\gamma$) with a branching ratio $\approx 100\%$. In addition, this measurement highlights the importance of the detection of forward emitted particles for the hyperon reconstruction. Chapter 5 presents a feasibility study for the radiative decay of excited hyperons using the upgraded HADES setup and the new forward detector, which is based on \overline{P} ANDA straw tubes.

EXPERIMENTAL SETUP

In this chapter, a brief description of the HADES and the future \bar{P} ANDA detector setups are presented. This includes a description of the experiment software tools that have been used in order to perform the Monte-Carlo simulations.

2.1 HADES DETECTOR SETUP

The High Acceptance Di-Electron Spectrometer (HADES) is located at the GSI Helmholtzzentrum für Schwerionenforschung in Darmstadt [16]. It is a fixed target experiment designed especially to study in-medium properties of the light vector mesons ρ , ω and ϕ via their rare di-electron decays e^+e^- . As its name suggests, the HADES detector has excellent capabilities for electron reconstruction and identification, but it also provides good hadron identification capabilities, which has been exploited in strangeness physics investigations (e.g [11, 12]). The detector setup operates at the SchwerIonen Synchrotron (SIS18) accelerator, which can deliver beams with kinetic energies in the range 1-2 AGeV for heavy-ions and proton beams up to 4.5 GeV.

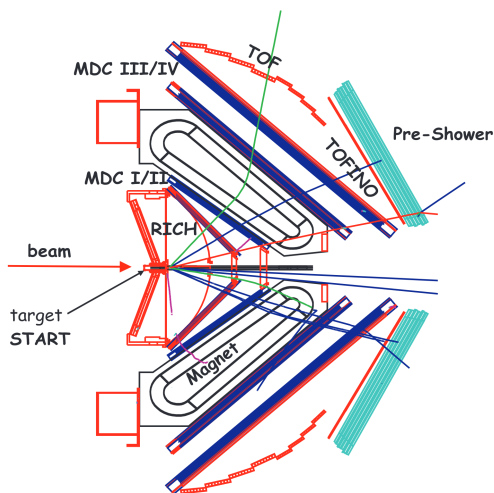


Figure 5: Schematic cross sectional view of the HADES detector setup [16].

Fig. 5 shows a schematic cross sectional view of the HADES setup. The detector is characterized by six identical sectors which cover almost the full azimuthal range and cover the polar angular range from $\theta = 18^\circ$ to $\theta = 85^\circ$. For proton-induced reactions, the relative momentum resolution for charged particle tracks was determined to be $\approx 4\%$ [29]. In the following the different sub-systems of the spectrometer are briefly described, a detailed description of the different HADES sub-systems can be found in [16].

2.1.1 *The Target*

The HADES target is placed in a magnetic field free region, various targets can be mounted in the setup depending on the physics experiment. For heavy ion collisions, a segmented solid state target is used, while the elementary reactions are studied with either a liquid hydrogen target (LH_2) or a polyethylene target (CH_4).

2.1.2 *START Detector*

In order to obtain a start signal for the time of-flight measurement, a dedicated START detector has placed upstream the target position. For high intensity proton beams, the START detector is based on mono-crystalline Chemical Vapor Deposition (CVD) diamond strip counters [96].

2.1.3 *The RICH Detector*

The Ring Imaging Cherenkov (RICH) detector is the first sub-detector encountered by the particles after the collision, which encloses the target and covers the full HADES acceptance. It is a hadron-blind system that designed to detect e^+e^- pairs with momenta in the range $0.1 < p$ [GeV/c] < 1.5 . It consists of a volume filled with C_4F_{10} having a characteristic Lorentz factor for Cherenkov radiation of $\gamma_{thr} = 18$, which suppresses Cherenkov light emitted by hadrons in this momentum range. The Cherenkov photons are reflected by an aluminum coated carbon mirror through a CaF_2 window and enter the photon detector volume filled by CH_4 , where they hit a CsI photo cathode. The produced photo-electrons are collected by Multi-Wire Proportional Chambers (MWPC), which are equipped with individual pad readout. Leptons can be identified by matching the RICH ring position with a reconstructed track.

2.1.4 *The Magnet*

The determination of a charged particle's momentum requires a magnetic field, since a charged particle traversing a magnetic field experiences the Lorentz force, which bends the particle trajectory. For this purpose, an in-homogeneous toroidal magnetic field (IronLess Superconducting Electromagnet ILSE) is installed between the MDC planes II and III (discussed below). It consists of six coils surrounding the beam axis and covers the full azimuthal angles. The created magnetic field intensity is very small around the target and MDC planes I and IV ensuring straight line tracks in those regions ($B \sim 0.08$ T in MDC I). A large field is only created between the two MDC planes II and III with $B = 0.9$ T in the center of a sector.

2.1.5 *The MDC Detector*

The HADES spectrometer is equipped with four planes of Multi-Wire Drift Chambers (MDC I-IV) in order to reconstruct charged particle trajectories. They are arranged in six sectors around the beam axis, with two planes are placed before the magnet (MDC I and MDC II) and two planes after the magnet (MDC III and MDC IV). The planes are oriented in different stereo angles to optimize the spatial resolution. The chambers are filled with a helium based counting gas ($He:C_4H_{10}=60:40$), a charged particle ionizes the gas along its trajectory and the produced electrons drift in the electric field created by the wires, create particle avalanches when they eventually reach the wires, thereby producing electric signals.

The charged particle track is reconstructed in two steps: first, the hit positions in MDC I and II are combined to an inner track segment and the hit positions from MDC III and IV are combined to an outer track segment. These line track segments are deflected with respect to each other due to the magnetic field. In the second step, the Runge-Kutta algorithm combines the information from the inner and outer segments in addition to the META (explained below) hits as start parameters and the particle equation of motion inside the magnetic field is solved numerically. The MDC sub-system also provides information about the energy loss of particles, which is used as a discriminating variable for the particle identification procedure.

2.1.6 *The META System*

The Multiplicity Electron Trigger Array (META) system is a combination of sub-detectors that is used for time-of-flight measurements and the determination of the

particle multiplicity in each event, which is used as a first-Level Trigger (LVL1), the META system consists of:

The TOF detector

The TOF is one of the HADES Time Of Flight sub-systems that covers the polar angles from $\theta = 44^\circ$ to $\theta = 88^\circ$. It is arranged in six sectors, each contains 64 plastic scintillators rods combined to 8 modules. When a charged particle hits the scintillator module it induces visible photons that are collected by Photo-Multiplier Tubes (PMTs), which measure the arrival time as well as the signal height. Therefore, the TOF provides information about the particle time-of-flight and the energy loss. The TOF intrinsic time resolution is $\sigma = 150$ ps.

The TOFinO detector

The TOFinO is Time Of Flight detector, which also consists of plastic scintillators, but with a low granularity of only eight paddles per sector. It covers polar angles from $\theta = 18^\circ$ to $\theta = 45^\circ$. Its time resolution is $\sigma = 400$ ps.

In 2009, the TOFinO was replaced by a much higher granularity Resistive Plate Chamber (RPC) detector with much better time resolution of $\sigma = 100$ ps [64].

The PreSHOWER detector

The PreSHOWER detector is an electromagnetic shower detector, located directly behind the TOFinO that provides further possibility for lepton identification. It consists of alternating layers of gas wire chambers filled with counter gas and lead converter planes Pb for shower creation. Unlike hadrons, leptons create an electromagnetic shower due to Bremsstrahlung and pair production in the Pb planes, the signal of the shower is collected at the cathode of the chambers, which has high granularity that is optimized to push the double hit probability below 5% in the Au+Au collisions. It is worth to mention that both hadrons and leptons deliver a signal in the PreSHOWER, however, the signal amplitude for leptons rises faster from one active layer to the next than for hadrons. Therefore, by comparing the integrated charge deposited in the wire chambers between the Pb converters, it is possible to distinguish electromagnetic showers from hadronic tracks.

2.1.7 *The Forward Wall*

The Forward Wall (FW) consists of a scintillating hodoscope placed 7 meters downstream of the target and covers the very forward polar angles from $\theta = 0.33^\circ$ to $\theta = 7^\circ$. It was installed to detect the spectator proton during the d+p beam time at 1.25 GeV and the event plane reconstruction in Au+Au collisions. It consists of three different module sizes: 1.5×1.5 cm (5-rows), 4×4 cm (2-rows), and 8×8 cm (3-rows), which are used to deliver the hit position of an incident particle. The FW measures the arrival time of particles with a time resolution $\sigma \sim 700$ ps [15].

2.2 HADES SOFTWARE TOOLS

Simulations are an important tool in particle physics. Monte-Carlo Simulations are needed to compare different theoretical predictions to the experimental data. Event generators are first used to simulate the particle generation based on physical assumptions, then the particle trajectories are propagated through the detector volume, which simulates the interaction of the particle with the detector material. *Hydra* is the HADES simulation and analysis framework [76], it has three main processes:

2.2.1 *Event Generator*

PLUTO is a Monte Carlo based event generator developed for the HADES experiment [59]. It can serve as an event generator for elementary reactions like p+p, proton-nucleus reactions (p+A) or nucleus-nucleus reactions (A+A). In PLUTO, the particle production is generally calculated according to the available phase space volume, but can also be modified to match used-provided angular distributions.

2.2.2 *HGeant*

The particle track information, obtained by PLUTO, is used as an input for the detector simulation software HGeant that is based on the Geant package [34]. HGeant provides a realistic description of the HADES setup including scattering processes, secondary collisions, energy loss and track curvature in the magnetic field.

2.2.3 DST

The digitization is the last step of the simulation process, where the particle hits are transformed into realistic signals. The obtained particle track information like momentum, energy loss etc. are stored in Data Summary Tape (DST) files, the same process also applies for real data. Starting from the DST files, the data and the simulations can be analyzed.

2.3 FACILITY FOR ANTIPROTON AND ION RESEARCH

The Facility for Antiproton and Ion Research (FAIR) is a future international accelerator complex located on the grounds of GSI at Darmstadt, Germany. It is a research facility planned to investigate a wide range of physics topics, e.g. the structure of matter. It offers infrastructure for experiments with high intensity antiproton and ion beams. The FAIR setup is shown in Fig. 7, it is currently under reconstruction on the grounds of the existing GSI facility. The GSI linear accelerator and the SIS18 ring are used as pre accelerators for the SIS100, the main accelerator ring for FAIR, which can accelerate proton beams to an energy of up to 29 GeV [133].

Antiprotons are produced from the proton beam, the proton beam collides with a metal target producing the reaction $p + A \rightarrow \bar{p} + X$, where X stands for any final particles. When the full facility is in operation, the antiprotons are collected and pre-cooled by the Collector Ring (CR) and then injected into the High Energy Storage Ring (HESR), the main ring for storing and accelerating the antiproton beam. The antiproton beam can be accelerated with momenta in the range 1.5 GeV/c to 15 GeV/c [133].

2.4 THE \bar{P} ANDA DETECTOR SETUP

The anti \bar{P} roton ANihilation at DArmstadt (\bar{P} ANDA) experiment is one of the key facilities at FAIR located in one of the straight sections of the HESR [26]. \bar{P} ANDA is a fixed target experiment, where antiprotons of beam momenta ranging from 1.5 GeV/c to 15 GeV/c will collide with a fixed proton target. This interaction enables a diverse research of hadron physics since particles of all quantum numbers can be produced.

The research topics of the experiment include:

- Hadron Spectroscopy: Investigation of [121] reveals a long list of mesons and baryons for which many of them the evidence is only fair or even poor. In the

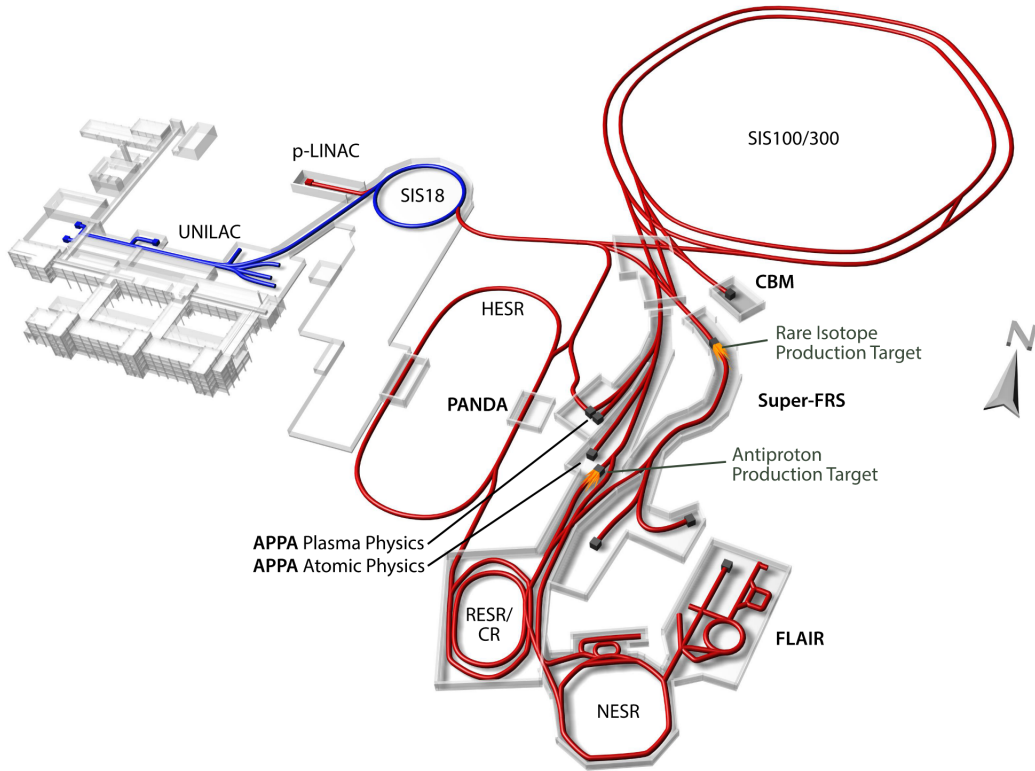


Figure 6: The future FAIR facility with different accelerators and experiments annotated [53].

charmonium sector, \bar{P} ANDA will be able to perform precise threshold scans due to the narrow beam momentum spread ($\frac{\Delta p}{p} \approx 4 \cdot 10^{-5}$) of HESR. Therefore, it will refine current measurements and establish new ones [26]. In the strangeness sector, the excitation spectrum is not well understood (e.g., Ξ^*), \bar{P} ANDA will run with a comprehensive baryon spectroscopy program as the production cross section for baryon-antibaryon final states is very large.

- **Nucleon Structure:** Nucleon structure investigation at \bar{P} ANDA can be achieved by studying Drell-Yan processes (e.g., $\bar{p}p \rightarrow e^+e^-$, which give access to the time-like region of the proton form factor. In addition, Dalitz decays of hyperon resonances (e.g., Λ^* , Σ^*) to a ground-state hyperon and a virtual photon give access to the electromagnetic transition form-factors, which carry information about the hyperon structure [30].
- **Gluonic Excitation:** The QCD allows hadronic states bound together by an excited gluon, either as gluonic excitations of valence quarks (hybrid mesons and baryons) or *glueballs* (states consists solely of gluons). However, none of these states have yet been seen clearly and unambiguously in experiments. Therefore, \bar{P} ANDA offers the opportunity to measure these states [26].

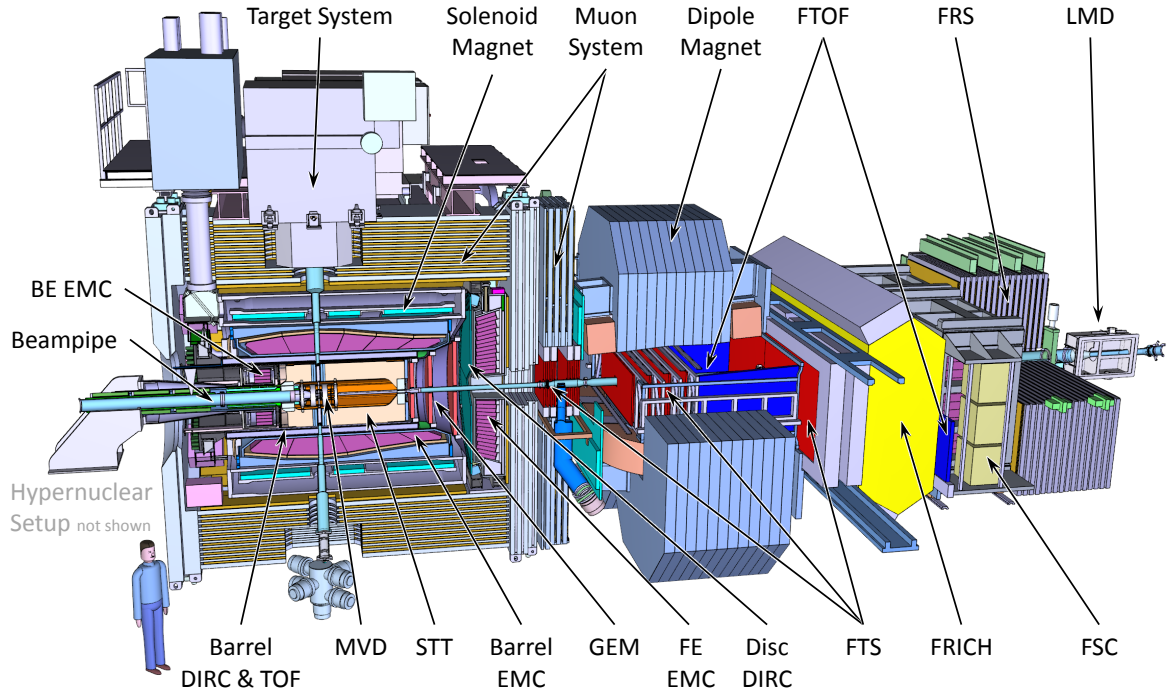


Figure 7: The \bar{P} ANDA detector setup [1].

The detector (shown in Fig. 7) has two main components, the *Target Spectrometer* (TS) and the *Forward Spectrometer* (FS). Each component has tracking, particle identification and calorimetry sub-systems.

The TS covers the central region around the interaction point and instruments nearly the full 4π solid angle. It is embedded inside a solenoid magnet, providing a homogeneous magnetic field up to 2T. The first component traversed by particles in the TS is the Micro Vertex Detector (MVD) followed by the Straw Tube Tracker (STT) as central tracking detectors. For the purpose of a charged particle identification, the DIRC (Detection Internally Reflected Cherenkov light) and ToF (Time-of-Flight) are planned. The reconstruction of neutral particles requires installation of the Electromagnetic Calorimeter (EMC). The Muon System is planned for muon identification. At the Endcap of the barrel part, Gas Electron Multiplier (GEM) chambers are planned as a tracking detector [26].

The FS is downstream of the interaction point and is dedicated to measure the forward boosted particles at small polar angles. It covers polar angles below 10° horizontally and 5° vertically. Particle identification is provided by the Forward ToF (FToF) and the Forward Ring Imaging CHerenkov (FRICH) systems. The forward detection of neutral particles is provided by a Shashlyk-type calorimeter. The Luminosity Detector (LMD) is planned at the very end of the forward spectrometer to measure the interaction rate. The forward tracking system is the main tracker of the FS.

2.4.1 Forward Tracking System

The Forward Tracking Stations (FTS) is foreseen to measure the momenta of forward emitted charged particles. It will be implemented inside a dipole magnet with a magnetic field of a maximum bending power of 2 Tm. The FTS consists of three pairs of tracking stations shown in Fig. 8, (FTS1, FTS2) placed before the magnet, the second pair (FTS3, FTS4) is placed inside the magnet gap and the last pair (FTS5, FTS6) after the magnet.

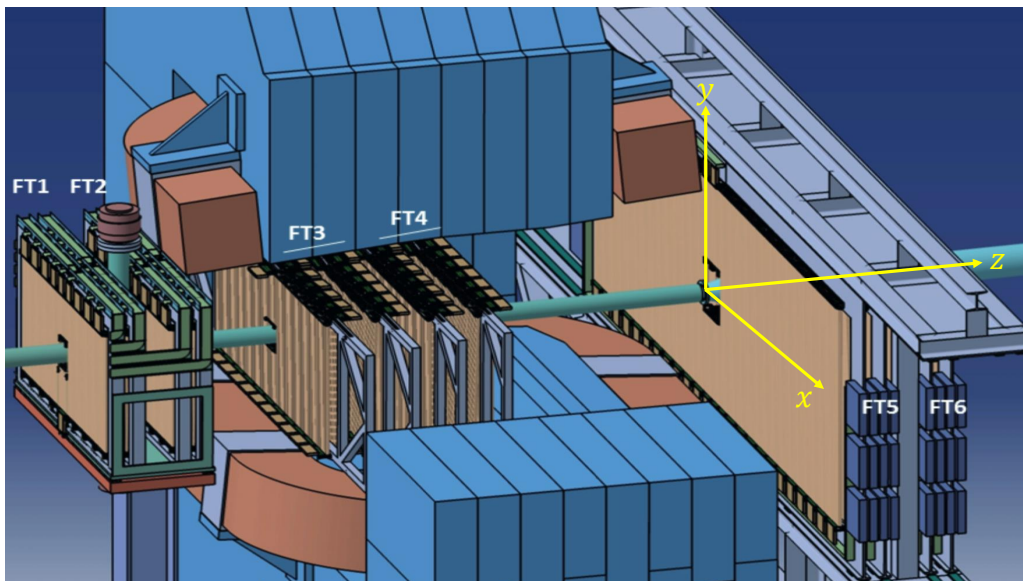


Figure 8: The \bar{P} ANDA Forward Tracking Stations, adapted from [114]. Each station consists of four double layers of straw tubes, the outer double layer are vertical, while the inner double layers are tilted by $\theta = \pm 5^\circ$.

Each tracking station is equipped with four double layers of self-supporting straw tubes. The outer double layers are vertically aligned and the inner double layers are tilted with respect to the vertical direction (y) by $\theta = +5^\circ$ and $\theta = -5^\circ$, respectively, a schematic depiction of the FTS is shown in Fig. 8.

The straw tubes are identical to the ones used for the STT, the tubes are made out of a $27\ \mu\text{m}$ thick aluminized Mylar cylinder with a 10 mm inner diameter, they are filled with a gas mixture Ar/CO_2 with a mixing ratio of 90/10 and operated at a gas overpressure of 1 bar, which provides their mechanical stability and maintains the anode wire tension. The anode at the center of the tube is made of gold-plated tungsten wire with $20\ \mu\text{m}$ diameter [114].

When a charged particle traverses the active volume of the tube, it ionizes the gas along its trajectory, the electrons drift towards the node wire and are multiplied by the avalanche effect and finally reach the wire, where they induce an electronic signal in the readout. The time it takes for the ionized electrons to travel to the wire is known as the *drift time*. Through a calibration procedure of the $r(t)$ curve, the *isochrone radius* can be calculated with the knowledge of the drift time, which represent a cylinder around the wire that contains all possible positions of where the particle might have traversed the tube and generated a signal of the measured drift time. Fig. 9 shows an illustration of the isochrone radius as the red dashed circles.

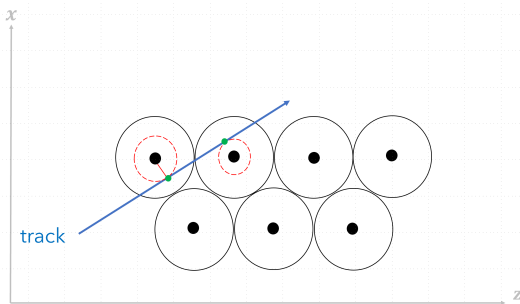


Figure 9: The $x - z$ projection of the FTS straw tubes. The black dots represent the anode wire position at the center of the tube, where the electronic signal is induced. The green dots are the correct hit position and the red circles represent the isochrones.

2.5 $\overline{\text{P}}\text{ANDA}$ SOFTWARE TOOLS

The $\overline{\text{P}}\text{ANDA}$ simulation, reconstruction and analysis software framework is called PandaRoot, it is an object oriented software written in C++ and built on top of FairRoot [126]. FairRoot is a common framework for multiple FAIR experiments including $\overline{\text{P}}\text{ANDA}$ and is built on top of ROOT, CERN's data analysis framework [22]. The PandaRoot workflow is shown in Fig. 10, which is modularized in main steps that are summarized as follows:

- **Event Generation:** PandaRoot has adopted several event generators including Pythia, EvtGen, Dual Parton Model DPM, box generator and other generators. The diversity of event generators enables PandaRoot to simulate different physical models [19].

- **Detector Simulation:** The output of event generators is used as an input for the next step, where the generated particles are transported through the \bar{P} ANDA detector implemented with the GEANT4 simulation toolkit [17]. The detector response to the hits created through the event propagation is then simulated in the digitization step.
- **Track Reconstruction:** In the next step the group of hits that belong to the same Monte-Carlo track are clustered together in a process known as *particle tracking*, which is the topic of the next chapter.
- **Particle Identification (PID):** The particle track reconstruction algorithm delivers a list of reconstructed tracks along with a set of parameters (e.g. charge, momentum, etc.). A PID algorithm determines the particle type given the information delivered by the tracking algorithm.
- **Analysis:** The final step is to analyze the particles and events. For this step, PandaRoot offers an analysis framework, the Rho package that provides a flexible physics analysis environment [72].

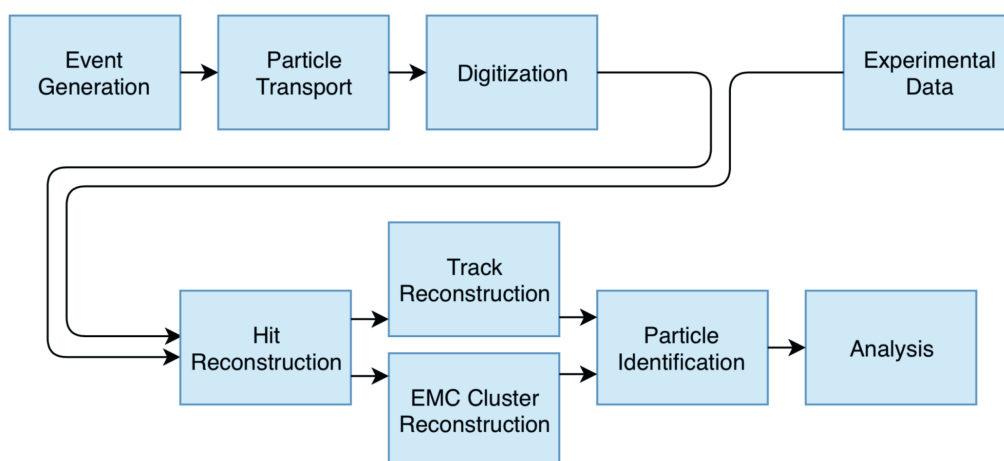


Figure 10: The PandaRoot workflow illustrating the main steps of the physics analysis chain [19].

DEEP LEARNING BASED TRACK RECONSTRUCTION

In this chapter, a deep learning based track reconstruction algorithm at the \bar{P} ANDA forward tracker is presented, in particular tracking with the state-of-art graph neural networks. The charged particles created in the collision of the beam and the target are recorded by the *tracking detectors* in the form of an interaction of particles with the detector material, which is a position measurement and termed *hits*. The main goal of a track reconstruction algorithm is to reconstruct the particles' trajectories by grouping the recorded detector hits. Therefore, the track reconstruction is a pattern recognition task, which is a well know problem in the field of machine learning and applied mathematics that makes use of cluster analysis, results of statistics, combinatorial optimization and other algorithms [61]. The track reconstruction is one of the most important and time consuming tasks in the physics analysis chain. A typical track reconstruction algorithm consists of two main steps, the *track finding*, which is the assignment of the detector hits to track candidates and the *track fitting*, which aims to determine track parameters and the covariance matrix for each track candidate. Since \bar{P} ANDA is a fixed target experiment, the reaction products will be boosted in the forward direction. Therefore, a robust track reconstruction algorithm for the forward angles is of crucial importance for various physics channels. The detection of forward peaking particles play a significant role in the reconstruction and analysis of the ground state and excited hyperons (Σ^0 , $\Sigma(1385)$, $\Lambda(1405)$ and $\Lambda(1520)$) as will be presented in chapters 4 and 5, respectively.

The focus of this chapter is on the track finding task in the \bar{P} ANDA FTS and how deep learning techniques can be incorporated to perform this task. Given a set of detector hits or position measurements, a track finding algorithm is equivalent to partitioning the position measurements into disjoint sets, where each set corresponds to a real particle trajectory.

3.1 INTRODUCTION

Track reconstruction is a combinatorial problem: the ability to find the correct hits that originate from the same particle from a given set of possible hit combinations. This can be more challenging in the presence of detector inefficiencies, which can lead to *noise hits* or *fake hits*. Machine Learning (ML) and Deep Learning (DL) methods proved to be a competitor to traditional algorithms, especially at high detector occupancy where traditional algorithms, e.g., Kalman filters [60], scale poorly.

Fundamentally, ML is a sub-field of Artificial Intelligence (AI) that involves building mathematical models to help understand data [127], i.e., using data to *train* a ML model to perform a specific task. ML can be categorized into two main categories: *supervised learning* and *unsupervised learning*.

Supervised learning involves modeling *labeled* data, i.e., finding the relation between the measured *features* of data and some associated *labels* or *target function*. This is further subdivided into *classification* and *regression* tasks [127].

Unsupervised learning involves modeling the features of a data-set without reference to any label [127], one example of *unsupervised learning* is *clustering*.

In 2018, a team of tracking experts from CERN set up a tracking ML challenge *TrackML* on the Kaggle platform to reach out computer scientists to find new types of algorithms and approaches to the tracking problem. Different approaches based on ML techniques were proposed as potential solutions for the TrackML challenge [81]. One of the proposed solutions, is the use of the DBSCAN clustering algorithm (Density-Based Spatial Clustering of Applications with Noise) [51]. A clustering algorithm is a category of *unsupervised learning* techniques that allows to discover hidden structures in the data, given the fact that we do not know the correct answer in advance. As its name implies, DBSCAN assigns cluster labels (in this case a track candidate) based on dense regions of points (hits). The notion of density is defined as the number of points within a pre-specified radius ϵ . One of the main advantages of the DBSCAN is that it does not assume that the clusters have a specific shape and its capability of removing noise points.

The tremendous increase in the computing power and the start of the *Big Data* era have increased the popularity of DL algorithms. Unlike traditional ML algorithms (e.g. DBSCAN), DL algorithms tend to perform better with increased training data size as shown in Fig. 11. Therefore, various DL based tracking algorithms were proposed. These algorithms can in general be classified into two categories, image-based approaches and point-based approaches [54], in the former approach, computer vision techniques like image segmentation and captioning are utilized and the detector hits are treated as an image, while in the latter, the hits are treated sequentially, i.e, the data is converted into

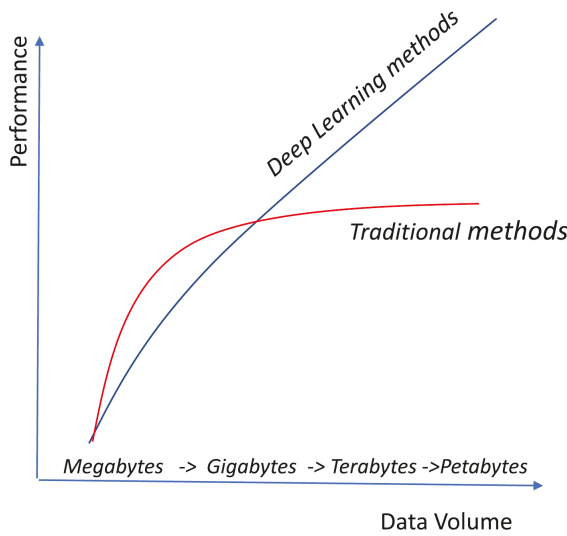


Figure 11: A comparison between the performance of traditional ML algorithms vs DL algorithms with increasing amounts of data [95].

a list. DL is a sub-field of ML that is concerned with training Artificial Neural Networks ANNs.

3.1.1 Artificial Neural Networks ANN

The ANN is inspired by how the biological neural system of the human brain works. ANNs are at the core of DL. They are powerful and capable of approximating any measurable function to the desired accuracy [75]. Artificial neurons are the building blocks of the ANNs, they were first introduced in 1943 by Warren McCulloch and Walter Pitts [89]. In their paper, McCulloch and Pitts proposed an artificial neuron that has one or more binary inputs and one binary output, it activates its output when more than a certain number of its inputs are active. They showed that this simple model is able to perform any logical computation. Afterwards, in 1957 Frank Rosenblatt proposed the *Perceptron* [103], a variant of artificial neuron, where the inputs and outputs are numbers and each input have a corresponding weight. The output of the Perceptron is calculated as a weighted sum of its inputs and then applies an *activation function* (e.g. sigmoid function) to that sum and outputs the result. A schematic diagram of a Perceptron is illustrated in Fig. 12.

Assume that the inputs are real-valued numbers x_1, x_2, \dots, x_n , the Perceptron output is calculated as follows:

$$O(\vec{x}) = \sigma(\vec{w} \cdot \vec{x} + x_0), \quad (3)$$

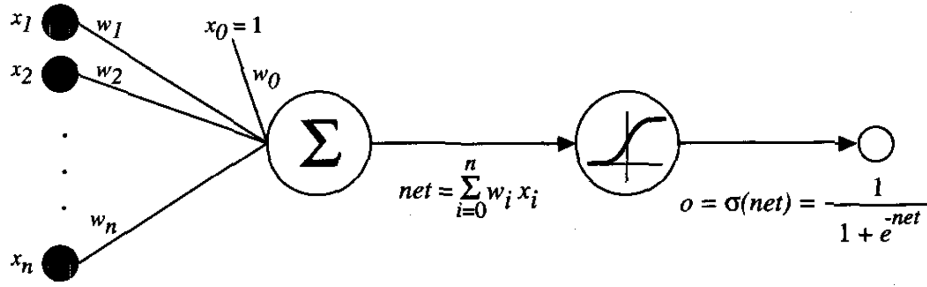


Figure 12: A Perceptron. The weighted sum of the inputs is calculated and then an activation function (a sigmoid function in this case) is applied. [90]

where x_0 is a bias, σ is the activation function and \vec{w} are the *weights* of the Perceptron, which are real-valued numbers that determines the strength or the contribution of each input x_i to the Perceptron output. Training the Perceptron or in general an ANN involves finding the appropriate set of weights such that the Perceptron gives the desired output [90].

The question is still how the Perceptron is trained or how the weights are determined. Several algorithms are known to solve this learning problem. One simple and common algorithm is called the *delta learning rule* [90] and is based on the gradient descent to search for the possible set of weights w_i that best fit the the *training data*. This rule is important because it provides the basis for the *back propagation*, which is the standard learning algorithm for ANNs with many inter-connected artificial neurons [90].

The *delta learning rule* begins with random weights, then iteratively apply Eq. 3 to each training example. The output of the Perceptron is compared to the true output or the *target*, this is done by defining a *cost function* that is a measure of the training error. The choice of the cost function depends on the problem at hand. A cost function for a *classification* problem is different from a *regression* problem. For the purpose of explaining the *delta learning rule*, a simple choice of the cost function can be the sum of the squared error [90]:

$$E(\vec{w}) = \sum (t_d - o_d)^2, \quad (4)$$

where t_d is the target output for the training example d (x_i) and o_d is the output of the Perceptron (Eq. 3) for training example d . The sum runs over all the training examples. The core idea behind the *delta learning rule* (also the *back propagation* algorithm) is to minimize the cost function or calculating the direction of steepest descent along the error hyper-surface. Mathematically, this can be found by computing the derivative of the cost function with respect to each component of the vector \vec{w} [90]:

$$\nabla E(\vec{w}) \equiv \left(\frac{\partial E}{\partial w_1}, \frac{\partial E}{\partial w_2}, \dots, \frac{\partial E}{\partial w_n} \right). \quad (5)$$

The weights are then updated according to *delta learning rule*:

$$\vec{w} = \vec{w} - \eta \nabla E(\vec{w}), \quad (6)$$

where η is the *learning rate*, a positive real number that moderate the degree to which weights are changed at each step [90].

A group of artificial neurons (or Perceptrons) can be arranged in layers to form a multilayer feed forward neural network; also called a MultiLayer Perceptron (MLP). When all the neurons in a layer are connected to every other neuron in the previous layer, the layer is called a fully connected layer. The first layer of the neural network is called the *input layer* and is used to represent the input values. The last layer is called the *output layer* and is used to represent the output values, the layers in between the input and output layer are called *hidden layers*. If the neural network consists of more than one *hidden layer*, it is called a *deep neural network*. The *back propagation* is the standard algorithm used to train a MLP or an ANN, which is a generalization of the *delta learning rule*. The idea introduced by David Rumelhart et. al. in 1986 under the name of *generalized delta rule* [104].

According to the *universal approximation theorem* [92], an ANN with non-linear activation functions and an appropriate set of weights can represent a wide range of interesting functions.

There are numerous architectures that can be implemented for a variety of problems. Fortunately, Fjodor van Veen from Asimov institute compiled a wonderful chart for the different neural network architectures, this chart can be found in [128].

One serious problem arise when training a large ANN is *overfitting* the training data (high model variance), which means that the model has so much flexibility such that it learns the underlying data distribution in addition to the associated random errors [127]. This results in a poor performance when the model is evaluated on new data.

Overfitting the training data is directly related to the behavior of the *validation curve* shown in Fig. 13. If the model capacity/complexity is very low, the model *underfits* the training data, which means it has a poor performance on both the training and the *validation* (unseen data) data-sets. On the other hand, for very high model capacity/complexity, the model *overfits* the training data, which means it describes the training data very well but fails for any unseen data. Therefore, the model complexity or

the model parameters have to be tuned such that the validation curve has a maximum value, which indicates a suitable trade-off between overfitting and underfitting [127].

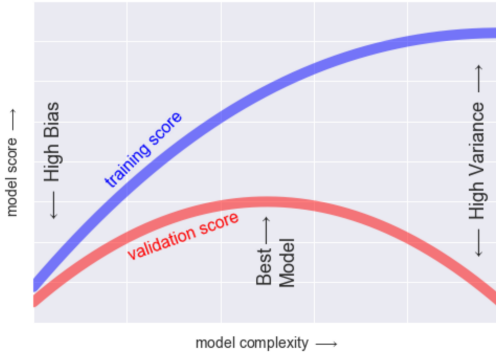


Figure 13: The validation curve, a relationship between model capacity, training score, and validation score [127].

A powerful technique to regularize the performance of the ANN and to reduce the overfitting is the *Dropout* [118]. During the training phase, some number of layer outputs are randomly ignored or *dropped out*, this has the effect of reducing the capacity of the neural network during training. Consequently, reducing the chance to overfit the training data. Dropout can be thought of as making bagging for ensembles of many large neural networks, which means training and evaluating multiple models. This technique is used for neural networks developed in this thesis. Fig. 14 shows an ANN with and without dropout layers [95].

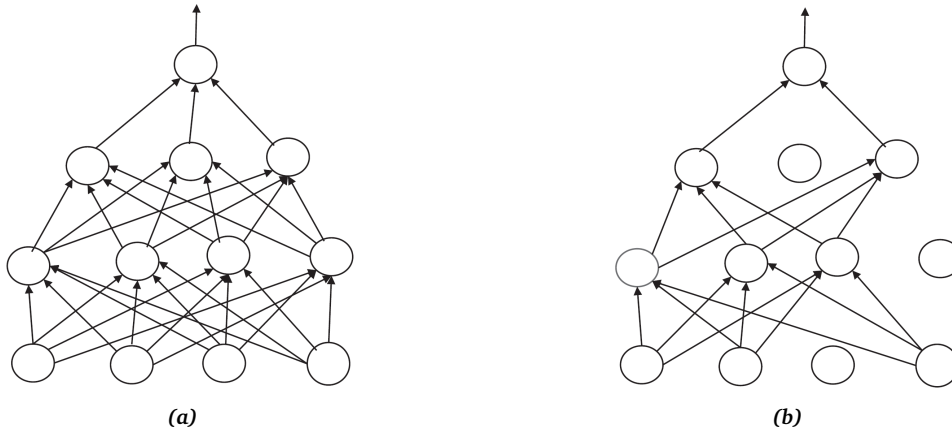


Figure 14: An ANN (a) without dropout (b) with dropout [95].

3.1.2 Related Work

In [55] Steven Farrel et al. proposed a type of Recurrent Neural Network RNN called LSTM (Long Short-Term Memory) [73] as a hit predictor model. A *track seed* (the first three hits in detector layers) is provided to the LSTM and the network predict the hit location in the next detector layers. The input to the LSTM is a detector layer in the

format of pixel array, the LSTM is followed by a fully connected layer that produces the hit predictions. The model was evaluated on a toy data-set and showed promising results. In the same reference, a Convolution Neural Network (CNN) [18] has been proposed to perform a pixel level classification, i.e, the CNN takes the detector image as an input and the task is to classify each pixel (hit) in the image, in other words, assign pixels to classes (track candidates).

The BM@N (Baryonic Matter at Nuclotron) Collaboration developed a deep neural network to improve the tracking efficiency of the GEM microstrip detector [24]. A main problem in the GEM is the great amount of *fake hits* that appears along with real hits because of extra spurious crossings of strips. A two step tracking algorithm has been investigated, on the first step, track seeds are created by a simple algorithm that has relatively low efficiency. Hits are combined into track candidates and the algorithm filters out tracks by a loose χ^2 criterion. The second step uses a deep neural network to classify which of the found tracks by the first step are real track and which are fake tracks. In their analysis they combined a 1D convolution layer with a Gated Recurrent Unit (GRU) (a type of RNN) [41], the main reason behind using a convolution layer is that it can produce a greater number of new meaningful features for the GRU. The model evaluated on a test sample with fakes factor with the value of 2 scores 98% tracking efficiency.

In [50], a first deep learning-based tracking algorithm has been proposed for the $\overline{\text{P}}\text{ANDA}$ forward tracker. This algorithm involves two steps: the first step uses a simple feed forward ANN as a binary classifier to build track segments in three different parts of the FTS, namely FTS1, FTS2, FTS3, FTS4, and FTS5, FTS6. The ANN takes the coordinates of hit pairs as input and classifies the pairs as being true or fake pairs. The output of the ANN can be used to combine multiple hits together into a track segment. The second step is to match the track segments from the different parts of the FTS to form a full track candidate based on an LSTM network. First, all possible combinations of the found track segments are made, then the LSTM is trained to classify true and fake combinations, i.e., which combination is a true track and which is not. Preliminary results on a test sample showed that the tracking efficiency was on average $\approx 85\%$.

3.1.3 Graph Neural Networks

Since the input data to a neural network are detector hits and the aim is to find the correct connections between those hits (track candidates), the data is best represented as an image, where the hits are the image pixels. The image can be considered as a function on the *Euclidean* space [32]. Convolutional architectures CNNs are the type of neural networks that are able to work on images and extract their hidden features.

A CNN is able to exploit the shift invariance and the local connectivity of image data [130]. However, there is a drawback of using CNNs for particle tracking, that is most tracking detectors have irregular shape (*non-Euclidean data*) while images should have a regular structure, i.e. certain height and width. Recently, there were many studies to extend DL for non-Euclidean geometric data [32]. A graph is the primary instance of a non-Euclidean datatype. Formally, a graph $G = (V, E)$ consists of a set of objects $V = \{v_1, v_2, \dots\}$ called *vertices* or *nodes* and another set $E = \{e_1, e_2, \dots\}$, whose elements are called *edges*, where each edge e_k connects a pair of vertices (v_i, v_j) [46]. There are two different types of graphs, a *directed graph*, in which the graph edges are directed from one vertex to another and *undirected graph*, here the graph edges do not have a direction, an edge connecting the ordered pair (v_i, v_j) is the same connecting the ordered pair (v_j, v_i) .

There is an increasing number of applications where data can be represented as a graph. For example, in social networks, the characteristics of users can be modeled as signals on the graph vertices [86]. In chemistry, molecules can be represented as graphs [65], where atoms are the vertices and the chemical bonds are the edges. In track reconstruction, an image of the detector hits can be represented as a graph, where the vertices of the graph are the hits [54]. Extending DL techniques to the non-Euclidean domain is often called *Geometric Deep Learning* (GDL) [32]. Motivated by CNNs, RNNs and autoencoders, new generalizations and operations have been developed to handle non-Euclidean geometric data. A good example is the convolution operation shown in Fig. 15, a similar operation can be performed on graphs by taking the weighted average of a vertex neighborhood information. *Graph Neural Networks* (GNNs) are a powerful class of neural networks that can operate on graphs. There are a variety of GNN architectures, *Convolutional graph neural networks ConvGNNs* generalizes the convolution operation, *Recurrent graph neural networks RecGNNs* aims to learn node representations with recurrent neural networks, *Graph AutoEncoders GAEs*, which are unsupervised learning frameworks that learn the network embeddings and *Message Passing Neural Networks MPNNs*, in which node features can be passed from one node to another along edges [130, 131].

Different GNN architecture can perform a variety of tasks that can be classified into three categories: *node-level*: this includes node classification, node regression and node clustering, *edge-level*: this includes edge classification and link prediction and *graph-level*: this includes the classification of the whole graph and graph regression [131].

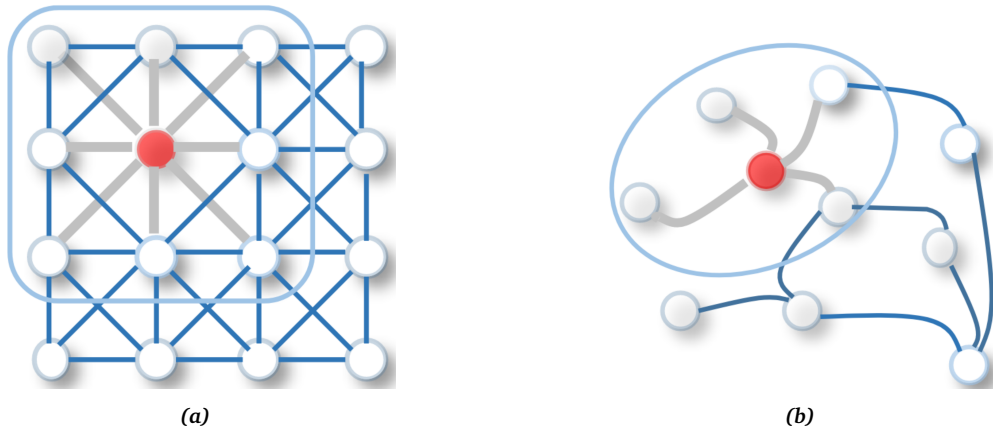


Figure 15: (a) Convolution operation on Euclidean datatype (an image), the weighted average of pixel values of the red vertex along with its neighbors is calculated by applying a filter shown by the light blue box. (b) Convolution operation on non-Euclidean datatype (a graph), the graph convolutional operation is to take the average value of the node features of the red vertex along with its neighbors. Unlike the image, the number of vertex neighbors in a graph can be different [130].

3.2 TRAINING PHASE

Inspired by the work of Exa.TrkX team [78], a GNN is developed for track finding at the \overline{P} ANDA FTS. The training data is generated by a particle gun (*the box generator*), where particle tracks are distributed uniformly in a parameter space of the user choice. Particle tracks in the momentum range $0.5 < p[\text{GeV}/c] < 15$, polar angle range $0 < \theta^\circ < 10$ and the full azimuthal range are generated. Fig. 16 shows the number of hits and the number of tracks per event. On average 4 tracks and ≈ 100 detector hits per event were generated.

First, the data-set is processed into a format suitable for model training, the generated data is converted into a *pandas dataframe* [123]. The hit coordinates are given by the anode wire position (the center of the tube), since the FTS straw tubes are aligned vertically (or tilted by $\pm 5^\circ$), at this stage of the algorithm only the projection in $x-z$ plane is used. In other words, the GNN reconstructs the $x-z$ projection of a given track. Furthermore, only detector hits in vertical layers are used for the GNN training. In a subsequent step, a separate algorithm was developed to use the skewed layers and the found $x-z$ projection to reconstruct the 3D track candidate. In addition to the hit coordinates x and z , the *isochrone radius* r is also used as an input feature for the GNN training.

To apply a GNN to this data-set, it was necessary to create a graph for each event. The graph is constructed by connecting detector hits in adjacent vertical layers, where the graph nodes (set V) are the detector hits and the connections between hits are the edges

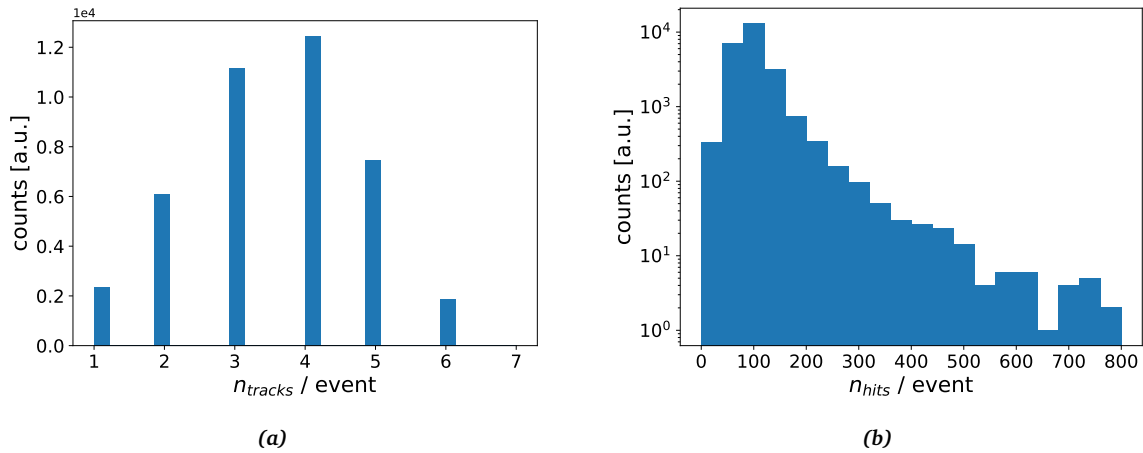


Figure 16: (a) The number of tracks in one event and (b) the number of FTS hits in one event.

(set E). The primary task of the GNN is to associate detector hits together by classifying the edges of the graph. An example of the input graph is shown in Fig. 17.

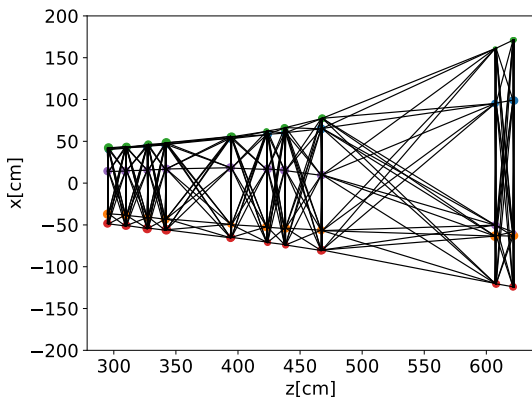


Figure 17: An example of an input graph to the GNN. Colored points represent the detector hits, where each color represent a different generated track. Black lines are the graph edges.

The architecture used is similar to that developed by the Exa.TrkX team [78]. The GNN has two main components that operate locally on the input graph. The first component is called the *Edge Network*, which computes weights for every edge of the graph using the features of the start and end nodes. The second component is called the *Node Network* and its task is to compute new node features or to learn node embedding for every node using the edge weights calculated by the edge network. Both the edge network and node network are implemented within the PyTorch framework [94] as MLPs with two layers each and *ELU* hidden activation and in addition a 50% dropout layer is added to prevent the model from overfitting. The full GNN model consists of an input transformation MLP followed by recurrent alternating applications of the edge network and node network. The model uses two graph iterations followed by a final classification layer with *sigmoid* activation that operates on every edge to predict whether it is a true or a fake edge. Since the sigmoid function squashes the input number between 0 and 1, the output of the GNN can be interpreted as a probability that quantifies the GNN confidence about a

specific edge. After 10 iteration, the network scored 99.5% classification accuracy on the training set and a hold-out data-set (a validation data-set) as shown in Fig. 18a. The GNN is trained on a high performance GPU NVIDIA® Tesla V100 with 16 GB memory for 10 epochs.

The *Receiver Operating Characteristic* (ROC) graph shown in Fig. 18b is another performance measurement. The ROC curve is a relationship between the True Positive Rate TPR (signal efficiency) and the False Positive Rate FPR (1-background efficiency). A perfect classification model should fall into the top-left corner of the graph with a TPR = 1 and an FPR = 0. The area under the ROC graph (AUC) is 1, indicating that the model classifies almost all the validation sample instances correctly.

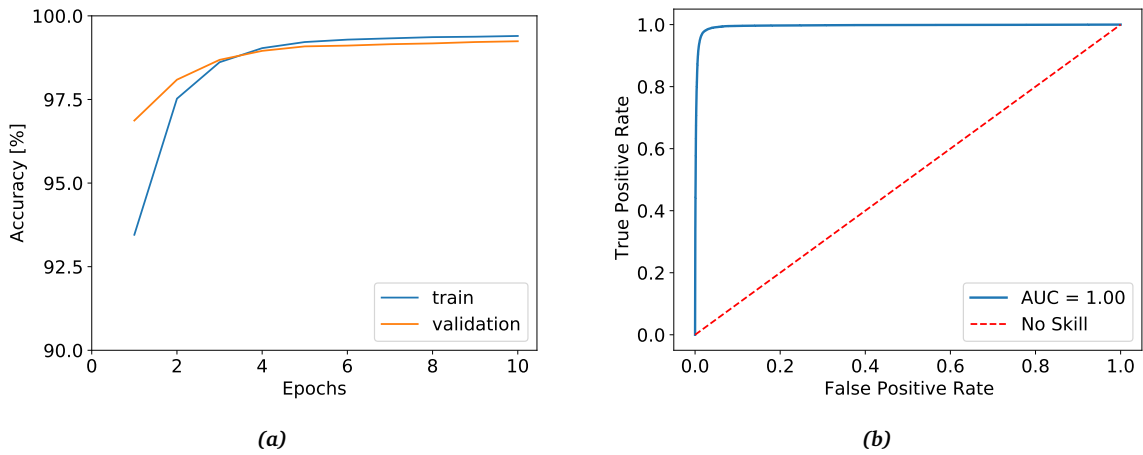


Figure 18: (a) Classification accuracy as function of the number of iterations for the training data-set and a hold-out data-set. (b) The ROC curve evaluated on the hold-out data-set, the dashed line is the performance of the no skill classifier.

By selecting edges with probability greater than a given threshold, it is possible to remove fake edges, which does not belong to any real track. In order to optimize the threshold, the *edge efficiency and purity* were defined as follows:

$$\begin{aligned} \text{efficiency} &= \frac{\text{number of true edges that pass the threshold cut}}{\text{total number of true edges}} \\ \text{purity} &= \frac{\text{number of true edges that pass the threshold cut}}{\text{all edges that pass the threshold cut}} \end{aligned} \quad (7)$$

Fig. 19a shows the GNN output for true and fake edges. Fig. 19b shows the edge efficiency and purity for different thresholds. The edge purity increases by increasing the threshold, but this comes at the cost of small efficiency. The intersection point between both curves corresponds to efficiency and purity $\approx 96\%$.

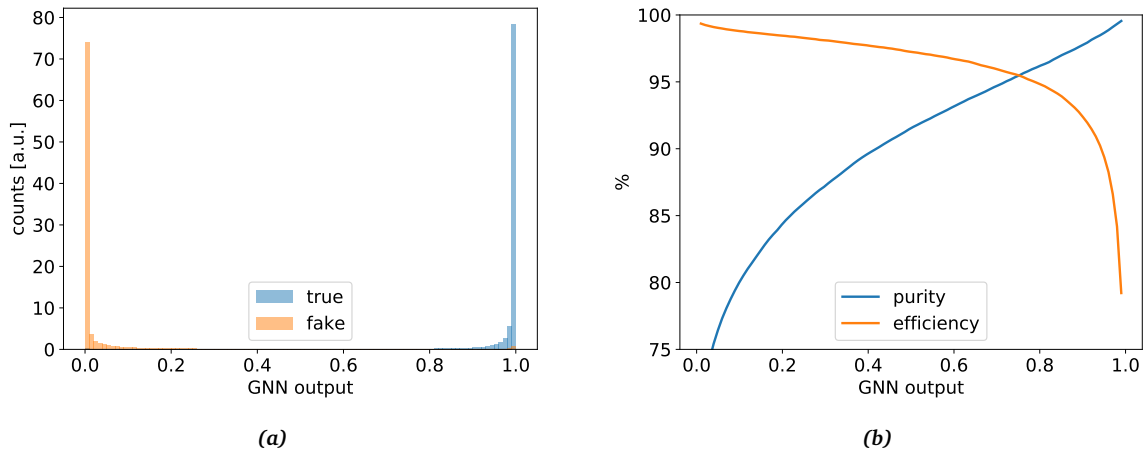


Figure 19: (a) The GNN output for true and fake edges. (b) The edge efficiency and purity as function of the GNN output.

Fig. 20a shows an example of the output graph (corresponding to the input graph shown in Fig. 17). The intensity of the connections reflects the GNN output value (black lines are those with the GNN output = 1, white lines corresponding to the GNN output = 0, and gray are those edges with the GNN output between 0 and 1). As can be seen from the GNN strengthen the true edges and weakens the fake ones. Fig. 20b shows the same graph after requiring the GNN output to be greater than 0.5, where it can be seen that only the true edges are kept.

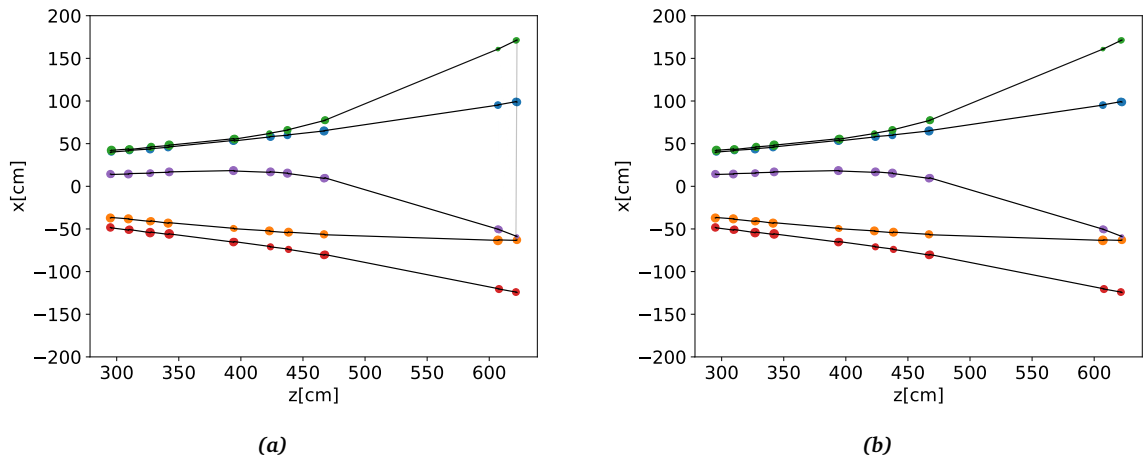


Figure 20: (a) The output graph corresponding to the input graph shown in Fig. 17). Colored points represent the detector hits, where each color represent a different generated track. The lines are the connections between the hits or the graph edges where the line intensity reflects the GNN output. (b) The same graph after requiring the GNN output to be > 0.5 .

3.3 PREDICTION PHASE

As described in the previous section, the GNN was implemented in PyTorch and the training was done in a python environment. Since the track finding algorithm comes at an early stage of the physics analysis chain (see Fig. 10), the developed algorithm has to be integrated within the experiment framework (the PandaRoot), which is written in C++.

PyTorch is a dynamic library that has an eager execution with tape based representation, which allows users to build dynamic computational graphs and makes PyTorch appealing for research purposes. It comes with a Just In Time (JIT) tracing engine that turns a trained PyTorch model into a *TorchScript* one. *TorchScript* is a way to create serializable and optimizable model from the PyTorch code, a TorchScript model can be saved from a PyTorch process and loaded in an environment where there is no python dependency (e.g. C++). It does this by passing an example PyTorch tensor through the trained model and returning a *ScriptModule* that contains the TorchScript representation of the original code.

By utilizing the PyTorch tracing engine, it was possible to load and integrate the trained GNN model within the PandaRoot framework.

Guided by the GNN outputs, the *Depth First Search* (DFS) algorithm has been implemented to reconstruct track candidates by connecting the hits, or in other words find the *sub-graphs* or search for the *connected components* in the GNN output graph. The DFS algorithm explores the output graph nodes depth-wise. It starts by marking all the graph nodes as not visited, the algorithm steps are summarized as follows:

1. Start the search at random node usually called the *root node* and mark it as visited.
2. Find the adjacent node, mark it as visited, then if the edge probability connecting the two nodes is greater than a pre-defined threshold, append the nodes to a list.
3. Repeat steps 1 and 2 until all the nodes are marked as visited.

The Test Sample

As the focus of the thesis is on the hyperon physics, the performance of the GNN tracking algorithm has been evaluated on a benchmark reaction that has been generated by the *EvtGen* event generator [106]:

$$p\bar{p} \rightarrow \Lambda\bar{\Lambda} \rightarrow (p\pi^-)(\bar{p}\pi^+).$$

In addition a set of background events has been generated by the *DPM* generator, which is used to describe the inelastic and elastic hadronic processes as well as Coulomb elastic scattering processes.

Algorithm Performance

The quality of the developed track reconstruction algorithm is determined by a set of Quality Assurance (QA) measurements that are listed below:

- **The track purity:** The purity specifies which fraction of hits in a reconstructed track come from the correct particle. The correct particle is defined as the Monte-Carlo (MC) generated particle, which has the majority of hits in the reconstructed track. A high purity track has a large fraction of hits originating from the correctly matched MC particle; a low purity track have hits from different MC tracks. The hit purity is defined as:

$$purity = \frac{n_{correct}}{n_{all}},$$

where $n_{correct}$ being the number of hits of the corrected MC particle and n_{all} the total number of hits in the reconstructed track. A common assumption in \bar{P} ANDA is that a track with $purity > 80\%$ is considered a reconstructed track. The category of tracks with $purity < 80\%$ is known as **ghost/fake** tracks.

- **MC Coverage:** A related quantity to hit purity is the coverage of a MC particle. This quantity relates the total number of hits of a MC track to the number of hits in a reconstructed track.

$$MC\ coverage = \frac{n_{reconstructed}^{correct}}{n_{MC}}$$

here n_{MC} is the number of MC hits of the generated MC track and $n_{reconstructed}^{correct}$ is the number of found hits belonging to the matched MC track in the reconstructed track. Ideally, all MC hits should be in exactly one reconstructed track (MC coverage = 100%).

- **The overall tracking efficiency ϵ :** The efficiency of track reconstruction can be defined as the ratio of the number of reconstructed tracks to the number of *reconstructible* tracks.

$$\epsilon = \frac{N_{reconstructed}}{N_{reconstructible}}.$$

The kind of tracks that are considered reconstructible depends on the sub-detector. In this study, a track is considered reconstructible if it contains at least 12 hits in the vertical straws that are distributed as 4 hits before, inside and after the magnetic field. A good tracking algorithm should have a high efficiency, i.e., to reconstruct as many as possible of the real particle trajectories. A good tracking algorithm should reconstruct with high purity, i.e., the tracks should contain hits from only one particle and having a small contamination from other particles. In this study, two categories of reconstructed tracks were defined: the **partially reconstructed** track and the **fully reconstructed** track. A fully reconstructed track has all hits come from a single MC particle, and all hits of the MC true particle are in one reconstructed track, in other words, a fully reconstructed should have purity = 100 % and MC coverage = 100 %. In a partially reconstructed the majority of hits come from a single MC particle, but not all MC hits are in one reconstructed track.

Fig. 21a shows the different performance measurement as function of the GNN output. The purity and MC coverage is constant for different GNN output values at about 100 %, the partially found percentage is almost constant at about 93 % while the fully found percentage is on average 89 % except for tight GNN cuts (> 0.9), where it drops to 85 %. The ghost ratio is on average 3 % for loose GNN cuts (< 0.2) and drops significantly to less than 0.5 % for tighter GNN cuts. Fig. 21b shows the same performance measurement as function of the generated absolute momentum P . Since the tracks are forward peaking, the transverse momentum component $P_t = \sqrt{P_x^2 + P_y^2}$ can be neglected when compared to the longitudinal component P_z , that is $P \approx P_z$. The reconstruction efficiency as function of momentum is on average 90 % except for low momentum tracks $P < 0.5 \text{ GeV}/c$, where it drops to 60 % since those tracks are mostly *secondary tracks* that are not produced directly in the $p\bar{p}$ collision.

3.4 ADDITION OF THE STEREO HITS

The goal of the GNN tracking algorithm is to reconstruct projections of track candidates in the $x - z$ bending plane, these $x - z$ track projections contain only hits from the vertical straws. The $y - z$ plane track motion is extracted from the skewed layers since their local frame is obtained from a rotation of the $x - y$ plane around the z direction by $\pm 5^\circ$.

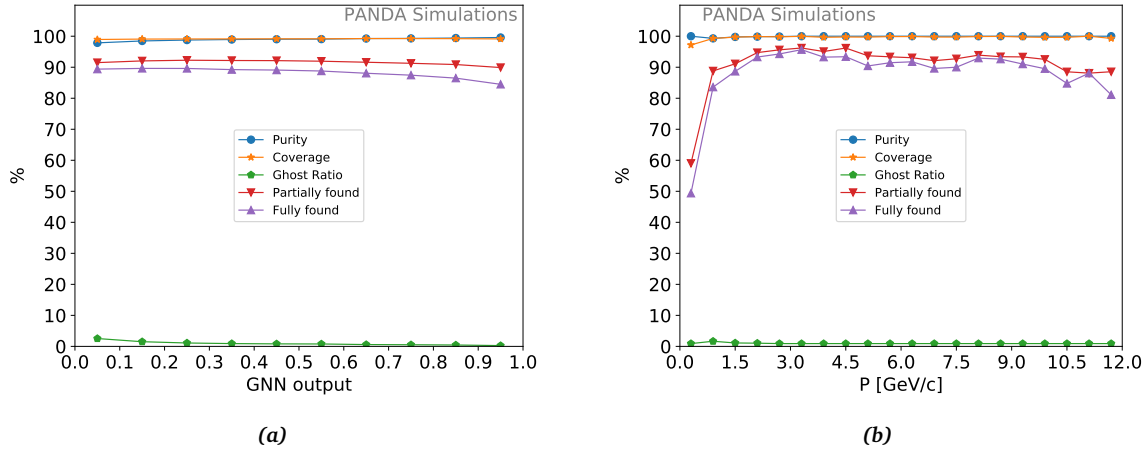


Figure 21: (a) The QA measurements as function of the GNN output. (b) The QA measurements as function of the momentum. The blue circles represents the purity, orange stars represents the MC coverage, the green pentagons are the ghost ratio, the down triangles represents the partially reconstructed percentage and the fully reconstructed percentage is represented by the up triangles.

Therefore, it is possible to obtain the complete information about the track motion in the 3D by investigating which of the skewed layer hits (*stereo hits*) are compatible with the reconstructed $x - z$ track projection. Thus, the $x - z$ projection candidates are used as an input for such task. The magnetic field effect on the $y - z$ plane is negligible compared to the $x - z$ bending plane, so a straight line trajectory a good approximation for the track model. The addition of stereo hits proceeds as follows:

1. Fit the $x - z$ projection.
2. Collect compatible stereo hits.
3. Assign a y measurement to the fitted $x - z$ projection at each skewed layer.

$x - z$ projection fitting

For straw stations outside the magnet, namely FTS1, FTS2, FTS5 and FTS6, the track is described by a simple linear model in the $x - z$ bending plane:

$$x(z) = x_0 + t_x(z - z_0), \quad (8)$$

where x_0 is the x coordinate at a reference position z_0 . Therefore, for each reconstructed track, the hits within these planes has been fit by the linear model in Eq. 8. The fit minimizes the sum of squared perpendicular distances from the hits in the reconstructed track to the regression line:

$$d = \frac{|x_0 z_i - x_i + b|}{\sqrt{x_0^2 + 1}},$$

where z_i and x_i are the straw wire position of the hit i , the corresponding isochrones are treated as errors in the explanatory z and the response x coordinates.

The stations FTS3 and FTS4 are located in the magnetic field \vec{B} of the dipole magnet, neglecting the multiple scattering and bremsstrahlung radiation the particle trajectory in this area can be described by a helix in 3D space. Based on the assumption that the magnetic field strength is constant within a defined range along the z -axis, the track motion in the $x - z$ bending plane can be approximated as part of a circle. Therefore, for each reconstructed track, the hits within these planes has been fit by:

$$x(z) = k \pm \sqrt{|\rho^2 - (z - h)^2|}, \quad (9)$$

where h and k are the coordinates of the circle center and ρ is the radius of curvature.

As the position of the hit is always generated exactly in the middle of the straw tube (the anode wire position). The corrected hit positions lie exactly at the points where the track is tangent to the isochrones. Since the fitted line/circle minimizes the perpendicular distances between the anode coordinate and the fit line/circle, it provides the correct hit positions. This is advantageous because in the later course of the process of track reconstruction, a Kalman filter based track fitting is made. A more accurate position of the hits used for the fitting improves the quality of the fit. Distributions of the residua of the corrected hit position and the corresponding MC points are shown in Fig. 22 for stations outside and inside the magnet. The distributions are described by double Gaussians with weighted average standard deviations $\sigma = 0.0124$ cm, $\sigma = 0.0604$ cm and $\sigma = 0.0188$ cm for FTS12, FTS34 and FTS56, respectively.

Collect compatible hits in skewed layers

For each $x - z$ projection, the predicted x position at the z position of skewed layers is evaluated from the fit model. The distance between the skewed layer x measurements (x_{skewed}) and the predicted x position ($x_{predicted}$) allows to identify for each skewed layer hit a corresponding y measurement. Therefore, all the hits that are *compatible* with respect to the $x - z$ projection are collected. The selection of the compatible hits was done in two steps:

1. Pre selection step.

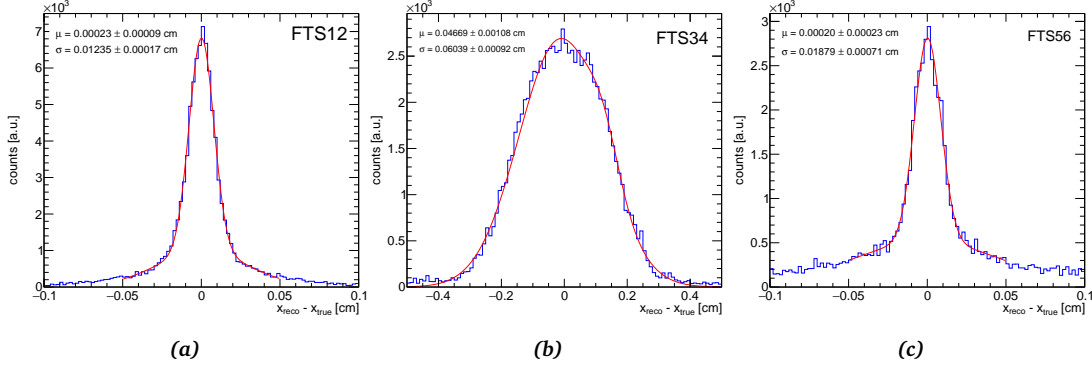


Figure 22: The distance between the reconstructed hit position and the actual hit position for (a) FTS1, FTS2, (b) FTS3, FTS4 and (c) FTS5 and FTS6. The red line is the double Gaussian fit, the weighted average means and standard deviations are indicated.

2. Selection of skewed layer hits that have similar values of the slopes $s = y/z$.

The first step was done by cutting on the distance between the measurement x_{skewed} and the model prediction $x_{predicted}$, this distance is shown in Fig. 23 for skewed layer hits that belong to the $x - z$ track based on the MC information and for skewed layer hits that does not belong to the $x - z$ track. This distance is required to be smaller than 3.2 cm, 4.6 cm and 6.0 cm for stations FTS12, FTS34 and FTS56, respectively. These cuts remove 72 %, 66 % and 62 % of incompatible skewed layer hits for stations FTS12, FTS34 and FTS56, respectively.

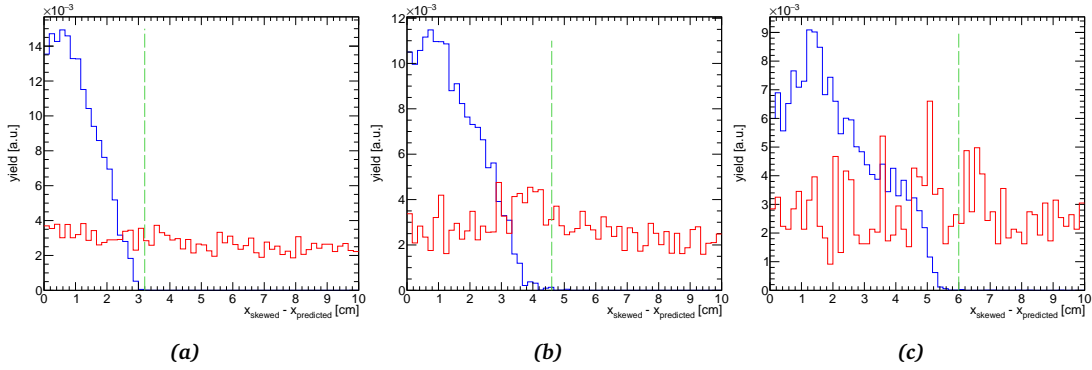


Figure 23: The distance between the skewed layer x measurements and the predicted x positions for true combinations (blue) and false combinations (red), the dashed vertical line indicates the cut value. The distance shown for stations (a) FTS1, FTS2, (b) FTS3, FTS4 and (c) FTS5 and FTS6.

In the second step, the Left/Right (L/R) ambiguity of the remaining skewed layer hits is tested and the y position is calculate as follows:

$$y = \frac{x_{predicted} - x_{skewed}}{\tan\theta},$$

where x_{skewed} is x position of the skewed layer hit, $x_{predicted}$ is the reconstructed x position, as calculated from the fit model and $\theta = \pm 5^\circ$ is the angle of inclination of skewed layers.

A sketch showing the usage of the FTS detector geometry and the $x-z$ projection to extract a y measurement is shown in Fig. 24.

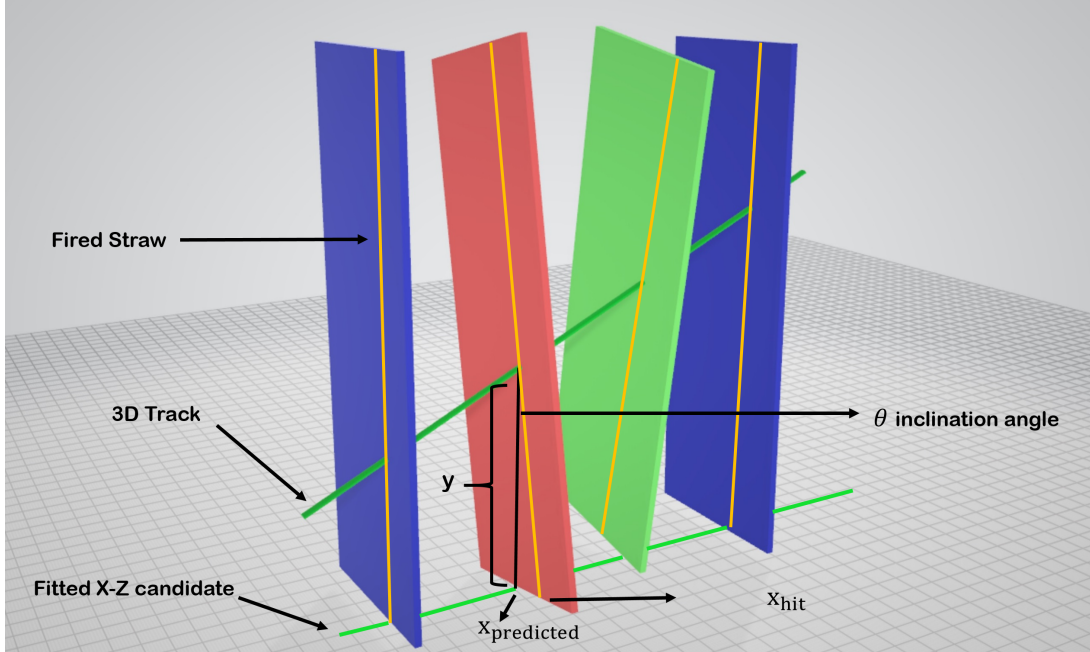


Figure 24: A drawing showing the geometrical interpretation of compatible hits based on the fitted $x-z$ projections [50].

The slope ($s = y/z$) of each skewed layer hit is calculated, since magnetic field effect on the $y-z$ plane is negligible compared to the $x-z$ bending plane, the group of hits sharing the same value of s defines a potential line candidate to be attached to the $x-z$ projection. Therefore, the set of compatible hits are grouped by histogramming the slopes of all skewed layer hits. A linear fit is then applied on the $y-z$ plane to extract the correct hit positions of the vertical layers. Distributions of the residua in the vertical direction between the corrected hit position and the corresponding MC points are shown in Fig. 25 for stations outside and inside the magnet. The distributions are described by double Gaussians with weighted average standard deviations $\sigma = 0.1640$ cm, $\sigma = 0.688$ cm and $\sigma = 0.150$ cm for FTS12, FTS34 and FTS56, respectively. The resolution in the vertical direction is about 11 times worse than the horizontal direction, since the ratio of the resolutions σ_y/σ_x depends on the inclination angle θ of the straws as $\cot\theta$, which is $\theta = 5^\circ$ for the present inclination.

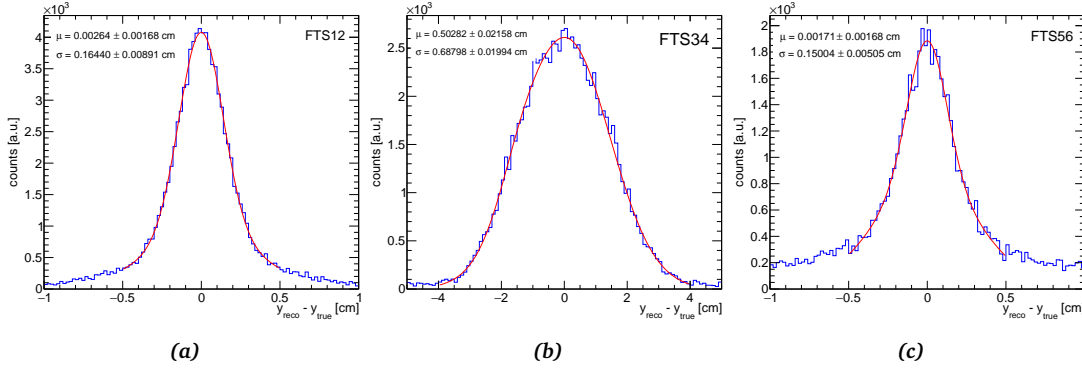


Figure 25: The distance between the reconstructed hit position and the actual hit position for (a) FTS1, FTS2, (b) FTS3, FTS4 and (c) FTS5 and FTS6. The red line is the double Gaussian fit, the weighted average means and standard deviations are indicated.

3.5 MOMENTUM ESTIMATION

The developed algorithm also provides the information about an approximate value of the particle momentum. The method used to estimate the momentum is known as the *p-kick* method and is based on the idea that the effect of the magnetic field can be described by an instantaneous kick of the momentum vector in the center of the magnet [125]. Since the magnetic field is oriented along the y axis, the deflection of charged particles is in the $x - z$ plane. The momentum change in the magnetic field depends on the integrated magnetic field along the particle's trajectory and is given by:

$$\Delta p = q \cdot \int_{s_1}^{s_2} \vec{v}(s) \times \vec{B}(s) \frac{dt}{ds} ds,$$

where s represents the arc length along the particle trajectory. In terms of the track parameters the ratio q/p is given by:

$$\frac{q}{p} = \frac{1}{\left(\int \vec{v} dt \times \vec{B}(s) \right)_x} \left[\left(\frac{t_x}{\sqrt{1 + t_x^2 + t_y^2}} \right)_{after} - \left(\frac{t_x}{\sqrt{1 + t_x^2 + t_y^2}} \right)_{before} \right],$$

where q is the particle charge, *before* and *after* indicates the fitted line segments before and after the magnetic field, t_x and t_y are the track slopes in the $x - z$ and $y - z$ planes, respectively.

Fig. 26a illustrate the *p-kick* method for an example track. Since the tracks of ingoing and outgoing tracks are straight, the deflection angle θ is the actual quantity to be measured, the variance of the deflection angle is proportional to the measurement error:

$$\sigma^2(\theta) \propto \sigma^2(x).$$

Since the particle momentum is estimated based on the deflection angle, the relative momentum resolution is given by:

$$\frac{\sigma(p)}{p} = \frac{\sigma(\theta)}{\theta}.$$

The relative momentum resolution obtained from the kick method integrated for all momentum values is shown in Fig. 26b. The distribution has been fit by a double Gaussian distribution with an average standard deviation 0.067.

Once initial track parameters have been obtained by the developed algorithm, a dedicated track fitting procedure based on Kalman Filter must be done. The Kalman Filter describes the particle motion inside the dipole magnetic field, where it takes into account the energy losses and the multiple scattering effects. In PandaRoot, the Kalman Filter employs the *GENFIT* package [100].

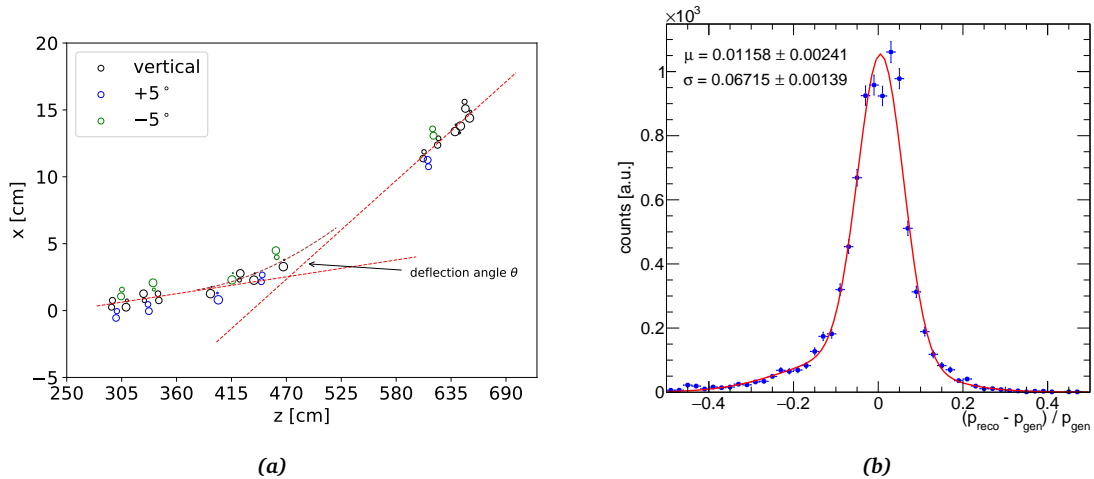


Figure 26: (a) The particle momentum is estimated from the kick that the particle receives in the magnetic field. The dashed red lines are the fit lines before and after the field, while the dashed brown curve is the circle fit for hits inside the field. The black circles are the isochrones of the vertical layer hits, the blue and green circles are the isochrones of skewed layer hits. (b) The relative momentum resolution.

3.6 SUMMARY

In this chapter, a track finding algorithm has been introduced for the \overline{P} ANDA forward tracker. The algorithm is based on the GNN, a type of neural networks that accepts non-Euclidean data as graphs. The input of the GNN is an image of the FTS, where the detector hits are the graph vertices and all possible connections between two hits in adjacent layers are the graph edges. The GNN was trained to classify the graph edges to true or fake edges, the architecture used is based on the one developed by the Exa.TrkX collaboration. The network converged quickly and scored 99.5% classification accuracy after 10 iterations. A clustering algorithm has been implemented to reconstruct track candidates guided by the output of the GNN. The aim of the clustering algorithm is to traverse the graph depth-wise in order to find the connected components in the output graph. The performance of the developed algorithm were evaluated based on defined QA measurements, which are the purity, the efficiency and the ghost rate. On average, the purity was found to be $\approx 100\%$, the efficiency $\approx 90\%$ and the ghost ratio less than 3%.

The aim of the GNN was to use the hits in the vertical layers to reconstruct projections of track candidates in the $x - z$ plane of the FTS. The second step of the track finding algorithm was aimed to use the reconstructed $x - z$ projections as “seeds” to build the $y - z$ plane track motion by adding the skewed layer hits. The $x - z$ projection has been fit by a linear model for track segments outside the magnetic field and a circular motion is assumed inside the magnetic field. In order to obtain a y measurement, the set of compatible hits in the skewed layer hits were collected by first testing the L/R ambiguity and then histogramming the slopes assuming the magnetic field effects in the $y - z$ plane is negligible. In addition, the fitting procedure provide more accurate hit positions. The vertical position resolution is about 11 times worse than the horizontal resolution since it depends on the inclination angle. The algorithm also provides an estimate value for the particle momentum that is calculated by the p-kick method. The relative momentum resolution was found to be 6.7%.

Σ^0 PRODUCTION IN P + P COLLISIONS

This chapter presents the reconstruction of Σ^0 hyperons created in proton-proton collisions at a center-of-mass energy of $\sqrt{s} = 3.18$ GeV recorded with the HADES detector setup. In particular the focus is on the exclusive reconstruction of the reaction $p + p \rightarrow p + K^+ + \Sigma^0$. This is the energetically most favorable reaction in which a Σ^0 hyperon is produced due to strangeness conservation.

The study of hyperon production in proton-proton collisions at energies of a few GeV is important for a better understanding of the strong interaction including the strange quarks. It is also crucial as a baseline for in-depth studies of the heavy ion collisions, e.g. strangeness enhancement is proposed as a signature for the formation of the Quark Gluon Plasma (QGP) which is expected to form if the energy density is high enough [83]. It is also discussed as a way to study hot and dense nuclear matter [33]. Therefore the results of this work can give insight about input parameters (e.g. cross section) for an improved incorporation of the hyperon dynamics into transport models, which are used to simulate heavy ion collisions.

In addition, a measurement of the hyperon radiative decay $\Sigma^0 \rightarrow \Lambda \gamma$ provides a clean prob of the hyperon wave function as will be discussed in detail in the next chapter. Furthermore, a measurement of the Dalitz decay $\Sigma^0 \rightarrow \Lambda \gamma^* \rightarrow \Lambda e^+ + e^-$ (BR < 1%) can provide information on the hyperon form factors [6]. Therefore, this measurement can be considered as a step towards measuring the hyperon electromagnetic form factors.

Although there are numerous experimental results for Λ hyperon production [5, 8, 14, 23, 91], there are few measurements for Σ^0 hyperon [5, 6]. Results on $p + p \rightarrow p + K^+ + \Lambda$ near threshold show a significant deviation from a pure phase space distribution, and a proton-hyperon Final-State Interaction (FSI) has to be included to describe the data [5, 91]. It was found that the hyperon production is dominant by the excitation and subsequent decay of N^* resonances in the $K^+ \Lambda$ decay mode, in particular $N(1650)S_{11}$, $N(1710)P_{11}$ and $N(1720)P_{13}$ from which it has to be concluded that the exchange of non-strange mesons is the leading process in the production mechanism.

In the $p + p \rightarrow p + K^+ + \Sigma^0$ reaction the proton–hyperon FSI seems to be negligible and pure phase space distribution describes the data reasonably well. The cross section ratio $\sigma(pK^+\Lambda)/\sigma(pK^+\Sigma^0)$ below excess energies of ~ 20 MeV is about 28 and reduces drastically to about 2.5 for excess energies higher than 300 MeV [85]. This energy-dependence of the cross section ratio could be governed primarily by FSI effects in the $p + p \rightarrow p + K^+ + \Lambda$ reaction [110].

This chapter is organized as follows: The first section discusses general aspects of hyperon production in proton-proton reactions. In particular, the One-Boson-Exchange model is discussed. Furthermore, the center of mass frame, Gottfried-Jackson and helicity reference frames are presented as the experimental data are studied in these reference frames. The second section describes the analysis part and the cuts that has been applied for the event selection. The second section describes the application of the kinematic refit technique to reduce the background contribution and improve the mass resolution of the Σ^0 hyperon. The last section starts with the extraction of the Σ^0 yield the various steps of the analysis and then presents the angular distributions in the different reference frames.

4.1 THEORETICAL BACKGROUND

4.1.1 Phase Space Considerations

The exclusive reaction discussed here corresponds to $2 \rightarrow 3$ inelastic scattering, in quantum mechanics, the transition from an initial to a final state is calculated from Fermi’s golden rule. During the transition the four-momentum are conserved and thus the final state momentum vectors p_i cannot vary arbitrarily for a given initial state. Fermi’s golden rule states that the probability per unit time that a transition will take place from an initial state to a final state is:

$$\Gamma_i = \frac{2\pi}{\hbar} |\mathcal{M}_{fi}| \rho(E), \quad (10)$$

where \mathcal{M}_{fi} is the matrix element or the reaction amplitude, which contains the dynamics of the transition and $\rho(E)$ is the density of states available at the energy E that depends on the kinematics of the process being considered and is known as the *phase space density*. In general the matrix element may be unknown; in the simplest case of a constant matrix element ($\mathcal{M}_{fi}=1$), the momentum distributions of the final state particles are governed by the phase space factor. In this case the differential distributions and the cross section

are said to be given by the phase space. If the experimentally measured distributions tend to deviate from phase space this denotes a dynamical effect, for instance, a resonance.

In order to obtain experimental quantities, the transition rate has to be integrated. When the integration is done over all possible values of the momentum p_i , that is, over the entire phase space, the total cross section is obtained. If the integration is restricted to a subset of the phase space, a differential cross-section is obtained.

Consider a general $2 \rightarrow 3$ reaction labeled as $a + b \rightarrow 1 + 2 + 3$, the differential reaction cross section at fixed center of mass energy can then be written as [111]:

$$\frac{d\sigma}{ds_1 ds_2 ds t_1 dt_2} = \frac{|\mathcal{M}(s, s_1, s_2, t_1, t_2)_{fi}|^2}{2^{10} \pi^4 \lambda(s, m_a^2, m_b^2) \sqrt{-\Delta_4}}, \quad (11)$$

where the independent invariants are given by the 4-momentum of the initial and final state particles

$$\begin{aligned} s &= (p_a + p_b)^2 \\ s_1 &= (p_1 + p_2)^2 \\ s_2 &= (p_2 + p_3)^2 \\ t_1 &= (p_a - p_1)^2 \\ t_2 &= (p_a - p_3)^2 \end{aligned}$$

The $\lambda(s, m_a^2, m_b^2)$ is the Källén function ¹, also known as the triangle function and $-\Delta_4$ is the Gramm determinant of a 4×4 symmetric matrix whose elements are a combination of s, s_1, s_2, t_1, t_2 and the masses of the initial and final particles.

One of the methods to detect dynamical effects in the reaction under consideration is the Dalitz plot. It is a visual representation of the phase space of a three body system. The integration of Eq. 11 over t_1 and t_2 results in the Dalitz plot defined as the physical region in the $s_1 s_2$ plane. More generally, the Dalitz plot can be defined as the physical region in terms of any variables related to s_1 and s_2 by a linear transformation with a constant Jacobian [37].

A widely used Dalitz plot is represented as a correlation of the invariant mass squared of two particles in the final state (e.g. M_{12}^2 against M_{23}^2). The Dalitz plot has the important property that equal areas in the plot correspond to equal volumes in the three body phase space. A uniformly distributed Dalitz plot is an indication of the absence of intermediate resonances or FSI. If, for instance, a resonance occurs between particles 2

¹ In three variables, the Källén function is given by $\lambda(x, y, z) = x^2 + y^2 + z^2 - 2xy - 2yz - 2zx$

and 3, there will be an increased density of points in a band at fixed M_{23}^2 . The boundary of the Dalitz plot is fixed by momentum conservation and the total energy available to the system [35].

4.1.2 Production Mechanisms

Eq. 10 clearly states that the transition rate consists of two parts, the kinematical and the dynamical part. As mentioned in the previous section any deviation from phase space behavior could indicate a dynamical effect. In this section we discuss the dynamical part in the context of the One Boson Exchange model (OBE). This model dates back to 1930s when Yukawa proposed a theoretical model in an attempt to explain the nucleon-nucleon (NN) interactions. He made the hypothesis that nucleons interact through the exchange of a boson whose mass is related to the range of the interaction. The interaction between the boson and the initial nucleons (protons in this case) results in the production of the final state particles. The t-channel scattering process represented by the Feynman diagrams are illustrated in Fig. 27. Here Y stands for hyperons (e.g Λ , Σ^0 etc.) and R stands for every kind of nucleon resonances, that can be an isospin 1/2 N^* state or an isospin 3/2 Δ^* state. These production mechanisms are understood as being representatives of a whole class of reaction scenarios rather than of the concrete processes. Kaon exchange diagram represents a scenario where there is strangeness exchange, pion exchange diagram, on the other hand, stands for a scenario where no strangeness exchange occurs. The experimental angular distributions are determined by the properties of the exchange diagrams and the exchange meson itself. The correlation between the final and initial state baryon directions is determined by the mass of exchange meson [88]. The exchange of a heavy meson leads to very central collisions, in this case the nucleon and the hyperon are produced isotropically in the center of mass frame. Whereas light meson exchange, is correlated with very peripheral collisions as the exchange meson transfers small 4-momentum to the final state particles so that they are preferably emitted in the direction of the initial protons.

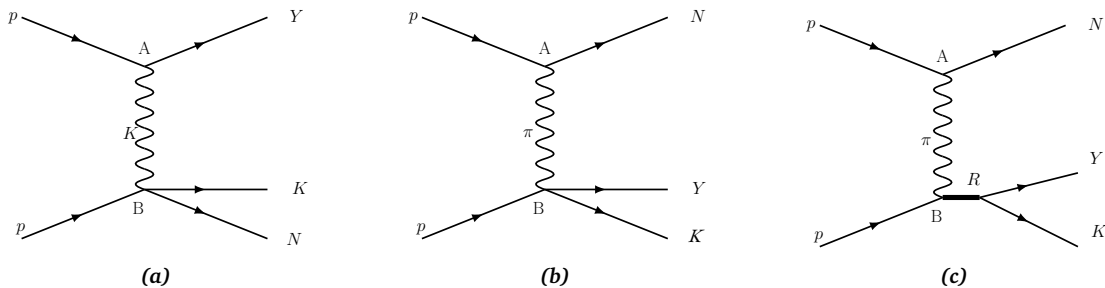


Figure 27: Feynman diagrams representing t-channel scattering in case of (a) kaon exchange, (b) pion exchange and (c) pion exchange with an intermediate resonance produced, which decays to a hyperon and a kaon.

The simplest way to calculate the contributions of the diagrams in Fig. 27 is to use the Chew-Low formula [40]:

$$\frac{d^4\sigma}{d(M^2)d(\Delta^2)d\Omega} = \frac{1}{4\pi} \frac{G^2}{4\pi} \frac{1}{(2p^*E^*)^2} \frac{\Delta^2 + (m_p - m)^2}{(\Delta^2 + \mu^2)^2} kM \frac{d\sigma(M)}{d\Omega}, \quad (12)$$

where

- $k = \frac{1}{M} \left[\frac{1}{4}M^4 - \frac{1}{2}M^2(m_p^2 + \mu^2) + \frac{1}{4}(m_p^2 - \mu^2) \right]^{\frac{1}{2}}$ is a kinematic factor, which can be identified as the momentum of the exchanged meson in the center of mass system of the two produced particles at vertex B.
- p^* and E^* are the center of mass momentum and energy of the incident proton, respectively.
- $\frac{G^2}{4\pi}$ is the meson baryon-baryon coupling constant describing vertex A in Fig. 27.
- Δ^2 is the 4-momentum squared of the exchange meson to the recoil baryon of mass m .
- μ and m_p are the masses of the exchange meson and the proton, respectively.
- M is the invariant mass of the particles emerging at vertex B.
- $\frac{d\sigma(M)}{d\Omega}$ is the differential cross section of the two particles at vertex B, $\pi p \rightarrow KY$ for pion exchange and $Kp \rightarrow Kp$ for kaon exchange.

This formula was found to reproduce the experimental angular distributions of final state baryons in the center of mass frame as can be shown in Fig. 28. This figure shows the absolute values of the cosine of the final state proton angle measured in the center of mass frame for (a) $p + p \rightarrow p + K^+ + \Lambda$ and (b) $p + p \rightarrow p + K^+ + \Sigma^0$, both angular distributions peak at $|\cos\theta| = 1$, which suggests that the particles are preferably emitted along the direction of the incoming protons. This can be easily understood by considering the denominator in Eq. 12 where the mass of the exchanged meson appears μ^2 , here the angular distribution will show anisotropy in the center of mass frame for light meson exchange. Furthermore the momentum transfer Δ^2 also appears in the denominator, the center of mass angular distributions of the final state baryons are closely related to the momentum transfer distribution [56]. As a result, a small momentum transfer produces anisotropic center of mass angular distributions, while a large momentum transfer produces isotropic distributions, as observed in the angular distributions of $\Lambda(1405)$ and $\Lambda(1520)$ [12].

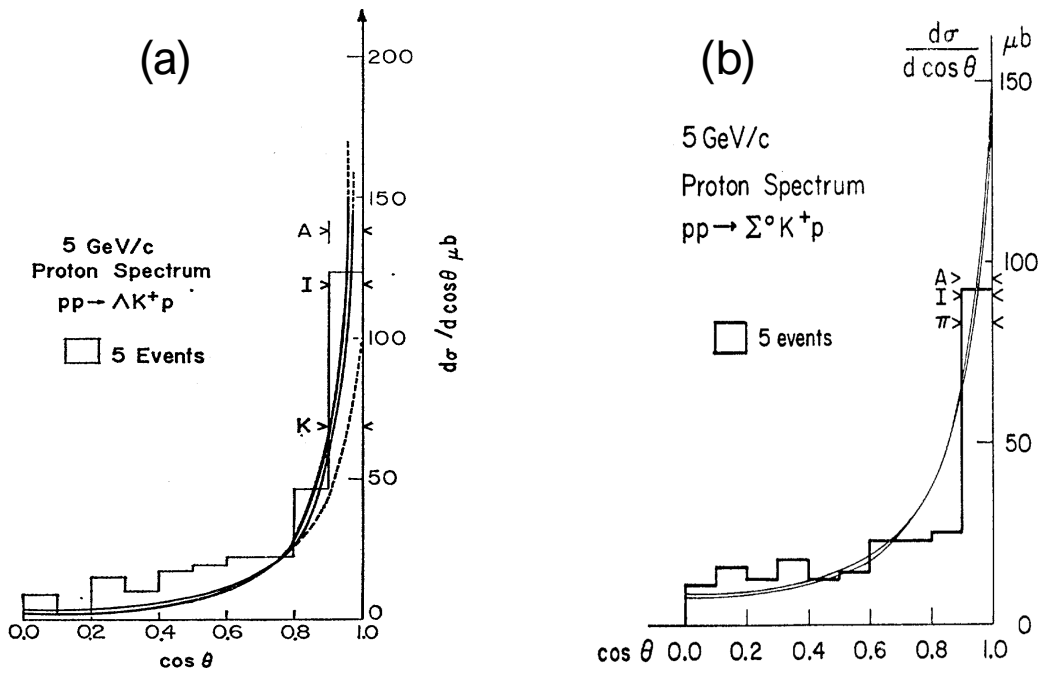


Figure 28: Angular distribution of final state protons in the center of mass frame measured at beam momentum 5 GeV/c for (a) $p + p \rightarrow p + K^+ + \Lambda$ and (b) $p + p \rightarrow p + K^+ + \Sigma^0$, the solid curve represents the prediction of the Chew-Low formula [56].

Another important term in Eq. 12 is $\frac{d\sigma(M)}{d\Omega}$, which represents the differential cross section of the $2 \rightarrow 2$ reaction at vertex B that is usually an unknown function and might be characterized by certain angular distributions or the production of intermediate resonances.

4.1.3 Reference Frames

In this section, a set of reference frames, defined by the properties of the initial and final states of the collision process, is introduced. Later on, the experimental angular distributions will be studied in these reference frames.

Center of Mass frame

The center-of-mass system (CMS) is a Lorentzian reference frame, where the beam and target proton have identical momenta in opposite directions, that is:

$$\vec{p}_{target} = -\vec{p}_{beam},$$

where \vec{p}_{target} and \vec{p}_{beam} are the momenta of the colliding protons. The CMS angle is the polar angle of one of three final state particles in the CMS frame as shown in Fig. 29a. The angular distribution in this reference frame must be symmetric with respect to $\cos\theta = 0$ since the proton-proton system is symmetric.

The OBE model relates the production anisotropy to the properties of the exchange meson. As an example, in the case of pure pion exchange, the primary proton interacts at vertex A and produces the virtual pion. Since the mass of the pion is relatively small, there will be a small 4-momentum transfer to the final state nucleon. Consequently, the deflection of the nucleon will be small, which results in anisotropic angular distributions. Because of momentum conservation, the sum of the momentum of the kaon-hyperon KY system produced at vertex B must equal to that of the nucleon N at vertex A, which means that the KY system is a mirror image of the N . Now consider the case where the KY system is produced via an intermediate resonance R (see Fig. 27c), the R resonance decays in its own rest frame back to back into a hyperon and kaon. The available energy for this decay depends on the mass of the resonance and takes values between zero and the threshold energy of the reaction $p + p \rightarrow p + (R \rightarrow K + Y)$, because the hyperon is heavier than the kaon, it will preserve the direction of flight of the resonance, while the kaon will be emitted isotropically. In conclusion, in the case of pure pion exchange, the nucleon and the hyperon CMS angular distributions show an anisotropy, while the kaon is produced rather isotropically. However the anisotropy is more pronounced for the nucleon.

In the case of pure kaon exchange, the roles of the nucleon and the hyperon are exchanged, the hyperon shows the strongest production anisotropy in the CMS frame. Because the nucleon-kaon system is a mirror image of the hyperon, their CMS angular distributions are just kinematic reflections of the hyperon.

One has to take the differential cross section $\frac{d\sigma(M)}{d\Omega}$ also into consideration, as it affects the particles produced at vertex B, which obviously influences their CMS angular distributions. This quantity is accessible in the Gottfried-Jackson frame.

Gottfried-Jackson frame

The Gottfried-Jackson frame (G-J) was introduced by Gottfried and Jackson in 1964 and defined as the rest frame of two out of the three produced particles [67]. The G-J angle $\cos\theta_{p,B}^{RF AB}$ is the polar angle between the final state particle B and the initial

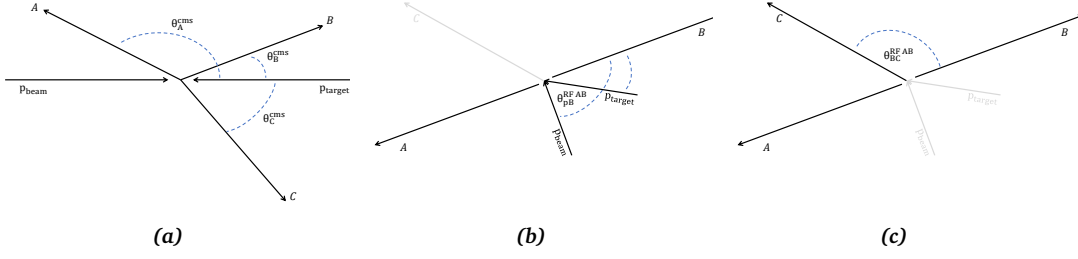


Figure 29: Definitions of different reference frames (a) center of mass frame, (b) Gottfried-Jackson frame and (c) the helicity frame.

proton as measured in the rest frame of particles A and B as illustrated in Fig. 29b, the superscript indicates which rest frame is used (RF stands for Rest Frame) and the subscript indicates the two particles, between which the angle is measured.

The motivation to study the G-J angular distribution is that it reduces the $2 \rightarrow 3$ reaction into $2 \rightarrow 2$ reaction of the form $K(\pi) + p \rightarrow N(Y) + K$. In addition it connects the exit and entrance channel and carries information not accessible by means of a Dalitz plot analysis [5].

Consider the pion exchange reaction $\pi + p \rightarrow K + Y$, which connects the particles produced at vertex B. Because of time reversal symmetry the inverse reaction $K + Y \rightarrow p + \pi$ should have the same properties, now consider the rest frame of KY which by definition is the KY G-J frame, the G-J angle $\cos\theta_{p,K}^{RF KY}$ gives information of the differential cross section $\frac{d\sigma(M)}{d\Omega}$ at vertex B and the partial waves involved. This is also true if the particle production does not happen directly, but via an intermediate resonance. The quantum numbers of the resonance is then reflected in this observable. The same argumentation should hold for the case of kaon exchange $p + K \rightarrow p + K$.

It should be noted, that there is no reason for the G-J angle to show any symmetry with respect to $\cos\theta_{p,K}^{RF KY} = 0$, as the colliding particles (p and π in this case) are not identical. A peculiarity arises from the fact that the two initial protons are indistinguishable. It is not known which of those protons contributes to the reaction. Therefore, the angular distribution is calculated by using the angle to both protons.

Similar to the Dalitz plot, the G-J angle (e.g. $\cos\theta_{p,K}^{RF KY}$) can be calculated as a function of the reaction invariants [111]:

$$\cos\theta_{p,K}^{RF KY} = \frac{2s_2(t_2 - m_a^2 - m_K^2) + (s_2 + m_a^2 - t_1)(s_2 + m_K^2 - m_Y^2)}{\lambda^2(s_2, m_a^2, t_1)\lambda^2(s_2, m_K^2, m_Y^2)}, \quad (13)$$

where the invariants are given by the 4-momentum of the initial and final state particles

$$\begin{aligned} s_2 &= (p_K + p_Y)^2 \\ t_1 &= (p_a - p_N)^2 \\ t_2 &= (p_a - p_K)^2. \end{aligned}$$

Here, λ is the Källén function, m_a is the mass of the initial proton, m_K is the kaon mass and m_Y is the hyperon mass.

Helicity frame

The helicity frame is defined in a similar way as the G-J frame, two of three particles in the final state are used to define the reference frame, but instead of calculating the angle with respect to the initial proton, the angle to the third produced particle is used, as shown in Fig. 29c. Therefore the helicity angle interrelates the three particles of the exit channel. The helicity angular distribution is a special projection of the Dalitz plot, hence it is a good observable to identify the dynamics behind the particle production mechanism. A uniformly populated Dalitz plot results in isotropic helicity angular distributions, whereas dynamical effects distorting the Dalitz plot will result in anisotropic helicity angular distributions [5].

If the reaction $p + p \rightarrow p + K + Y$ proceeds via an intermediate resonance, that is $p + p \rightarrow p + (R \rightarrow K + Y)$, the angular distributions $\cos\theta_{p,K}^{RF pY}$ and $\cos\theta_{K,Y}^{RF pK}$ will show characteristic behaviors, which reflect the mass and width of the resonance R . In contrast to this, the angular distribution, calculated in the rest frame of the two decay particles $\cos\theta_{p,Y}^{RF KY}$ is not influenced by the mass and width of the resonance. Only if the resonance carries angular momentum $L > 0$ or if it is polarized will this distribution be different from isotropic [79]. However, if more than one resonance contributes to the decay into Y and K interference effects can influence the helicity angular distribution $\cos\theta_{p,Y}^{RF KY}$ [5].

The helicity angle (e.g. $\cos\theta_{p,Y}^{RF KY}$) can be written as the following function of the reaction [111]:

$$\cos\theta_{p,Y}^{RF KY} = \frac{2s_2(m_p^2 + m_K^2 - s_1) + (s - s_2 - m_p^2)(s_2 + m_K - m_Y)}{\lambda^{1/2}(s, s_2, m_p^2)\lambda^{1/2}(s_2, m_K^2, m_Y^2)}. \quad (14)$$

4.2 ANALYSIS PROCEDURE

In the following sections we investigate the exclusive reconstruction of the reaction Σ^0 hyperon produced in proton-proton collisions at beam kinetic energy 3.5 GeV and an intensity of $\sim 10^7$ particles/s [13], the data has been collected by HADES in 2007. The proton beam was incident on a liquid hydrogen target (LH_2) with a density of 0.35 g/cm^2 , a thickness of 50 mm and a total interaction probability of $\sim 0.7 \%$. In total there were 1.14×10^9 first-level triggered events, which required at least three hits in the META system (M3) [8]. The Σ^0 hyperon is a member of the $J^P = \frac{1}{2}^+$ baryon octet and decays electromagnetically with a branching ratio $\text{BR}(\Sigma^0 \rightarrow \Lambda \gamma) \approx 100\%$. The daughter Λ hyperon has two main decay modes $\text{BR}(\Lambda \rightarrow p \pi^-) = 63.9 \%$ and $\text{BR}(\Lambda \rightarrow n \pi^0) = 35.8\%$ [121]. As mentioned in chapter 2, the HADES detector setup is designed only to reconstruct charged particles, therefore, the only possible channel for this analysis is:

$$p + p \rightarrow p + K^+ + \Sigma^0 \rightarrow p + K^+ + p + \pi^- + \gamma. \quad (15)$$

The neutral photon can be identified as a missing particle via the missing mass technique, as will be explained below. The reconstruction of this signal is done in two different ways, in the first case, events with four charged particles identified to be ($2p$, $1\pi^-$ and $1 K^+$) are required to be within the acceptance of the main HADES setup, in the other case, only three charged particles identified as ($1p$, $1\pi^-$ and $1 K^+$) are required to be within the acceptance of the main HADES setup and at least one hit in the Forward Wall hodoscope. In the following these two data sets are referred to as the HADES data-set and FWall data-set, respectively.

4.2.1 Simulations

Event Generation

In this section we present a description of the simulations of possible contributing channels to the final spectrum presented later. All channels are simulated by the PLUTO phase space generator [59] and then propagated through HGeant, which contains a detailed description of the detector geometry and emulates all the particle interactions with the detector material. The existing data base for the production cross section for the different channels at beam energy 3.5 GeV is limited, this cross section is needed in order to quantify the contribution of each channel. Therefore, the following procedure was applied to estimate the cross sections for various channels at this beam energy. First

the cross sections at various beam energies are collected from [57], and then they have been fit by a phase space distribution according to the following parametrization:

$$\sigma(s) = a \cdot \left(1 - \frac{s_0}{s}\right)^b \cdot \left(\frac{s_0}{s}\right)^c,$$

where s is the center of mass energy (here $\sqrt{s} = 3.18$ GeV), s_0 is the threshold energy of the reaction, a , b and c are the free parameters of the fit. Examples of the fit are shown in Fig. 30 and a summary of all the determined cross sections is listed in Tab. 1.

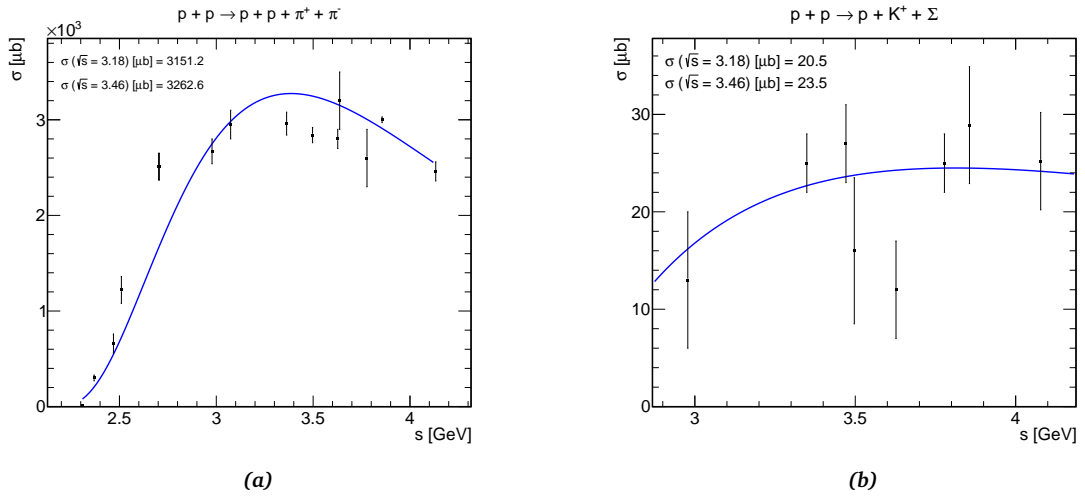


Figure 30: An example of the phase space fit for (a) $p + p \rightarrow p + p + \pi^+ + \pi^-$ (b) $p + p \rightarrow p + K^+ + \Sigma^0$. Determined cross section at beam energy 3.5 GeV and 4.5 GeV are shown.

	Channel	σ [μb]
1	$p + p \rightarrow p + K^+ + \Lambda$	35.26
2	$p + p \rightarrow p + K^+ + \Sigma(1385)$	6.0
3	$p + p \rightarrow p + K^+ + \Lambda(1405)$	9.2
4	$p + p \rightarrow p + p + \pi^+ + \pi^-$	3151.2
5	$p + p \rightarrow p + p + \pi^+ + \pi^- + \pi^0$	1304.0
6	$p + p \rightarrow p + K^+ + \Sigma^0$	20.5
7	$p + p \rightarrow p + K^+ + \Lambda + \pi^0$	6.0
8	$p + p \rightarrow p + K^+ + \Sigma^0 + \pi^0$	14.7
9	$p + p \rightarrow p + K^+ + \Sigma^+ + \pi^-$	4.3

Table 1: Production cross section of the simulated channels. Cross sections of channels 1, 2 and 3 are taken from [8], the rest are estimated by a phase space fit.

Momentum correction

During the event selection the missing mass technique is used for the event selection method, which require that the mass peaks should be in the correct position; e.g. the Λ hyperon mass peak should be around $1.116 \text{ GeV}/c^2$. If this is not the case, this will lead to a bias in the event selection. A shift of the mass peak position is a result of incorrect momentum measurement. The momentum measurement is affected by the energy loss of the daughter particles in the detector material. This is especially important at low momenta where this influence cannot be neglected. Therefore, a momentum correction is applied to all simulated channels. The procedure is summarized as follows, first the absolute difference between the reconstructed momentum and the generated momentum is plotted as function of the reconstructed momentum for each particle species (blue filled circles), then this is fit by a polynomial function as shown in Fig. 31. This fit function is then used to correct the momentum of the particles. As can be shown from the figure, the momentum difference after the correction (red open circles) is correctly centered around zero.

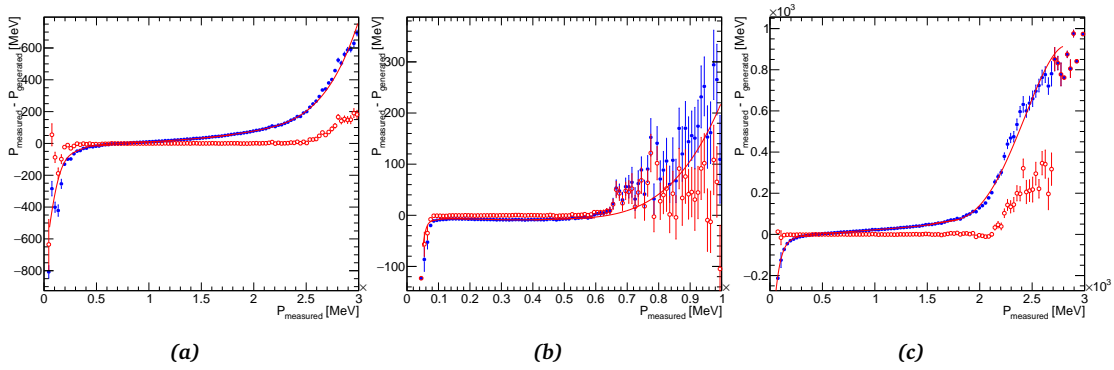


Figure 31: The absolute difference between the reconstructed momentum and the generated momentum as a function of the reconstructed momentum for (a) protons p , (b) pions π^- and (c) kaons K^+ . The momentum correction function is shown by the red curve, the red dots shows the particle momentum difference after the correction procedure.

Fig. 32 shows the effect of the momentum correction on the missing mass of the primary proton and the kaon $MM(pK^+)$ (see Eq. 23), as shown in the figure the peaks due to $p + p \rightarrow p + K^+ + \Lambda$ and $p + p \rightarrow p + K^+ + \Sigma^0$ are shifted to the correct position after the momentum correction.

4.2.2 Start Time t_0 Reconstruction

During the $p + p$ 2007 beam time the START detector was not in operation, because interactions of the high intensity proton beam with the START detector and the surround-

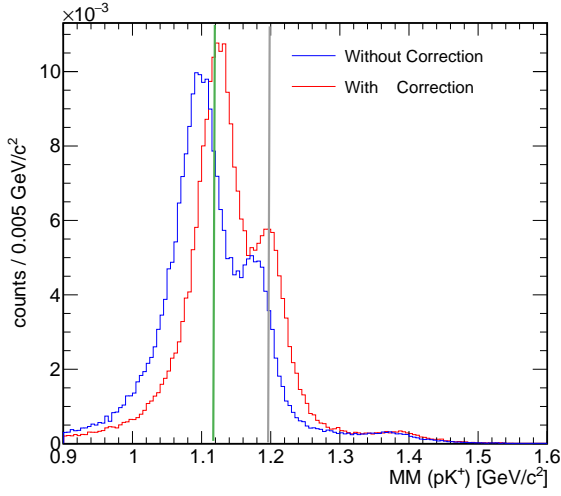


Figure 32: $MM(pK^+)$ missing mass distribution of the sum of all simulated channels before (blue) and after (red) the momentum correction. The sum is weighted according to the estimated cross section. The green vertical line indicates the nominal Λ mass ($1.11568 \text{ GeV}/c^2$) and the gray line indicates the nominal Σ^0 mass ($1.19264 \text{ GeV}/c^2$)

ing material prevented a stable RICH operation. As a consequence there is no common start time t_0 reference for all tracks and the time-of-flight (tof) of tracks is not directly accessible [96]. The tof measurement allows to perform the particle identification in combination with the momentum information provided by the tracking system. The time of flight system is constituted by the START detector along with the TOF and TOFINO systems, since the TOF and TOFINO systems do not measure the particle tof , but its difference in time with respect to the particle which triggered the data acquisition, so the start time t_0 has to be reconstructed in order to perform a proper time of flight measurement.

The algorithm to reconstruct t_0 works on an event by event basis. As mentioned above, the tof of a particle is given by the difference between the stop time t_s as measured by the TOF or TOFINO minus the start time t_0 measured by the START detector:

$$tof = t_s - t_0 \quad (16)$$

So in order to reconstruct the start time t_0 , at least one particle has to be identified, because t_0 is common for all particles in the event, the tof of the other particles in the same event can be calculated from the reconstructed t_0 and the stop times t_s . Starting from the relativistic momentum definition:

$$p = \frac{m\beta}{\sqrt{1 - \beta^2}}, \quad (17)$$

where p is the momentum of the particle, m is its mass and $\beta = \frac{v}{c}$ is its reduced velocity. Since the velocity can be given by $\beta = \frac{L/tof}{c}$, where L is the path length of the particle, thus the theoretical tof can be calculated by reformulating Eq. 17:

$$tof = \frac{L}{c} \cdot \frac{\sqrt{p^2 + m^2}}{p}. \quad (18)$$

Both p and L are given by the tracking algorithm. If we can identify one particle in the event we can assume its mass and thus calculate its theoretical time of flight. The start time t_0 is then calculated from the difference between the measured stop time t_s and the theoretical time of flight.

Because there is one negative charged particle in the final state being investigated, it can be assumed to be either an electron e^- or a pion π^- , depending upon the angular correlation between inner track segment in the MDC and rings in the RICH detector.

In order to quantify the correlation between the ring position and the track segment position, the following two quantities are computed:

$$\begin{aligned} \Delta\theta &= \theta_{RICH} - \theta_{MDC} \\ \Delta\phi \cdot \sin\theta_{MDC} &= (\phi_{RICH} - \phi_{MDC}) \cdot \sin\theta_{MDC}, \end{aligned} \quad (19)$$

where θ_{RICH} and ϕ_{RICH} are the polar and azimuthal angles of a ring in the RICH detector in the laboratory frame, θ_{MDC} and ϕ_{MDC} are the angular coordinates of the inner MDC segment. The multiplication by a factor of $\sin\theta_{MDC}$ is introduced to keep the solid angle spanned constant [52]. Based on Eqs. 19, the RICH matching quality is defined as:

$$d = \sqrt{(\Delta\theta)^2 + (\Delta\phi \cdot \sin\theta_{MDC})^2} \quad (20)$$

A ring in the RICH detector is considered matched to MDC track if the RICH matching quality d is the smallest, in this case the track is identified as an electron e^- , otherwise it is identified as a pion π^- . The distribution of the RICH matching quality d is shown in Fig. 33.

By identifying a particle in the event, we can assume its mass and then the start time t_0 can be calculated as the difference between the stop time t_s and the theoretical tof . If more than one particle is used in the t_0 reconstruction, the average \bar{t}_0 is calculated according to:

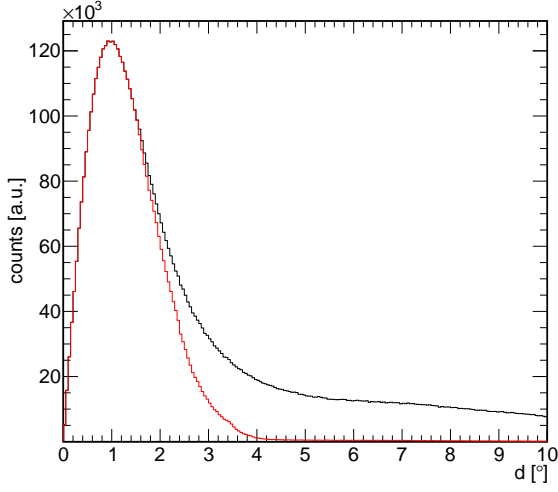


Figure 33: The RICH matching quality for everything (in black) and for matched rings (in red).

$$\bar{t}_0 = \frac{\sum_i w_i t_{0,i}}{\sum_i w_i}, \quad (21)$$

where w_i is a weight factor that is $w_i = 2.5$ if the t_s is measured by the TOF system or $w_i = 1$ if the t_s is measured by the TOFINO system, this is because the TOF resolution is about 2.5 times better than the TOFINO resolution. The velocity β of positively charged tracks as a function of momentum before and after t_0 reconstruction is shown in Fig. 34. As can be shown after t_0 reconstruction the data points are centered around the theoretical curves.

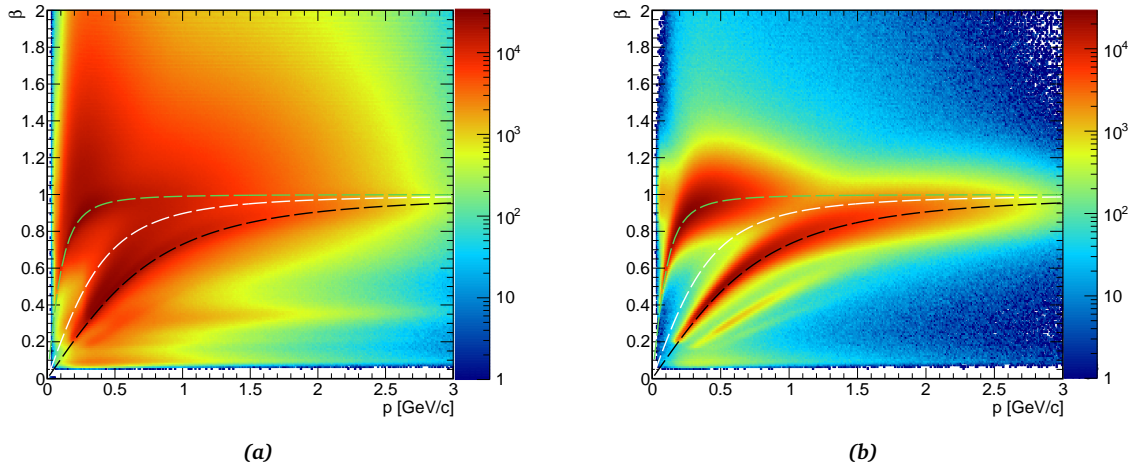


Figure 34: The velocity β as a function of momentum (a) before t_0 and (b) after t_0 reconstruction (under the condition $|t_0| < 1$ ns). The green, white and black dashed lines represents the theoretical values for pions, kaons and protons, respectively.

4.2.3 Particle Identification PID

Conventional PID method

The next step after reconstructing the time of flight, is the charged particle identification (PID). In the reaction we are investigating (Eq. 15) there are three positively charged particles, one negatively charged particle and one neutral particle. The neutral particle γ is identified as a missing particle, and as mentioned in the previous section the π^- is identified as any negatively charged track that is geometrically uncorrelated to a ring in the RICH detector. This means that the problem is reduced to identify protons p and kaons K^+ .

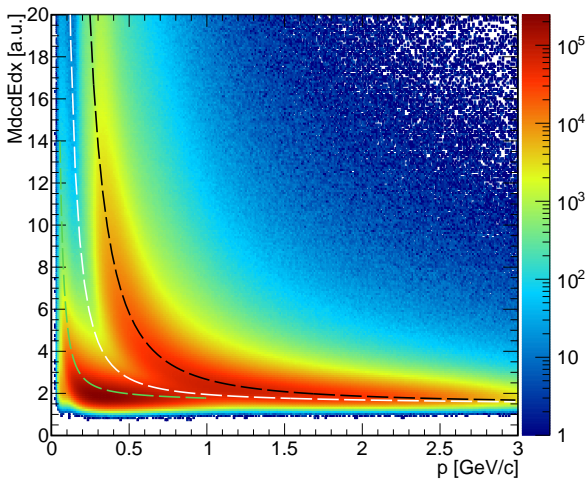


Figure 35: The Energy loss dE/dx as a function of the momentum for all particle candidates. The green, white and black dashed lines represents the theoretical Bethe-Bloch values for pions, kaons and protons, respectively.

Many of the HADES analyses rely on the energy loss as a function of momentum as a PID method by placing graphical cuts around the theoretical Bethe-Bloch curves as shown in Fig. 35. However as can be seen from the figure, kaons are not visible, as they are suppressed in this energy range with respect to protons and pions. Therefore, by this PID method kaons are heavily contaminated by pions and protons.

Deep Learning Based PID

In order to overcome this problem and obtain a relatively clean sample of kaons, we rely on DL algorithms, because of their capability to model complex and non-linear data dependencies. For this purpose a neural network is trained to classify particle tracks into three classes or categories; protons p , kaons K^+ and pions π^+ . Therefore, this is a multi-class classification problem, which means that the training data should be labeled, in other words, the network should be trained with simulated events.

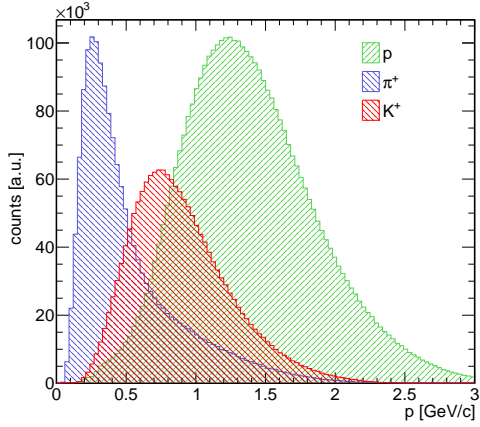
One problem arises here from the fact that simulations do not model real data perfectly, this can be due to mis-modelling of some detector effects. As a result, a neural network trained on simulation might not perform well on real data. This is a well know problem in DL, if the unseen data has a different distribution, then a *domain shift* exists [98]. To address this problem a variational auto-encoder is trained in a *semi-supervised* way simultaneously on real data and simulations. A Semi-supervised learning [132] falls between unsupervised and supervised learning that make use of both labeled and unlabeled data points.

Variational Auto-Encoders VAE

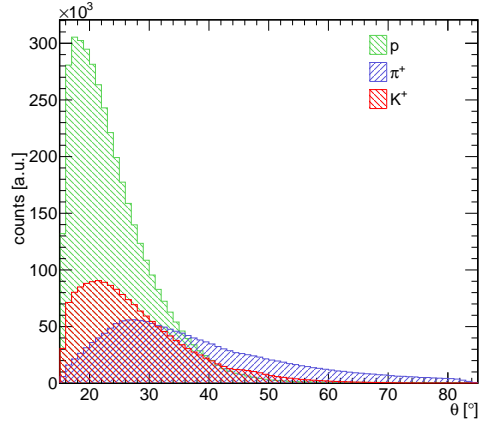
An auto-encoder is a neural network that learns how to efficiently encode input data into a bottleneck layer (a *latent representation*) by compressing the input features, then learns how to reconstruct it back from the compressed encoded representation. A typical auto-encoder consists of two connected networks, the *encoder* and the *decoder*. The encoder compresses the input into a latent representation, that can be considered as new features extracted from the input features, and the decoder uses the latent representation and tries to reconstruct the original input.

A VAE is an auto-encoder with the assumption that the input data has an underlying probability distribution and then the VAE attempts to find the parameters of the distribution, from this definition, it follows that the VAE is a generative model. A VAE is intended to learn a latent space z , given set of training samples x . In particular, the model consists of a generative model (the encoder) $p(x|z)$ given a fixed prior $p(z)$, and an inference model (the decoder) $q(z|x)$, the VAE is trained by minimizing the Kullback-Leibler (KL) divergence, which is a measure of the difference between two probability distributions [47].

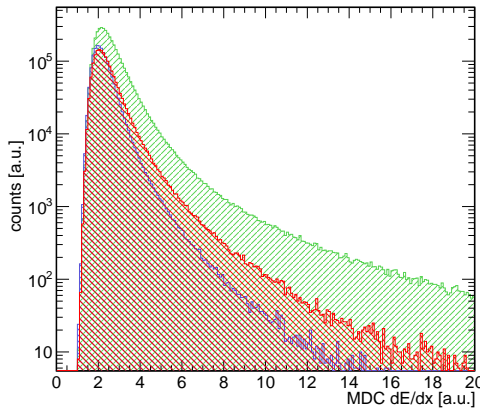
A schematic diagram of the VAE model used for the PID is shown in Fig. 37. The model takes labeled (simulations) and unlabeled (real data) events, it learns the combined features of both real and simulated events and compress it to the *latent space*. The real data takes the upper path, where the decoder tries to reconstruct the input from the latent space. The simulations takes the lower path, where a classification layer is stacked on top of the bottleneck layer (the latent space). The network is trained by a semi-supervised technique, for which the upper path is completely unsupervised and the lower path is completely supervised [82]. The model implemented is inspired by the M2 model proposed by Kingma et. al. in [82]. The VAE is implemented in PyTorch [94] with two hidden layers. In addition, a 50% dropout layer is applied in order to prevent the model from overfitting and to quantify the uncertainty of the network.



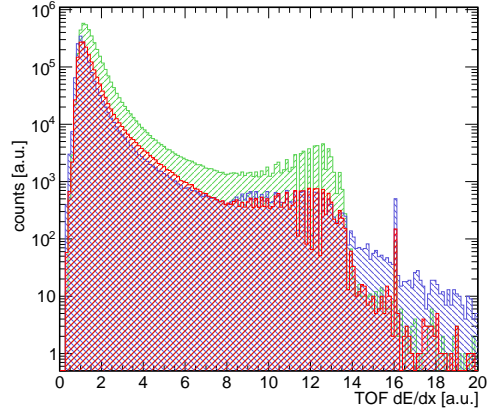
(a) Momentum



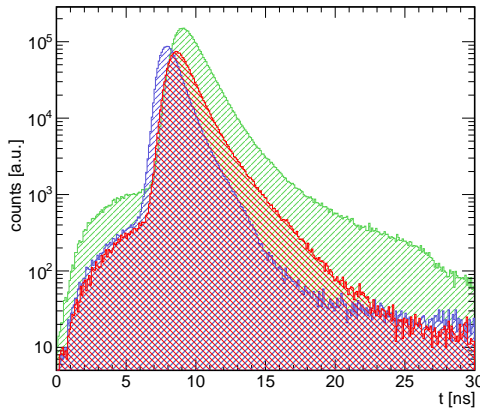
(b) Polar angle



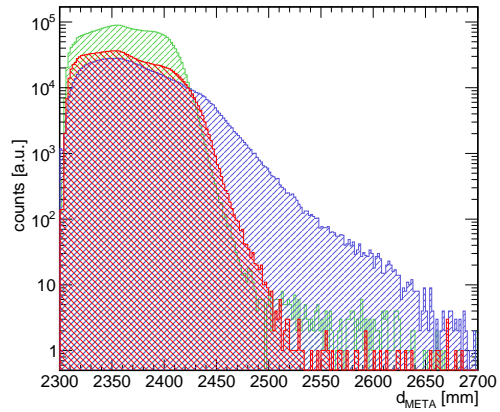
(c) Energy loss dE/dx in the MDC system



(d) Energy loss dE/dx in the TOF system



(e) Reconstructed time of flight



(f) Distance to the TOF/TOFINO systems (META)

Figure 36: Input features for the VAE for protons (green) and pions (blue) and kaons (red).

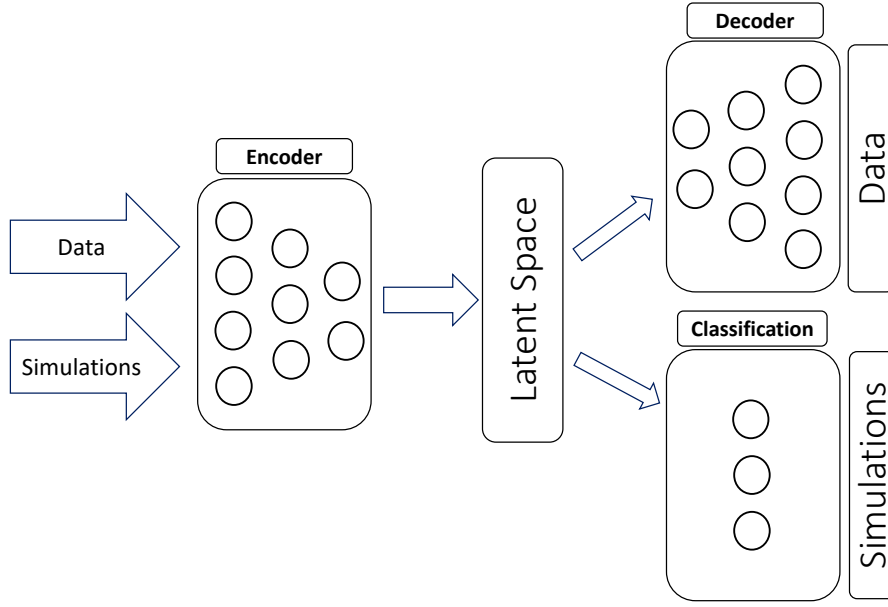


Figure 37: A schematic diagram of the VAE used for the purpose of the PID task.

Training sample

The VAE is trained on the following set of simulated events:

$$\begin{aligned}
 p + p &\rightarrow p + p + \pi^+ + \pi^- \\
 p + p &\rightarrow p + K^+ + \Lambda \\
 p + p &\rightarrow p + K^+ + \Lambda + \pi^0.
 \end{aligned} \tag{22}$$

The input features are the momentum p , the polar angle θ , the energy loss dE/dx in the MDC and TOF systems, the reconstructed tof and the distance to the TOF/TOFINO hit (META hit) d_{META} . These are shown in Fig. 36 for the three classes p , π^+ and K^+ .

In addition a random sample of real events is selected in such way that each beam time day is equally represented in the sample.

Performance

The performance of the VAE evaluated on a test simulation sample is quantified by means of the *Confusion Matrix* CM shown in Fig. 38a. The CM shows the correlation

between the true labels (y -axis) and the predicted labels (x -axis), ideally the diagonal elements should be equal to 1, which means 100% correct classification. The off-diagonal elements quantify the mis-classified labels. As can be shown the network was able to classify 98% of protons p , 92 % of pions π^+ and 76% of kaons K^+ correctly.

Another important performance measure is the ROC curve shown in Fig. 38b, where the area under the ROC curve (AUC) is above 94% for all classes. The selection efficiency and purity as function of phase space variables evaluated on the hold out data-set is presented in Appendix A.

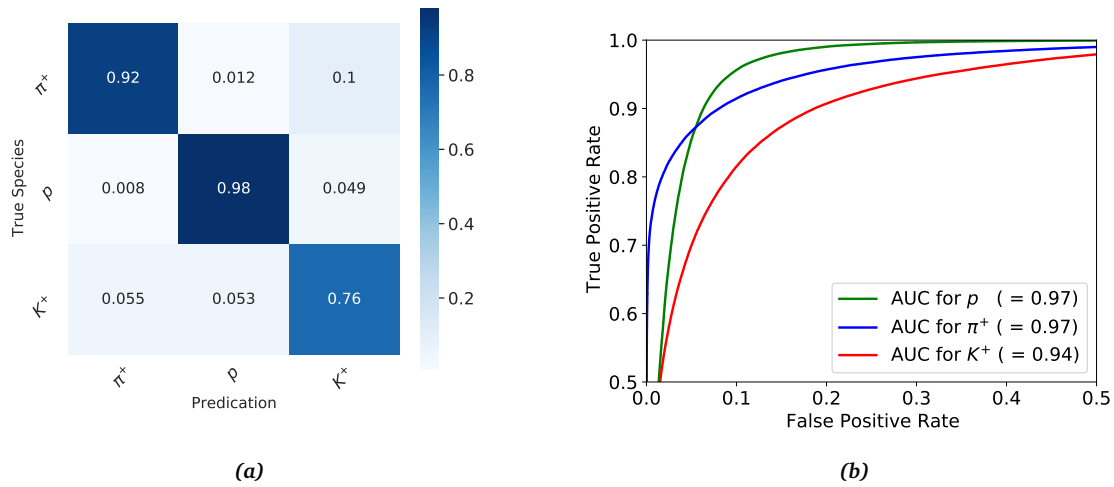


Figure 38: (a) The Confusion matrix. (b) The ROC graph for protons p (green), pions π^+ (blue) and kaons K^+ . The inset shows values of the area under curve AUC for the three classes.

It is also important to judge the performance of the network when applied to real events, however it is not possible to calculate the accuracy in this case; since the real data is unlabeled, so another approach is used. The output of the classification layer is plotted as function of the particle mass squared (see Eq. 17), where the mass is calculated from the reconstructed tof and the momentum p . The output layer has three nodes corresponding to the three classes. Each node outputs a number between 0 and 1, all output numbers sum to 1, so that each number can be interpreted as a probability of being a specific particle species. As shown in Fig. 39 for each output node, an accumulation of events is visible around a probability of 1 and around the correct particle mass and nearly zero probability otherwise. For the case of kaons K^+ the network is less confident and the maximum probability is about 0.9 around the kaon mass squared $\approx 0.25 \text{ GeV}^2/c^4$, so the PID can be assigned to each track by selecting on the network output. Because the network outputs three numbers/probabilities for each particle track, the maximum probability is chosen to identify tracks, for example if the proton node has the maximum probability, then the track is identified as a proton. The masses of the particles are set to their nominal values after the PID.

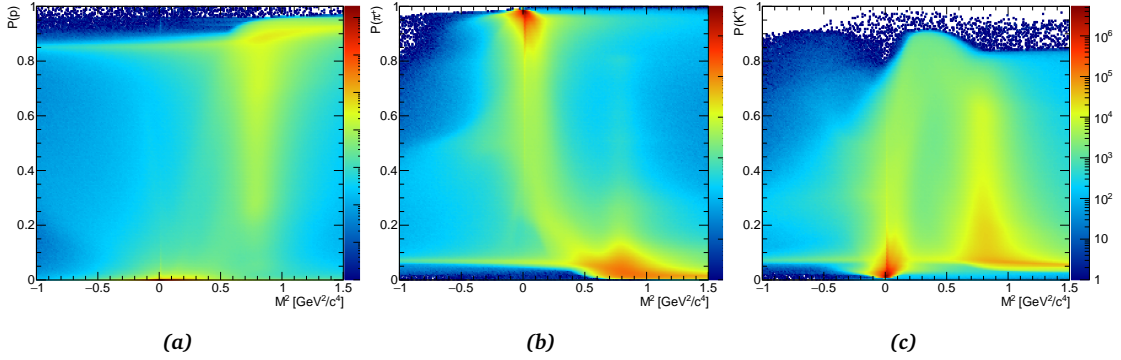


Figure 39: The output probability of the network as applied to real data as function of the particle mass squared for (a) protons p , (b) pions π^+ and (c) kaons K^+ .

4.2.4 The Λ Hyperon Reconstruction

The next step after the PID is the reconstruction of the intermediate Λ hyperon, which is reconstructed from its decay products, namely the proton p and the pion π^- . The Λ is reconstructed separately in the HADES acceptance (HADES data-set) and the forward wall acceptance (FWall data-set).

HADES data-set

For the HADES data-set, the Λ is reconstructed from its decay products in combination with a set of topological cuts. The Λ hyperon decays weakly with a mean decay length $c\tau = 7.89$ cm, considering the energy and momentum conservation during the Λ decay, the proton should fly almost in the same direction of the Λ since the proton mass is close to the Λ mass, while the pion π^- will be emitted at a larger angle relative to the direction of the Λ , as shown in Fig. 40.

For each event, the intersection point or the Point of Closest Approach (PCA) between the proton track and the kaon track was defined as the primary vertex. Because there is more than one proton in each event, the proton and the kaon pair that have the smallest Distance of Closest Approach (DCA) is used to construct the primary vertex. To reduce the contribution from off-target events a two dimensional cut is applied to the primary vertex position as illustrated by the white dashed line in Fig. 41a. Accepted events are required to be within $-65 < z[mm] < -5$. The beam spot was shifted during the beam time, this shift has been quantified previously to be 3-4 mm [29]. Therefore, accepted events are required to satisfy $r[mm] < 5$, which takes the beam spot shift into consideration.

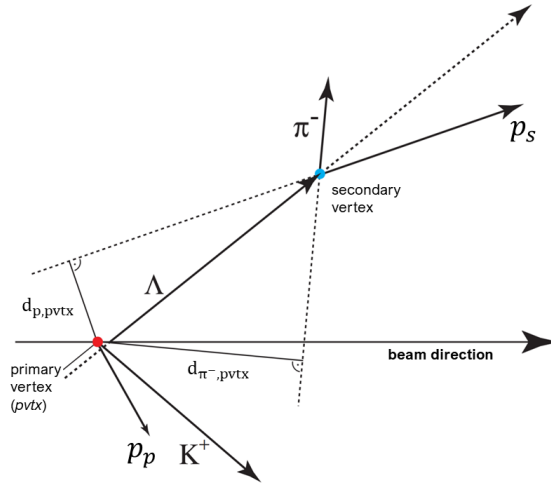


Figure 40: The Λ hyperon decay topology. The different topological cuts used in the analysis are indicated. The red point represents the primary vertex and the light blue point indicates where the Λ decayed. Figure adapted from [113].

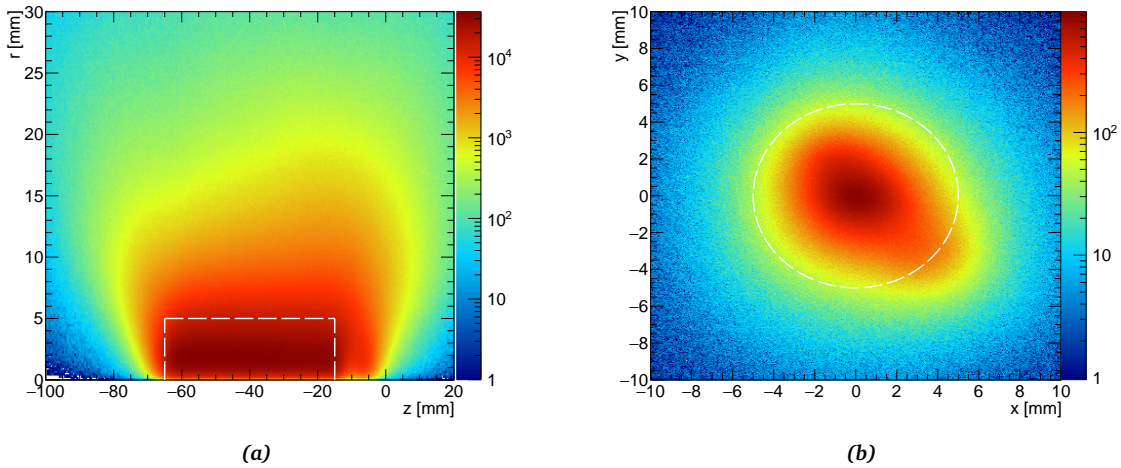


Figure 41: (a) The primary vertex transverse position as function of the longitudinal position. Accepted events are within $-65 < z[\text{mm}] < -5$ and $r[\text{mm}] < 5$ as indicated by the white dashed line. (b) The primary vertex distribution in the $x - y$ plane for events in the target region $-65 < z[\text{mm}] < -5$.

The DCA between the p , and π^- tracks is expected to be small if the tracks emerge from the same vertex. Therefore, $d_{p\pi^-} < 10$ mm is demanded in order to reduce combinatorial background. Following the energy conservation condition, the DCA between the p track and the primary vertex $d_{p,pvtx}$ is required to be smaller than the DCA between the π^- track and the primary vertex $d_{\pi^-,pvtx}$. One last topological cut is introduced, the DCA between the Λ track and the primary vertex is required to be smaller than 6 mm. The distributions of the topological variables are shown in Fig. 42, where the cuts are indicated by the dashed lines. At this stage of the analysis, the proton used in the Λ

reconstruction is tagged as the secondary proton (in this case p_{hades}), while the other proton in the event is tagged as a primary proton p .

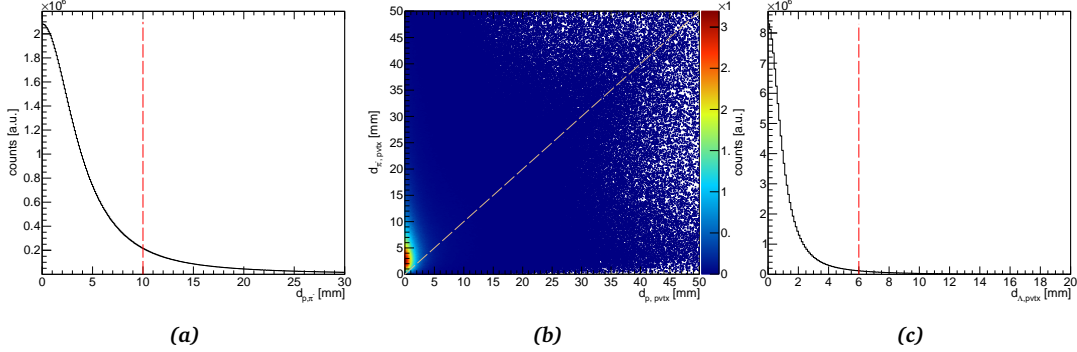


Figure 42: (a) The DCA between the p , and π^- tracks. (b) The DCA between the π^- track and the primary vertex $d_{\pi,pvtx}$ as a function of the DCA between the p track and the primary vertex $d_{p,pvtx}$. (c) The DCA between the Λ track and the primary vertex.

To further purify the Λ sample, we rely on the kinematics of the exclusive reaction under study. In particular we use the missing mass squared calculated as follows

$$MM^2 = \frac{1}{c^4} \cdot \left[E_{beam} + E_{target} - \sum_{i=1}^n E_i \right]^2 - \left[\vec{p}_{beam} + \vec{p}_{target} - \sum_{i=1}^n \vec{p}_i \right]^2 c^2 \quad (23)$$

The missing mass squared distribution of the primary proton and Λ should be in the range of the square kaon plus photon mass. Fig. 43 shows the missing mass squared distribution of $p\Lambda$, two peak structures are visible, the first one at 0.02 GeV^2 is due to the multi pion production reaction $pp \rightarrow pp\pi^+\pi^-$, where one of the protons and the π^- is identified as a Λ candidate and the π^+ is incorrectly identified as a K^+ , the other broader peak is due to $pp \rightarrow pK^+\Lambda$ and $pp \rightarrow pK^+\Sigma^0$ events, thus events in the range $MM^2(p p_{hades} \pi^-) [\text{GeV}^2/c^4] > 0.2$ are selected.

The invariant mass spectrum of the p_{hades} and π^- after applying the topological cuts and the missing mass cut is shown in Fig. 44. A peak around the Λ nominal mass is visible on top of the background. The signal peak has been fit by a Gaussian distribution and the background is modeled by a fourth order polynomial. Events are further processed if they are in the range of $\mu \pm 3\sigma$, the calculated signal to background ratio in this range is $S/B = 1.9$.

FWall data-set

In the FWall data-set the hit in the forward wall is assumed to be due to the secondary proton from the Λ decay (this will be justified in the next chapter). Because the FWall

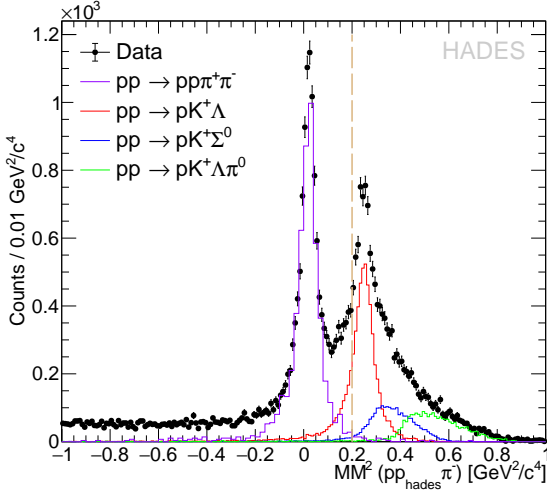


Figure 43: The missing mass squared distribution of $pp_{\text{hades}}\pi^-$. The data are shown as black dots, the violet histogram is the simulation of $pp \rightarrow pp\pi^+\pi^-$, the red one is $pp \rightarrow pK^+\Lambda$ and the blue one is $pp \rightarrow pK^+\Sigma^0$ simulation. The dashed line indicates the cut value.

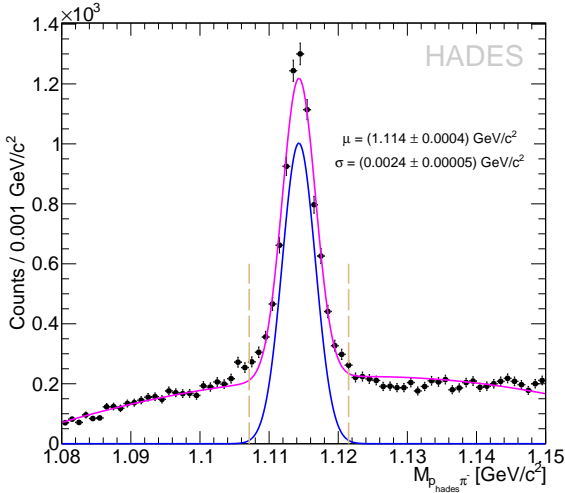


Figure 44: The invariant mass spectrum of the p_{hades} and π^- . The peak was fit by a Gaussian distribution and the background was fit by a fourth order polynomial. Events are accepted if they are in the range of $\mu \pm 3\sigma$ as indicated by the dashed lines.

is in a magnetic field free region, the proton (in this case p_{wall}) was reconstructed as a straight line from the primary vertex to the hit point in the FWall, then the proton mass is assumed and the momentum is calculated from Eq. 17. In this case the topological cuts are not as effective to suppress the background as there is no track information. So in order to enhance the Λ sample, events fulfilling the following conditions were selected:

1. $-0.02 < MM^2(pK^+p_{\text{wall}}\pi^-)[\text{GeV}^2/c^4] < 0.01$, for both reactions this missing mass spectrum should peak at zero, since the photon in the final state has no mass. This cut is asymmetric to suppress contamination from π^0 events, e.g. the reaction $pp \rightarrow pK^+\Lambda\pi^0$ the missing mass squared should have a peak value $MM^2(pK^+p_{\text{wall}}\pi^-) \approx 0.02 \text{ GeV}^2/c^4$ (see Fig. 45a).
2. $MM^2(pp_{\text{wall}}\pi^-)[\text{GeV}^2/c^4] > 0.2$ (see Fig. 45b).

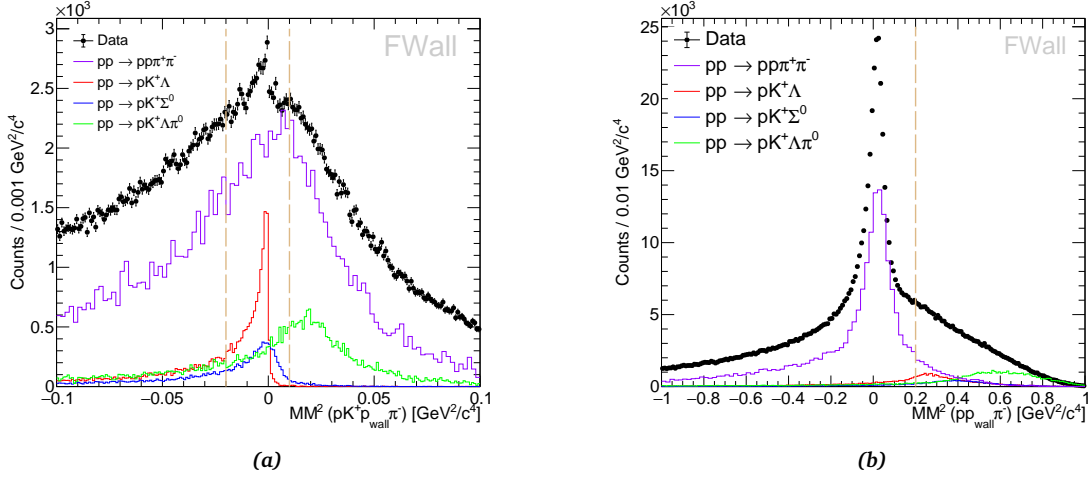


Figure 45: (a) The missing mass squared distribution of $pK^+p_{wall}\pi^-$. (b) The missing mass squared distribution of $pp_{wall}\pi^-$. The data are shown as black dots, the violet histogram is the simulation of $pp \rightarrow pp\pi^+\pi^-$, the red one is $pp \rightarrow pK^+\Lambda$ and the blue one is $pp \rightarrow pK^+\Sigma^0$ simulation. The dashed line indicate the cut values. The simulations here are not to scale.

The invariant mass spectrum of the p_{wall} and π^- after applying these cuts is shown in Fig. 46. A peak around the nominal Λ mass is visible on top of background. The signal peak has been fit by a Gaussian distribution and the background by a fourth order polynomial. The mass resolution of the HADES Λ signal (Fig. 44) is better than the signal from the FWall signal, since in the latter case the proton was detected in the FWall, which has a worse time resolution.

Events are further processed if they are in the range of $\mu \pm 3\sigma$, the calculated signal to background ratio in this range is $S/B = 1.8$

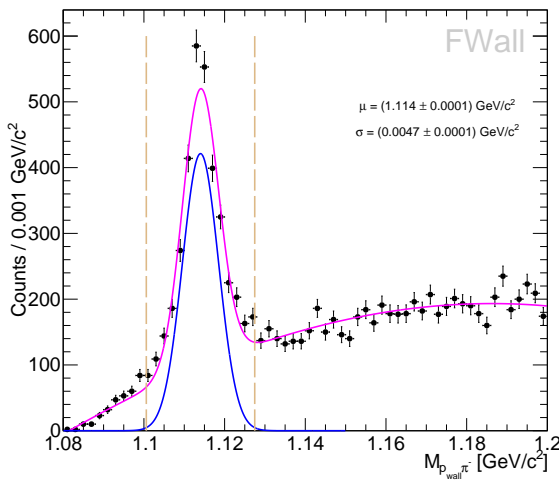


Figure 46: The invariant mass spectrum of the p_{wall} detected in the FWall and π^- detected in HADES. The peak has been fit by a Gaussian distribution and the background by a fourth order polynomial. Events are accepted if they are in the range of $\mu \pm 3\sigma$ as indicated by the dashed line.

4.3 KINEMATIC REFIT

After selecting a relatively pure sample of events containing a Λ , the next step is to select those events containing Σ^0 hyperons. In order to achieve this and to suppress the remaining background we use a kinematic refit based on Lagrange multiplier theory [58].

4.3.1 Theory

Kinematic Refit is a well known tool in the exclusive analysis of particle reactions that can be used to reduce background and to improve the mass resolution of particles.

The track parameters reconstructed by the tracking algorithm are assumed to be randomly distributed about the true values. Thus the goal of a kinematic refit is to estimate the true values of the track parameters to be as close as possible to the measured values and at the same time fulfill a set of constraints given by the kinematics of the reaction under study. These constraints can be either fundamental principles as energy and momentum conservation or a fixed invariant or missing mass of reconstructed particles, or geometrical correlations such as common vertices and kinematics topology.

In order to quantify the “as close as possible” between the true values and the measured values, one needs a measure of distance. This can be quantified for instance by the simple least square method. In this case, suppose that at the observational points x_1, x_2, \dots, x_n the experimental values are y_1, y_2, \dots, y_n and the corresponding true values $\eta_1, \eta_2, \dots, \eta_n$ are not known. Assume that a theoretical model exists, which predicts the true value associated with x_i :

$$f_i = f(\theta_1, \theta_2, \dots, \theta_l, x_i),$$

where θ_i is the set of model parameters. The least square principle states that the best estimate of the model parameters are those for which the χ^2 is minimum

$$\chi^2 = \sum_i \left(\frac{y_i - f_i}{\sigma_i} \right)^2 \approx \text{minimum},$$

where σ_i are the uncertainties associated with each measurement x_i . This equation can be written in terms of matrix notation

$$\chi^2 = (\mathbf{y} - \boldsymbol{\theta})^T V^{-1} (\mathbf{y} - \boldsymbol{\theta}), \quad (24)$$

where the measurements and the model parameters are arranged in column vectors as follows:

$$\begin{bmatrix} y_1 \\ y_2 \\ \vdots \\ y_n \end{bmatrix} \quad \begin{bmatrix} \theta_1 \\ \theta_2 \\ \vdots \\ \theta_n \end{bmatrix},$$

and the uncertainties are given by an $n \times n$ covariance matrix:

$$V = \begin{bmatrix} \sigma_1^2 & \sigma_{12}^2 & \dots & \sigma_{1n}^2 \\ \vdots & \sigma_2^2 & \dots & \vdots \\ \sigma_{n1}^2 & \dots & \dots & \sigma_n^2 \end{bmatrix},$$

where it is a diagonal matrix only if the measurements are independent.

In a simple least square problem, the basic unknowns are the model parameters θ_i and the χ^2 has to be minimized in order to find the best estimates of θ_i . But in a typical kinematic refit problem, the basic unknowns are the true observables themselves η_i , and the χ^2 has to be minimized in order to find the best estimates $\hat{\eta}_i$ of the true observables η_i , where $\hat{\eta}_i$ are referred as the *improved measurements* or the *fitted parameters*, in this case the χ^2 is minimized under some kinematical constraints.

In general, the constraint condition can be on a set of *measurable* variables η_i and *unmeasurable* variables ξ_i . Assume that there are N measurable variables $\eta_1, \eta_2, \dots, \eta_n$ and J unmeasurable variables $\xi_1, \xi_2, \dots, \xi_n$ that are related by a set of k constraint equations:

$$f_k = f(\eta_1, \eta_2, \dots, \eta_n, \xi_1, \xi_2, \dots, \xi_n) = 0, \quad k = 1, 2, \dots, K$$

then the best estimate of η_i and ξ_i are those for which:

$$\begin{aligned} \chi^2 &= (\mathbf{y} - \boldsymbol{\eta})^T V^{-1} (\mathbf{y} - \boldsymbol{\eta}) \approx \text{minimum} \\ f(\boldsymbol{\eta}, \boldsymbol{\xi}) &= 0 \end{aligned} \quad (25)$$

In general, this can be solved by the elimination method, that is eliminating K unknowns from the constraint equation, then minimizing the χ^2 with respect to the remaining $N+J-K$ variables. However, this approach requires difficult algebraic computations.

Another approach that is used here, is the Lagrange multipliers, which provides a way to transform the constrained minimization into minimizing a single *Lagrange function* \mathcal{L} . Eq. 25 can be reformulated by introducing K additional variables that are referred as *Lagrange multipliers* $\lambda_1, \lambda_2, \dots, \lambda_K$ as follows [58]:

$$\chi^2 = (y - \eta)^T V^{-1} (y - \eta) + 2\lambda^T f(\eta, \xi) \approx \text{minimum} \quad (26)$$

Minimizing Eq. 26 involves finding the derivatives of χ^2 with respect to all unknowns η, ξ, λ and then setting the derivative equal to zero. This procedure is usually done iteratively, with each iteration producing better approximations for η and ξ .

The procedure of the minimization can be summarized as follows [58]:

1. Suppose that the iteration number ν has been performed and it is necessary to find a better solution. First introduce the notations

$$\begin{aligned} r &= f^\nu + F_\eta^\nu (y - \eta^\nu) \\ S &= F_\eta^\nu V (F_\eta^\nu)^T, \end{aligned}$$

where F_η is a $K \times N$ Jacobian matrix ($F_\eta = \frac{\partial f}{\partial \eta}$), i.e. the derivative of the constraint equations with respect to η .

2. Find the updated unmeasurable variables $\xi^{\nu+1}$

$$\tilde{\xi}^{\nu+1} = \xi^\nu - (F_\xi^T S^{-1} F_\xi)^{-1} F_\xi^T S^{-1} r,$$

where F_ξ is a $K \times J$ Jacobian matrix ($F_\xi = \frac{\partial f}{\partial \xi}$), i.e. the derivative of the constraint equations with respect to ξ .

3. Find the updated Lagrange multipliers $\lambda^{\nu+1}$

$$\lambda^{\nu+1} = S^{-1} \left(r + F_\xi (\tilde{\xi}^{\nu+1} - \xi^\nu) \right).$$

4. Find the updated *fitted parameters* $\eta^{\nu+1}$

$$\eta^{\nu+1} = y - V F_\eta^T \lambda^{\nu+1}.$$

5. Find the updated covariance matrix $V^{\nu+1}$

$$V^{\nu+1} = V^{\nu} - V^{\nu} \left[F_{\eta}^T S^{-1} F_{\eta} - \left((F_{\eta}^T S^{-1} F_{\zeta}) (F_{\zeta}^T S^{-1} F_{\zeta})^{-1} (F_{\eta}^T S^{-1} F_{\zeta})^T \right) \right] V^{\nu}.$$

6. Calculate the new χ^2 and compare the results with the previous iteration. A stopping criteria can be for instance the difference between χ^2 for two successive iterations.

4.3.2 Quality of the kinematic refit

As the kinematic refit crucially depends on the measured variables y and the quality of the covariance matrix, it is important to have a set of quality criteria, which gives a measure for the quality of the fit.

Because the kinematic refit is based on the minimization of χ^2 , the final χ^2 distribution can be used to give a measure of the quality of the fit. If the covariance matrix is correctly estimated, then the χ^2 probability density function will be given by [58]:

$$f(\chi^2, \nu) = \frac{1}{2^{\nu/2} \Gamma(\nu/2)} (\chi^2)^{\nu/2-1} e^{-\frac{1}{2}\chi^2}, \quad (27)$$

where ν is the number of degrees of freedom of the fit and Γ is the gamma function. Fig. 47 shows the χ^2 probability density function for different values of ν . A χ^2 distribution, which roughly follows Eq. 27 indicates that the fit was performed correctly.

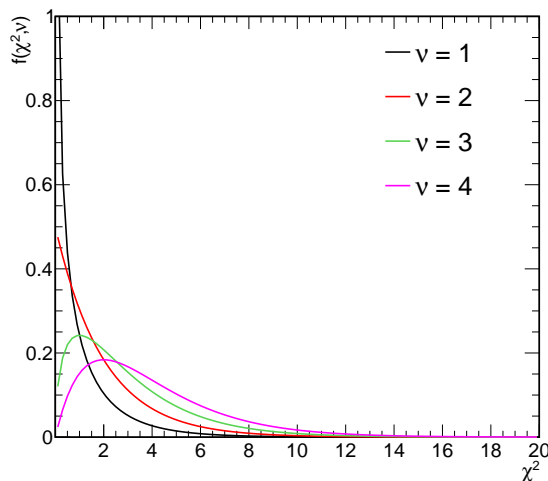


Figure 47: The χ^2 probability density function for different numbers of degrees of freedom.

At this point, it is convenient to define the *p-value* or the probability that a χ^2 of the theoretical distribution is greater than or equal to the χ^2 value found from the fit:

$$P(\chi^2) = \int_{\chi^2}^{\infty} f(x, \nu) dx. \quad (28)$$

The $P(\chi^2)$ distribution is uniformly distributed between 0 and 1, a small χ^2 values corresponds to a large $P(\chi^2)$ values or a good fit. Events that do not satisfy the constraint equations tend to have small $P(\chi^2)$ values towards 0, so selecting events with larger p-values provides a method to suppress background events.

Another important quality criteria for the kinematic fit is the *pull distribution* or the *stretch function*, which is defined as the difference between the measured y and the fitted parameters η normalized by the quadratic error difference:

$$z = \frac{y - \eta}{\sqrt{\sigma_y^2 - \sigma_\eta^2}}. \quad (29)$$

Ideally if the covariance matrix is estimated correctly the pull distribution should be a Gaussian with a mean value μ around zero and a standard deviation of $\sigma = 1$. If the shape of the pull distribution is shifted with respect to zero, this indicates that there is a systematic bias in the corresponding measured variable. Similarly, if the width of the pull distribution is different from $\sigma = 1$, this indicates that the covariance matrix is wrongly estimated.

4.3.3 Kinematic refit applied to $p + p \rightarrow p + K^+ + \Sigma^0$

Before applying the kinematic refit to the reaction $p + p \rightarrow p + K^+ + \Sigma^0$, the track parameters that need to be fit must be defined. Spherical coordinates are used in this analysis for the track parameterization, which is defined as follows:

$$y = \begin{bmatrix} 1/p \\ \theta \\ \phi \end{bmatrix}, \quad (30)$$

where $1/p$ is the inverse of the absolute momentum, θ and ϕ are the polar and azimuthal angles of the track, the inverse of the momentum $1/p$ is used instead of the momentum since the tracking algorithm of HADES determines the momentum via the curvature of the track inside the magnetic field. Therefore, $1/p$ is the measured quantity, that is Gaussian distributed. Another input needed by the kinematic refit is the covariance matrix. In some cases, this may be known in advance, e.g. if a kalman filter is used for

track fitting, however this is not the case here and the covariance matrix needs to be estimated. The procedure to estimate the covariance matrix is presented in Appendix B.

The next input of kinematic refit are the constraint equations. The invariant mass of secondary proton from Λ decay (marked as p_s) and the pion is constrained to the nominal mass of the Lambda $M_\Lambda = 1.115683 \text{ GeV}/c^2$. In addition, the four particles (p_s , π^- , p and K^+) are constrained to have zero missing mass, since there is a photon in the final state $M_\gamma = 0 \text{ GeV}/c^2$. These constraints can be collectively written as a matrix:

$$f = \begin{pmatrix} (E_{p_s} + E_{\pi^-})^2 - (\vec{p}_{p_s} + \vec{p}_{\pi^-})_x^2 - (\vec{p}_{p_s} + \vec{p}_{\pi^-})_y^2 - (\vec{p}_{p_s} + \vec{p}_{\pi^-})_z^2 - M_\Lambda^2 \\ (E_t + E_b - \sum_{i=1}^4 E_i)^2 - (\vec{p}_t + \vec{p}_b - \sum_{i=1}^4 \vec{p}_i)^2 - M_\gamma^2 \end{pmatrix} = 0 \quad (31)$$

The kinematic refit algorithm explained in section 4.3.1 was implemented with the help of the PyTorch framework [94]. Only the constraint Eq. 31 are implemented as a PyTorch tensor and the Jacobian matrix $F_\eta = \frac{\partial f}{\partial \eta}$ is calculated by utilizing the PyTorch's automatic differentiation engine.

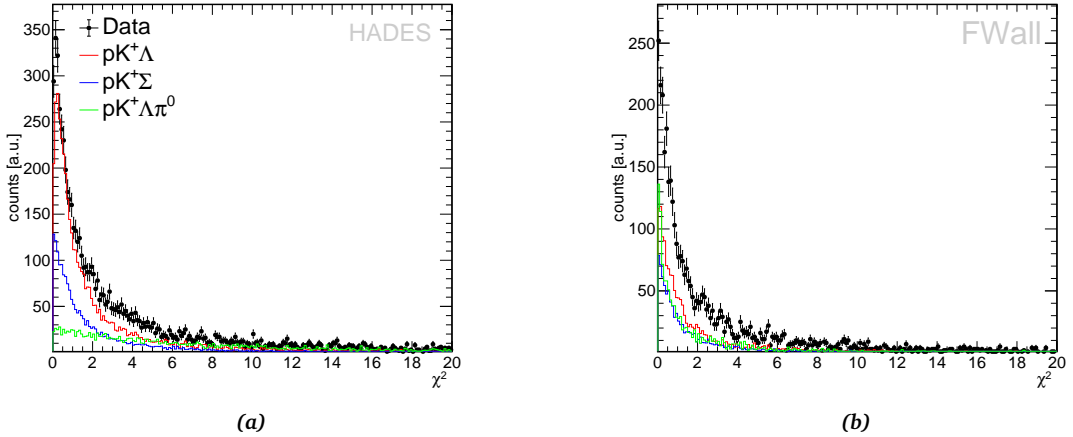


Figure 48: The χ^2 distribution of (a) the HADES data-set and (b) the FWall data-set. The data is shown as black dots, the red histogram is the $pp \rightarrow pK^+\Lambda$ simulation, the blue histogram is the $pp \rightarrow pK^+\Sigma^0$ simulation and the green histogram is the simulation of $pp \rightarrow pK^+\Lambda\pi^0$.

The χ^2 distributions for the HADES and the FWall data-sets are shown in Fig. 48 and the corresponding p-value distributions are shown in Fig. 49. The χ^2 distributions are consistent with $f(\chi^2, \nu)$ with $\nu = 2$ shown in Fig. 47. The simulation of $pp \rightarrow pK^+\Lambda$ and $pp \rightarrow pK^+\Sigma^0$ have similar distributions, which is attributed to the very similar kinematics as both have $MM(pK^+\Lambda) = 0$. This makes these two reactions hard to distinguish. In addition, the channel $pp \rightarrow pK^+\Lambda\pi^0$ should ideally have zero p-value since $MM(pK^+\Lambda) = M_{\pi^0}$, however, due to the limited resolution it has p-values greater than zero. This is especially evident in the FWall data-set as can be seen from the green

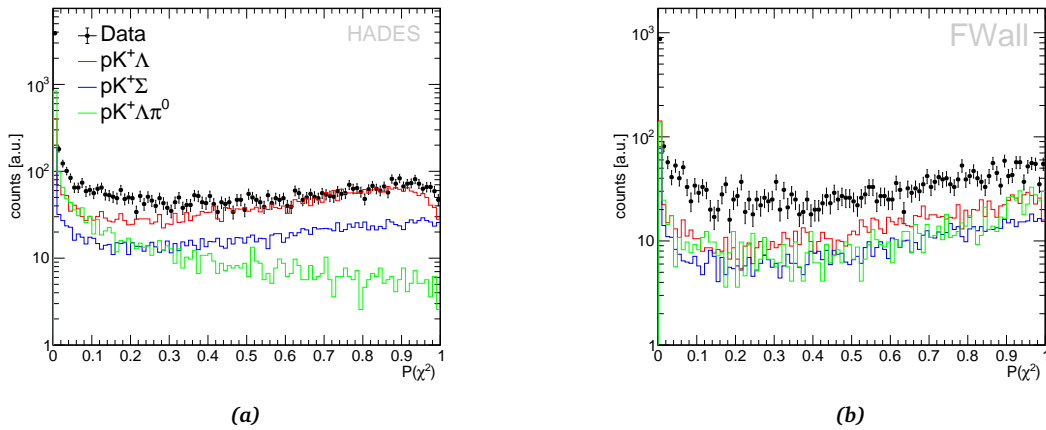


Figure 49: The p -value $P(\chi^2)$ of (a) the HADES data-set and (b) the FWall data-set. The data is shown as black dots, the red histogram is the $pp \rightarrow pK^+\Lambda$ simulation, the blue histogram is the $pp \rightarrow pK^+\Sigma^0$ simulation and the green histogram is the simulation of $pp \rightarrow pK^+\Lambda\pi^0$.

missing mass spectrum shown in Fig. 45a, where the tail of the distribution towards $MM^2(pK^+p_{wall}\pi^-)=0$ is contributing to large p -values.

In order to obtain a good compromise between efficiency and purity, the data selection was constrained to events with $P(\chi^2) > 0.01$. Demanding a larger p -value cut could improve the signal purity but on the other hand reduces the signal statistics. After this selection the missing mass of pK^+ (the primary proton and the kaon) is investigated, which is shown in Fig. 50 this should correspond to the hyperon mass. As can be shown the kinematic refit improves the mass resolution and eliminates a considerable amount of background events.

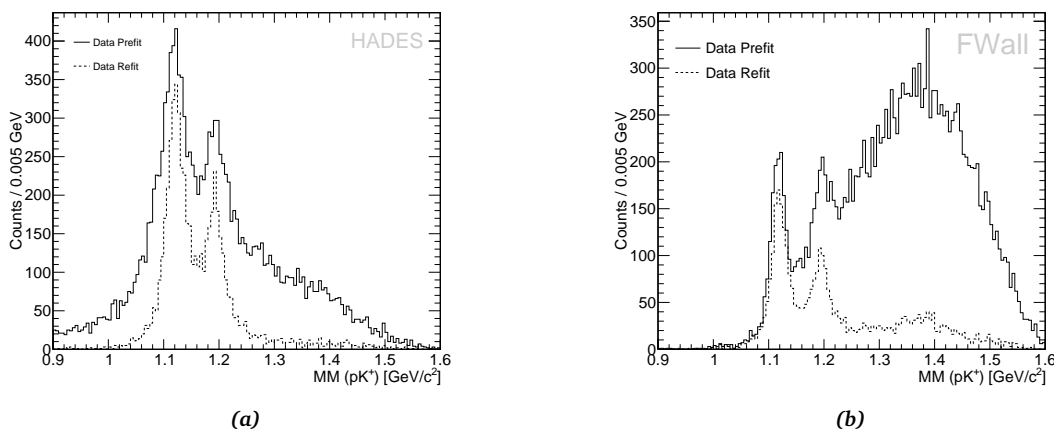


Figure 50: The missing mass distribution of pK^+ before and after the kinematic refit for the (a) HADES data-set and (b) the FWall data-set.

4.4 RESULTS

4.4.1 Signal Extraction

As discussed in the previous section the two reactions $pp \rightarrow pK^+\Lambda$ and $pp \rightarrow pK^+\Sigma^0$ are hard to distinguish, this can also be seen from Fig. 50, where the tail of one channel is under the peak of the other. In addition to $pp \rightarrow pK^+\Lambda$ there is another contribution in the high mass region in the case of the FWall data-set that needs to be identified. Therefore, a method to evaluate the different contributions of the signal and background channels to the missing mass $MM(pK^+)$ spectrum is needed.

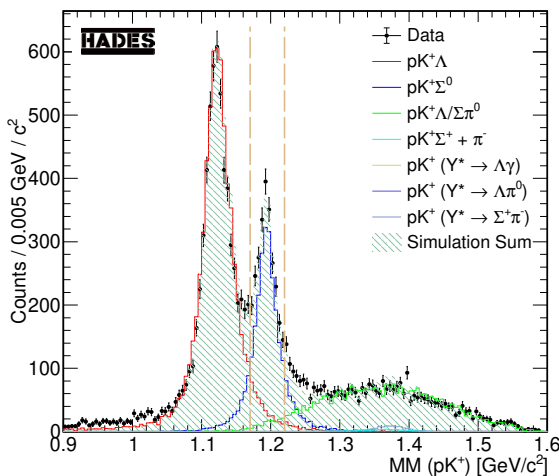


Figure 51: The missing mass distribution of the primary proton and the kaon for the sum of the HADES and the FWall data-sets. Two peaks, corresponding to $pp \rightarrow pK^+\Lambda$ and $pp \rightarrow pK^+\Sigma^0$ are shown by the red and the blue histograms, respectively. The green histogram is the simulation of $pp \rightarrow pK^+\Lambda/\Sigma^0\pi^0$. The filled histogram is the sum of all simulation channels. The vertical dashed lines indicates the mass window applied in order to select Σ^0 events.

In order to determine the contributions of the different simulation channels listed in Tab. 1, a fit of the missing mass spectrum $MM(pK^+)$ has been carried out. The fit quality is quantified by a χ^2 minimization:

$$\chi^2 = \sum_i^{n_{bins}} \frac{(n_{data} - \sum_{ch} (f^{ch} \times n_{simulation}^{ch}))^2}{\sigma_{data}^2 + \sigma_{simulation}^2}, \quad (32)$$

where the summation runs over the number of bins of the missing mass spectrum, n_{data} is the number of data events in each bin, $n_{simulation}^{ch}$ is the number of simulated events in each bin for each channel and f^{ch} is a scaling factor for each channel. The starting values of the scaling factors are determined by the estimated cross section and integrated luminosity of the beam time, that is $f^{ch} = \frac{\sigma \mathcal{L}}{N}$, where N is the number of generated events.

The missing mass spectrum $MM(pK^+)$ for the combined data-set (HADES and FWall) after the fit is shown in Fig. 51, the χ^2/ndf was found to be 1.07. The signal simulation is shown by the blue histogram, two main background sources found by the fitting technique are $pK^+\Lambda$ and $pK^+\Lambda/\Sigma^0\pi^0$ shown by the red and the green histograms, respectively. The other simulated channels have small contributions. A mass window of $1.170 < MM(pK^+)[GeV/c^2] < 1.220$ is applied to select Σ^0 hyperon yield. In total 2613 Σ^0 hyperons are collected, 58% of events are within the HADES acceptance and 42% within the FWall acceptance. The signal purity calculated from the simulations and found to be 81%.

The photon from the Σ^0 decay $\Sigma^0 \rightarrow \Lambda\gamma$ should have an energy $E_\gamma = M_{\Sigma^0} - M_\Lambda \approx 77$ MeV, this photon is identified as a missing particle according to

$$p_\gamma = p_{beam} + p_{target} - (p_p + p_{K^+} + p_\Lambda),$$

where p_γ is the 4-momentum of the photon. The photon energy spectrum is shown in Fig. 52. This energy spectrum is calculated in the rest frame of the Σ^0 hyperon, the width of the distribution is fully attributed to the finite momentum resolution of the detector.

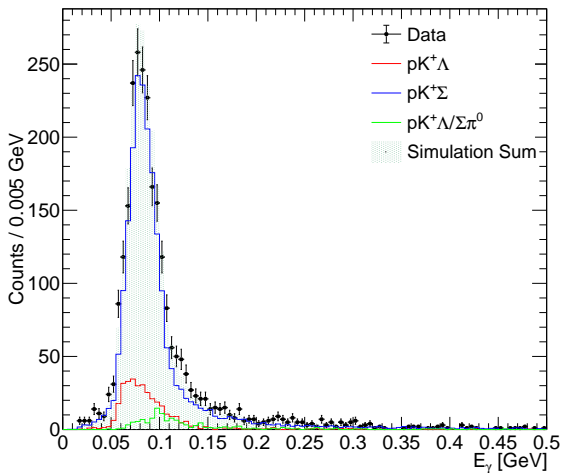


Figure 52: The photon energy spectrum calculated in the rest frame of the Σ^0 hyperon. The signal is shown by the blue histogram, and the two main background channels shown by the red and the green histograms.

4.4.2 Angular Distributions

As a first step towards understanding the Σ^0 production mechanism the angular distributions mentioned above are studied within the detector acceptance and efficiency, as shown in Fig. 53. The first row shows the CMS polar angles of the Σ^0 hyperon, the proton p and the kaon K^+ in the CMS. The second row shows the angular distributions in the three G-J frames. Here, the label $p_{b,t}$ stands for the beam and target proton, relative

to which the angles are measured. The last row shows the distributions for the three helicity angles. The signal simulation and the two contributing background channels are shown by the blue, the red and green histograms, respectively. The structure of the FWall is clearly visible in the $\cos\theta_{\Sigma^0}^{cms} > 0.6$ forward region shown in Fig. 53a as the Λ ($\Sigma^0 \rightarrow \Lambda\gamma$) is partly reconstructed in the FWall. This is not the case for $\cos\theta_p^{cms}$ and $\cos\theta_{K^+}^{cms}$ as the primary proton and the kaon are detected only in HADES.

In all nine distributions, the $pp \rightarrow pK^+\Sigma^0$ phase space simulations do not describe the data well, this is more pronounced in the helicity angular distributions.

However, these experimental distributions are heavily distorted by the acceptance and the efficiency of the detector setup. The limited acceptance is caused not only by the uncovered region in the HADES setup ($7^\circ < \theta < 15^\circ$ and $\theta > 85^\circ$) but also the influence by the detector material, that might cause particle scattering in the mechanical structures. Furthermore, in the case of an exclusive measurement, the acceptance drops significantly, since all final state particle are required to be detected in coincidence.

In addition to the limited acceptance, losses due to sources like the detector response, the trigger decision, the tracking algorithm and the analysis cut flow need to be taken into account. All these efficiency losses and limited acceptance distort and modify the resulting experimental distributions. Therefore, a correction of the data for these effects is crucial in order to draw physics conclusions.

4.4.3 Acceptance and Efficiency Correction

Comparisons between data and theoretical predictions need to be performed in a consistent way, either the raw experimental distributions are compared to the theoretical predictions folded by the detector effects, i.e., the distributions are compared at the *detector level*, or the data are first corrected for the detector effects and then compared to the theoretical predictions, i.e., the distributions are compared at the *generator level*. The first approach is inconvenient, because the model needs to be folded by the specific detector effects, which might be complicated and does not model the detector response perfectly well. In contrast, the second method is more flexible and straightforward: by correcting the data for the detector effects, it is possible to compare the results with predictions from any model. The procedure of correcting the data to the *generator level* is often called *unfolding for the detector effects*, which reflects the fact that the “real” data is folded (i.e. convoluted) with the detector response. Mathematically any measured distribution $M(x)$ can be expressed as:

$$M(x) = \int_{\Omega} R(x|x')T(x')dx', \quad (33)$$

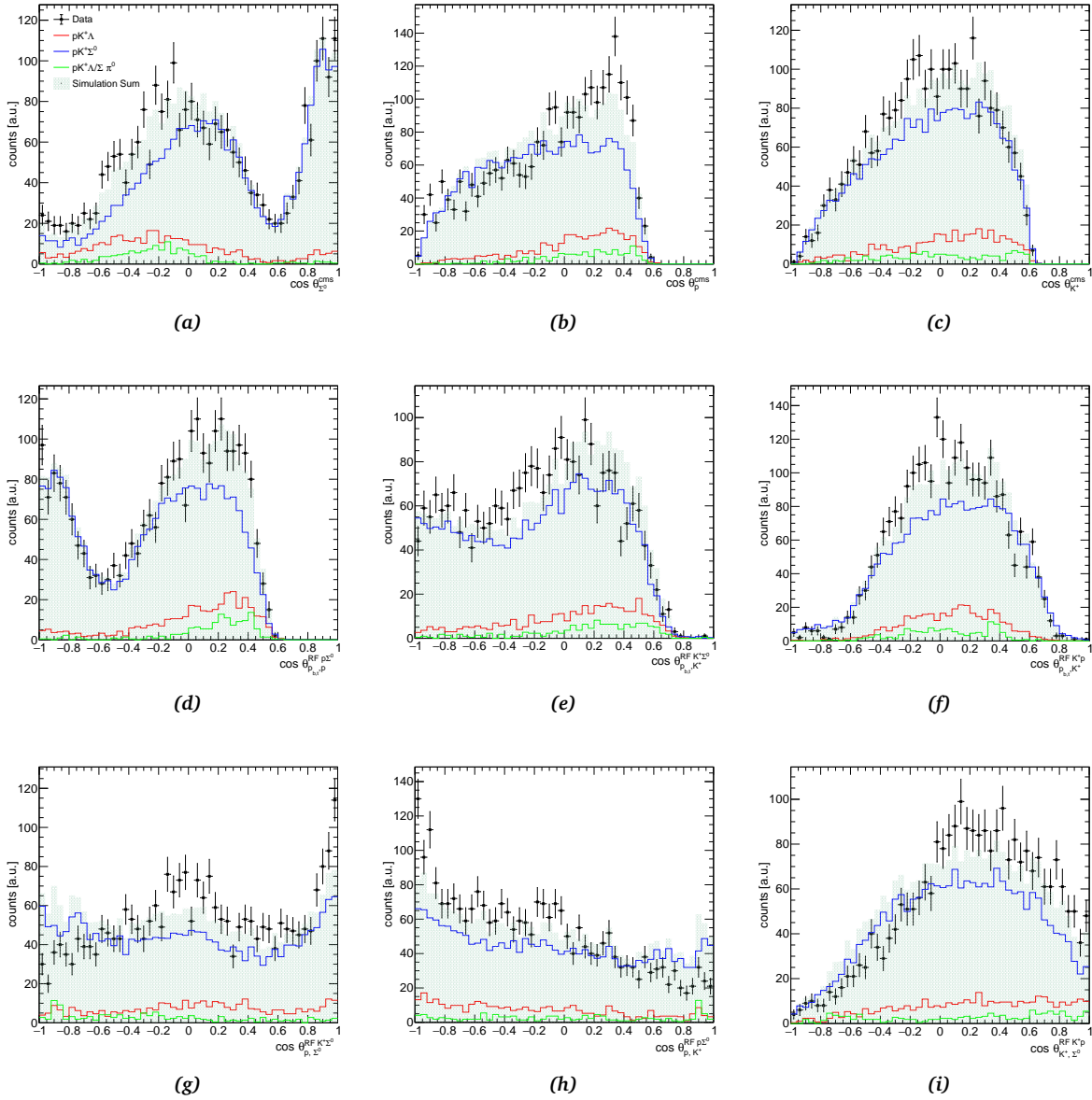


Figure 53: Angular distributions in experimental data and simulation. The first row shows the CMS angular distributions of the Σ^0 hyperon, the proton p and the kaon K^+ , the second row shows the distributions for the three G-J angles and the third row shows the distributions for the three helicity angles.

where $T(x')$ is the true distribution and $R(x|x')$ is a kernel function describing the detector response (the limited acceptance and efficiency), also called the *response function*. The integral is performed over the phase space volume available.

Since there are three particles in the final state in our reaction, there are three 4-vectors containing a total of 12 components. Three degrees of freedom are fixed by the known masses of the final state particles, three by momentum conservation and one by energy

conservation. One observable additionally vanishes due to the azimuthal symmetry ϕ (i.e. unpolarized beam and target). This means that the production of three particles in the final state is determined by four independent kinematic variables. Therefore, a model independent unfolding procedure needs to be performed in four dimensions simultaneously. This approach, however, is not feasible since it requires a huge number of simulated events in order to populate each bin in a four dimensional correction matrix with sufficient statistics in order not to be dominated by statistical fluctuations. Another approach is to integrate the acceptance over some of the kinematical variables (e.g. $\cos\theta_{cms}-p_{cms}$ or p_t-y), the correction stability is justified if the results are self consistent when the correction has been determined as a function of different sets of kinematical observables. Thus, by knowing the kinematical distributions of the initial simulation (*generator level* or the PLUTO output) and of the final full-scale simulation after propagating through GEANT3, DST production and selection cuts (*detector level*), it is possible to calculate the response function for an experimental spectrum.

The experimental distributions are usually represented by binned histograms, so Eq. 33 can be written in a matrix form

$$M = RT, \quad (34)$$

where R now is the *response matrix*, and each element is given by [43]

$$R_{ij} = P(\text{reconstructed in bin } i \mid \text{generated in bin } j).$$

Each matrix element is the conditional probability that an event is reconstructed in bin i given that it was generated in bin j . Ideally, the response matrix is a diagonal matrix, the off-diagonal elements represent the migration effects.

The unfolding procedure corresponds to the solution of the matrix Eq. 34 which connects detector and generator level, i.e. solving for true distribution T given the inverse response matrix R^{-1} and the measured distribution M .

The most intuitive way to solve Eq. 34 is the analytical inversion of the response matrix, that is by multiplying Eq. 34 from the right side by R^{-1} . However, there is no guarantee that the response matrix has an inverse, without which the inversion method will not give meaningful solution. Hence, different approaches have been developed, starting from the simple bin-by-bin corrections, to more sophisticated methods, like the D'Agostini and the SVD methods. In the following, these methods are presented briefly.

Bin-by-Bin Correction

The simplest unfolding method is the bin-by-bin correction. This method assumes that in any bin i the migration from other bins into it equals the migration out of this bin. By knowing the kinematical distributions at the generator level and at the detector level it is possible to calculate a correction matrix for the experimental spectra

$$C = \frac{M_{gen}}{M_{reco}},$$

where M_{reco} and M_{gen} are the binned distributions, measured at the detector and generator level, respectively. Note that the M_{reco} and M_{gen} should have the same binning, then the ratio between the two numbers in a considered bin is the correction factor to be applied. The calculation of the uncertainties is also straightforward, each bin content is assumed to follow a poissonian distribution and the associated uncertainty in bin i is simply $C_i \sqrt{M_{gen,i}}$. Due to the limited detector acceptance, it can happen that some bins are empty in the detector level spectrum M_{reco} , which leads that the corresponding elements in the inverse response matrix C^{-1} are mathematically undefined. This makes the use of this method quite unreliable and is used only as an initial cross check.

D'Agostini Correction

The D'Agostini method [44] is based on a Bayesian approach of the unfolding problem. The number of events $\hat{n}(C_i)$ produced by a specific cause (a physics process) can be written as a product of the total number of reconstructed events $\hat{n}(E_j)$, which are the result of a specific effect E_j and the conditional probability of the cause C_i to produce the effect E_j :

$$\hat{n}(C_i) = \sum_j \hat{n}(E_j) P(C_i|E_j).$$

The Bayes' theorem can then be used to determine the unknown "response matrix" $P(C_i|E_j)$

$$P(C_i|E_j) = \frac{P(E_j C_i) P(C_i)}{\sum_i P(E_j C_i) P(C_i)},$$

where $P(E_j|C_i)$ is the conditional probability to obtain the effect E_j given the cause C_i and $P(C_i)$ is the prior distribution or the initial probability of the cause, which can be obtained from the simulations at generator level.

The D'Agostini method is about determining the $P(C_i|E_j)$ through an iteration procedure, i.e., the obtained distribution is used as new input for the prior. A stopping criteria for the iteration can be quantified by χ^2 between two successive iterations. The uncertainties are also calculated within the formalism of the Bayes' theorem as explained more thoroughly in [44].

Singular Value Decomposition Correction

A Singular Value Decomposition (SVD) is a factorization of the response matrix through orthogonal matrices to isolate its singular values. The singular values contain valuable information about the properties of the matrix, this can be expressed as:

$$R = USV^T, \quad (35)$$

where U and V are orthogonal matrices and S is a diagonal matrix with non-negative elements. The solution of the linear system Eq. 35 looks like:

$$\begin{aligned} USV^T T &= M \\ SV^T T &= U^T M, \end{aligned} \quad (36)$$

where the last equality follows from the orthogonality of U ($U^T U = I$). If the elements of the vectors $V^T T$ and $U^T M$ are z_i and d_i , respectively,

$$\begin{aligned} s_i z_i = d_i &\Rightarrow z_i = \frac{d_i}{s_i} \\ t_i &= V_{ij} \frac{d_j}{s_j}, \end{aligned} \quad (37)$$

where s_i are the elements of the matrix S and t_i are the elements of T . Then the problem of inverting a matrix reduces to the problem of finding the singular values of the response matrix. At this point, two problems arises, the first one, due to errors in M some of d_i are poorly known, while the second one is that some singular values s_i may be too small.

Both of these occurrences result in an unstable behaviour for the unfolded procedure [80]. In order to avoid these problems, the SVD method applies a rescaling of Eq. 34 according to the errors in M , and it introduces a regularization term, in order to suppress possible oscillating solutions for small singular values s_i [74]. It has been shown that this method gives reliable results with a proper treatment of uncertainties and correlation effects [80].

Comparison between different correction methods

In this section, a comparison between the different correction methods discussed above to the angular distribution of the Σ^0 in CMS frame $\cos\theta_{\Sigma^0}^{cms}$ is presented. All of these methods are implemented in the RooUnfold framework [10].

As previously mentioned, the correction procedure is done using two independent observables, the first one is the CMS angle of the Σ^0 hyperon $\cos\theta_{\Sigma^0}^{cms}$ and the second is it's momentum in the CMS frame $p_{\Sigma^0}^{cms}$. The main input needed is the response matrix, which is implemented through the class RooUnfoldResponse that has the advantage of including miss events (e.g. events outside of the detector acceptance). Due to low statistics for the reconstructed Σ^0 events, the phase space is divide into only 32 bins distributed as 8 $\cos\theta_{\Sigma^0}^{cms}$ bins and 4 $p_{\Sigma^0}^{cms}$ bins. The response matrix is shown in Fig. 54a, the x -axis and y -axis represents the detector and generator level respectively, while the z -axis represents the signal reconstruction efficiency ϵ . Ideally the matrix should have only diagonal elements with $\epsilon=1$, however, due to the limited detector acceptance, tracking efficiency, PID, etc, the signal reconstruction efficiency is much smaller than 1. The off-diagonal elements are events that have been generated in a certain phase space bin but due to the detector resolution have been reconstructed in a different bin.

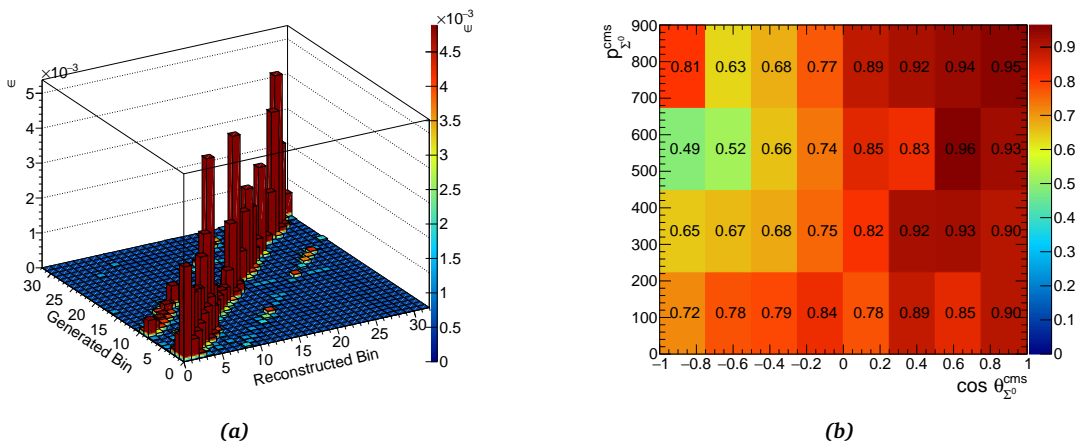


Figure 54: (a) The response matrix of the two kinematical variables $\cos\theta_{\Sigma^0}^{cms}$ and $p_{\Sigma^0}^{cms}$ and (b) the purity matrix.

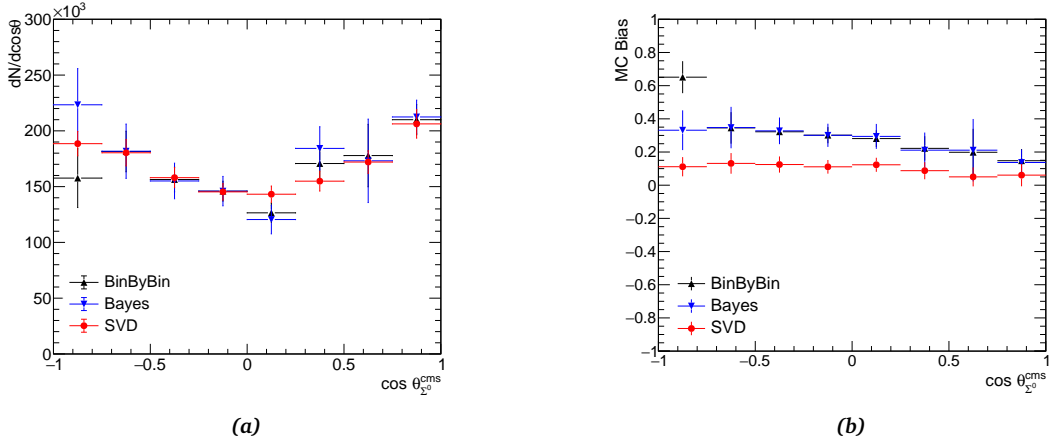


Figure 55: Comparison between different correction methods. (a) The corrected $dN/d\cos\theta$ data distribution and (b) the bias to the Monte Carlo simulation. The black up-triangles, the blue down-triangles and the red dots are the data points corrected by the Bin-by-Bin, D’Agostini and SVD method, respectively. The error bars are only statistical uncertainties.

As can be seen from Fig. 51, the tails of $pp \rightarrow pK^+\Lambda$ and $pp \rightarrow pK^+\Lambda\pi^0$ contribute to the signal region $1.170 < MM(pK^+)[GeV/c^2] < 1.220$, so in order to take this contribution into account, a *purity matrix* has been constructed from the simulation. After scaling each channel with the corresponding scale factor f^{ch} , a two dimensional matrix of $\cos\theta_{\Sigma^0}^{cms}$ and $p_{\Sigma^0}^{cms}$ is constructed, the bin content in this matrix is defined as follows:

$$P_{bin} = \frac{n(pK^+\Sigma^0)}{n(pK^+\Lambda) + n(pK^+\Sigma^0) + n(pK^+\Lambda\pi^0)},$$

where $n(pK^+\Sigma^0)$, $n(pK^+\Lambda)$ and $n(pK^+\Lambda\pi^0)$ are the number of events of the corresponding channel in the specified bin. The purity matrix is shown in Fig. 54b, the purity of Σ^0 events is not constant over the phase space but ranges from 49% to 95%.

After constructing the purity and response matrices, the response matrix is inverted by one of the aforementioned algorithms, then the true distribution (generator level distribution) is obtained as follows:

$$T = R^{-1}MP,$$

where R^{-1} is the inverse response matrix, M is the measured distribution (detector level distribution) and P is the purity matrix.

The differential distribution $dN/d\cos\theta$ is then calculated by integrating over the CMS momentum $p_{\Sigma^0}^{cms}$, this distribution is shown in Fig. 55a for the different correction methods. Because the proton-proton system is symmetric in the CMS frame, this distribution must be symmetric around $\cos\theta_{\Sigma^0}^{cms} = 0$. A quantitative measure of the unfolding procedure can be calculated from a test simulation sample and known as the *Monte Carlo bias*, which is defined as the relative difference between the true (the *generator level* 4π simulations) and the corrected values in each bin:

$$\text{MC Bias} = \frac{\text{true } 4\pi \text{ simulations} - \text{corrected simulations}}{\text{true } 4\pi \text{ simulations}}$$

Ideally this should be constant at 0, since the phase space simulations are flat in all angular distributions. The error bars shown are only of statistical nature.

In order to quantify the quality of the correction, the Monte Carlo bias of the different corrections has been fit by a straight line $ax + b$. A perfect correction must result in $a = 0$ and $b = 0$, Tab. 2 lists the fit results for the different correction methods.

Method	a	b
Bin by Bin	0.295 ± 0.024	-0.198 ± 0.051
D'Agostini	0.274 ± 0.033	-0.128 ± 0.063
SVD	0.103 ± 0.018	-0.040 ± 0.037

Table 2: Parameters of fit to the Monte Carlo bias for the different correction methods.

From the fit parameters listed in Tab. 2 for the different correction methods, it was concluded that the SVD is the most stable correction method, and it has been used for correcting all of the distributions presented in this work. However, as will be discussed later, the result of the correction procedure depends on the simulation model.

4.4.4 Absolute Normalization

The corrected number of Σ^0 events emitted into the corresponding phase space region of $\cos\theta_{\Sigma^0}^{cms}$ shown in Fig. 55 can be transformed into a differential cross section by normalizing to the proton-proton elastic cross section as a reference measurement [13]. The cross section of Σ^0 can then be expressed as:

$$\sigma_{\Sigma^0}[\mu b] = \frac{1}{N_{files}} \cdot \frac{\sigma_{pp}^{elastic}}{N_{pp}^{elastic}} \cdot N_{\Sigma^0} \cdot f_{downscale} \cdot 10^3, \quad (38)$$

where $\sigma_{pp}^{elastic}$ is the known cross section for proton-proton elastic scattering at the same beam energy, $N_{pp}^{elastic}$ is the number of reconstructed proton-proton elastic events corrected for the acceptance and efficiency, N_{Σ^0} is the number of corrected Σ^0 events in the corresponding phase space bin, N_{files} is the number of analyzed files (in this work $N_{files}=11856$) and $f_{downscale}$ is a factor that corrects for the LVL1 trigger down-scaling and has a value of 3 (i.e, only every third event is recorded). The ratio $N_{pp}^{elastic}/\sigma_{pp}^{elastic}$ is expressed by the Rustamov-Factor [13]:

$$Rustamov - Factor = \frac{N_{pp}^{elastic}}{\sigma_{pp}^{elastic}} = 22271.7 .$$

The differential cross section of the Σ^0 hyperon in the CMS frame is shown in Fig. 56.

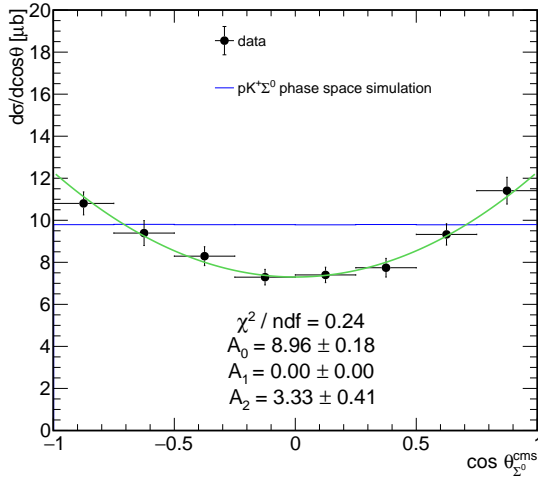


Figure 56: Differential cross section of the Σ^0 hyperon in the CMS frame. Black points are the experimental data and the blue line is the $pK^+\Sigma^0$ phase space simulation. The green line represent the Legendre fit, where the reduced χ^2 of the fit and the fit parameters are stated.

A quantitative description of the angular distribution is given by fitting it with the sum of Legendre polynomials. These coefficients are connected to the partial wave contributions. Therefore the data points are fitted by a Legendre polynomial expressed by:

$$P(\cos\theta) = A_0P_0 + A_1P_1 + A_2P_2 + A_3P_3 + A_4P_4, \quad (39)$$

where the Legendre Polynomials are given by

$$\begin{aligned}
P_0 &= 1 \\
P_1 &= \cos\theta \\
P_2 &= \frac{1}{2}(3\cos^2\theta - 1) \\
P_3 &= \frac{1}{2}(5\cos^3\theta - 3\cos\theta) \\
P_4 &= \frac{1}{2}(35\cos^4\theta + 30\cos^2\theta + 3)
\end{aligned}$$

and A_i are the fit parameters or the Legendre coefficients. Since the differential distributions in the CMS must be symmetric, only even powers are used in the fit. In particular, the coefficients A_0 and A_2 are used, the inclusion of A_4 has no significant effect in the fit as it is compatible with zero. The total production cross section is calculated by integrating the fit function. The integral of a Legendre polynomial is given by:

$$\sigma = \int_{-1}^1 \sum_i A_i P_i(\cos\theta) d\cos\theta = 2A_0.$$

In this way the Σ^0 total production cross section of reaction is determined to be $\sigma = (17.92 \pm 0.36) \mu b$, where the error quoted is the statistical error. Since the phase space simulation does not adequately describe the data and it was used for the acceptance and efficiency corrections, this cross section value is not yet the final result. After tuning the simulation model, a more accurate value of the cross section will be presented.

4.4.5 Systematic Uncertainties

The statistical uncertainty quoted in the calculated cross section value is not the only source of error, but also the systematic uncertainties are part of the reported result. A standard definition of systematic uncertainties is that: “Systematic uncertainties are all uncertainties that are not directly due to the statistics of the data” [28]. From this definition, possible sources of systematic uncertainties can be for example, uncertainties related to theoretical models, incorrect detector calibrations, a bias in the analysis cut flow to obtain a specific outcome or the normalization to literature cross section.

The systematic uncertainties are usually unknown and have to be estimated, there are different approaches on how to estimate the systematics, the approach used in this thesis is the *cut variations*, that is the different selection cuts are varied and an independent

Cut	Nominal	Variation 1	Variation 2
$DCA(p, \pi^-)$ [mm]	10	$\pm 20\%$	$\pm 30\%$
2D $d_{[p, \pi^-], pvtx}$	$d_{p, pvtx} < d_{\pi^-, pvtx}$	not used	-
$d_{\Lambda, pvtx}$ [mm]	10	$\pm 20\%$	$\pm 30\%$
$MM^2(p\Lambda)$ [GeV^2/c^4]	0.2	$\pm 25\%$	$\pm 50\%$
Low mass $MM^2(pK^+\Lambda)$ [GeV^2/c^4]	-0.02	$\pm 25\%$	$\pm 50\%$
High mass $MM^2(pK^+\Lambda)$ [GeV^2/c^4]	0.01	$\pm 25\%$	$\pm 50\%$
M_{p, π^-} [GeV/c^2]	3σ	2σ	-

Table 3: The variation of different cuts used to evaluate the systematic uncertainty.

analysis chain is created for every cut combination and the cross section is calculated as described above. The variation of the different cross sections calculated can then give an estimate of the size of the systematic uncertainties related to the different selection criteria. Since the analysis relies on missing mass cuts and the off-vertex cuts of the Λ selection, these might be a possible source of systematic errors. Each cut is varied in two steps in either direction, in addition the Λ mass window is varied by 2σ or 3σ around the mean value. These cut variations are listed in Tab. 3.

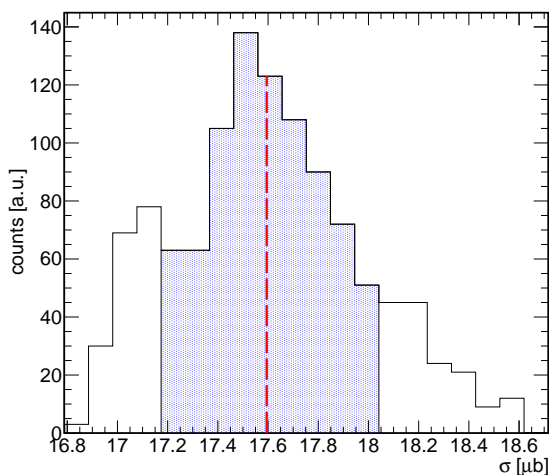


Figure 57: The distribution of the of the determined cross section for different values of the selection criteria in the analysis. The blue filled histogram represents the accepted values and the red dashed line represents the median value.

Fig. 57 shows the distribution of the calculated cross sections obtained from the combinations of different cuts. The systematic uncertainty is defined as the 68% confidence central interval of this distribution represented by the blue histogram, the red dashed line represents the median value of the accepted cross sections and is equal to $(17.6^{+0.38}_{-0.34})\mu b$, where the upper and lower errors are chosen in such a way that 16% of the distribution is rejected on each side.

Another possible source of the systematic errors is the PID, which is evaluated by activating the dropout layers of the VAE during the inference time as this is equivalent to doing a Bayesian approximation [62]. Following this procedure, the estimated size

of the systematic error related to PID is $\approx 5\%$. In addition to the PID and selection cuts systematic errors, the normalization to the elastic proton-proton cross section introduces 7% systematic uncertainty.

4.4.6 Angular Distributions Revisited

In this section, the angular distributions corrected for the acceptance and efficiency are presented. The correction procedure require the response matrix as an input, which by itself depends on the simulation that has been used. Therefore the simulation model has to be tuned in order to describe the different angular distributions.

The deviation from homogeneously populated phase space can arise from either an anisotropic production of the Σ^0 caused by a boson exchange as explained earlier, which affects mainly the CMS and the G-J distributions, or that the production proceeds via an intermediate resonance $pp \rightarrow p + (R \rightarrow \Sigma^0 K^+)$, which affects the helicity distributions.

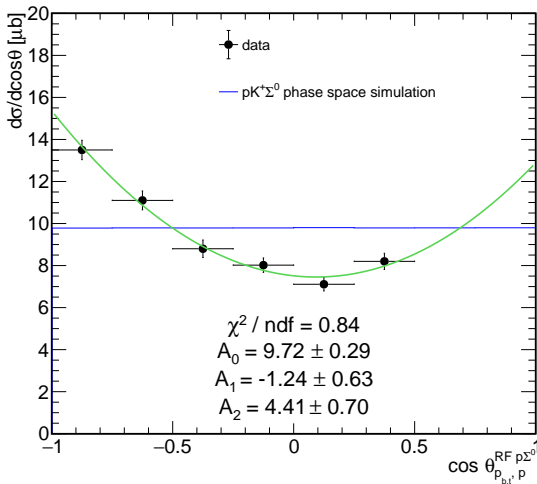


Figure 58: The proton G-J angle in the $p\Sigma$ reference frame. The Black points are the experimental and the blue line is the $pK^+\Sigma^0$ phase space simulation. The reduced χ^2 of the Legendre fit and the fit parameters are stated.

From Fig. 56, it can be seen that the Σ^0 production is anisotropic, which can be quantified by the A_2 coefficient. So in order to account for the observed production anisotropy, the isotropic simulations Σ^0 has been folded by the Legendre fit function $F(\cos\theta_{\Sigma^0}^{cms})$ which is determined from the data. However, it was found that this does not reproduce all of the observed CMS and G-J angular distributions. So, in addition to the $F(\cos\theta_{\Sigma^0}^{cms})$ weight function, the simulations are folded at the same time by the fit function obtained from the proton G-J angle $F(\cos\theta_{p_b, t, p}^{RF p \Sigma})$ shown in Fig. 58. In this way, the weighted phase space results in a satisfactory description of the CMS and the G-J angular distributions. The helicity angular distributions are not affected by this weighting/folding since they are kinematically uncorrelated with the CMS and G-J angular distributions.

One has to note also that the $pp \rightarrow pK^+\Lambda$ events cannot be completely separated from the signal and has a minor contribution. Therefore, the kinematics of the Λ has to be modeled correctly as the purity matrix depends on the Λ kinematics. The Λ production mechanism has been studied extensively by HADES at the same beam energy [15] and it was found that the Λ hyperon is produced with a strong anisotropy in the CMS frame. In order to take this anisotropy into account, Λ like events have been selected by applying a mass window $1.090 < MM(pK^+)[\text{GeV}/c^2] < 1.150$, the acceptance correction procedure (in this case, correction is done using $\cos\theta_{\Lambda}^{\text{cms}}$ and p_{Λ}^{cms}) and the normalization to the elastic p+p cross section described before was applied to those events. The obtained angular distribution of the Λ hyperon in the CMS frame $F(\cos\theta_{\Lambda}^{\text{cms}})$ shown in Fig. 59 is fit by a Legendre polynomial and the fit function is used to weight the phase space simulations of the $pp \rightarrow pK^+\Lambda$ reaction.

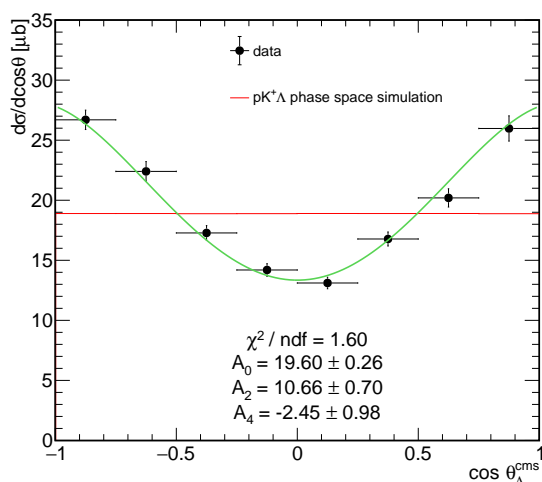


Figure 59: Differential cross section of the Λ hyperon in the CMS frame. The Black dots are the experimental data and the red line is the $pK^+\Lambda$ phase space simulation. The reduced χ^2 of the Legendre fit and the fit parameters are stated.

CMS Angular Distributions

The angular distributions of the three final state particles in the CMS are shown in Fig. 60 together with the Legendre polynomial coefficients obtained from the fit. If the particles would be produced in S-wave only, the distributions would be flat, and the Legendre coefficients above A_0 would be zero. The contribution of higher order Legendre polynomials causes an anisotropic angular distribution and indicates higher angular momenta between the particles. Since the p+p system is a symmetric system in the CMS, so also the angular distributions must be symmetric with respect to $\cos\theta = 0$. The angular distribution of the proton and the Σ^0 hyperon shows an anisotropy, where this is more pronounced in the case of the proton. From the observed anisotropies and the fit parameters one deduces that there is a non-zero relative angular momentum, L , in both the $(p - K^+\Sigma^0)$ and $(\Sigma^0 - pK^+)$ systems. This is in contrast to the kaon, where the angular distribution is almost isotropic. If we consider the case of pure pion exchange as

shown in Fig. 27b, the proton is the leading particle in this case, due to the small mass of the pion, there is a small 4-momentum transfer so that the final state proton is preferably emitted in the direction of the initial protons, which could explain the anisotropy in this proton angular distribution. Due to momentum conservation, the Σ^0 hyperon and the kaon distributions are just kinematical reflections of the proton.

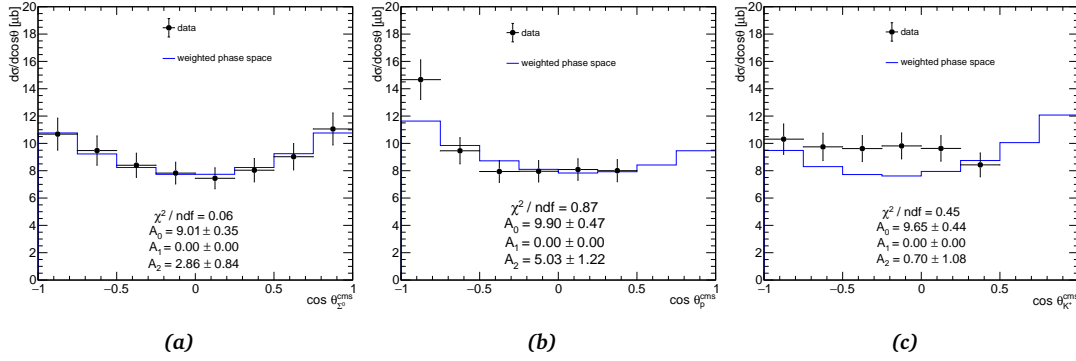


Figure 60: Angular distributions in the CMS frame for (a) the Σ^0 , (b) the proton p and (c) the kaon K^+ . The black line represents the weighted simulations.

G-J Angular Distributions

The angular distributions in the three G-J frames are shown in Fig. 61. A pronounced anisotropy is observed in the $p\Sigma^0$ G-J frame, which could be attributed to a relative angular momentum in the $p\Sigma^0$ system. This is also observed in the angular distributions of proton and Σ^0 in the CMS as they are related by the kinematics. The angular distribution in the $K^+\Sigma^0$ G-J frame tends to be asymmetric, which could be caused by the excitation of nucleon resonances decaying into the $K^+\Sigma^0$ channel. A long list of N^* or Δ^* resonances could contribute to the reaction. The angular distribution of a true two-body resonance reaction is asymmetric only if resonances with opposite parities are simultaneously excited through interfering amplitudes [5]. Hence, this distribution in the $K^+\Sigma^0$ G-J frame can be an indication that more than one nucleon resonance with opposite parity participates in the production process. The angular distribution in the K^+p G-J frame is expected to be basically isotropic if the reaction proceeds in two steps via an intermediate resonance as the final state protons and kaons do not originate from the same vertex. However, by inspection of the fit coefficients, one finds that it is difficult to judge the isotropy of the distribution due to the limited detector acceptance in this case.

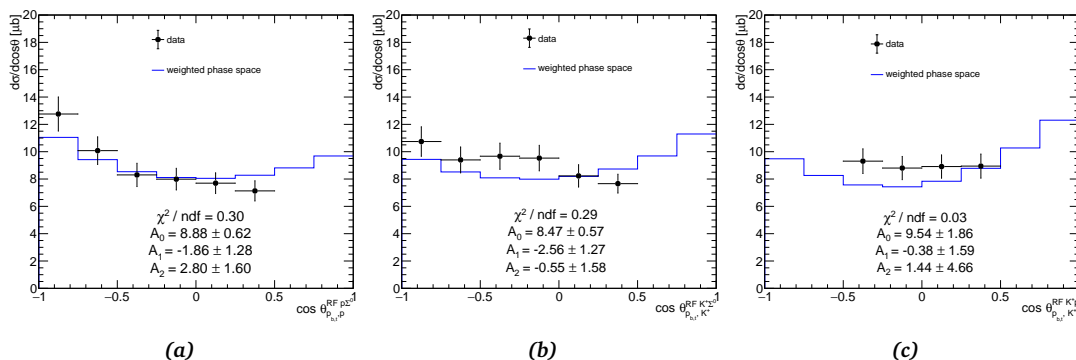


Figure 61: Angular distributions in the G-J frames (a) G-J angle of the proton in the $p\Sigma$ frame, (b) G-J angle of the kaon in the $K^+\Sigma$ frame and (c) G-J angle of the kaon in the K^+p frame.

Helicity Angular Distributions

Since the helicity angular distribution is a special projection of the Dalitz plot, it is a suitable observable to study the possible contributions of intermediate resonances, decaying into two of the three final state particles. FSI also distort the Dalitz plot and consequently its effects are seen in the helicity angular distribution. The helicity angular distributions are shown in Fig. 62. The weighted phase space simulation is flat in the helicity angular distributions since the helicity angle is kinematically uncorrelated with the CMS angle or the G-J angle. From Fig. 62, one can conclude that all distributions are far from isotropic, which is consistent with the reaction $pp \rightarrow pK^+\Sigma^0$ being dominated by intermediate resonant production. Therefore, an inclusion of intermediate resonances is necessary in order to give a better description of the helicity angular distributions.

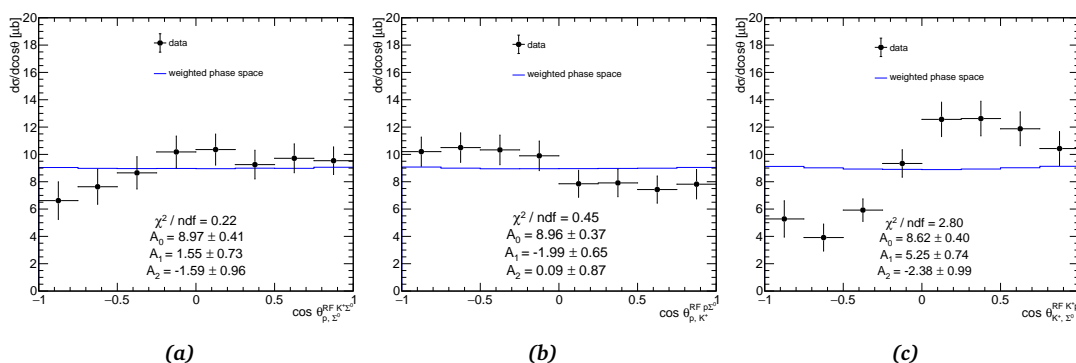


Figure 62: Angular distributions in the helicity frames (a) the helicity angle between p, Σ in the $K^+\Sigma$ frame, (b) the helicity angle between p, K^+ in the $p\Sigma$ frame and (c) the helicity angle between K^+, Σ in the K^+p frame.

The Incoherent Sum

Inspection of [121] reveals a long list of nucleon resonances, which can be either isospin 1/2 N^* or isospin 3/2 Δ^* resonances. However, only few of those listed in Tab. 4 contribute at this beam energy and have a measured (or seen) branching ratio to the $K^+\Sigma^0$ final state.

Resonance	Mass [GeV/c^2]	Width [GeV/c^2]	J^P	BR ($K^+\Sigma^0$)	ϵ [MeV]
$N^*(1710)$	1.710	0.140	$\frac{1}{2}^+$	seen	528
$N^*(1875)$	1.875	0.200	$\frac{3}{2}^-$	seen	363
$N^*(1880)$	1.880	0.300	$\frac{1}{2}^+$	10-24%	358
$N^*(1895)$	1.895	0.120	$\frac{1}{2}^-$	6-20%	343
$N^*(1900)$	1.920	0.200	$\frac{3}{2}^+$	3-7%	338
$\Delta^*(1900)$	1.860	0.250	$\frac{1}{2}^-$	seen	338
$\Delta^*(1910)$	1.900	0.300	$\frac{1}{2}^+$	4-14%	328
$\Delta^*(1920)$	1.920	0.300	$\frac{3}{2}^+$	2-6%	318

Table 4: A list of N^* and Δ^* resonances that might contribute to the $pK^+\Sigma^0$ reaction. The mass, width, spin-parity quantum numbers and the branching ratios were taken from [121], the last column lists the excess energy (ϵ) of the reaction $pp \rightarrow p + N^*/\Delta^*$.

Fig. 63 shows Pluto simulations of Σ^0 hyperon production $pp \rightarrow p + (N^*/\Delta^* \rightarrow K^+\Sigma^0)$ in which N^* resonances with different properties were simulated and the effect of the kinematics in the $K^+\Sigma^0$ and $p\Sigma^0$ invariant mass spectra is apparent.

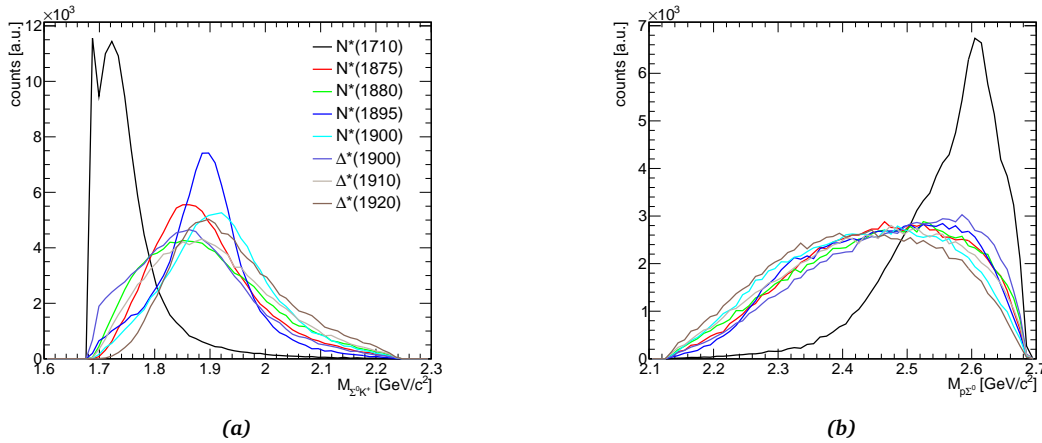


Figure 63: Pluto simulations of Σ^0 resonant production. (a) The $K^+\Sigma^0$ invariant mass and (b) the $p\Sigma^0$ invariant mass.

In order to quantify the contribution of each resonance, the different resonances and the phase space have been scaled to match the experimental data by means of a χ^2

minimization as described in section 4.4.1, the minimization is done in the $K^+\Sigma^0$ and $p\Sigma^0$ invariant mass spectra simultaneously as they are sensitive to the resonance masses and widths. It was found that the fit prefers $\Delta^*(1900)$, $N^*(1880)$, $N^*(1710)$ and $N^*(1895)$ with 55%, 4.3%, 6.7% and 3%, respectively, while about 31% is a pure phase space contribution. The different contributions compared to data are shown in Fig. 64. The agreement between the experimental data and the incoherent sum is quantified by a reduced χ^2 value. A fit of a pure phase space simulation $pp \rightarrow pK^+\Sigma^0$ has resulted in $\chi^2/ndf \approx 4.1$.

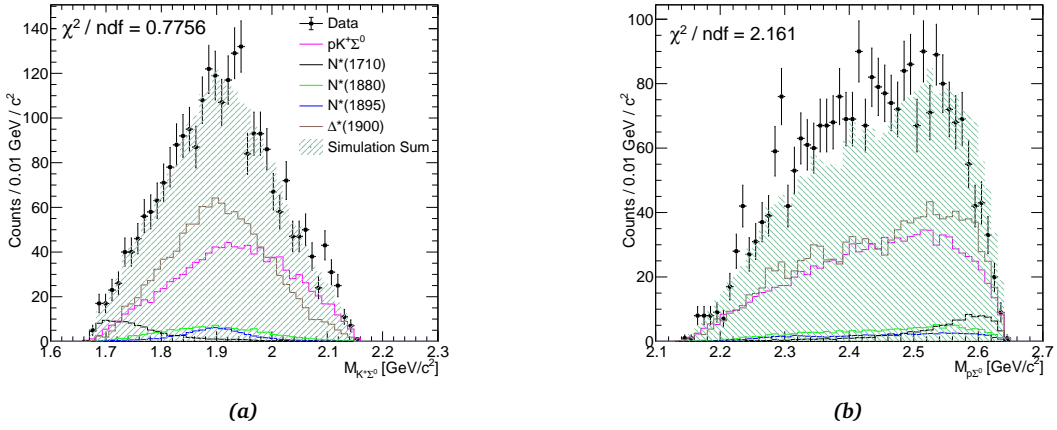


Figure 64: The contributions of phase space and resonance production of Σ^0 compared to the experimental data, the reduced χ^2 is stated for both invariant masses. (a) The $K^+\Sigma^0$ invariant mass distribution and (b) the $p\Sigma^0$ invariant mass distribution.

The incoherent sum of the phase space and the resonant production is then used for the acceptance and the efficiency correction. The helicity angular distributions corrected by the incoherent sum are shown in Fig. 65.

The tuned simulation model correctly reproduces the helicity angles (p, K^+) and (K^+, Σ^0), as both of these angles are sensitive to the mass and the width of the resonance. The helicity angle (p, Σ^0) calculated in the rest frame of the resonance is not influenced by its mass and width. However, if more than one nucleon resonance contributes, interference effects can influence this distribution, which might be the case here as the simulation model is just the incoherent sum of the different contributions and does not take the interference effects into account.

4.5 PARTIAL WAVE ANALYSIS

From the presented results so far, it was concluded that the experimental data can not be described by phase space simulations, but there must be a resonant component in

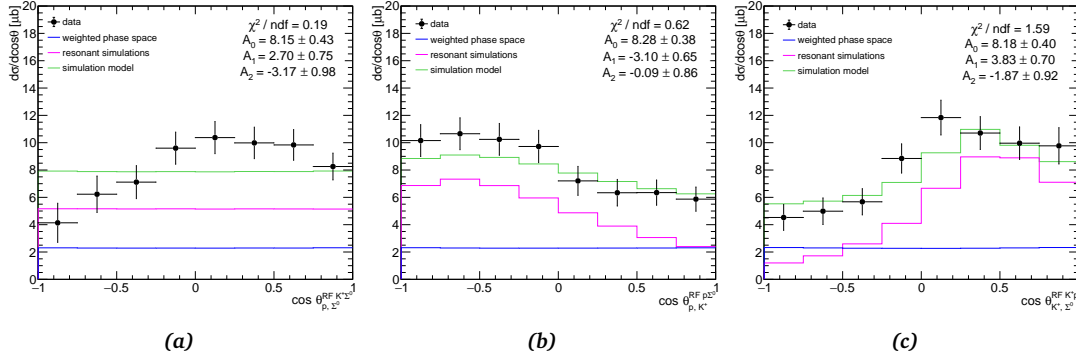


Figure 65: Angular distributions in the helicity frames corrected by the incoherent sum of the phase space and the resonant production, the weighted phase space is shown by the blue line, the resonant contribution by the purple line and the sum by the green line. (a) The helicity angle between p, Σ in the $K^+\Sigma$ frame, (b) the helicity angle between p, K^+ in the $p\Sigma$ frame and (c) the helicity angle between K^+, Σ in the K^+p frame.

addition to the phase space. This result was expected as it was already shown in [5]. The incoherent sum of the phase space and different nucleon resonances provides a better description of the experimental data. However, a still open question is the interference between different channels.

A Partial Wave Analysis (PWA) is a technique used in quantum scattering theory, where the initial state can be considered as a series of spherical waves each of definite angular momentum $l\hbar$ (partial waves) and the aim of the PWA is to decompose each wave into its constituent angular momentum components. Each transition is described by a partial wave amplitude, a PWA aims to determine the partial wave amplitudes.

The framework used in this thesis is the Bonn-Gatchina Partial Wave Analysis (BG-PWA) [109]. In the BG-PWA the differential cross section of the scattering process (in this case $a + b \rightarrow 1 + 2 + 3$) can be written as [49]:

$$d\sigma = \frac{(2\pi)^4 |A|^2}{4|\vec{k}|\sqrt{s}} d\phi_3(P, q_1, q_2, q_3)$$

$$P = k_1 + k_2,$$

where $d\phi_3$ is the phase space element of the three final state particles with the 4-momenta q_i ; $|\vec{k}|$ is the combined 3-momenta of the two initial state protons; $|k|$ is the absolute value of the momentum of the beam proton calculated in the CMS frame; \sqrt{s} is the center of mass energy of the colliding system; A is the total transition amplitude from the initial to the final state. This total transition amplitude is given by a sum over all partial waves, which gives rise to interference patterns between different partial waves:

$$A = \sum_{\alpha} A_{tr}^{\alpha}(s) Q_{\mu_1, \dots, \mu_j}^{in}(S, L, J) A_{2b}(S_2, L_2, J_2)(s_i) Q_{\mu_1, \dots, \mu_j}^{fin}(i, S_2, L_2, J_2, S', L', J),$$

where S , L and J are the spin, orbital angular momentum and total angular momentum of the initial state. For each partial wave α , the final state is treated as two-particle subsystem with quantum numbers S_2 , L_2 , J_2 indicating the combined spin, orbital momentum and total angular momentum of the subsystem and the third particle is treated with respect to this sub-system. The quantum numbers of the total final state (in this case $pK^+\Sigma^0$) is then described by S' , L' and J , where S' is the total spin of the two-particle subsystem when combined with the third particle and L' denotes the orbital momentum between the third particle and the subsystem.

$A_{tr}^{\alpha}(s)$ is the transition amplitude from the initial to the final state where the multiindex α donates all possible combinations of S , L , J , S_2 , L_2 , J_2 , S' , L' and i associated with certain waves. $Q_{\mu_1, \dots, \mu_j}^{in}(S, L, J)$ and $Q_{\mu_1, \dots, \mu_j}^{fin}(i, S_2, L_2, J_2, S', L', J)$ are the spin-momentum operators of the initial and final state, respectively. The exact form of the operators can be found in [21].

The transition amplitude is parametrized by three parameter α_i as follows:

$$A_{tr}^{\alpha}(s) = (\alpha_1 + \alpha_3 \sqrt{s}) e^{i\alpha_2}.$$

Because the center of mass energy of this experiment is fixed ($\sqrt{s} = 3.18 GeV$) the third parameter α_3 , which is responsible for the energy dependence of each partial wave was set to zero. This means that each partial wave α is described only by the strength α_1 and phase α_2 parameters.

$A_{2b}(S_2, L_2, J_2)(s_i)$ describes the rescattering processes in the final two-particle sub-system and is parameterized as follows:

$$A_{2b}^{\beta}(s) = \frac{\alpha_{\gamma\gamma'}^{\beta} \sqrt{s}}{1 - \frac{1}{2} r_{\gamma\gamma'}^{\beta} q^2 \alpha_{\gamma\gamma'}^{\beta} + i q \alpha_{\gamma\gamma'}^{\beta} q^{2L_2} / F(q, r_{\gamma\gamma'}^{\beta}, L_2)},$$

where $\alpha_{\gamma\gamma'}^{\beta}$ is parameter that describes the scattering length of the two particles γ and γ' , $r_{\gamma\gamma'}^{\beta}$ describes the effective range of the two particle sub-system and q is the relative angular momentum between the two particles. The $F(q, r_{\gamma\gamma'}^{\beta}, L_2)$ is the Blatt-Weisskopf form factor, which is used for normalization [49] and the multiindex donates all possible combinations of the two particle sub-system with quantum numbers S_2 , L_2 and J_2 .

In case of resonant production; where the two particle sub-system is produced via an intermediate resonance; the $A_{2b}(S_2, L_2, J_2)(s_i)$ is parametrized as a relativistic Breit-Wigner in the following form [21]:

$$A_{2b}^\beta(s) = \frac{M\Gamma_{tot}}{M^2 - s - iM\Gamma_{tot}},$$

with M and Γ_{tot} expressing the pole mass and width of the intermediate resonance. The angular dependence of the scattering amplitude, that is characteristic for a partial wave decomposition, is contained in the momentum part of the spin-momentum operators and is parametrized by Legendre polynomials [20].

4.5.1 Quantum Numbers of the Initial State

In this experiment, the initial state consists of two protons ($J^P = \frac{1}{2}^+$). The spins of the two protons can be combined to form a *singlet* ($S = 0$) or a *triplet* state ($S = 1$), respectively. In addition to the spin, a relative orbital angular momentum can appear between the two protons giving rise to different combinations. The maximum value of the orbital angular momentum which can contribute to the p+p scattering is $L \approx kR$, where R is the range of the interaction and k corresponds to the incident proton beam momentum. If the range of the interaction is $R \approx 1/m_p$, where m_p is the proton mass, then the maximum value of the orbital angular momentum which contributes to the scattering at beam kinetic energy 3.5 GeV is $L = 3$, that is only S , P , D and F waves need to be considered. Since the two protons are indistinguishable fermions the total wave function of the initial state has to be antisymmetric, which means that the following relation must hold:

$$(-1)^{S+L+1} = -1.$$

Tab. 5 lists all possible combinations of the two initial protons, by imposing the antisymmetrization condition, the grey shaded states are forbidden. Given the spectroscopic notation:

$$^{2S+1}L_J,$$

the possible initial states can be written as 1S_0 , 3P_0 , 3P_1 , 3P_2 , 1D_2 , 3F_2 , 3F_3 and 3F_4 .

J^P	$S = 0$	$S = 1$
S-wave L=0	0^+	1^+
P-wave L=1	1^-	$0^-, 1^-, 2^-$
D-wave L=2	2^+	$1^+, 2^+, 3^+$
F-wave L=3	3^-	$2^-, 3^-, 4^-$

Table 5: Possible combinations of the initial state of two protons with $J^P = \frac{1}{2}^+$.

4.5.2 Quantum Numbers of the Final State

The final state is a twofold problem, the non-resonant or direct production $p + p \rightarrow p + K^+ + \Sigma^0$ and the resonant production $p + p \rightarrow p + (R \rightarrow K^+ + \Sigma^0)$, where R is a nucleon resonance.

Non-Resonant Production of $pK^+\Sigma^0$

In the BG-PWA framework the non-resonant production proceed as follows; the proton p ($J^P = \frac{1}{2}^+$) and the hyperon (in this case Σ^0 with $J^P = \frac{1}{2}^+$) are combined into a two particle sub-system and then the kaon K^+ ($J^P = 0^-$) is combined with this sub-system to produce the three body final state. The quantum numbers of the $p\Sigma^0$ sub-system are listed in Tab. 6. If for example the $p\Sigma^0$ 1S_0 state is combined with the K^+ , the result would be $(^1S_0) 1S$, $(^1P_1) 3P$, $(^1D_2) 5D$ and $(^1F_3) 7F$ for the three body final state, the number outside the brackets stands for $(2S + 1)$ of the combined final state and the letter denotes the angular momentum between the K^+ and the $p\Sigma^0$ state. The J^P quantum number conservation limits the transition to specific states as listed in Tab. 6.

Resonant Production of $pK^+\Sigma^0$

In case of the resonant production, the proton p ($J^P = \frac{1}{2}^+$) is combined with the one of the resonances listed in Tab. 4 (N^*-p or Δ^*-p) to produce the final state $pK^+\Sigma^0$. These resonances can be grouped into four different categories according the spin parity J^P quantum number: $J^P = \frac{1}{2}^+$, $J^P = \frac{1}{2}^-$, $J^P = \frac{3}{2}^+$ and $J^P = \frac{3}{2}^-$. The J^P quantum number conservation limits the transition to those specific states listed in Tab. 7. The states listed are limited only to the F-wave.

p-p Initial State $^{2S+1}L_J$	Final State $^{2S+1}L_J$ ($p\Sigma^0$) K^+
1S_0	$(^3S_1) 3P, (^3P_0) 1S, (^3p_2) 5D,$ $(^3D_1) 3P, (^3D_3) 7F$
3P_0	$(^1S_0) 1S, (^1P_1) 3P, (^1D_2) 5D,$ $(^3P_1) 3P, (^3D_2) 5D$
3P_1	$(^1P_1) 3P, (^1D_2) 5D, (^3S_1) 3S,$ $(^3S_1) 3D, (^3P_0) 1P, (^3P_1) 3P,$ $(^3P_2) 5P, (^3P_2) 5F, (^3D_1) 3S,$ $(^3D_1) 3D, (^3D_2) 5D, (^3D_2) 7D$
3P_2	$(^1S_0) 1D, (^1P_1) 3P, (^1P_1) 3F,$ $(^1D_2) 5S, (^1D_2) 5D, (^3S_1) 3D,$ $(^3P_1) 3P, (^3P_2) 5P, (^3P_2) 5F,$ $(^3D_1) 3D, (^3D_2) 5D, (^3D_3) 7D$
1D_2	$(^1P_1) 3D, (^1D_2) 5P, (^1D_2) 5F,$ $(^3S_1) 3P, (^3S_1) 3F, (^3P_0) 1D,$ $(^3P_1) 3D, (^3P_2) 5D, (^3D_1) 3P,$ $(^3D_1) 3F, (^3D_2) 5P, (^3D_2) 5F,$ $(^3D_3) 7P, (^3D_3) 7F$
3F_2	$(^1S_0) 1D, (^1P_1) 3P, (^1P_1) 3F,$ $(^1D_2) 5S, (^1D_2) 5D, (^3S_1) 3D,$ $(^3P_1) 3P, (^3P_2) 5P, (^3P_2) 5F,$ $(^3D_1) 3D, (^3D_2) 5D, (^3D_3) 7D$

Table 6: Possible combinations of the non-resonant production of $pK^+\Sigma^0$ used in this study. Inside the brackets is the $p\Sigma^0$ state, the number outside the brackets stands for $(2S + 1)$ of the combined final state and the letter denotes the angular momentum between the K^+ and the $p\Sigma^0$ state.

4.5.3 BG-PWA Analysis Method

As an input, the BG-PWA framework needs the reconstructed experimental data together with a set of reconstructed phase space simulations (at the *detector level*), both are provided in a form of a list containing the components of the 4-momentum of the final state particles; the p , the K^+ and the hyperon Σ^0 . In addition, a list of possible transition waves that may contribute to the final state has to be provided. The transition waves used in this analysis are listed in Tab. 6 and 7. In case of the resonant production, the resonance mass and width were fixed to the PDG values (listed in Tab. 4) to reduce the number of the fit free parameters. The mass and width of each resonance is provided to the code in an extra input list.

The strength α_1 and the phase α_2 of each transition wave are determined by fitting the partial wave amplitude to the experimental data on an event by event basis (an

p-p Initial State $^{2S+1}L_J$	Final State $(N^*, \Delta^*)-p$
1S_0	$(N^*(1710) - p) 1S, (N^*(1875) - p) 3P, (N^*(1880) - p) 1S, (N^*(1895) - p) 3P, (N^*(1900) - p) 5D, (\Delta^*(1900) - p) 3P, (\Delta^*(1910) - p) 1S, (\Delta^*(1920) - p) 5D$
3P_0	$(N^*(1710) - p) 3P, (N^*(1875) - p) 5D, (N^*(1880) - p) 3P, (N^*(1895) - p) 1S, (N^*(1900) - p) 3P, (\Delta^*(1900) - p) 1S, (\Delta^*(1910) - p) 3P, (\Delta^*(1920) - p) 3P$
3P_1	$(N^*(1710) - p) 1P, (N^*(1710) - p) 3P, (N^*(1875) - p) 3S, (N^*(1875) - p) 3D, (N^*(1875) - p) 5D, (N^*(1880) - p) 1P, (N^*(1880) - p) 3P, (N^*(1895) - p) 3D, (N^*(1900) - p) 3P, (N^*(1900) - p) 5P, (\Delta^*(1900) - p) 3D, (\Delta^*(1910) - p) 1P, (\Delta^*(1910) - p) 3P, (\Delta^*(1920) - p) 3P, (\Delta^*(1920) - p) 5P$
3P_2	$(N^*(1710) - p) 3P, (N^*(1710) - p) 3F, (N^*(1875) - p) 5S, (N^*(1875) - p) 3D, (N^*(1880) - p) 3P, (N^*(1895) - p) 1D, (N^*(1900) - p) 3P, (N^*(1900) - p) 5P, (\Delta^*(1900) - p) 1D, (\Delta^*(1910) - p) 3P, (\Delta^*(1910) - p) 3F, (\Delta^*(1920) - p) 3P, (\Delta^*(1920) - p) 5P$
1D_2	$(N^*(1710) - p) 1D, (N^*(1710) - p) 3D, (N^*(1875) - p) 5P, (N^*(1880) - p) 3D, (N^*(1880) - p) 3D, (N^*(1895) - p) 3P, (\Delta^*(1900) - p) 3P, (N^*(1900) - p) 5S, (N^*(1900) - p) 3D, (N^*(1900) - p) 5D, (\Delta^*(1910) - p) 1D, (\Delta^*(1910) - p) 3D, (\Delta^*(1920) - p) 5P, (\Delta^*(1920) - p) 5S, (\Delta^*(1920) - p) 3D$
3F_2	$(N^*(1710) - p) 3P, (N^*(1710) - p) 3F, (N^*(1875) - p) 5S, (N^*(1875) - p) 3D, (N^*(1880) - p) 3P, (N^*(1895) - p) 1D, (N^*(1900) - p) 3P, (N^*(1900) - p) 5P, (\Delta^*(1900) - p) 1D, (\Delta^*(1910) - p) 3P, (\Delta^*(1910) - p) 3F, (\Delta^*(1920) - p) 3P, (\Delta^*(1920) - p) 5P$

Table 7: Possible combinations of the proton and a nucleon resonance (N^*-p or Δ^*-p) to produce the final state $pK^+\Sigma^0$ out of a certain $p-p$ initial state. Inside the brackets is the resonance-proton combined state (N^*-p or Δ^*-p), the number outside the brackets stands for $(2S + 1)$ of the total final state and the letter denotes the angular momentum between the p and the resonance.

unbinned fit). Since the experimental data may contain an amount of background (mainly $p + p \rightarrow p + K^+ + \Lambda$), an additional list of background events has to be provided with a negative weight to the BG-PWA framework. The fit is based on a log-likelihood minimization, the fitting procedure is repeated for many iterations until no further improvement of the log-likelihood value. By comparing the log-likelihood value of many fits the best fit can be obtained through the largest negative value.

As an output, the BG-PWA gives the fitted values of the parameters α_1 and α_2 and a list of simulated events that have been used as an input but with each event being assigned with a weighting factor, which gives the contribution of this event to the total yield. From those events it was possible to present the fit result in a graphical way using different kinematical observables.

Since the fitting works on an event-by-event basis, it is necessary to determine the background events and add them to the experimental data list with a negative weight. It was shown previously that in the signal region $1.170 < MM(pK^+)[GeV/c^2] < 1.220$ there are contribution from $pp \rightarrow pK^+\Lambda$ and $pp \rightarrow pK^+\Lambda\pi^0$ channels (see Fig. 51), which were estimated to be 14% and 5%, respectively. In this PWA method, only the $pp \rightarrow pK^+\Lambda$ channel was considered since it's contribution is three times larger than for the $pp \rightarrow pK^+\Lambda\pi^0$ channel. The $pp \rightarrow pK^+\Lambda$ events contributing to the signal were determined as explained in Appendix C.

p-p Initial State	non-resonant $pK^+\Sigma^0$	$N^*(1710)$	$N^*(1900)$	$\Delta^*(1900)$
1S_0	90.99	26.96	01.11	02.85
3P_0	00.00	02.60	00.00	00.43
3P_1	01.06	00.00	00.00	00.67
3P_2	00.00	00.00	28.17	00.00
1D_2	12.89	00.00	00.00	00.00
3F_2	00.00	00.00	02.16	00.00

Table 8: Partial wave contributions to the total $pK^+\Sigma^0$ production.

The best PWA solution (log-likelihood value $\mathcal{L} = -333.65$) was obtained by including p+p initial waves 1S_0 , 3P_0 , 3P_1 , 3P_2 , 1D_2 and 3F_2 as shown in Tab. 8. As the waves interfere with each other the sum of the different waves can exceed 100%. Due to the limited statistics, a clear statement of the exact contribution of each resonance is not possible since these contributions varies significantly for different solutions. However, resonances with mass around $1.710 GeV/c^2$ ($N^*(1710)$) and $1.900 GeV/c^2$ ($N^*(1900)$ or $\Delta^*(1900)$) are preferred by the fit.

A comparison between the best PWA solution and the experimental data is shown in Fig. 66 and Fig. 67 for different kinematic observables and angular distributions, respectively. The agreement between the PWA solution and experimental data is quantified by a reduced χ^2 value for each observable calculated as follows:

$$\chi^2/ndf = \sum_{bins} \frac{(n_{simu} - n_{data})^2}{\sigma_{simu}^2 + \sigma_{data}^2} / ndf, \quad (40)$$

where the summations runs over the number of bins for each histogram, n_{simu} is the number of simulated events in each bin, n_{data} is the number of data events in each bin and ndf is the number of degrees of freedom. The χ^2 average value over all the distributions shown in Fig. 66 and Fig. 67 is 1.4, which is an acceptable agreement between the PWA solution and the experimental data.

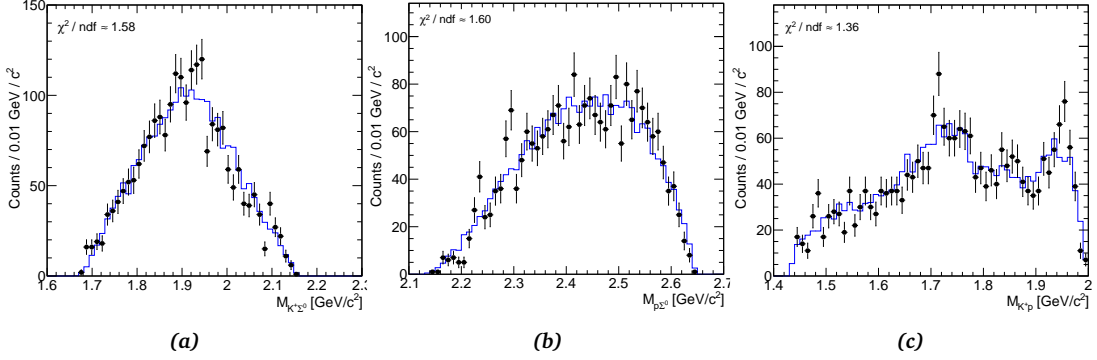


Figure 66: A comparison between the experimental data (black points) and the best PWA solution (blue histogram) given in Tab. 8 for (a) the $K^+\Sigma^0$ invariant mass, (b) the $p\Sigma^0$ invariant mass and (c) the K^+p invariant mass distributions.

The $K^+\Sigma^0$ and $p\Sigma^0$ invariant mass spectra are sensitive to the mass and width of the included resonances, while K^+p invariant mass shape is fully attributed to the detector acceptance, since the K^+p can not be the decay product of a nucleon resonance.

As the PWA solution describes the experimental data in a good way, it can be used for the acceptance and efficiency correction. The simulated phase space events that have been assigned a PWA weight are filtered through the full simulation and analysis chain, the obtained spectra for each observable at the detector and generator level are then used to build the response matrices. The response matrices are inverted by the SVD technique (discussed in section 4.4.3) and then used for the acceptance and efficiency correction. The corrected invariant mass distributions are shown in Fig. 68 and the corrected CMS, G-J and helicity angular distributions are shown in Fig. 69.

Each one of the nine distributions has been fit by a Legendre polynomial (see Eq. 39), the fit quality and parameters are given for each distribution. The Σ^0 hyperon and the p are produced anisotropically in the CMS frame, where the anisotropy is more pronounced in the case of the protons ($A_2 = 5.76$), indicating that production proceeds via the pion exchange mechanism. The K^+ CMS angular distribution is compatible with isotropy.

As discussed previously the G-J angle measured in the K^+p frame is expected to be isotropic. However, if the kaon exchange mechanism plays a significant role in the Σ^0 production it could affect this G-J angular distribution. Similar effects might potentially arise from an unknown pentaquark-resonance [5].

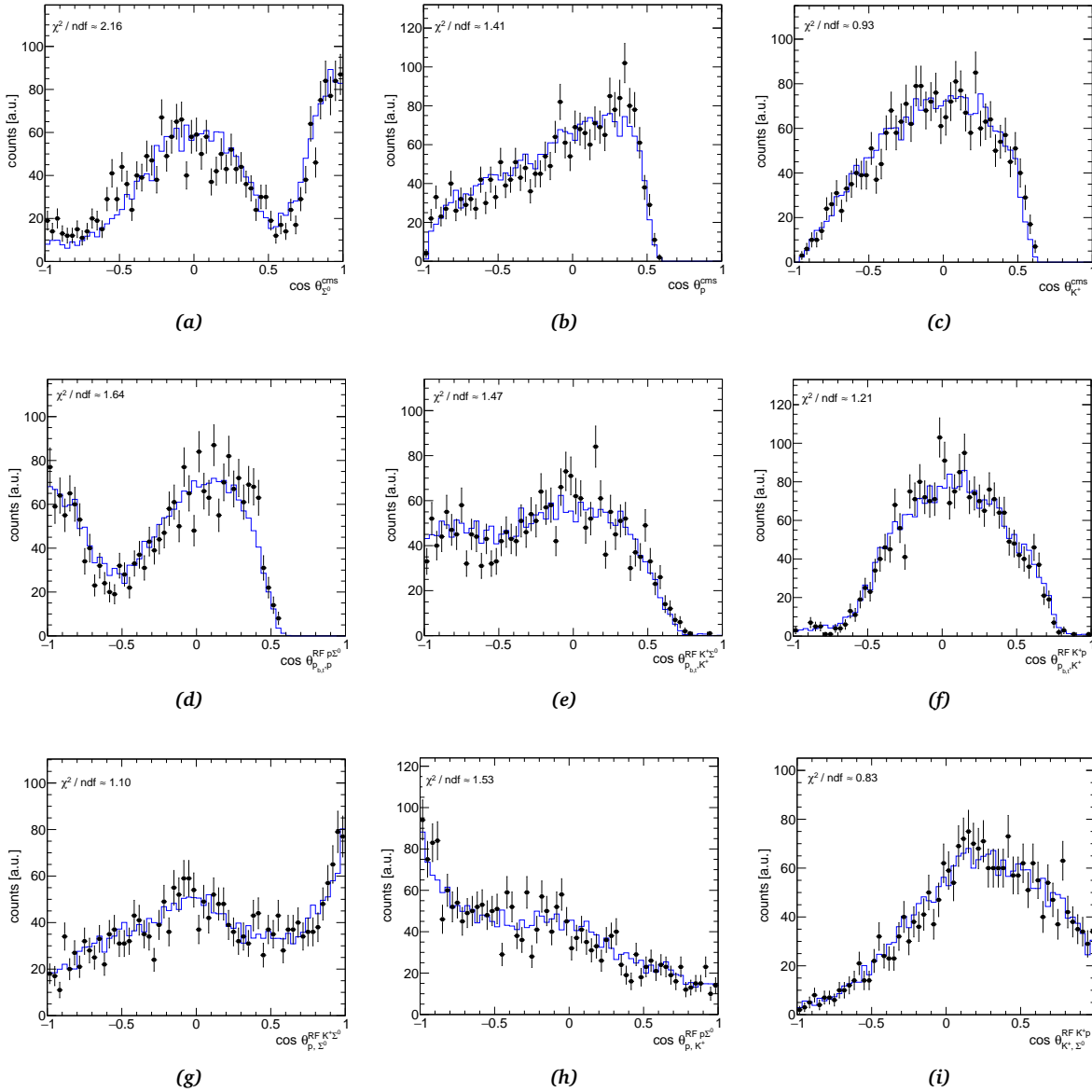


Figure 67: A comparison between the experimental data (black points) and the best PWA solution (blue histogram) given in Tab. 8. The upper row shows the CMS angular distributions, the middle row shows the G-J angular distributions and the bottom row shows the helicity angular distributions.

As explained, the helicity angular distributions depend on and reflect the masses and the widths of the contributing nucleon resonances. The asymmetry of the helicity angular distribution $\cos\theta_{p,\Sigma^0}^{K^+,\Sigma^0}$ could be attributed to the interference between the contributing nucleon resonances. However, a $p\Sigma^0$ FSI could also result in an asymmetric distribution with enhanced cross section towards $\cos\theta_{p,\Sigma^0}^{K^+,\Sigma^0} = 1$ [5]. This can be also reflected in the Dalitz plot since the $\cos\theta_{p,\Sigma^0}^{K^+,\Sigma^0}$ helicity angular distribution is a type of projection of the whole Dalitz plot. Fig. 70 shows the Dalitz plot constructed from the invariant masses

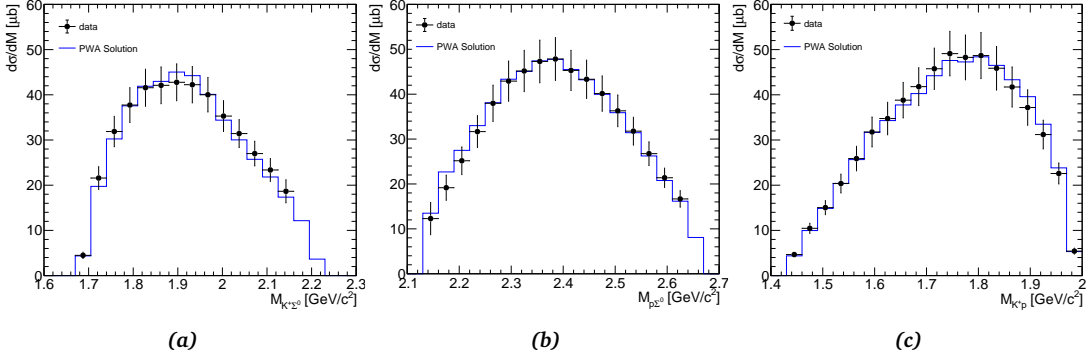


Figure 68: Invariant mass spectra corrected with the best PWA solution. (a) The $K^+\Sigma^0$ invariant mass, (b) the $p\Sigma^0$ invariant mass and (c) the K^+p invariant mass distributions.

$M^2(p\Sigma^0)$ and $M^2(K^+\Sigma^0)$. In the uncorrected Dalitz plot (Fig. 70a), the anisotropies are primarily the result of the detector acceptance. However, the corrected plot (Fig. 70b)² shows strong deviations from a uniform distribution, which is a result of the contributions from the nucleon resonances and the interference terms.

From the presented results, we can conclude, that the experimental data can be reproduced by a incorporating different nucleon resonances and non-resonant components, the interference effect seems play a major role since the data can not be described by the simple incoherent sum.

4.5.4 PWA Systematics

Due to the limited $pK^+\Sigma^0$ statistics and the large number of fit parameters, it was not possible to determine the exact contribution of each resonance, in addition, the solution is not very sensitive to the input wave composition. Therefore, it was necessary to test different solutions in order minimize bias to the cross section calculation.

A systematic variation of the input partial waves was performed, and in addition, the number of the non-resonant and resonant final partial waves was varied, the quality of the PWA solution was determined by the loglikelihood value of the fit. However, only few of the tested combinations produced a converging solution. Tab. 9 summarizes the best five solutions, the agreement between the experimental and the PWA is quantified by a reduced χ^2 averaged over the $M_{K^+\Sigma^0}$, $M_{p\Sigma^0}$, M_{pK^+} invariant mass distributions and the angular distributions in the CMS, G-J and helicity frames. The calculated cross section (section 4.5.5) of different solutions fluctuates within 1.2% that is taken as an addition uncertainty.

² The correction is done as explained in section 4.4.3.

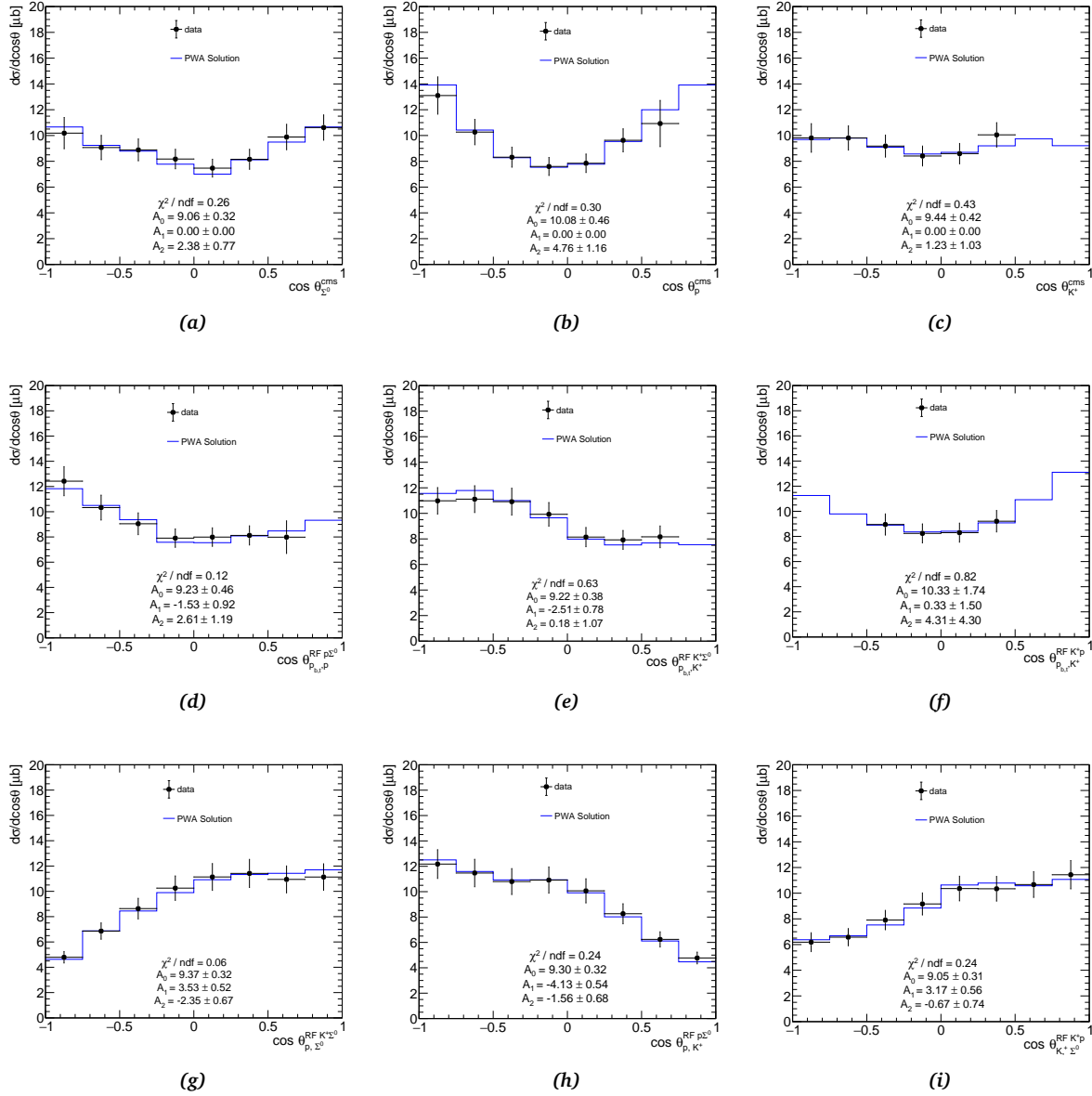


Figure 69: Angular distributions in experimental data corrected by the best PWA solution. The upper row shows the CMS angular distributions, middle row shows the G-J angular distributions and the bottom row shows the helicity angular distributions.

4.5.5 Total production cross section

The total production cross section of the Σ^0 hyperon can be obtained by integrating the yield for different differential distributions. Tab. 10 lists the cross section extracted from the different angular distributions. The cross sections are compatible with each other within the calculated uncertainties, which is considered as a self consistency check for the acceptance and efficiency correction procedure.

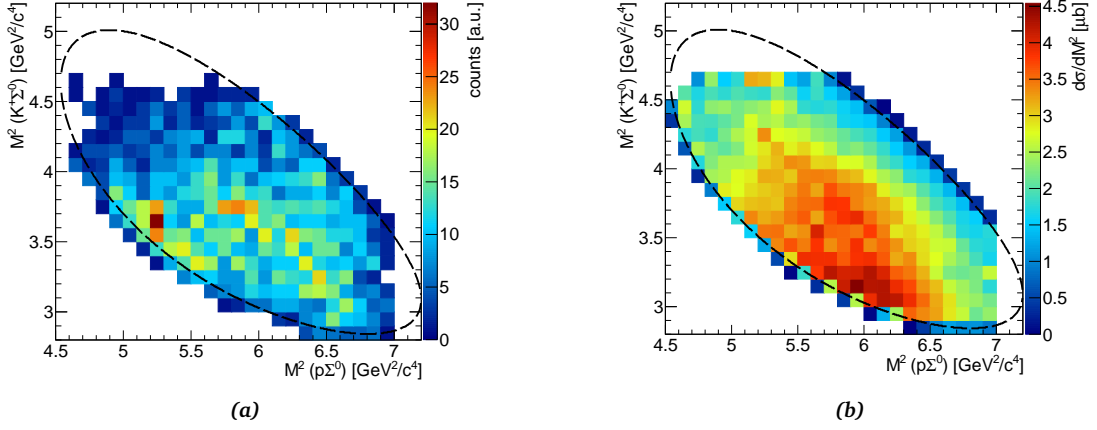


Figure 70: The Dalitz plot, the black line marks the kinematic boundary. (a) Before efficiency and acceptance correction and (b) after the correction.

Solution	Initial State	non-resonant contributions	resonant contributions	\mathcal{L}
solution 1	$^1S_0, ^1D_2$ $^3P_0, ^3P_1$ $^3P_2, ^3F_2$	61.77 %	$N^*(1710) \approx 17.40$ % $N^*(1900) \approx 18.51$ % $\Delta^*(1900) \approx 02.31$ %	-333.65
solution 2	$^1S_0, ^1D_2$	25.79 %	$N^*(1710) \approx 22.25$ % $N^*(1900) \approx 09.82$ % $\Delta^*(1900) \approx 42.15$ %	-184.40
solution 3	$^1S_0, ^1D_2$ $^3P_0, ^3P_1$ 3P_2	45.06 %	$N^*(1710) \approx 21.40$ % $N^*(1895) \approx 16.17$ % $N^*(1900) \approx 15.88$ % $\Delta^*(1900) \approx 01.49$ %	-181.80
solution 4	$^1S_0, ^1D_2$ $^3P_0, ^3P_1$ $^3P_2, ^3F_2$	33.10 %	$N^*(1710) \approx 26.8$ % $N^*(1880) \approx 40.1$ %	-151.34
solution 5	1S_0	16.75 %	$N^*(1710) \approx 78.55$ % $\Delta^*(1900) \approx 04.62$ %	-122.71

Table 9: The best five PWA solutions.

A weighted average cross section can be calculated and was found to be:

$$\sigma(pK^+\Sigma^0)[\mu b] = 18.74 \pm 1.01(stat) \pm 1.71(syst)$$

The calculated cross section value is included in Fig. 71, which shows a compilation of the cross section of $p + p \rightarrow \Sigma^0 + K^+ + p$ as function of the excess energy ϵ [12], our data point corresponds to $\epsilon = 556\text{MeV}$, which is depicted by the green square, this is

Observable	σ [μb]
$\cos\theta_{\Sigma}^{cms}$	18.12 ± 0.65 (stat) $^{+1.64}_{-1.63}$ (syst)
$\cos\theta_p^{cms}$	20.16 ± 0.84 (stat) $^{+1.83}_{-1.82}$ (syst)
$\cos\theta_{K^+}^{cms}$	18.88 ± 0.86 (stat) $^{+1.71}_{-1.70}$ (syst)
$\cos\theta_{p_{b,t},p}^{RFp\Sigma^0}$	18.46 ± 0.94 (stat) $^{+1.68}_{-1.67}$ (syst)
$\cos\theta_{p_{b,t},K^+}^{RFK\Sigma^0}$	18.44 ± 0.78 (stat) $^{+1.67}_{-1.67}$ (syst)
$\cos\theta_{p_{b,t},K^+}^{RFK^+p}$	20.66 ± 3.00 (stat) $^{+1.87}_{-1.87}$ (syst)
$\cos\theta_{p,\Sigma^0}^{RFK^+\Sigma^0}$	18.74 ± 0.65 (stat) $^{+1.70}_{-1.69}$ (syst)
$\cos\theta_{p,K^+}^{RFp\Sigma^0}$	18.60 ± 0.65 (stat) $^{+1.69}_{-1.68}$ (syst)
$\cos\theta_{K^+,\Sigma^0}^{RFK^+p}$	18.10 ± 0.63 (stat) $^{+1.64}_{-1.63}$ (syst)

Table 10: The extracted total production cross section from the different differential distributions.

compatible with the value obtained by the phase space parameterization presented in Tab. 1. The $p + p \rightarrow p + K^+ + \Lambda$ was determined by the HADES collaboration to be [15]:

$$\sigma(p + K^+ + \Lambda)[\mu\text{b}] = 35.26 \pm 0.43(\text{stat})_{-2.83}^{+3.55}(\text{syst}) \pm 2.67(\text{normalization}) - 2.86(\text{background})$$

Based on the cross sections, the ratio $\sigma(pK^+\Lambda)/\sigma(pK^+\Sigma^0)$ is 1.73 ± 0.31 . The obtained ratio is in agreement with the high energy limit of 2.2 that is measured experimentally for $\epsilon > 700$ MeV [5].

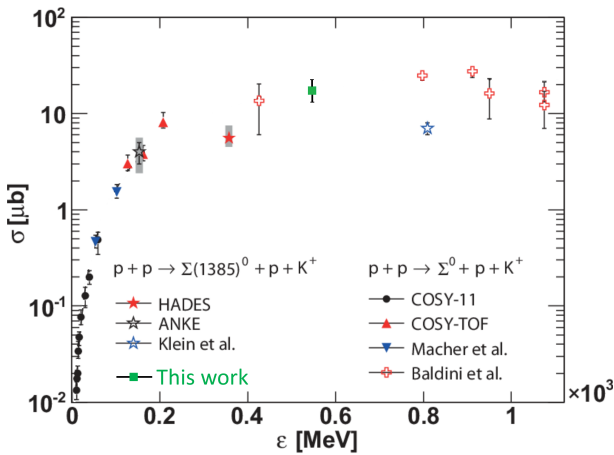


Figure 71: Compilation of cross sections from different experiments. The calculated production cross section of $p + p \rightarrow p + K^+ + \Sigma^0$ is shown by the green square.

4.6 INVESTIGATION OF THE Y^* RESONANCE REGION

In this section we investigate the high mass region of $MM(pK^+)$. The mass region where $MM(pK^+) > 1.2 \text{ GeV}/c^2$ is sensitive to the excited state hyperons Y^* , where Y^* stands for $\Sigma(1385)$, $\Lambda(1405)$ or $\Lambda(1520)$. These resonances have been studied extensively by many experiments including HADES [11, 12], however, the focus here is on the radiative decays of these resonances. The physics motivation to study the radiative transitions of the low lying excited state hyperons will be presented in the next chapter in more detail.

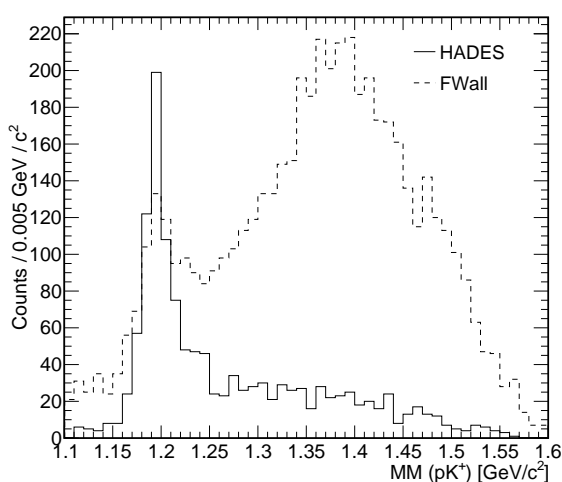


Figure 72: The missing mass of pK^+ after a tighter cut on the missing mass squared of $p\Lambda$ ($MM^2(p\Lambda) > 0.4 \text{ GeV}^2/c^4$) for the HADES (solid line) and the FWall datasets (dashed line).

Since the same final state is discussed here $p + p \rightarrow p + K^+ + (Y^* \rightarrow \Lambda \gamma)$, the signal selection strategy stays the same except for the missing mass cut $MM^2(p\Lambda)$, where a tighter cut is used in order to suppress the contributions from the ground states (Λ and Σ^0), that is $MM^2(p\Lambda) > 0.4 \text{ GeV}^2/c^4$. The resulting spectrum of $MM(pK^+)$ is shown in Fig. 72 for the HADES and the FWall datasets. From Fig. 72 it can be seen that there is a peak structure in the FWall dataset around $(1.350 - 1.400 \text{ GeV}/c^2)$ corresponding to the mass of the $\Sigma(1385)$ resonance. So in order to determine the contributions of the different simulation channels to the spectrum shown in Fig. 72 the fitting procedure explained in section 4.4.1 is utilized again here. However, it is not possible to differentiate between the different decay modes of the resonance Y^* using only the missing mass of pK^+ . Therefore, the fitting procedure is performed simultaneously on

1. $MM(pK^+\Lambda)$
2. $MM(pK^+)$
3. $MM(p\Lambda)$

The different missing mass spectra for the combined data-set (HADES and FWall) after the fit is shown in Fig. 73. It was found from the fit that the peak structure in $MM(pK^+)$ is described mainly by $p + p \rightarrow p + K^+ + \Lambda + \pi^0$ in addition to small contributions from resonant and non-resonant $p + p \rightarrow p + K^+ + \Sigma^+ + \pi^-$ shown by the light blue and cyan histograms, respectively. In a previous measurement the $\Sigma(1385)$ yield was determined from a simultaneous fit of all the simulations to the experimental data in the $\Lambda\pi^0$ decay mode and found to be ≈ 670 events [112]. Since the radiative decay branching ratio is about 1% [121], the expected number of events in the radiative decay mode of the $\Sigma(1385)$ resonance should be $670 \times (1/0.87) \times 0.01 = 8$ events, where $BR(\Sigma(1385) \rightarrow \Lambda\pi^0) = 0.87$. However, the $\Lambda(1405)$ resonance is also contributing in the same region (around $MM(pK^+) \approx 1.4 \text{ GeV}/c^2$), so the number of events due to radiative decays should be larger than 8 depending on the ratio of the cross sections $\frac{\sigma(p+p \rightarrow p+K^++\Lambda(1405))}{\sigma(p+p \rightarrow p+K^++\Sigma(1385))}$ and the branching ratio $BR(\Lambda(1405) \rightarrow \Lambda\gamma)$. The case of $\Lambda(1520)$ is even worse due to the limited statistics in the high mass region $MM(pK^+) > 1.5$.

To give a quantitative description, we assume that the experimental data are described only by background events, i.e. all contributing channels shown in Fig. 73 represented by the filled green histogram expect the radiative decays of excited states. We then rely on statistical methods to assess the validity of this assumption. The approach developed here is to define a *test statistic* or a discrepancy variable that quantifies the agreement between the data and the hypothesis [27]. Based on the argumentation in reference [27], the Pearson χ^2 statistic:

$$\chi_p^2 = \sum_i \frac{(m_i - \lambda_i)^2}{\lambda_i},$$

is defined as a discrepancy variable. Here, the summation runs over the number of bins, m_i represents the number of measured events in bin i , and λ_i are the number of expected events in the bin according to the hypothesis. The observed χ_p^2 can take any value between 0 and ∞ . Rather than using χ_p^2 distribution directly, one uses the p-value as defined in Eq. 28 as it is constructed as the integral over the probability density function (in this case $pdf(\chi_p^2, ndf)$, where ndf is the numbers of degrees of freedom) of the test statistic. A small p-value is an indication that a wrong hypothesis is used for comparison. This is the reason why p-values can be used to discriminate between different hypotheses.

Since we assume that the data are described only by background events, the hypothesis is referred to as the *null hypothesis* H_0 . The search for radiative decays of excited hyperons (signal events) aims to reject the null hypothesis. The χ_p^2 was calculated for each mass bin of the $MM(pK^+)$ separately, and in this case the test statistic probability is referred to as the local p-value [15]. The local p-value is shown in Fig. 74, as can be seen for the

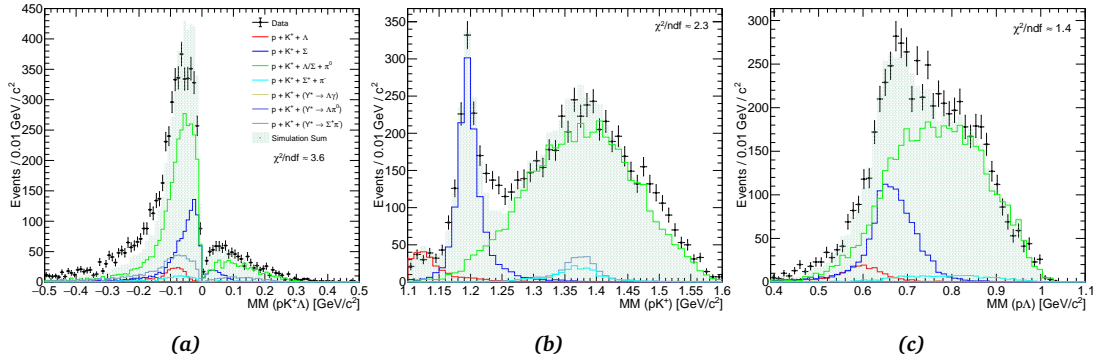


Figure 73: The different missing mass spectra after the fit to the simulation, the reduced χ^2 value is stated for each spectrum, (a) $MM(pK^+\Lambda)$, (b) $MM(pK^+)$ and (c) $MM(pK^+\Lambda)$.

excited hyperon mass range $MM(pK^+) > 1.2$, the local p-value is almost one, which can be interpreted as the data is consistent with the null hypothesis H_0 or in other words, there no evidence for radiative decays up to 3σ confidence level assuming that the data is described by the simulation sum (the green filled histogram).

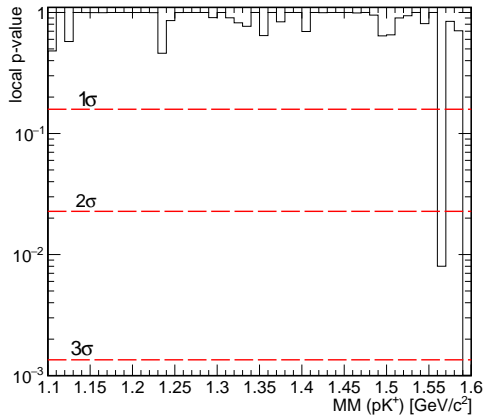


Figure 74: Local p-value as function of the $MM(pK^+)$. Large p-value is an indication that the data is consistent with the assumed hypothesis, which in this case the null hypothesis H_0 . The red dashed lines indicate the confidence levels.

4.7 SUMMARY

The exclusive analysis of the reaction $p + p \rightarrow p + K^+ + \Sigma^0$ at a beam kinetic energy of 3.5 GeV has been presented. The daughter photon of the Σ^0 was identified as a missing mass and the Λ intermediate hyperon was reconstructed separately within the HADES acceptance and the FWall acceptance. A kinematic refit was applied by constraining the secondary proton and the pion equal to the Λ mass and the overall missing mass to the photon mass, this helped to remove considerable amount of background and improved the mass resolution of the Σ^0 . In total, 2613 Σ^0 events were reconstructed 58% are within the HADES acceptance and 42% within the FWall acceptance. Furthermore, the

dynamics of the reaction $p + p \rightarrow p + K^+ + \Sigma^0$ were investigated. For this purpose, the angular distributions in the CMS, G-J and helicity-frames were studied. The phase space simulations was weighted by the angular distribution of the Σ^0 in the CMS and the G-J angle of the proton in the $p\Sigma^0$ reference frame in order to match the experimental data. Afterwards, these simulations was used for the acceptance and efficiency corrections. All the angular distributions have been corrected using the inverse of the detector response matrix calculated by the SVD factorization method.

The corrected CMS distributions of the Σ^0 and the proton show anisotropies, where in the case of the proton is more pronounced, which is the expected behavior if pion exchange dominates the particle production process. In addition, the helicity angular distributions are far different from isotropy, which indicates that Σ^0 production is procced via resonant production in addition to the pure phase space. The influence of different N^* resonances has been tested by means of an incoherent sum of the phase space and N^* contributions. It was found that phase space, $\Delta^*(1900)$, $N^*(1880)$, $N^*(1710)$ and $N^*(1895)$ have contributions 31%, 55%, 4.3%, 6.7% and 3%, respectively.

A partial wave analysis using BG-PWA has been performed for the $pK^+\Sigma^0$ final state. The BG-PWA determines the contribution of different partial waves to the $pK^+\Sigma^0$ production. The non-resonant waves were constructed by combining the proton and the hyperon into a two-particle sub-system $p\Sigma^0$ and then the kaon was combined to this sub-system $(p\Sigma^0)-K^+$. The nucleon resonances with a measured branching ratio to the $K^+\Sigma^0$ have been included as resonant components. Multiple fits have been performed by and the fit quality is calculated based on the log-likelihood value. The best solution was obtained by including the initial proton-proton waves 1S_0 , 3P_0 , 3P_1 , 3P_2 , 1D_2 and 3F_2 with log-likelihood value -333.65. Due to the limited statistics, it was not possible to obtain the exact contributions of nucleon resonance. However, resonances with mass around $1.710 \text{ GeV}/c^2$ ($N^*(1710)$) and $1.900 \text{ GeV}/c^2$ ($N^*(1900)$ or $\Delta^*(1900)$) is certainly required by the fit.

The total production cross section of the Σ^0 hyperon was obtained by integrating the yield for the different angular distributions and found to be $\sigma[\mu b] = 18.74 \pm 1.01(stat) \pm 1.71(syst)$ and the ratio $\sigma(pK^+\Lambda)/\sigma(pK^+\Sigma^0)$ found to be 1.73 ± 0.31 .

A search for radiative decays of excited hyperons has been performed by calculating the Pearson χ^2 test statistic and the corresponding local p-value for the missing mass spectrum $MM(pK^+)$. It was found that the data supports the null hypothesis H_0 up to 3σ . A measurement of the radiative decays provides information about the baryon wave function. Therefore, this measurement is important to understand the internal structure of hyperons. The next chapter presents a feasibility study o measure radiative hyperon decays with the upgraded HADES setup for the upcoming p+p experiment at a beam kinetic energy of 4.5 GeV.

FEASIBILITY STUDY FOR RADIATIVE DECAYS OF EXCITED HYPERONS

This chapter presents a feasibility study for the radiative decay of excited hyperons produced in p+p collisions at beam energy 4.5 GeV using the upgraded HADES detector setup. These Electromagnetic decays (EM) provide considerable information on the underlying structure of hyperons since it offers a clean probe of the initial and final state wave functions. The quark model predicts the EM properties of the ground state hyperons (e.g., $\Sigma^0 \rightarrow \Lambda\gamma$) reasonably well; however, it is less successful in understanding the EM properties of excited states [84, 45]. Several other theoretical approaches have been proposed to give more accurate predictions of these transitions. Therefore, measuring EM decays provides a means of discriminating between different theoretical models.

This chapter is organized as follows: The first section gives an overview of the FAIR Phase-0 physics program and the upgrade of the different subsystems of the HADES detector setup. In particular, the installation of the new electromagnetic calorimeter and forward detector. The second section presents the theoretical aspects of the radiative decays of excited state hyperons. The third section explains the signal and background simulations and the selection strategy used to reconstruct the signal. The fourth section describes the application of the kinematic refit technique to reduce the contamination of background events containing π^0 . The last section gives the expected count rates of the upcoming scheduled proton beam time at a kinetic energy 4.5 GeV.

5.1 FAIR PHASE-0 AND THE HADES UPGRADE

5.1.1 FAIR Phase-0 Physics Program

Future HADES operation within the new FAIR facility, will enable measurements with proton beam energies up to 29 GeV. The proton beam physics program of the FAIR

Phase-0 covers different aspects of the strong interaction in the non-perturbative regime. HADES has already studied p+p and p+Nb collisions at 3.5 GeV. Yet, many of the interesting observations made so far, hadronic decays of hyperons, ω production, and Σ^0 production presented in the previous chapter, suffer from poor statistical significance or call for further multi-differential analyses. In addition, an analysis of the contribution of nucleon resonances to different final states, including the effect of interference among broad resonances should be repeated to establish a solid reference. Runs with higher proton beam energy (4.5 GeV) will enable detailed studies of the excitation function of multi-strange baryon production, excited hyperons and for the first time measurements of Dalitz decays, which are complementary to the planned studies of hyperon production in proton-antiproton collisions with the $\overline{\text{P}}\text{ANDA}$ setup.

The physics program of the FAIR phase-0 with a proton beam is summarized in the following [9]:

Hyperon EM decays $Y^ \rightarrow \gamma\Lambda$ and $Y^* \rightarrow \gamma^*\Lambda$*

Measurements of the EM decays of excited hyperons provide an important insight into their structure. The baryon structure can be probed by measurements of the electromagnetic Transition Form Factors (eTFF), which are in general a function of the four momentum transfer q^2 of the virtual photon exchanged between the initial and final state baryon. The eTFF are often studied in scattering experiments (space-like domain where $q^2 < 0$), or in Dalitz decays $Y^* \rightarrow \Lambda(\gamma^* \rightarrow e^+e^-)$ (time-like domain where $q^2 > 0$). The case where $q^2 = 0$ corresponds to radiative decays or the emission of real photons $Y^* \rightarrow \gamma\Lambda$. Results published by HADES for the $\Delta(1232)$ baryon [7] indicate a significant role for an intermediate ρ vector meson, in agreement with the Vector Meson Dominance (VMD) model [107].

Differential studies of the decay width as a function of q^2 and the angular distribution of the leptons would enable the magnetic and electric transition form factors of the radiative decays to be measured. Hence, results from HADES on both real and virtual photon decays will have significant impact on the understanding of the structure of hyperons in the region of small q^2 .

Hyperon hadronic decays

Hyperon hadronic decays provides a complementary approach to investigations of hadron structure with electromagnetic decays. An important question is whether the $\Lambda(1405)$ is a conventional three-quark state, it has been suggested to be a resonance with two poles: one below the KN threshold and the other in the $\Sigma\pi$ system or as

a molecular state [71]. Previous HADES measurement of the $\Lambda(1405)$ line-shape in the $\Sigma^\pm\pi^\mp$ channels observed a dominance of the $\Sigma\pi$ pole [12]. Therefore, a high-precision measurement of the $\Lambda(1405)$ line-shape could give clear understanding of the resonance structure. The hadronic decay channel $\Lambda(1520) \rightarrow \Lambda\pi^+\pi^-$ constitutes an important benchmark for the Dalitz branching fraction measurements, and provides complementary constraints for VMD tests.

Finally, extensive studies of other excited hyperons decaying into various hadronic final states give a more complete picture of the hyperon spectrum.

Double strange production

The production of double strange hyperons is of particular importance to understand the properties of hot and dense nuclear matter. The excess production of Ξ s in cold nuclear matter has several implications for the interpretation of heavy-ion data, since its origin seems to be present in the elementary channels such as p-p.

The measurement of double Lambda production $\Lambda - \Lambda$ addresses the important topic of baryon-baryon correlations. These correlations constrain the rather poorly known hyperon-hyperon interaction, which has a key role in $\Lambda - \Lambda$ double hypernuclei, neutron stars core studies and the Ξ^- production mechanism [66]. The proposed measurement will complement upcoming studies of the $\Lambda\bar{\Lambda}$ by the $\overline{\text{P}}\text{ANDA}$ collaboration [120].

5.1.2 *HADES Upgrade*

With the start of the FAIR Phase-0 program, most of the detector subsystems will have reached an age of about 17 years, so in order to prepare for the new experimental challenges, the HADES setup will upgrade or replace several subsystems. These consist of the upgraded RICH, MDC, DAQ and the Forward Resistive Plate Chamber (FRPC), as well as a new START detector, an inner TOF detector, an Electromagnetic Calorimeter (EMC) and the Forward Detector (FD).

For the start time t_0 determination, dedicated and newly developed sensors based on Low Gain Avalanche Detector (LGAD) [117] technology will be used, it has an excellent time resolution of 53 ps, measured using a proton beam of kinetic energy 1.92 GeV [9].

The RICH photon detector is replaced by an arrangement of multi-anode photo multiplier tubes with blue-enhanced high quantum efficiency photo cathodes. The RICH upgrade increases the mean number of photoelectrons per ring, and thus increases the dilepton efficiency by a factor 3 [9].

A new segmented plastic TOF hodoscope called inner TOF will be placed in front of the first MDC layer of HADES and will cover the 6 MDC sectors, each module includes three separate plastic scintillator plates with a nominal thickness of 6.4 mm, that are read out by SiPMs. This will be used as a trigger detector to reduce the trigger rate originating from background in proton induced reactions [69].

The Electromagnetic Calorimeter

The addition of an electromagnetic calorimeter (EMC) to HADES will allow to study new reaction channels involving e.g. the production of neutral mesons, neutral hyperons (e.g., Σ^0 or $\Sigma(1385)$ resonances) in elementary and heavy-ion reactions via photon measurements. The new EMC replaces the Pre-Shower detector and is based on lead glass modules recycled from the OPAL experiment [119]. It is divided into 6 sectors, and it will cover forward polar angles of $15^\circ < \theta < 45^\circ$ and almost the full azimuthal angle.

In addition to photon identification, the installation of the EMC will have the advantage of improving the electron/pion separation at large momenta. A full GEANT simulation shows that the single photon efficiency for p+p collision is on average 80% and photon energy resolution $\approx 6\%/\sqrt{E}$ [119]. The EMC layout is shown in Fig. 75. Detailed information of the installed EMC can be found in [119].

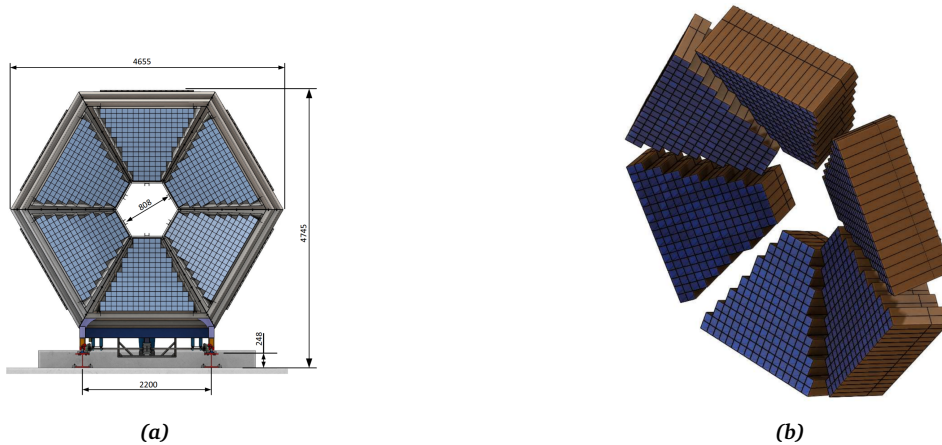


Figure 75: (a) Front view of the EMC, dimensions measured in millimeters. (b) 3D arrangement of the EMC modules [119].

The Forward Detector

Chapter 4 pointed out the importance of the detection of forward going particles, especially for the reconstruction of excited hyperons. To extend the acceptance of the

HADES Spectrometer towards lower polar angles $0.5^\circ < \theta < 7^\circ$, a dedicated Forward Detector (FD) has been installed with almost the full azimuthal coverage. It consists of two Straw Tracking Stations (STS1, STS2) developed by the Jülich and Krakow groups and are based on instrumentation developed for the \bar{P} ANDA forward tracker [115, 116]. In addition, a Forward Resistive Plate Chamber (FRPC) detector has been installed for time of flight *tof* measurements. The tracking stations and the FRPC are placed downstream of the target as shown in Fig. 76. The STS1 and STS2 each consist of four double-layers. The STS1 double layers are aligned with respect to the vertical direction by an inclination of 0° , 90° , 90° and 0° , respectively, while the STS2 double layers are rotated by 90° , 0° , $+45^\circ$ and -45° , respectively. This configuration allows for an unambiguous reconstruction of multi-track events. The straw tubes are operated with a gas mixture of $ArCO_2$ (90:10) at 2 bar absolute pressure. The operating voltage of the anode wires is 1800 V. The spatial resolution of individual straw tubes has been measured to be about $\sigma = 0.13$ mm for minimum ionizing protons and the efficiency is measured to be above 95%. The FRPC detector consists of individually shielded hybrid (metal glass) strip-like RPC counters, which consist of three aluminum electrodes (2 mm thick) and two glass electrodes (1 mm thick). The time resolution of the FRPC detector is expected to be better than 100 ps [9].

The combination of the *tof* measurement from the FRPC with the reconstructed track information from the straw tracking stations STS1 and STS2 will enable the momentum of the particles to be calculated.

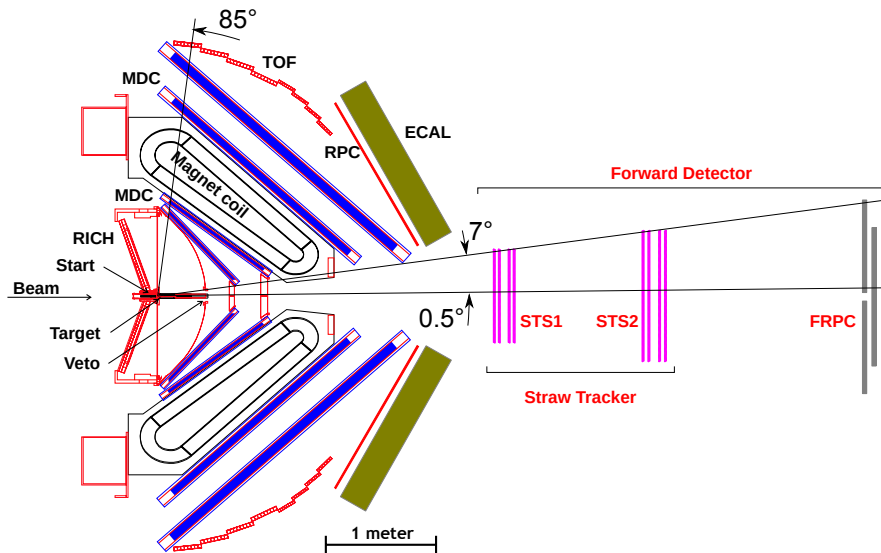


Figure 76: Schematic cross sectional view of the upgrade HADES detector setup including the EMC and the FD [9].

For the purpose of the feasibility study presented here, the track reconstruction in the FD is a rather simple algorithm and proceeds in two steps: a low resolution LR mode and a high resolution HR mode. In the LR mode only the straw anode coordinates are

used and all hits from the same straw double-layer are grouped into clusters of one or two hits, then all combinations of clusters from all layers are fit with straight lines where the wrong combinations are rejected based on the χ^2 value. The track is then matched to a hit in the FRPC. In the HR mode, the *tof* from the FRPC is used to calculate the distance of closest approach of the track to the anode wire from the drift time in the individual straw tubes [9].

The simulations were done assuming a beam intensity of 7.5×10^7 p/s and a beam kinetic energy of 4.5 GeV. The beam is incident on the 4.6 cm long HADES LH_2 target, corresponding to 0.8% interaction rate, which was used previously for proton beam experiments in HADES. These conditions correspond to an instantaneous luminosity of $\mathcal{L} = 1.5 \times 10^{31} \text{cm}^{-2}\text{s}^{-1}$. The data trigger requires a multiplicity of at least three charged particles (M3) to be registered in the inner TOF system [9]. The current HADES DAQ system can readout a maximum trigger rate of 50 kHz, which is the expected rate of the running conditions mentioned above.

5.2 PHYSICS MOTIVATIONS

Measuring the excited as well as ground state baryon masses and studying the various transitions provides valuable information on the dynamics of non-pQCD. In particular, the electromagnetic decays provide a clean probe of the baryon wave function. Here the focus is on the low lying excited state hyperons $\Sigma(1385)$ ($J^P = \frac{3}{2}^+$), $\Lambda(1405)$ ($J^P = \frac{1}{2}^-$) and $\Lambda(1520)$ ($J^P = \frac{3}{2}^-$). In particular, $\Lambda(1405)$ is a very interesting state since its wave function cannot be described by q^3 baryonic structure [87] and does not fit into the quark model. As an alternative, a bound state of nucleon and anti-kaon $\bar{K}N$ ($\bar{q}q^4$) has been proposed. Another interesting behavior is the EM transitions between an octet baryon and a decuplet baryon (e.g. $\Sigma(1385) \rightarrow \Lambda\gamma$), which are related to the magnetic transition form factors. One of the strong motivations to study the $\Sigma(1385) \rightarrow \Lambda\gamma$ transition is to clarify the role of the meson cloud dressing, which is of fundamental importance, as explained in [99]. The radiative decay hierarchy of lower lying excited state hyperons is shown in Fig. 77.

Within the framework of the Isgur-Karl non-relativistic quark model (NRQM) [77], the low lying excited state hyperons are simple three quark states q^3 and the wave functions can be written as [45]:

$$\begin{aligned} |\Sigma(1385)\rangle &= |\Sigma_{10}, {}^4S_S\rangle \\ |\Lambda(1405)\rangle &= 0.90 |\Lambda_1, {}^2P_M\rangle + 0.43 |\Lambda_8, {}^2P_M\rangle - 0.06 |\Lambda_8, {}^4P_M\rangle, \\ |\Lambda(1520)\rangle &= 0.91 |\Lambda_1, {}^2P_M\rangle + 0.40 |\Lambda_8, {}^2P_M\rangle - 0.01 |\Lambda_8, {}^4P_M\rangle \end{aligned}$$

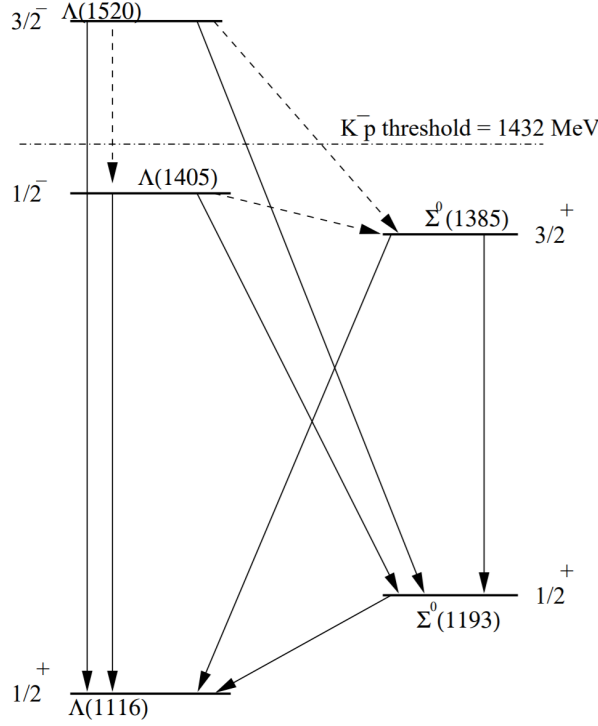


Figure 77: Radiative decays of the lower lying excited state hyperons. The transitions shown by dashed lines are suppressed or very rare in most models [122].

using the notation $|X_M, {}^{2J+1}L_\sigma\rangle$, where M is the SU(3) multiplet, J is the total spin, L is the orbital angular momentum and σ is the SU(6) permutation symmetry. Using the wave functions defined above, the radiative decay widths and amplitudes can be calculated by assuming that the photon is radiated through the de-excitation of a single quark. In the non-relativistic limit the radiative width is given by [48]:

$$\Gamma = 2\pi \frac{m_f}{m_i} \frac{k^2}{(2\pi)^3} \frac{4\pi}{2J_i + 1} \sum_{M_i\lambda} |A_{M_i\lambda}|^2$$

$$H_{int} = \left(\frac{2\pi}{k}\right)^{1/2} \left[-\frac{e_j}{m_j} \vec{p}_j \cdot \vec{\epsilon}_\lambda^*(\vec{k}) + i \frac{e_j}{m_j} \vec{s}_j \cdot \vec{k} \times \vec{\epsilon}_\lambda^*(\vec{k}) \right] e^{-\vec{k} \cdot \vec{r}_j},$$

where e_j is the charge, m_j is the mass, s_j is the spin and \vec{p}_j is the momentum of the j^{th} quark. The $\vec{\epsilon}_\lambda^*(\vec{k})$ is the photon polarization vector, \vec{k} is the photon momentum, λ is the photon helicity and M_i is the z-component of the angular momentum of the decaying baryon. Finally $A_{M_i\lambda}$ is the matrix element of the interaction Hamiltonian H_{int} between the initial and final states.

However, the simple assumption of the wave function of hyperons within the quark model does not reproduce the experimental radiative decay widths. Therefore, several theoretical models have been proposed to understand the hyperon wave functions, which

includes the NRQM [77, 45, 48], the Relativized Constituent Quark Model (RCQM) [129], the MIT bag model [48], the algebraic model of hadron structure [31] and the calculations within the framework of the Heavy Baryon chiral Perturbation Theory (HB χ PT) [36]. The predictions of the various models can vary significantly making it experimentally tractable to rule out certain models. Consequently, the radiative transitions provides a means of differentiating between these models. Tab. 11 summarizes the theoretical predictions of the proposed models and the experimental values measured by the CLAS collaboration [122].

Model	$\Sigma(1385) \rightarrow \Lambda\gamma$	$\Lambda(1405) \rightarrow \Lambda\gamma$	$\Lambda(1520) \rightarrow \Lambda\gamma$
NRQM	263	200	156
RCQM	267	118	215
MIT Bag	152	60	46
Algebraic model	221	117	85
HB χ PT	290-470	-	-
CLAS Experiment	$479 \pm 120^{+81}_{-100}$	-	$176 \pm 43^{+26}_{-12}$

Table 11: EM transition $Y^* \rightarrow \Lambda\gamma$ decay widths in keV as predicted by the NRQM [45, 48], the RCQM [129], the MIT Bag model [48], the algebraic model of hadron structure [31], and the (HB χ PT) [36]. The last row shows the experimental values measured by the CLAS collaboration [122].

5.3 SIGNAL RECONSTRUCTION STRATEGY

In this section the signal simulation and the reconstruction strategy used to select signal events are described. The focus of this thesis is on the exclusive reaction $p + p \rightarrow p + K^+ + (Y^* \rightarrow \Lambda\gamma)$, which is generated by PLUTO, where Y^* stands for any lower lying excited state hyperon $\Sigma(1385)$, $\Lambda(1405)$ or $\Lambda(1520)$. The branching fractions of the EM transition is obtained from the CLAS experiment, and are 1.4%, 0.05%, 1.1% for $\Sigma(1385)$, $\Lambda(1405)$, and $\Lambda(1520)$, respectively [122]. The intermediate Λ hyperon is reconstructed from the decay mode $\Lambda \rightarrow p\pi^-$ (BR \approx 64%). The topology of the reaction is shown in Fig. 78.

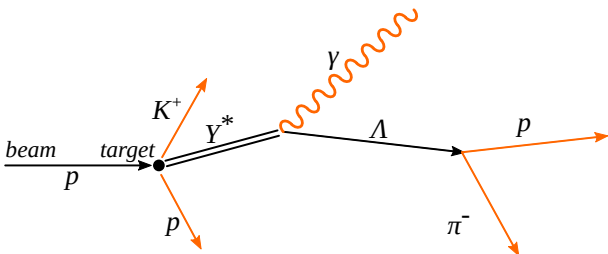


Figure 78: Topology of EM decay for the exclusive reaction $p + p \rightarrow p + K^+ + (Y^* \rightarrow \Lambda\gamma)$. The orange tracks indicate the particles that are used in the event reconstruction [9].

The output of PLUTO is analyzed to estimate the percentage of final state particles within the HADES acceptance and the FD acceptance. Fig. 79 shows the polar angle

distribution of final state particles at the generator level (PLUTO output). Tab. 12 quantifies the percentage of the acceptance values for both HADES spectrometer and the FD. On average 62% of the kaons are within the HADES acceptance, while only 7% are within the FD acceptance. Pions have similar values of about 57% within the HADES acceptance and about 8.5% within the FD acceptance. Primary protons $p_{primary}$ have smaller acceptance of about 44% within the HADES acceptance and 11.5% within the FD acceptance. Of particular interest are the secondary protons $p_{secondary}$ ($Y^* \rightarrow \gamma(\Lambda \rightarrow p_{secondary}\pi^-)$) of which 16.5% of them are within the FD acceptance. This supports the assumption that any forward emitted particle is a proton, since the other particles have a relatively smaller acceptance compared to secondary protons.

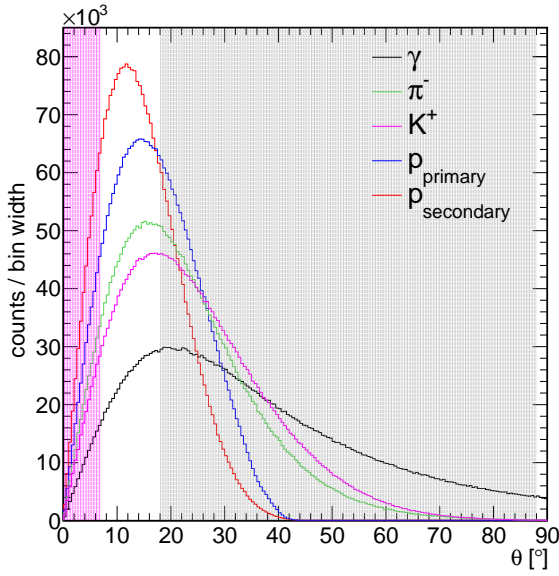


Figure 79: The polar angle distributions of the final state particles at the generator level for the reaction $p + p \rightarrow p + K^+ + (Y^* \rightarrow \Lambda\gamma)$. The gray shaded area represents the HADES acceptance and the pink shaded area shows the FD acceptance.

About 44% of photons from $Y^* \rightarrow \Lambda\gamma$ are emitted within the EMC acceptance ($15^\circ < \theta < 45^\circ$). These numbers are an estimate of the acceptance for a simple phase space distribution. A previous measurement of the $\Sigma^+(1385)$ at the same beam energy [11] shows that the resonance is forward peaked and consequently its decay products $\Sigma^+(1385) \rightarrow \Lambda\pi^+$ are also forward peaked. In this case the importance of the FD will be more pronounced.

	$\Sigma(1385)$		$\Lambda(1405)$		$\Lambda(1520)$	
	HADES	FD	HADES	FD	HADES	FD
π^-	57.0%	8.5%	57.0%	8.6%	56.7%	8.5%
$p_{secondary}$	31.0%	15.6%	30.3%	16.0%	28.0%	18.1%
$p_{primary}$	46.0%	11.0%	45.3%	11.2%	39.7%	12.5%
K^+	63.8%	6.9%	63.3%	7.0%	60.5%	7.6%

Table 12: The acceptance of final state particles of signal events as calculated from the PLUTO output.

In addition to the signal events, a number of background channels could mimic the signal final state or contaminate the signal. The background channels could be classified into two main categories, the first category, includes the multi-pion production channels (e.g. $p + p + \pi^+ + \pi^- + \pi^0$), where one of the protons p and the π^- could introduce a combinatorial background in the intermediate Λ invariant mass distribution. In addition, the π^0 decays to almost 99% into two photons and could introduce a background in the single photon spectrum. The second category, includes the associated strangeness production, for example $p + K^+ + \Lambda + \pi^0$ is the most dominant background channel since one of the photons $\pi^0 \rightarrow \gamma\gamma$ could have a low laboratory energy and escape detection, leaving exactly the same signature of the signal events ($p + K^+ + \Lambda + \gamma$). The cross sections for the background channels have been estimated as explained in chapter 4. The signal cross section is estimated based on previous measurements in the range $2.5 < \sqrt{s}[\text{GeV}] < 6$ by several experiments as explained in [9].

A specific number of events has been simulated for both signal events and background processes, so in order to get the expected number of events for the future 4.5 GeV proton beam run; the different processes are scaled to the expected integrated luminosity using the event weight:

$$w = \frac{\sigma L}{N_{\text{generated}}},$$

where σ is the cross section, $N_{\text{generated}}$ is the number of generated events and L is the integrated luminosity. Assuming 28 days of data taking, L is given by:

$$L = \int_t \mathcal{L} dt = 3,628,800 \mu\text{b}^{-1},$$

where \mathcal{L} is the instantaneous luminosity ($\mathcal{L} = 1.5 \times 10^{31} \text{ cm}^{-2}\text{s}^{-1} = 15 \mu\text{b}^{-1}\text{s}^{-1}$). Tab. 13 lists the signal and background channels that have been simulated with the corresponding cross section and the weight factor.

All channels are generated by PLUTO and then propagated through HGeant for detailed detector simulations including the FD.

The momentum correction procedure explained in the previous chapter is applied here in order to avoid a systematic shift of the missing mass peaks. In addition, this correction is crucial for the kinematic refit applied later since an incorrect momentum could cause unreliable results. Therefore, a momentum correction is applied to all simulated channels. The difference between the reconstructed momentum and the

Channel	σ [μb]	w
$p + p \rightarrow p + K^+ + \Sigma(1385)$	56.2	2.85717
$p + p \rightarrow p + K^+ + \Lambda(1405)$	32.2	0.05842
$p + p \rightarrow p + K^+ + \Sigma(1385)$	70.0	2.79418
$p + p \rightarrow p + p + \pi^+ + \pi^- + \pi^0$	1840	133.540
$p + p \rightarrow p + p + \pi^+ + \pi^- + \pi^0 + \pi^0$	300	217.728
$p + p \rightarrow p + K^+ + \Lambda$	54.4	39.4813
$p + p \rightarrow p + K^+ + \Sigma$	23.5	17.0554
$p + p \rightarrow p + K^+ + \Lambda + \pi^0$	43.0	31.2077
$p + p \rightarrow p + K^+ + \Lambda + \pi^+ + \pi^-$	20.0	14.5152
$p + p \rightarrow p + K^+ + \Lambda + \pi^0 + \pi^0$	10.0	7.25760
$p + p \rightarrow p + K^+ + \Sigma^0 + \pi^0$	20.0	14.5152
$p + p \rightarrow p + K^+ + \Sigma^0 + \pi^+ + \pi^-$	2.0	1.45152
$p + p \rightarrow p + K^+ + K_S^0 + \pi^+ \pi^-$	4.0	2.90304
$p + p \rightarrow p + K^+ + K_L^0$	33.0	23.9501
$p + p \rightarrow p + K^+ + K_L^0 + \pi^0$	13.0	9.43488

Table 13: Signal and background channels simulated with the corresponding estimated cross section and the weight factor.

generated momentum is plotted as a function of the reconstructed momentum for each particle species, then this is fit by a polynomial function, as shown in Fig. 80. The fit function is then used to correct for the momentum of particles.

All signal and background channels are added together after scaling with the corresponding weight factor w .

5.3.1 Particle Identification PID

The first step in the signal reconstruction is the charged particle identification. The PID was only done for particles within the HADES acceptance, any forward going track that hits the FD is assumed to be a proton. The PID was done using a simple feed forward neural network ANN implemented within the PyTorch framework [94]. The ANN is used as a multi-class classifier to distinguish among three particle species, namely p , π^+ and K^+ , the π^- is identified as any negative charged track that is geometrically uncorrelated to a ring in the RICH detector. The network is trained on the following simulated channels:

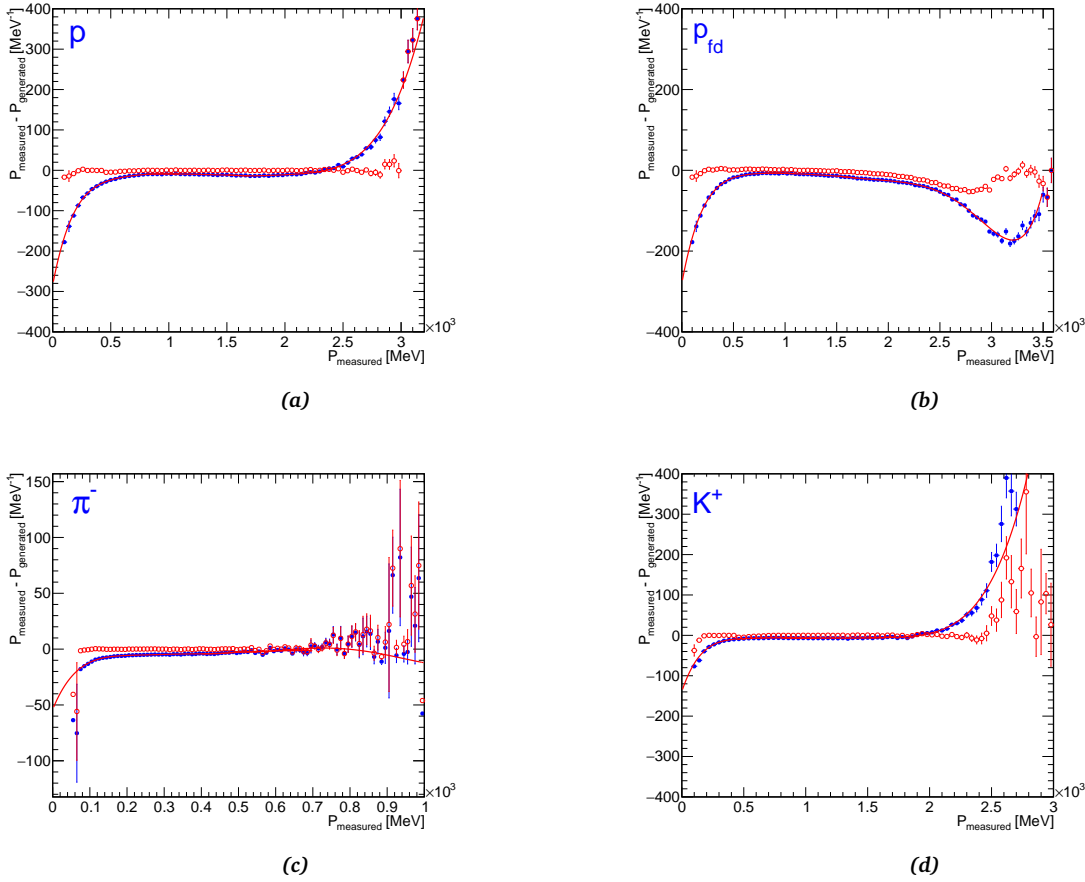


Figure 80: The difference between the reconstructed momentum and the generated momentum as a function of the reconstructed momentum for (a) protons p , (b) protons detected in the FD p_{fd} (c) pions π^- and (d) kaons K^+ . The momentum correction function is shown by the red curve, the red dots shows the particle momentum difference after the correction procedure.

$$p + p \rightarrow p + p + \pi^- + \pi^+ + \pi^0$$

$$p + p \rightarrow p + p + \Lambda$$

$$p + p \rightarrow p + p + \Lambda + \pi^- + \pi^+$$

The data-set is balanced by introducing a weight factor for each class in the multi-class cross entropy loss function. The input layer of the ANN consists of seven neurons corresponding to the number of features, which are the absolute momentum p , the polar angle θ , the azimuthal angle ϕ , the energy loss in the MDC and TOF subsystems and the velocity of the particles β . The distributions of the input features are shown in Fig. 81.

The best validation accuracy was obtained by sequentially combining three fully connected layers. In addition, a 50% dropout to each layer was applied to prevent the

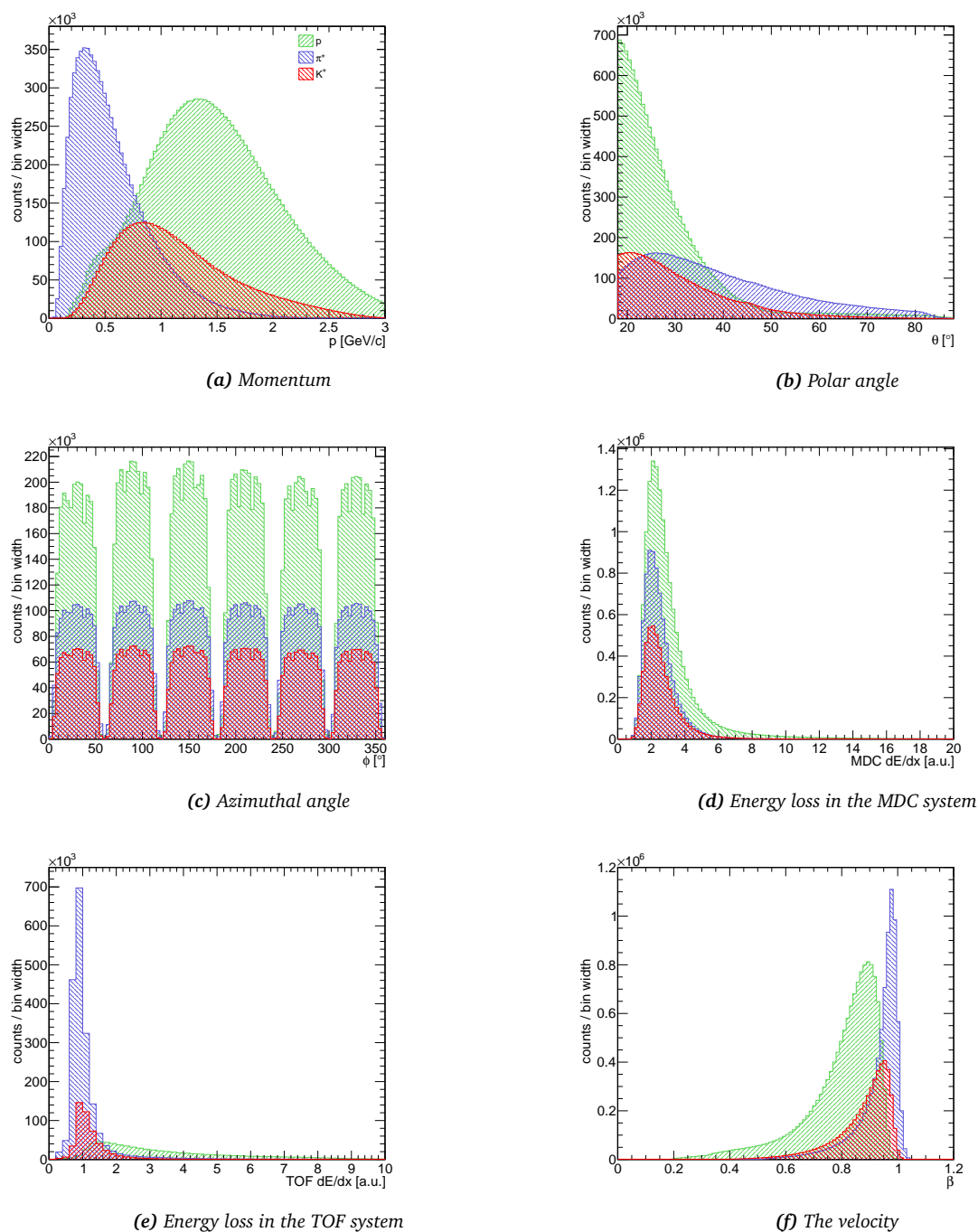


Figure 81: Distributions of input features to the neural network used for the PID. The three classes are the protons (green) and pions (blue) and kaons (red).

model from over-fitting. The network converged quickly and has a classification accuracy of 98%. The confusion matrix and the ROC curve evaluated on a hold-out data-set are shown in Fig. 82a and 82b, respectively. As can be seen the classification accuracy for pions is almost 100%, for protons 99% and 93% for kaons. The selection efficiency and

purity as a function of the phase space variables evaluated on a hold out data-set is presented in Appendix A.

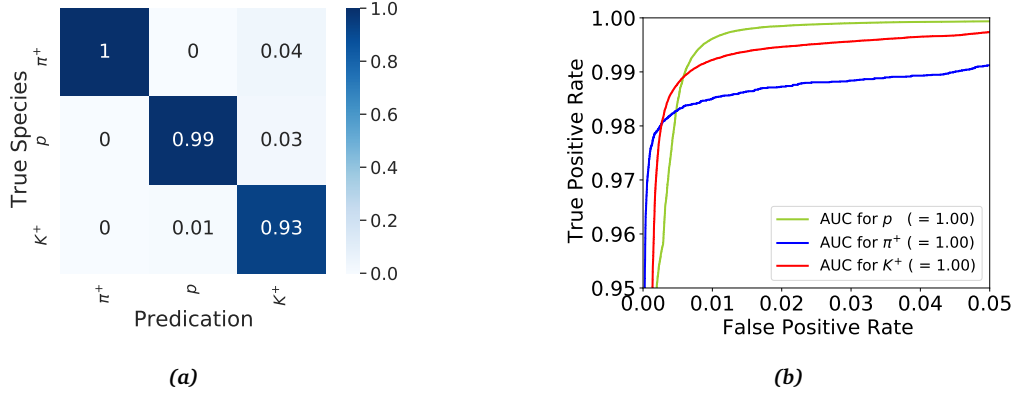


Figure 82: (a) The Confusion matrix. (b) The ROC graph for protons p (green), pions π^+ (blue) and kaons K^+ . The inset shows values of the area under curve AUC for the three classes.

5.3.2 The Λ Hyperon Reconstruction

The procedure followed in chapter 4 for the Λ reconstruction is also applied here. Two data-sets have been identified, the HADES data-set where all final state particles are required to be within the HADES acceptance. The FD data-set, where 1 p , 1 K^+ and 1 π^- are required to be within the HADES acceptance and in an addition, at least one track in the FD acceptance.

HADES data-set

For the HADES data-set, the Λ hyperon is reconstructed by combining its decay products, namely the p and the π^- . The topology of the Λ decay (see Fig. 40) was used to define further off-vertex selection.

First off, for each event, the intersection point or the PCA between the primary proton track p_p and the kaon K^+ track was defined as the primary vertex. Since there is more than one proton per event, the DCA between each proton and the kaon tracks $d(p_p, K^+)$ is calculated as shown in Fig. 83. The proton and the kaon pair that has the smallest DCA are used to construct the primary vertex. Furthermore the primary vertex is required to be located within the target volume $-60 < z[mm] < -5$ and $r[mm] < 5$ as indicated by the dashed lines in Fig. 84. The secondary vertex is defined as the PCA between the proton and the pion tracks.

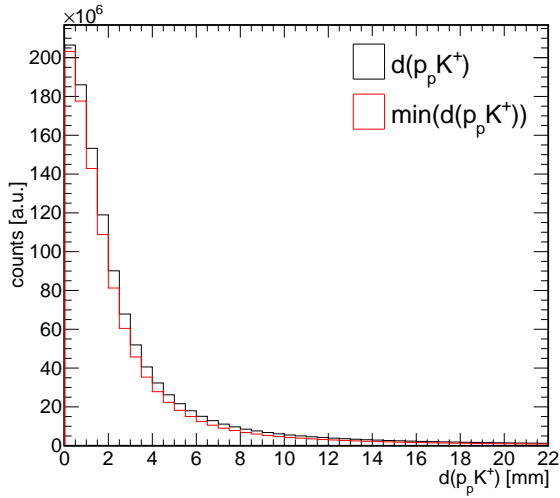


Figure 83: The DCA between the proton and the kaon tracks for all combinations is shown in black and the red histogram shows the distribution of the smallest DCA value in a given event.

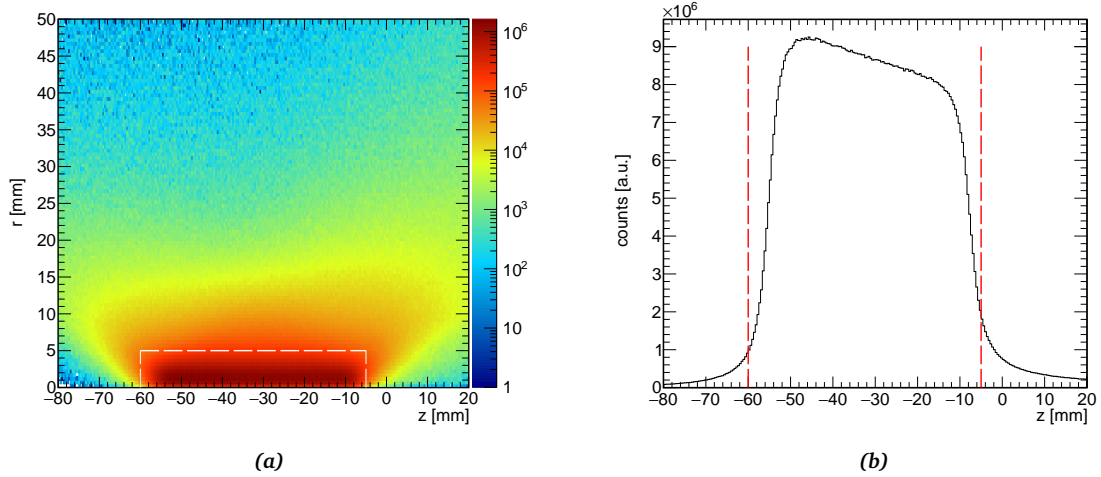


Figure 84: (a) The primary vertex transverse position as function of the longitudinal position. Accepted events are within $-60 < z[\text{mm}] < -5$ and $r[\text{mm}] < 5$ as indicated by the white dashed line. (b) The projection on the z -axis.

After constructing a primary vertex for each event, the following set of topological cuts are applied to select the Λ hyperon:

- The DCA between the p track and the π^- track $d(p, \pi^-)$ is required to be smaller than 15 mm.
- Following momentum and energy conservation, the DCA of the p track and the primary vertex $d(p, pvtx)$ is required to be smaller than the DCA between the π^- track and the primary vertex $d(\pi^-, pvtx)$.

- A pointing vector angle pva is determined by the scalar product of the spatial vector connecting the primary and the secondary vertex with the Λ momentum vector. The pva is required to be smaller than 0.5 rad.

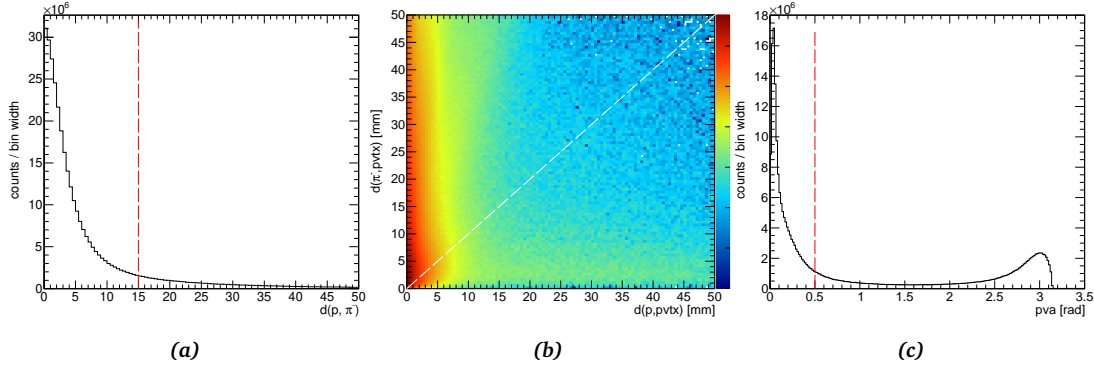


Figure 85: (a) The DCA distribution between the p , and π^- tracks, (b) The DCA distribution between the π^- track and the primary vertex $d(\pi^-, pvtx)$ as a function of the DCA between the p track and the primary vertex $d(p, pvtx)$ and (c) the pointing angle vector distribution.

The distributions of the topological variables are shown in Fig. 85, where the cuts are indicated by the dashed lines. The invariant mass spectrum M_{p,π^-} before and after applying the topological cuts is shown in Fig. 86. An event is further processed if it is in the range $1.108 < M_{p,\pi^-} [GeV/c^2] < 1.122$. The applied cuts improve the S/B ratio from 5.3 to 12.2.

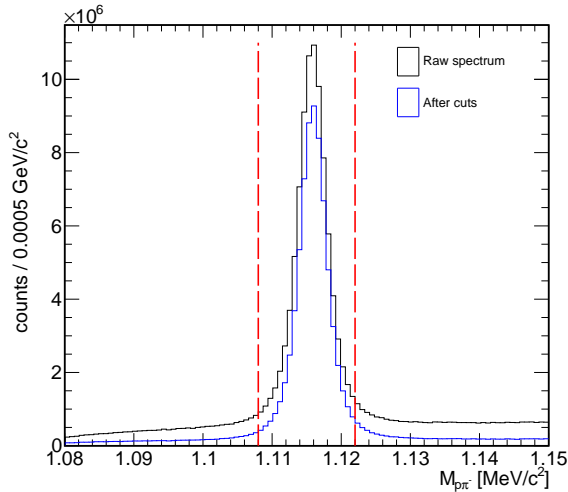


Figure 86: The invariant mass distribution M_{p,π^-} before and after the topological cuts. The dashed lines indicate the accepted region.

The FD data-set

Since the FD is installed in a magnetic field-free region, the FD tracks are reconstructed as straight lines, thus no direct momentum measurement is possible. Instead, for a given

mass hypothesis the momentum of a track can be calculated from the tof measurement provided by the FRPC.

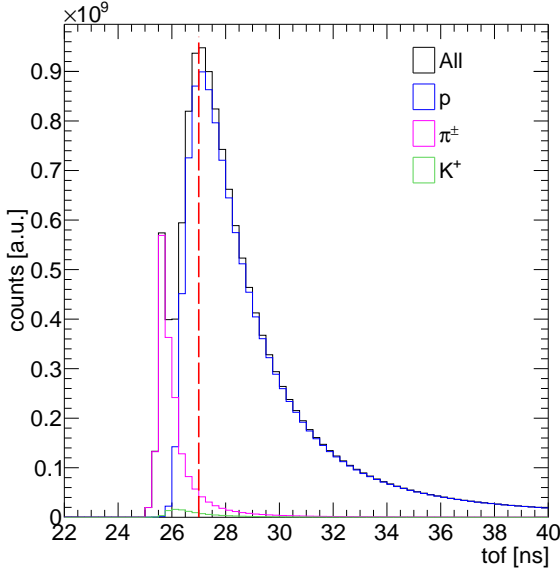


Figure 87: The FRPC tof spectra for different particle species. The cut value is indicated by the dashed line.

Since the secondary proton has the largest probability to be detected in the FD acceptance, therefore, the FD data-set assumes that any track reconstructed in the FD is due to secondary protons stemming from the Λ decay. In order to reduce the contamination from other particles, the FRPC tof is required to be greater than 27 ns , as shown in Fig. 87. This cut suppresses the pion contamination by 84%, kaons by more than 99%, while keeping about 80% of the proton signal.

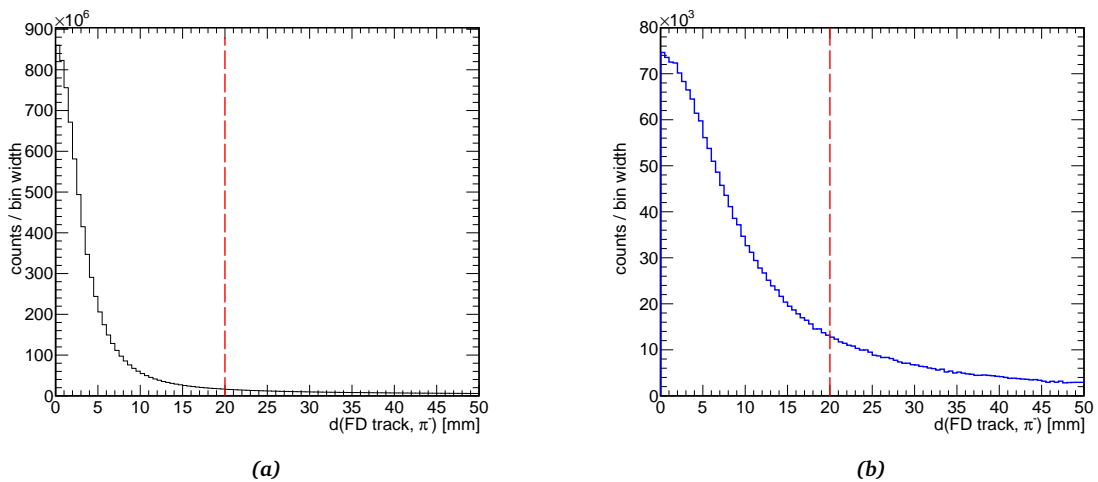


Figure 88: (a) The DCA between the FD proton track and the π^- for all channels and (b) for signal events. The dashed line indicates the cut value.

To reconstruct the Λ in the FD data-set, the DCA between the FD proton track and the π^- track is calculated (see Fig. 88) and any pair that has DCA > 20 mm is rejected. Finally, the FD proton track is combined with the π^- track and the corresponding invariant mass spectrum is shown in Fig. 89. An event is further processed if it is in the range $1.108 < M_{p,\pi^-} [\text{GeV}/c^2] < 1.122$. The applied cuts improve the S/B ratio from 0.47 to 0.95.

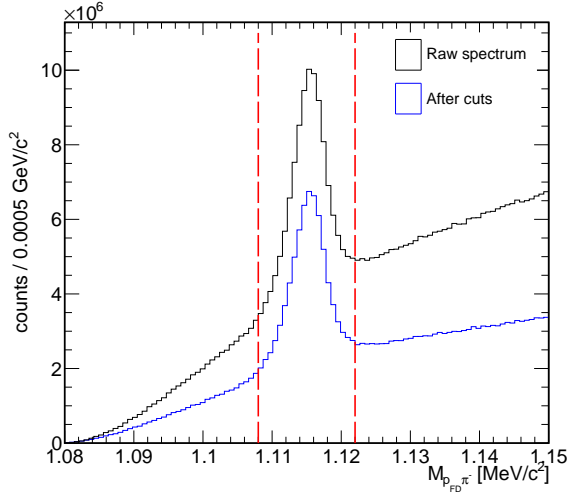


Figure 89: The invariant mass distribution M_{p_{FD},π^-} before (black) and after (blue) the tof and DCA cuts. The dashed lines indicate the accepted region.

5.3.3 Background Suppression

Several background channels could contribute to the final spectrum. In particular, the main irreducible background is the π^0 production through the process $p + p \rightarrow p + K^+ + \Lambda + \pi^0$, when one of the photons $\pi^0 \rightarrow \gamma\gamma$ escapes detection leaving the same observed final state as the signal. So in order to suppress the background, two kinematic variables were introduced:

- The squared missing mass of the primary proton and the kaon is required to be in the excited hyperon production range $1.6 < MM^2(p_p K^+) [\text{GeV}^2/c^4] < 2.6$. As can be seen from Fig. 90 this restriction removes the contribution from the ground state hyperons (Λ and Σ^0) almost completely. In general, this cut suppresses the background by 56% while keeping 93% of the signal.
- The squared missing mass of all final state charged particles should peak at zero since there is a photon in the final state. Thus, this is required to be in the range $-0.04 < MM^2(p_p K^+ \Lambda) [\text{GeV}^2/c^4] < 0.01$. This cut is asymmetric about $MM^2(p_p K^+ \Lambda) = 0$ to reduce contamination from the $p + p \rightarrow p + K^+ + \Lambda + \pi^0$ background, which is peaked at the square of the π^0 mass ($M_{\pi^0}^2 = 0.02 \text{ GeV}^2/c^4$).

The corresponding spectra is shown in Fig. 91. This cut suppresses the background by 70% while keeping 84% of the signal.

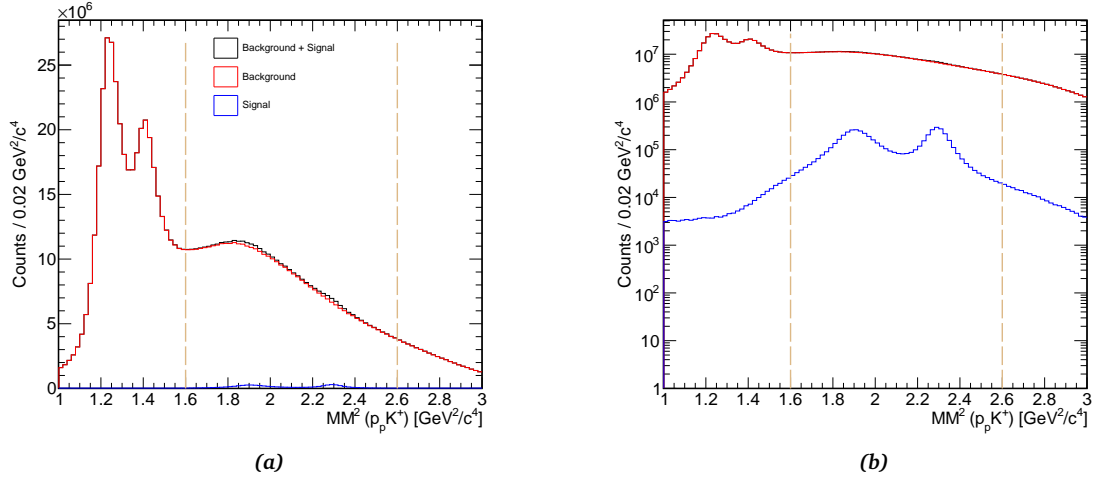


Figure 90: The squared missing mass $MM^2(p_p K^+)$ distribution in (a) linear and (b) logarithmic scale. The black histogram is the sum of the background and the signal simulation, the red histogram is the background and the blue histogram is the signal simulation. The dashed lines indicate the cut range.

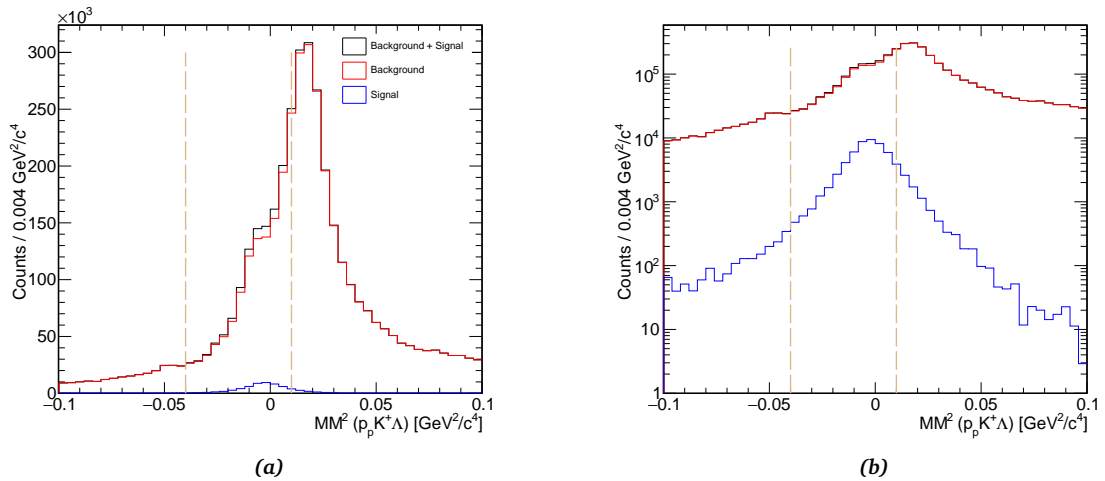


Figure 91: The squared missing mass $MM^2(p_p K^+ \Lambda)$ distributions in (a) linear and (b) logarithmic scale. The black histogram is the sum of the background and the signal simulation, the red histogram is the background and the blue histogram is the signal simulation. The dashed lines indicate the cut range.

5.3.4 Photon Identification

The excited hyperon is reconstructed in the $\Lambda\gamma$ invariant mass. In this study, photon candidates are identified as energy clusters in the EMC, where a cluster is defined as a set of adjacent crystals with an energy deposition above a certain threshold. The position of the cluster provides information on the photon 4-vector [119].

In order to suppress the contribution from charged particles, the cluster is required to be spatially uncorrelated with the charged tracks. In addition, the photon candidates are required to have $0.96 < \beta < 1.04$ as shown in Fig. 92. Since low energy photons can be selected by these cuts, an energy deposition in the EMC cluster above 0.200 GeV is required (see Fig. 91b), which is optimized based on the signal significance (defined as $S/\sqrt{S+B}$) as presented in Fig. 91a. Since S is proportional to the efficiency (ϵ) and B is proportional to $(1-p) \cdot S$ (where p is the signal purity). Therefore, optimizing the significance is equivalent to optimizing $\epsilon/\epsilon(2-p)$.

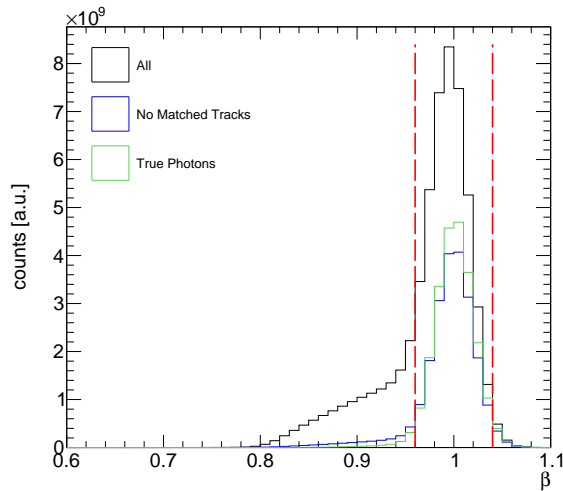


Figure 92: The velocity ($\beta = v/c$) spectrum for all photon candidates (black), photons with clusters that are geometrically uncorrelated with charged tracks (blue) and real photons (green). The red dashed lines indicate the cut range.

The momentum correction procedure introduced for charged particles is again applied to the identified photon candidates. The difference between the reconstructed energy cluster and the generated photon energy is plotted as a function of the reconstructed energy, then this is fit by a polynomial function, as shown in Fig. 94a. The fit function is then used to correct for the energy of the photon candidates. This procedure has the effect of shifting the mass peaks of the resonances into the correct position as seen in the $\Lambda\gamma$ invariant mass distribution shown in Fig. 94b.

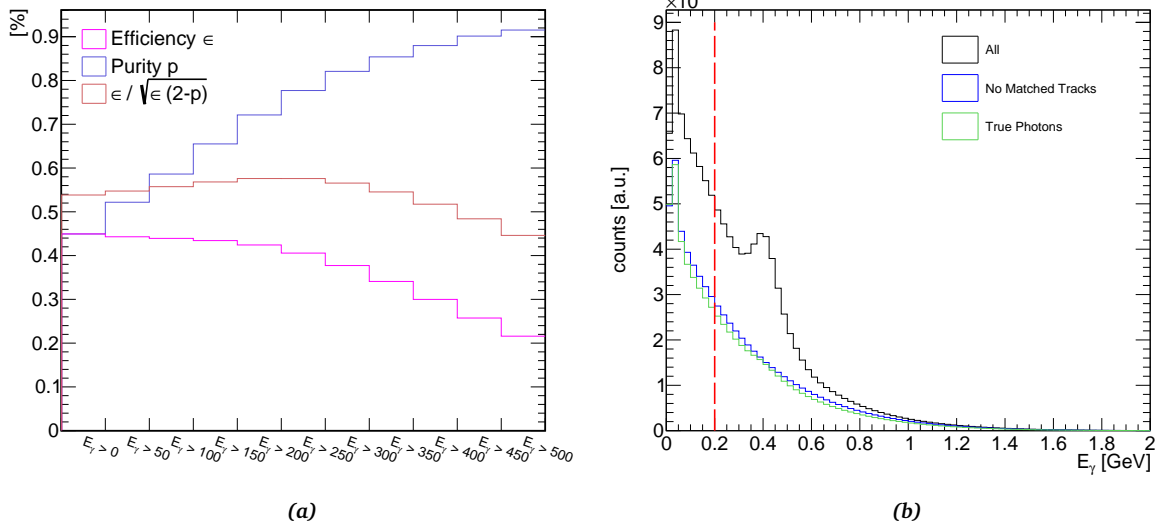


Figure 93: (a) The optimization of the photon energy cut and (b) the reconstructed photon energy for all clusters (black), photons with clusters that are geometrically uncorrelated with charged tracks (blue) and real photons (green). The dashed line indicates the cut value.

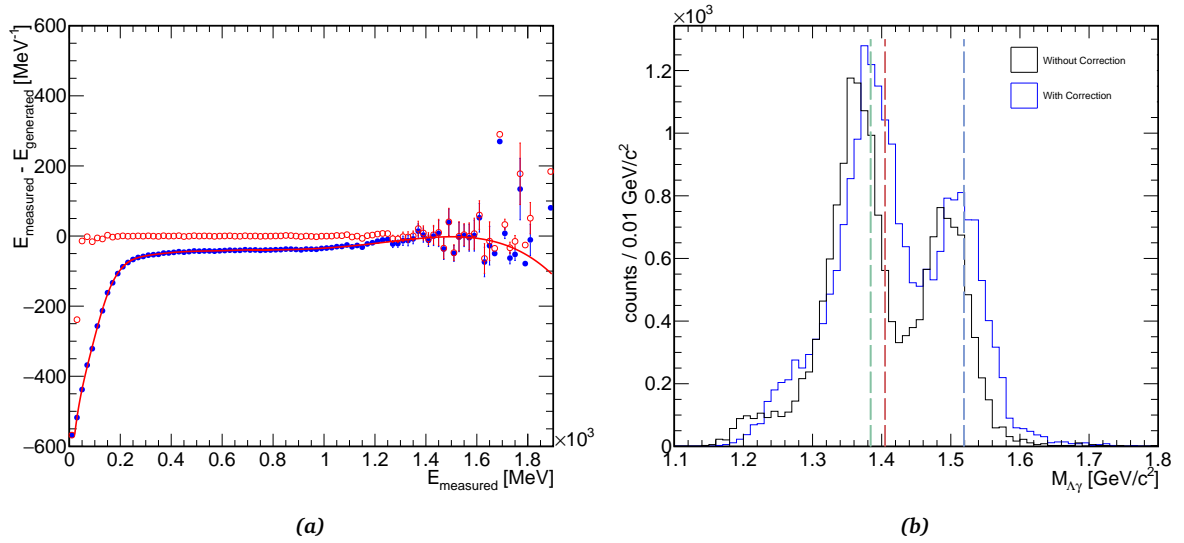


Figure 94: (a) The difference between the EMC cluster energy and the generated photon energy as a function of the cluster energy. The energy correction function is shown by the red curve, the red dots shows the photon energy difference after the correction procedure. (b) The $\Lambda\gamma$ invariant mass distribution of the resonances before (black) and after (blue) the energy correction. The vertical dashed lines indicates the PDG masses of the $\Sigma(1385)$ (green), $\Lambda(1405)$ (red) and $\Lambda(1520)$ (blue).

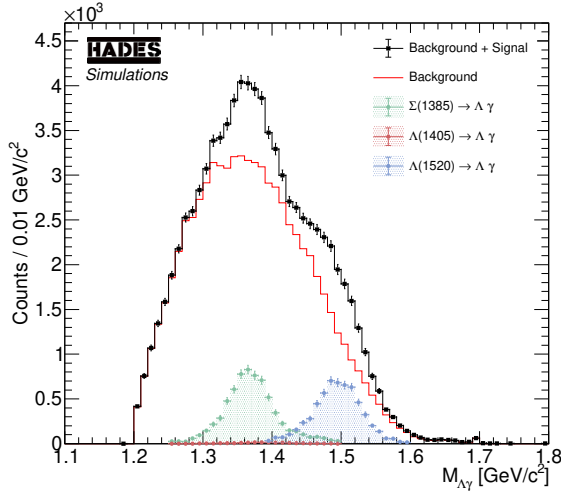


Figure 95: The $\Lambda\gamma$ invariant mass distribution after all cuts. The red histogram is the background contribution and the black histogram is the sum of the background and the signal.

5.4 EXCITED HYPERON Y^* YIELD

After photon identification and the Λ reconstruction, the excited hyperon is reconstructed in the $\Lambda\gamma$ invariant mass distribution and presented in Fig. 95. The background is mostly from the $p + p \rightarrow p + K^+ + \Lambda + \pi^0$ channel as indicated in Tab. 14.

Channel	Without OA cut [%]	With OA cut [%]
$p + p \rightarrow p + p + \pi^+ + \pi^- + \pi^0$	7.25	3.70
$p + p \rightarrow p + p + \pi^+ + \pi^- + \pi^0 + \pi^0$	0.31	0.00
$p + p \rightarrow p + K^+ + \Lambda$	0.34	0.31
$p + p \rightarrow p + K^+ + \Sigma$	0.51	0.20
$p + p \rightarrow p + K^+ + \Lambda + \pi^0$	88.4	94.0
$p + p \rightarrow p + K^+ + \Lambda + \pi^+ + \pi^-$	0.00	0.00
$p + p \rightarrow p + K^+ + \Lambda + \pi^0 + \pi^0$	0.11	0.00
$p + p \rightarrow p + K^+ + \Sigma^0 + \pi^0$	3.03	1.78
$p + p \rightarrow p + K^+ + \Sigma^0 + \pi^+ + \pi^-$	0.00	0.00
$p + p \rightarrow p + K^+ + K_S^0 + \pi^+ \pi^-$	0.00	0.00
$p + p \rightarrow p + K^+ + K_L^0$	0.00	0.00
$p + p \rightarrow p + K^+ + K_L^0 + \pi^0$	0.00	0.00

Table 14: Contributions of the different background channels to the invariant mass spectrum $M_{\Lambda\gamma}$ presented in Fig. 95.

In order to further suppress the contribution from $p + p \rightarrow p + K^+ + \Lambda + \pi^0$ channel, the opening angle between the photon and the Lambda ($OA(\gamma\Lambda)$) is introduced as another discriminating variable. The $OA(\gamma\Lambda)$ is calculated in the rest frame of the excited hyperon defined in this case as the missing particle $p_\gamma = p_{beam} + p_{target} - (p_{primary} + p_{K^+})$, where p_γ is the hyperon 4-vector. In the ideal case, they should be emitted back-to-back,

i.e. $OA(\gamma\Lambda) = 180^\circ$, in reality the $OA(\gamma\Lambda)$ distribution is smeared by the detector resolution. Thus, the opening angle is required to be greater than 165° (see Fig. 96a), which is optimized based on the signal significance. This cut suppresses the background by 53% compared to only 8% for the signal. The $\Lambda\gamma$ invariant mass distribution after the opening angle cut is presented in Fig. 96b.

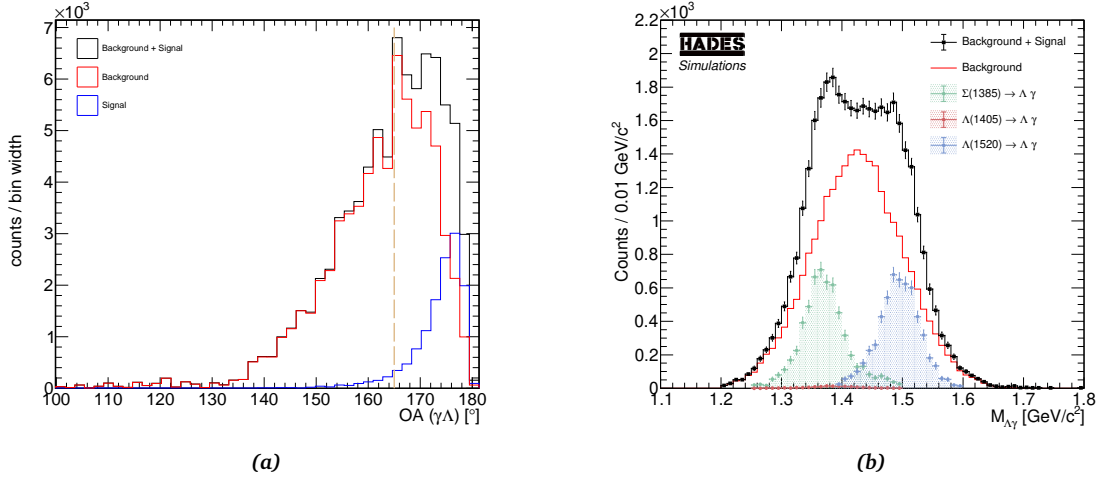


Figure 96: (a) The opening angle between the Lambda and the photon $OA(\Lambda\gamma)$ in the hyperon rest frame and (b) The $\Lambda\gamma$ invariant mass distribution after the opening angle cut ($OA(\Lambda\gamma) > 165^\circ$).

5.4.1 Kinematic Refit

The kinematic refit technique developed in the previous chapter can also be applied here to reject the dominant background from $pK^+\Lambda\pi^0$ events. Since the only difference between signal events and the main background events $pK^+\Lambda\pi^0$ is the π^0 . Therefore, two event hypothesis can be tested by constraining the missing mass of all charged particles in the final state, then the quality of the fit quantified by the χ^2 value can be used to discriminate between the hypotheses.

The track is parameterized in this case by five parameters that can be written as a column vector:

$$y = \begin{bmatrix} 1/p \\ \theta \\ \phi \\ \rho \\ z \end{bmatrix}, \quad (41)$$

where $1/p$ is the inverse of the absolute value of the momentum, θ is the polar angle, ϕ is the azimuthal angle, ρ is defined as the DCA between the track and the beam axis (0,0,1) and z is the z-coordinate of the PCA between the track and the beam axis. This is the default parameterization for the main HADES setup. In the FD acceptance, tracks are reconstructed as straight lines parameterized as $[x \ y \ T_x \ T_y]$, where x, y are two points on the line and T_x, T_y indicates the direction of the line. Therefore, this parameterization is transformed into the one given by Eq. 41.

In the inner MDC, the track is approximated by a straight line, which has the general form

$$l = b + md, \quad (42)$$

where, b is a base vector, d is a direction vector and m is a scalar parameter. In Cartesian coordinates, the base and direction vectors are given by [105]:

$$\begin{aligned} b &= \rho \cos(\phi + \pi/2) \vec{i} + \rho \sin(\phi + \pi/2) \vec{j} + z \vec{k} \\ d &= \sin(\theta) \cos(\phi) \vec{i} + \sin(\theta) \sin(\phi) \vec{j} + \cos(\theta) \vec{k}. \end{aligned} \quad (43)$$

Four constraints have been applied:

1. The invariant mass of the secondary proton (p_s) and the π^- are constrained to have the nominal Λ mass $M_\Lambda = 1.1156 \text{ GeV}/c^2$.
2. The secondary proton and the π^- are constrained to the same vertex.
3. Similar to the previous constraint, the primary proton (p_p) and the kaon tracks to the same vertex.
4. Finally, all final state charged particles p_p, K^+, p_s and π^- are constrained to have a missing mass equal to either the photon mass $M_\gamma = 0$ (the photon hypothesis or the signal hypothesis) or the pion mass $M_{\pi^0} = 0.135 \text{ GeV}/c^2$ (the pion hypothesis or the background hypothesis).

These can be written collectively as:

$$f = \begin{pmatrix} (E_{p_s} + E_{\pi^-})^2 - (P_{p_s} + P_{\pi^-})_x^2 - (P_{p_s} + P_{\pi^-})_y^2 - (P_{p_s} + P_{\pi^-})_z^2 - M_\Lambda^2 \\ (d_{p_s} \times d_{\pi^-}) \cdot (b_{p_s} - b_{\pi^-}) / |d_{p_s} \times d_{\pi^-}| \\ (d_{p_p} \times d_{K^+}) \cdot (b_{p_p} - b_{K^+}) / |d_{p_p} \times d_{K^+}| \\ (E_t + E_b - \sum_{i=1}^4 E_i)^2 - (\vec{p}_t + \vec{p}_b - \sum_{i=1}^4 \vec{p}_i)^2 - (M_\gamma^2, M_{\pi^0}^2) \end{pmatrix} = 0. \quad (44)$$

The kinematic refit is applied on the combined data-set of the HADES and the FD. The χ^2 distribution for the photon and the pion hypotheses are shown in Fig. 97 and the corresponding p-values are shown in Fig. 98. The χ^2 distribution is consistent with $f(\chi^2, \nu)$ with four degrees of freedom ($\nu = 4$).

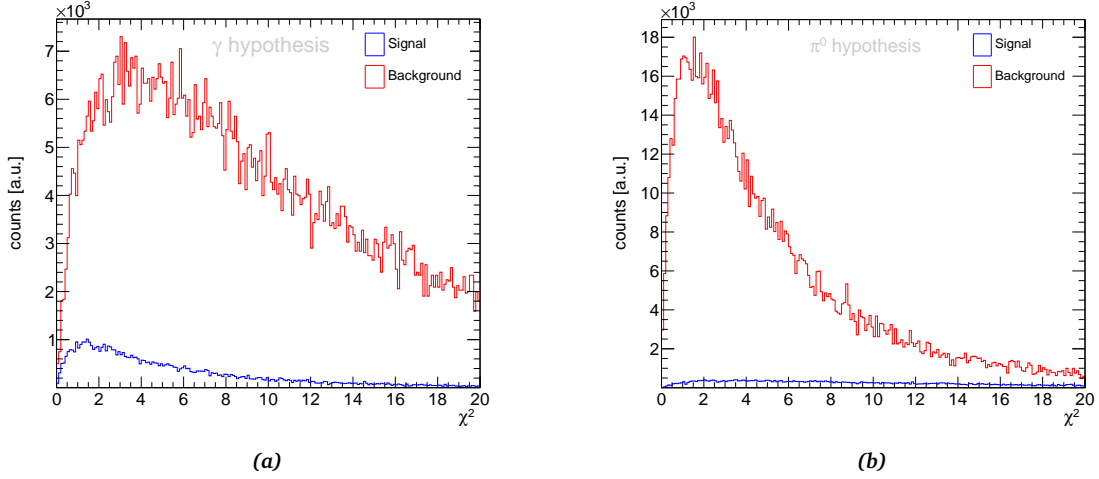


Figure 97: The χ^2 distribution for (a) the photon hypothesis M_γ and (b) the pion hypothesis M_{π^0} . The signal is shown by the blue histogram and the background by the red histogram.

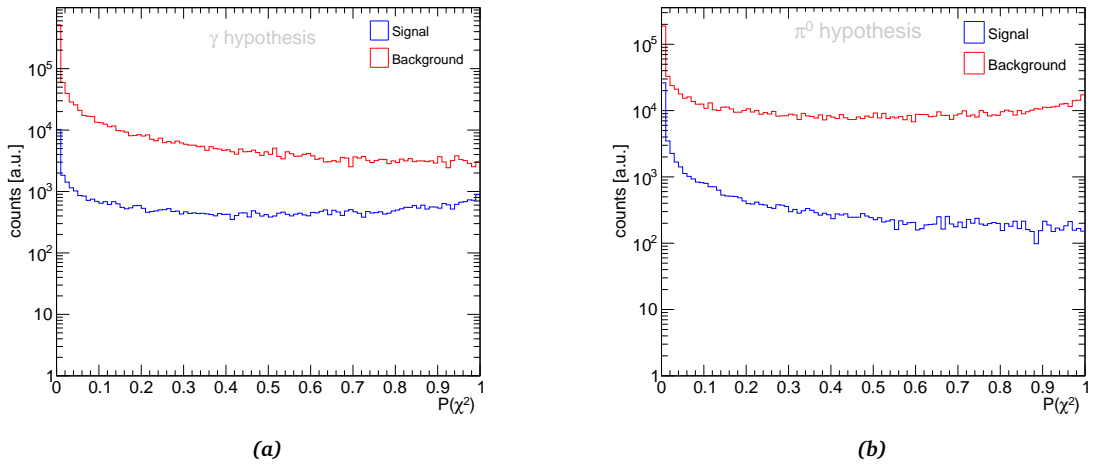


Figure 98: The p-value for (a) the photon hypothesis and (b) the pion hypothesis. The signal is shown by the blue histogram and the background by the red histogram.

The correlation between the p-values of both the photon and pion hypotheses were used as a discriminator variable to select signal events. Since the p-value is limited between 0 and 1, the logarithm of the p-value is shown in Fig. 99 for signal and background events. From Fig. 99 it can be seen that most of the signal events have p-values of the photon hypothesis greater than p-values of the pion hypothesis. Therefore, events are further processed if $P(\chi^2)_\gamma > P(\chi^2)_\pi$, as marked by the black dashed line.

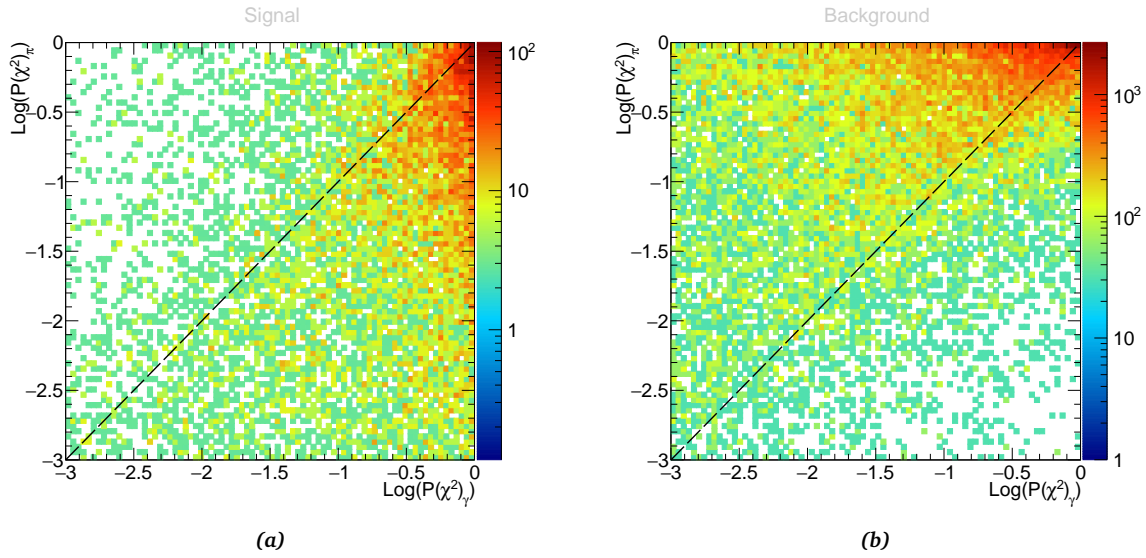


Figure 99: The logarithm of the p-value for the photon hypothesis on the x-axis and for the pion hypothesis on the y-axis for (a) signal events and for (b) background events. The dashed line indicates the cut value ($P(\chi^2)_\gamma > P(\chi^2)_\pi$).

The $M_{\Lambda\gamma}$ invariant mass distribution after applying the p-value cut is shown in Fig. 100 with and without the opening angle cut.

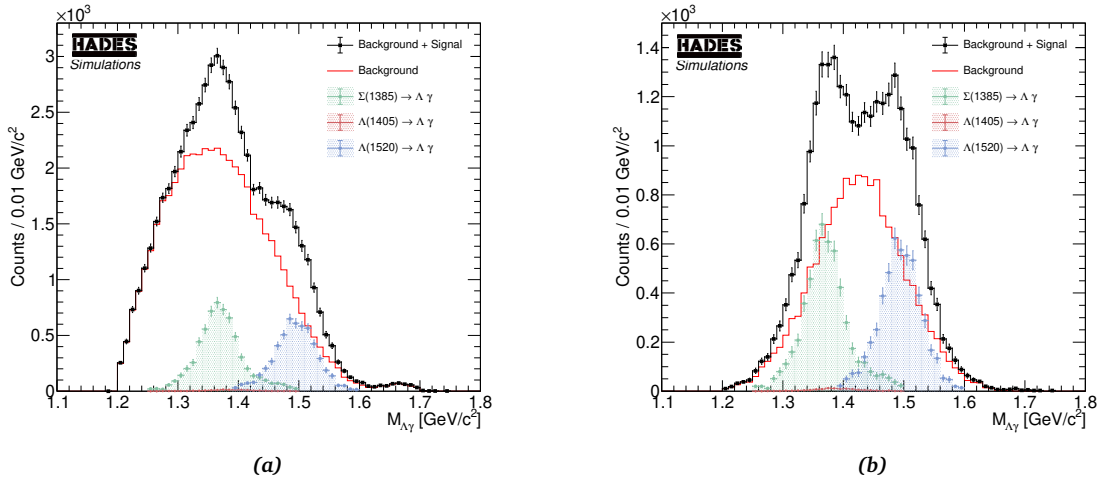


Figure 100: The $\Lambda\gamma$ invariant mass distribution after applying the χ^2 cut (a) without the $OA(\Lambda\gamma)$ cut and (b) with the $OA(\Lambda\gamma)$ cut applied.

Finally, Tab. 15 lists a comparison between the four invariant mass spectra $M_{\Lambda\gamma}$ presented in terms of the overall signal reconstruction efficiency (ϵ) and the signal significance (ss).

Based on the reconstruction efficiencies, the count rates of EM decay for excited hyperons can be calculated by assuming the following conditions: (i) a liquid hydrogen

	$\Sigma(1385)$		$\Lambda(1405)$		$\Lambda(1520)$	
	ϵ [%]	ss	ϵ [%]	ss	ϵ [%]	ss
No Refit + No OA	0.0246	25.58	0.0249	0.549	0.0226	31.52
No Refit + OA	0.0209	34.84	0.0212	0.800	0.0214	36.56
Refit + No OA	0.0230	28.31	0.0230	0.573	0.0205	24.00
Refit + OA	0.0196	42.41	0.0196	0.861	0.0193	39.98

Table 15: Comparison between the four invariant mass spectra $M_{\Lambda\gamma}$ in terms of the signal significance (ss) and the signal reconstruction efficiency (ϵ %).

target LH_2 with instantaneous luminosity $\mathcal{L} = 1.5 \times 10^{31} \text{cm}^{-2}\text{s}^{-1}$ and (ii) 50% beam duty cycle. The count rates are listed in Tab. 16.

	$\Sigma(1385)$	$\Lambda(1405)$	$\Lambda(1520)$
No Refit + No OA	125	3	113
No Refit + OA	107	3	107
Refit + No OA	117	3	103
Refit + OA	100	1	96

Table 16: Estimated count rates (events/day) for the EM decay of low lying excited state hyperons for the future beam time.

The ongoing upgrade of the HADES DAQ will enable operation up to 200 kHz. In this case, there is a possibility to operate with a higher luminosity for the same beam current $7.5 \times 10^7 \text{p/s}$ by replacing the LH_2 target with a polyethylene (PE) target. Because of the increased density of protons in the PE target, the count rates listed in Tab. 16 are expected to be increased by a factor of 7 [9].

5.5 SUMMARY

A feasibility study of the EM decay of low lying excited state hyperons ($\Sigma(1358)$, $\Lambda(1405)$ and $\Lambda(1520)$) with the upgraded HADES setup and the new FD at the future run is presented. As different theoretical models expect different EM decay widths, the measurement of the EM decays provides a means to differentiate between the theoretical models.

The study was done by investigating the exclusive reaction $p + p \rightarrow p + K + (Y^* \rightarrow \Lambda\gamma)$. Two data-sets have been identified, the HADES data-set in which all charged particles are detected in the HADES spectrometer and the FD data-set in which the daughter proton from the Λ decay is reconstructed in the FD, the three other particles are reconstructed in the HADES setup. The PID was done by a feed forward neural network. Since the FD

operates in a magnetic field free region, there is no direct PID method. Therefore, any track in the FD is assumed to be a proton. In the HADES data-set, the Λ was reconstructed based on a set of topological cuts. In the FD data-set, the FD proton track is combined with the π^- detected in HADES to form Λ candidates. Photons have been identified as clusters in the EMC which have an energy above a given threshold. In order to suppress background events, two missing mass cuts were introduced, (i) the squared missing mass of the primary proton and the kaon $1.6 < MM^2(p_p K^+) [GeV^2/c^4] < 2.6$ and (ii) the squared missing mass of all charged particles $-0.04 < MM^2(p_p K^+ \Lambda) [GeV^2/c^4] < 0.01$, where it is asymmetric to reduce contamination from $p + p \rightarrow p + K^+ + \Lambda + \pi^0$ background channel.

A kinematic refit was applied by introducing four constraints. The secondary proton and the pion are constrained to have the same vertex and the nominal Λ mass. In addition, the primary proton and the kaon are constrained to have the same vertex. In order to suppress the huge contamination from $p + p \rightarrow p + K^+ + \Lambda + \pi^0$, the missing mass of all charged particles is constrained to either have the photon mass (signal hypothesis) or to have the pion mass (background hypothesis). An optimal cut was obtained by requiring that $P(\chi^2)_\gamma > P(\chi^2)_\pi$.

An additional discriminating variable was introduced, the opening angle $OA(\gamma\Lambda)$ in the Y^* rest frame, which is required to be greater than 165° .

Finally, the overall signal reconstruction efficiency (ϵ) was calculated and found to be in the range 0.0250 – 0.0193 % depending if the kinematic refit and the $OA(\gamma\Lambda)$ cuts were applied or not. The count rates for the upcoming 4.5 GeV proton beam time in 2022 was calculated and introduced for the different cut combinations.

CONCLUSIONS AND OUTLOOK

In this thesis, three topics were investigated:

- Developing a deep-learning based track finding algorithm for the future \bar{P} ANDA experiment forward tracker.
- Investigation of the production mechanism of the Σ^0 hyperon produced in p+p collisions measured by the HADES setup in April 2007.
- A feasibility study has been done for the reconstruction of the excited hyperon radiative decays $Y^* \rightarrow \Lambda\gamma$ using the \bar{P} ANDA@HADES detector setup.

6.1 DEEP LEARNING BASED TRACK RECONSTRUCTION:

Chapter 3 presented a deep learning-based track finding algorithm that has been implemented for the \bar{P} ANDA forward tracker system (FTS). The developed algorithm was based on the state-of-art graph neural networks (GNN), a powerful class of methods from geometric deep learning, which works on non-Euclidean data. The GNN takes a graph $G = (V, E)$ as input an image, where the graph is the image of the detector. The graph vertices (V) are the FTS hits and the edges (E) are all the possible connections between hits in adjacent layers. The GNN was trained as a binary classifier to classify graph edges as *true* or *fake* edges. The GNN architecture first introduced in [54] was adapted and developed for the FTS. The GNN outputs a number between 0 and 1 that can be interpreted as an edge quality, an edge with score close to 0 is considered a fake edge and an edge with score close to 1 is a true edge. Guided by this output, a clustering algorithm that traverse the graph depth-wise has been implemented in order to reconstruct track candidates, this clustering algorithm is known as the *Depth First Search* (DFS). The model is implemented in PyTorch, trained in a Python environment and loaded with the help of the PyTorch tracing engine in a C++ environment.

In order to evaluate the performance of the GNN, a set of quality assurance measurements was defined: the reconstructed track purity, the overall tracking efficiency and the ghost rate. Averaged over all momentum values and over all particle species, the purity was found to be $\approx 100\%$, the efficiency $\approx 90\%$ and the ghost ratio less than 3%.

The developed model reconstructs only $x-z$ track projections since it uses information from vertical straw layers. Therefore, the model was followed by a second step that uses the $x-z$ projections as an input to build the $y-z$ track motion by using the information from the skewed layers. First, track segments outside the dipole magnetic field were fit by a linear model and segments inside the field were subsequently fit by a circular model. Then, the set of compatible hits were collected by histogramming the slopes, calculated for each skewed layer hit assuming the magnetic field component in the $y-z$ plane is negligible. The developed algorithm provides an estimate for the particle momentum, which is calculated by the p-kick method.

Now that a prototype of \bar{P} ANDA forward tracker is installed in the HADES detector setup [9] (the Forward Detector FD), the opportunity now exists to test the performance of the GNN tracking algorithm on a simplified setup using real data. Therefore, as a future plan, the GNN tracking algorithm will be integrated with the HADES software framework (*Hydra*) and tested in the upcoming proton beam time in 2022.

One weak point of the developed algorithm is the DFS clustering algorithm. In the future, a more robust algorithm has to be implemented, e.g., the future algorithm should take the *isochrones* into account.

The promising results of the GNN suggest to use it for the \bar{P} ANDA central tracker (MVD+STT), where particle tracks move in helices due to the magnetic field and are contaminated by *secondary tracks*, which complicates the problem. Therefore, future work may explore the application of GNN based tracking algorithm for the central tracker, which is expected to outperform the currently implemented algorithms.

6.2 Σ^0 PRODUCTION IN P-P COLLISIONS:

In chapter 4, the exclusive reconstruction of the reaction $p + p \rightarrow p + K^+ + \Sigma^0$ at a beam kinetic energy of 3.5 GeV with the HADES detector setup was presented. The Σ^0 hyperon decays electromagnetically with a branching ratio $BR(\Sigma^0 \rightarrow \Lambda\gamma) \approx 100\%$. The daughter Λ hyperon was reconstructed with the decay mode $\Lambda \rightarrow p\pi^-$ and the daughter photon was reconstructed as a missing particle since HADES was not equipped with an electromagnetic calorimeter at that time.

The first step in the analysis was to identify the charged final state particles. For this purpose, a neural network in a form of variational auto-encoder (VAE) has been trained on *real data* and *simulations* simultaneously using a semi-supervised technique. Evaluated on a hold-out sample, the VAE classified 98% of protons p , 92 % of pions π^+ and 76% of kaons K^+ correctly.

After identifying final state particles, two data-sets have been identified. The first, is called the *HADES* data-set, where the four charged particles ($2p$, π^- and K^+) are required to be within the acceptance of the main HADES setup. In this data-set, the daughter Λ was reconstructed from its decay products, then off-vertex cuts were defined and applied to enhance the S/B ratio. Finally, events in the range $MM^2(pp_{hades}\pi^-)[GeV^2/c^4] > 0.2$ were selected.

In the second set, the *FWall* data-set, only three charged particles ($1p$, π^- and K^+) are required to be within the main HADES acceptance and at least one hit in the forward wall. Events fulfilling the following kinematical conditions were selected:

- $-0.02 < MM^2(pK^+p_{wall}\pi^-)[GeV^2/c^4] < 0.01$
- $MM^2(pp_{wall}\pi^-)[GeV^2/c^4] > 0.2$

A kinematic refit is then applied for the *HADES* and *FWall* data-sets separately, which constrains the secondary proton and the pion to the nominal Λ mass and the overall missing mass to the photon mass. The Σ^0 yield was extracted from the missing mass $MM(pK^+)$ spectrum, where in total 2613 Σ^0 events were reconstructed, 58% are within the HADES acceptance and 42% within the FWall acceptance.

After selecting a relatively clean sample of Σ^0 hyperons, the angular distributions in the CMS, G-J and helicity-frames were investigated. The different distributions were corrected for the detector acceptance and efficiency using the inverse of the detector response matrix calculated by the SVD factorization method.

The angular distributions in the CMS of the Σ^0 hyperon and the proton show anisotropies, where the anisotropy is more pronounced in the case of the proton. This is a clear indication that the reaction proceeds dominantly via the pion exchange mechanism. The G-J angle of the kaon in the $K^+\Sigma^0$ frame tends to be asymmetric, which can be caused by the excitation of nucleon resonances decaying into the $K^+\Sigma^0$ channel. All the helicity angular distributions are clearly non-isotropic, which indicates significant resonant production.

In order to provide a better description of the experimental angular distributions and to estimate the contributions of nucleon resonances to the Σ^0 production, a partial wave analysis (PWA) has been performed using the BG-PWA framework. The non-

resonant waves were constructed first by combining the proton and the hyperon into a two-particle sub-system $p\Sigma^0$ and then the kaon is combined to produce the three-body final state $(p\Sigma^0) - K^+$. Nucleon resonances with a measured $K^+\Sigma^0$ branching ratio have been included as resonant components. The BG-PWA framework performs an unbinned fit, where the fit quality is determined by a log-likelihood value. However, due to the low statistics, it was not possible to obtain the quantitative contributions of nucleon resonance. Nevertheless, resonances $N^*(1710)$, $N^*(1900)$ and $\Delta^*(1900)$ are required by the fit.

Finally, the total production cross section of the Σ^0 hyperon was determined to be $\sigma = 18.74 \pm 1.01(stat) \pm 1.71(syst) \mu b$ by integrating the yield for the different angular distributions and the ratio $\sigma(pK^+\Lambda)/\sigma(pK^+\Sigma^0)$ found to be 1.73 ± 0.31 , in agreement with the high energy limit of 2.2.

Recently, the HADES detector setup has been upgraded by an electromagnetic calorimeter (EMC) and a FD based on \overline{P} ANDA straw tubes, which offers the opportunity to repeat the same measurement with an upgraded setup in the upcoming beam time 2022 at higher beam energy of 4.5 GeV. This upgrade will allow the measurement of the daughter photon ($\Sigma^0 \rightarrow \Lambda\gamma$), in addition, it will improve the mass resolution of the Λ hyperon in the FD acceptance and consequently improves the quality of the kinematic refit. Simulations show that the expected count rate at the upcoming beam time of $p + p \rightarrow p + K^+ + \Sigma^0$ is ≈ 2500 reconstructed events per day, assuming a cross section of $18.5 \mu b$. The planned four week beamtime will provide sufficient statistics to extract quantitative contributions of the different nucleon resonance and a measurement of their $K^+\Sigma^0$ branching ratios, which will improve our understanding of the Σ^0 production mechanism.

In addition, a measurement of the Dalitz decays $\Sigma^0 \rightarrow \Lambda e^+e^-$ is planned since it is complementary to the real photon decays and provides information on the hyperon form factor [6]. This measurement is a challenge as it requires the identification of an electron pair with momenta below the spectrometer acceptance threshold ($p_{threshold} \approx 50 \text{ MeV}/c$) needed for full track and momentum reconstruction [6].

6.3 FEASIBILITY STUDY FOR RADIATIVE DECAYS OF EXCITED HYPERONS

In chapter 5, a feasibility study of the radiative decays of lower lying excited state hyperons Y^* ($\Sigma(1385)$, $\Lambda(1405)$ and $\Lambda(1520)$) with the upgraded HADES setup was presented. Once again, two data-set have been identified, the HADES data-set in which all charged particles are detected in the main HADES spectrometer and the FD data-set in which the daughter proton of $\Lambda \rightarrow p\pi^-$ is reconstructed in the FD, while the other three particles are reconstructed in the main HADES detector.

The PID in the main HADES setup was done by a feed forward neural network and the daughter Λ ($Y^* \rightarrow \Lambda\gamma$) was reconstructed based on a set of topological cuts, while any track in the FD is assumed to be a proton since there is no direct PID method. The FD proton track is combined with the π^- detected in HADES to reconstruct the Λ candidates in the FD acceptance.

The excited hyperon is reconstructed in the $\Lambda\gamma$ invariant mass distribution, where the background contribution is mostly from the $p + p \rightarrow p + K^+ + \Lambda + \pi^0$ channel. Therefore, the following missing mass cuts were introduced to suppress background contributions:

- $1.6 < MM^2(p_p K^+) [GeV^2/c^4] < 2.6$.
- $-0.04 < MM^2(p_p K^+ \Lambda) [GeV^2/c^4] < 0.01$.

Moreover, a kinematic refit is introduced by constraining the Λ mass and vertex and the primary proton and the kaon are constrained to emerge from the same vertex. Furthermore, the missing mass of all charged particles are constrained to either have the photon mass (a signal hypothesis) or to have the pion mass (a background hypothesis), then a 2D cut was defined by requiring $P(\chi^2)_\gamma > P(\chi^2)_\pi$. This measurement emphasizes the role of the FD in the future measurements of the radiative decays of lower-lying excited state hyperons since it almost doubles the statistics. Finally, the count rates for the upcoming 4.5 GeV proton beam time in 2022 were presented.

In the future, a measurement of the branching ratios and decay widths of the excited hyperon radiative decays will be performed with the upgraded HADES setup. Several theoretical models have been proposed, which predict their decay widths. These predictions vary significantly making it experimentally tractable to rule out certain models. Consequently, this measurement is complementary to the CLAS measurement and provides a means to differentiate between the models [122]. Furthermore, the investigation of excited hyperon Dalitz decays ($Y^* \rightarrow \Lambda\gamma^*$) offers the chance to probe the internal structure of the resonance in the time-like region ($q^2 > 0$). The measurement of the Dalitz decays provide access to the electromagnetic Transition Form Factors (eTFF) and in contrast to the $\Delta(1232)$ resonance [7], no data are available on the eTFF for strange baryons. In addition, this measurement will test whether the Vector Dominance Model (VDM) is valid in the strange sector [30].

Appendices



PERFORMANCE PLOTS OF THE PID MODEL

A.1 PERFORMANCE OF THE VAE FOR $p(3.5\text{GeV})p \rightarrow pK^+\Sigma^0$

The efficiency and the purity of the pions π^+ , protons p and kaons K^+ selected by the VAE has been evaluated on a separate hold out data-set (see Eq. 22). Assume that a particle track belongs to class i (could be π^+ , p or K^+), the efficiency and the purity are defined as follows:

$$\begin{aligned} \text{efficiency} &= \frac{\text{the number of particles that belongs to the class } i \text{ selected by the VAE}}{\text{the total number of particles that belongs to the class } i} \\ \text{purity} &= \frac{\text{the number of particles that belongs to the class } i \text{ selected by the VAE}}{\text{the total number of particles}} \end{aligned} \tag{45}$$

Both the efficiency and purity have been evaluated as a function of the momentum P and the polar angle θ . Fig. 101 shows the momentum as function of the polar angle for the three particle species. Fig. 102 and Fig. 103 shows the efficiency and purity maps for pions, protons and kaons, respectively.

For pions, the efficiency and purity is almost uniform over the whole phase space except for momentum values greater than 0.9 GeV/c where pions have a low production rate. On average the efficiency and purity is 92.6% and 95.5%, respectively.

The average efficiency for protons and kaons is 95.6% and 81%, respectively. As protons and kaons overlap for momentum values greater than 1 GeV/c, it is difficult to distinguish between the two particle species. This is can be seen from the purity maps, where the average purity for protons and kaons is 79.1% and 66.3%, respectively.

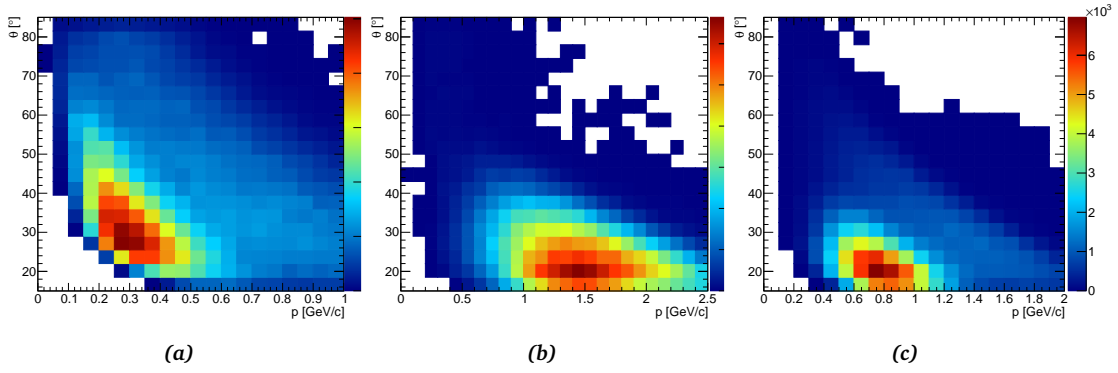


Figure 101: The momentum as a function of the polar angle for the (a) π^+ , (b) p and (c) K^+ .

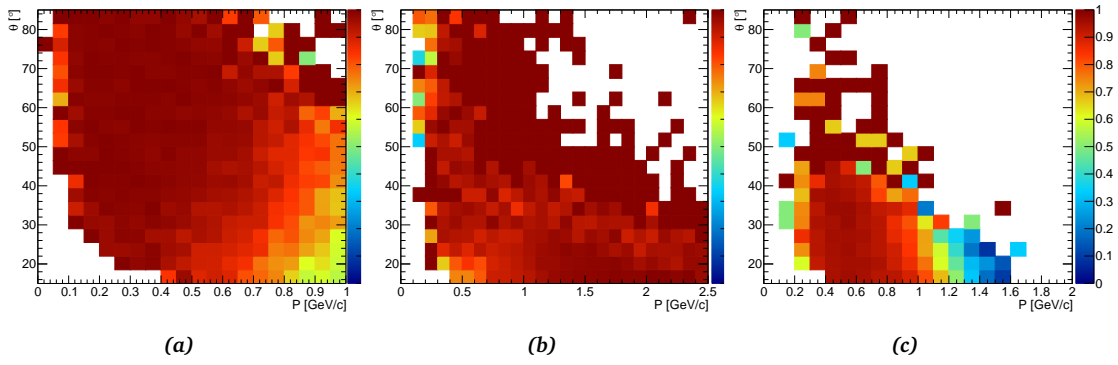


Figure 102: The efficiency map for the (a) π^+ , (b) p and (c) K^+ .

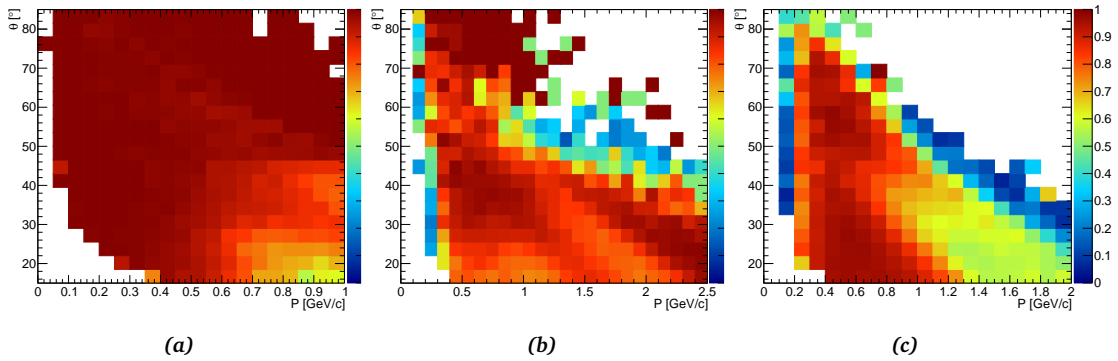


Figure 103: The purity map for the (a) π^+ , (b) p and (c) K^+ .

A.2 PERFORMANCE OF THE PID NN MODEL FOR $p(4.5\text{GeV})p \rightarrow pK^+Y^*$

The efficiency and the purity (defined in Eq. 45) of the pions π^+ , protons p and kaons K^+ selected by the PID NN has been evaluated on a separate hold out data-set. Fig. 104 shows the momentum as a function of the polar angle for the three particle species. Fig. 105 and Fig. 106 shows the efficiency and purity maps for pions, protons and kaons, respectively.

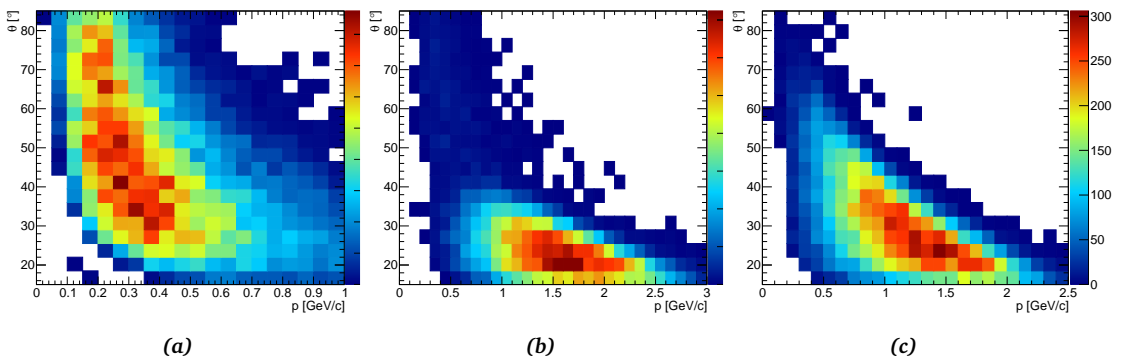


Figure 104: The momentum as a function of the polar angle for the (a) π^+ , (b) p and (c) K^+ .

The average selection efficiency for pions, protons and kaons is 97.2%, 98.4% and 90%, respectively. The average purity for pions, protons and kaons is 99.8%, 95.3% and 95%, respectively.

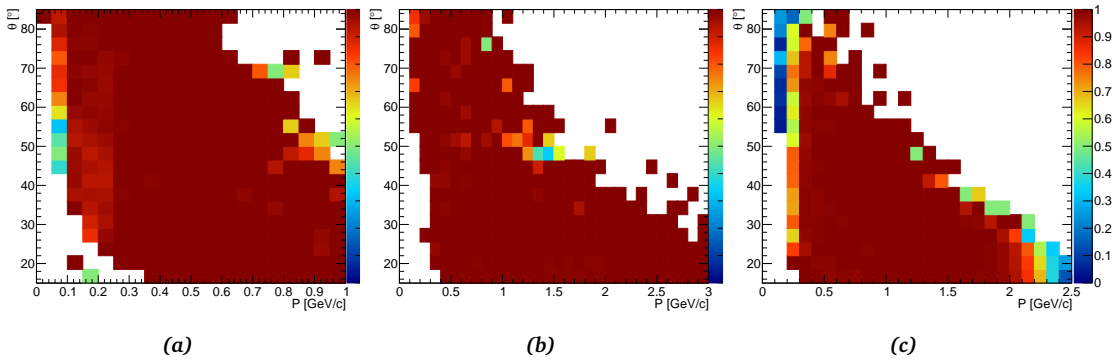


Figure 105: The efficiency map for the (a) π^+ , (b) p and (c) K^+ .

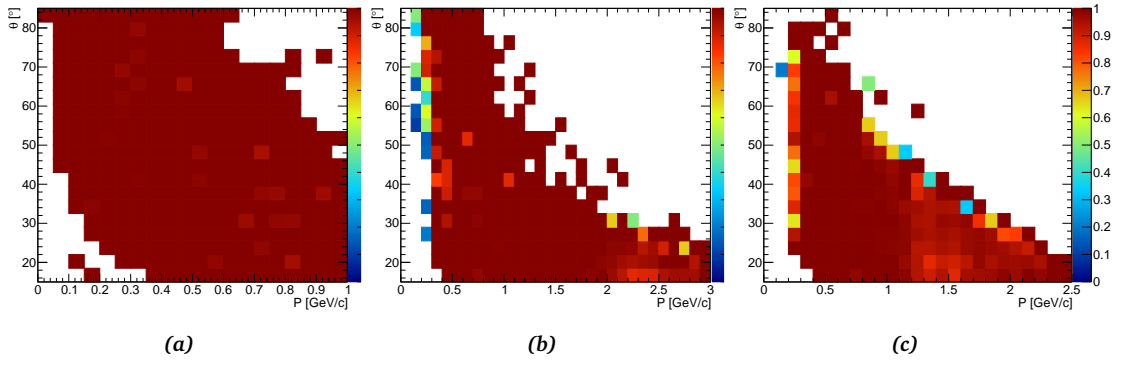


Figure 106: The purity map for the (a) π^+ , (b) p and (c) K^+ .

COVARIANCE MATRIX ESTIMATION

B.1 COVARIANCE MATRIX ESTIMATION FOR $p + p \rightarrow p + K^+ + \Sigma^0$ ANALYSIS

The errors on the track parameters $1/p$, θ and ϕ are not given by the tracking algorithm and have to be estimated. These errors are estimated from the simulation by investigating the difference between the reconstructed variable value and the generated value as this difference is a measure the detector resolution for the particular variable. Figures (107 to 109) show the resolution plots for protons, kaons and pions. All distributions were fitted by the sum of three Gaussian, the average mean μ and standard deviation σ is stated for each plot. The variance (σ^2) for the different variables are used as an initial guess for the covariance matrix diagonal elements, where it has been assumed that there are no correlations between track parameters. Therefore, the off-diagonal elements are set to zero. After applying the kinematic refit and obtaining the pull distributions (see figures (110 to 113)), the elements of the covariance matrix have been tuned in order to keep the pull as standard normal distributions $N(0,1)$. The assumption of diagonal matrix was found to be a good approximation to the covariance matrix.

B.2 COVARIANCE MATRIX ESTIMATION FOR $p + p \rightarrow p + K^+ + Y^*$ FEASIBILITY STUDY:

The estimation of the covariance matrix used for the $p + p \rightarrow p + K^+ + Y^*$ feasibility study presented in chapter 5 follows exactly the same method described in the previous section. First, the resolution plots provided an initial guess of the covariance matrix elements (see figures (119 to 123)), then the errors are adjusted to keep the pull distributions (see figures (110 to 113)) as standard normal distributions $N(0,1)$.

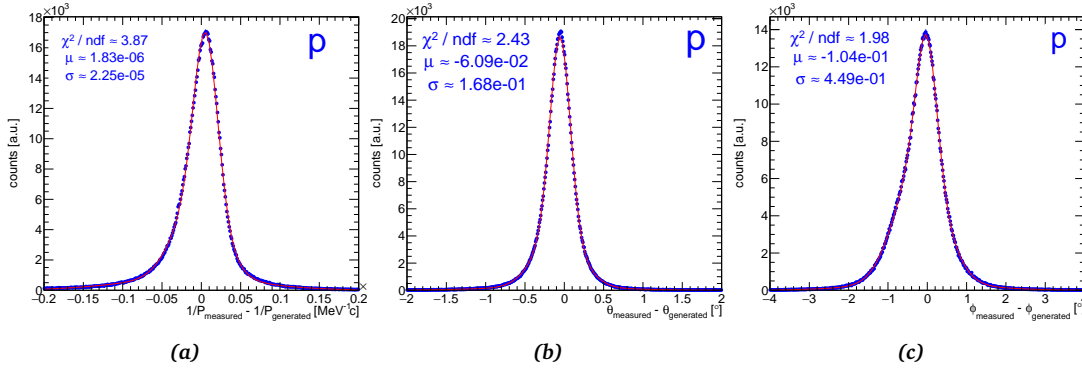


Figure 107: The resolution plots of protons detected in the main HADES detector setup for (a) the absolute momentum inverse ($1/p$), (b) polar angle (θ) and (c) azimuthal angle (ϕ). The fit quality is determined by a reduced χ^2 value, the mean and standard deviation are shown for each distribution.

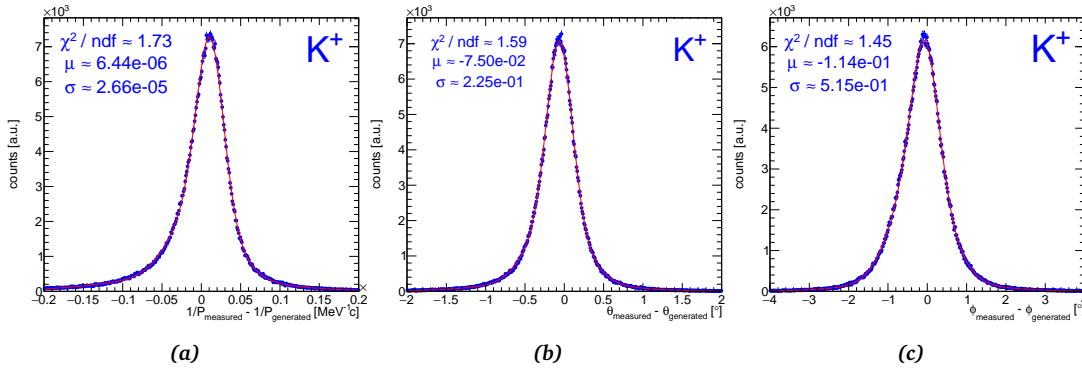


Figure 108: The resolution plots of kaons for (a) the absolute momentum inverse ($1/p$), (b) polar angle (θ) and (c) azimuthal angle (ϕ).

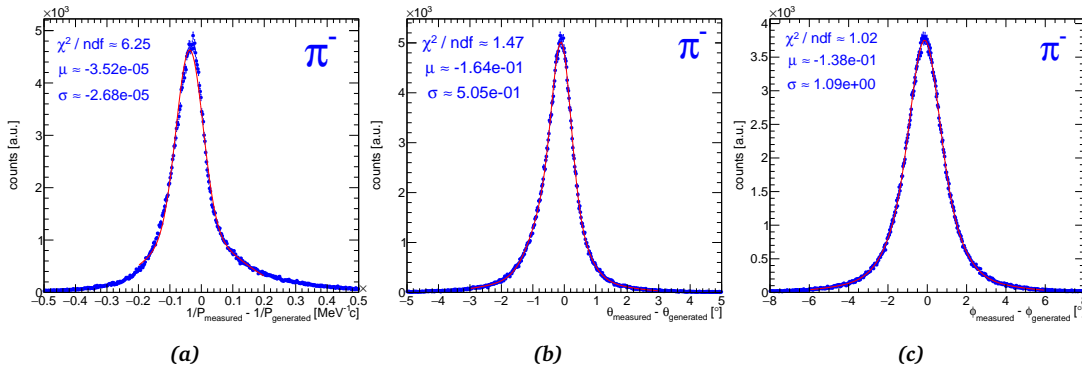


Figure 109: The resolution plots of pions for (a) the absolute momentum inverse ($1/p$), (b) polar angle (θ) and (c) azimuthal angle (ϕ).

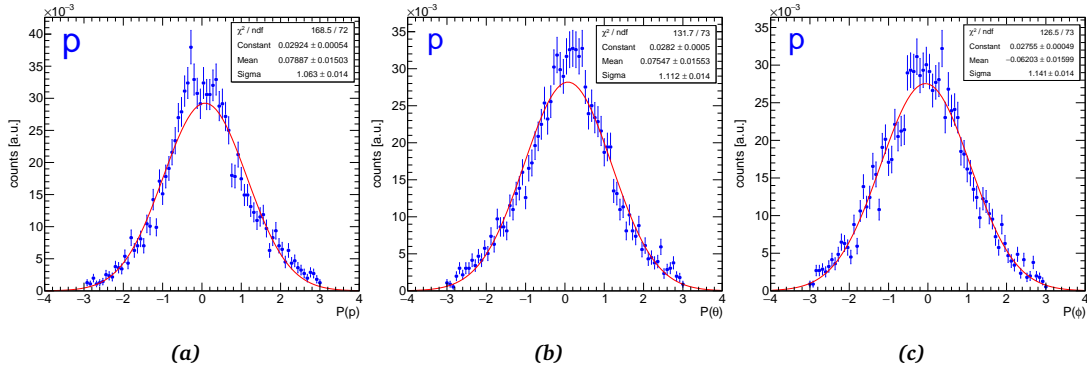


Figure 110: The pull distributions (see Eq. 29) of protons detected in the main HADES detector setup for (a) the absolute momentum inverse ($1/p$), (b) polar angle (θ) and (c) azimuthal angle (ϕ). Each distribution has been fit by a Gaussian distribution and the fit parameters are stated in the inset.

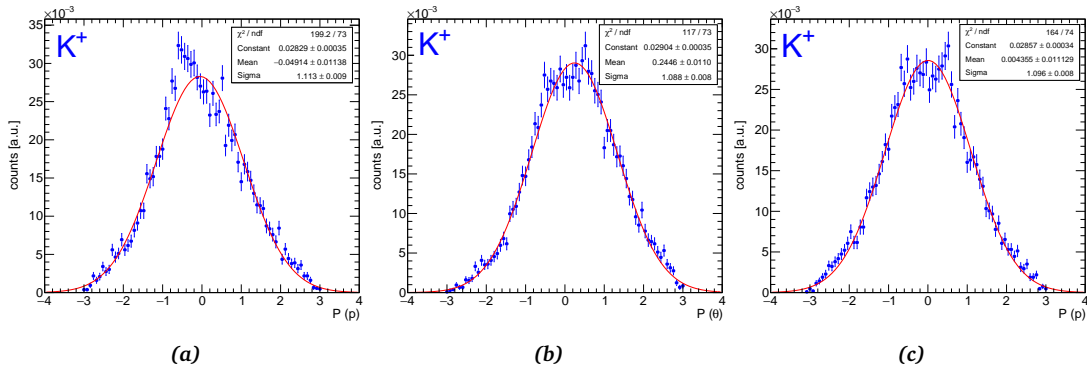


Figure 111: The pull distributions (see Eq. 29) of kaons detected in the main HADES detector setup for (a) the absolute momentum inverse ($1/p$), (b) polar angle (θ) and (c) azimuthal angle (ϕ).

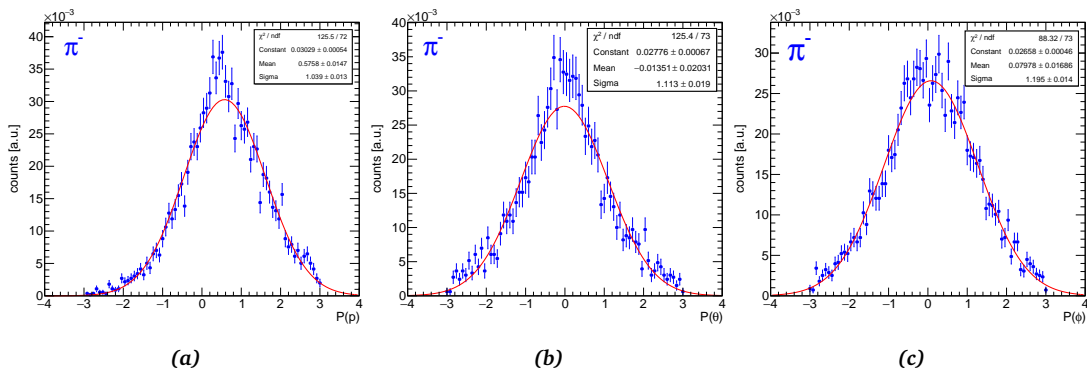


Figure 112: The pull distributions (see Eq. 29) of pions for (a) the absolute momentum inverse ($1/p$), (b) polar angle (θ) and (c) azimuthal angle (ϕ).

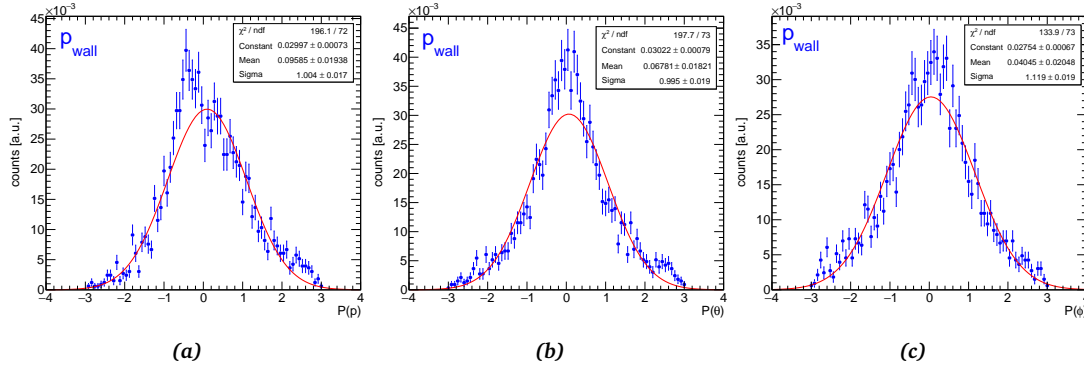


Figure 113: The pull distributions (see Eq. 29) of protons reconstructed in the forward wall detector setup for (a) the absolute momentum inverse ($1/p$), (b) polar angle (θ) and (c) azimuthal angle (ϕ).

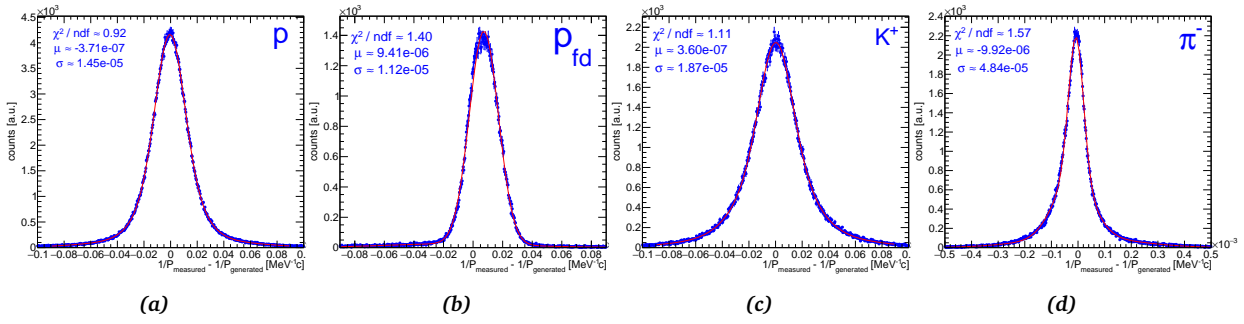


Figure 114: The resolution plots for the absolute momentum inverse ($1/p$) (a) of protons detected in the main HADES detector setup, (b) of protons detected in the FD, (c) kaons and (d) pions. The fit quality is determined by a reduced χ^2 value, the mean and standard deviation is shown for each distribution.

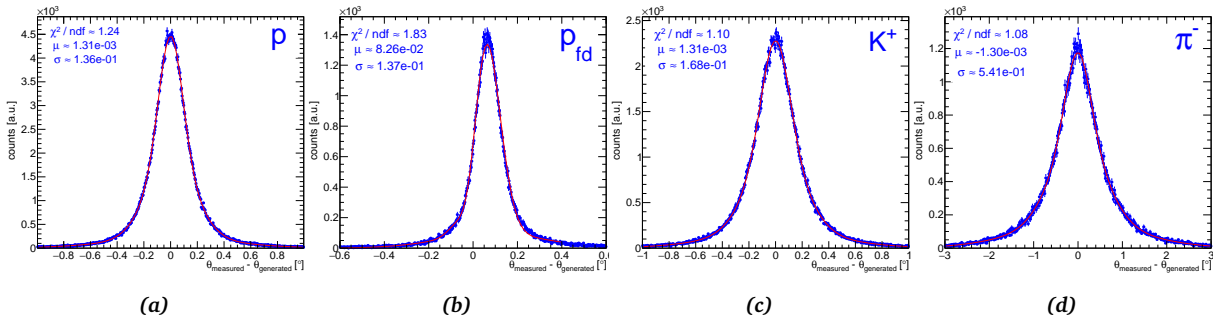


Figure 115: The resolution plots for the polar angle (θ) (a) of protons detected in the main HADES detector setup, (b) of protons detected in the FD, (c) kaons and (d) pions.

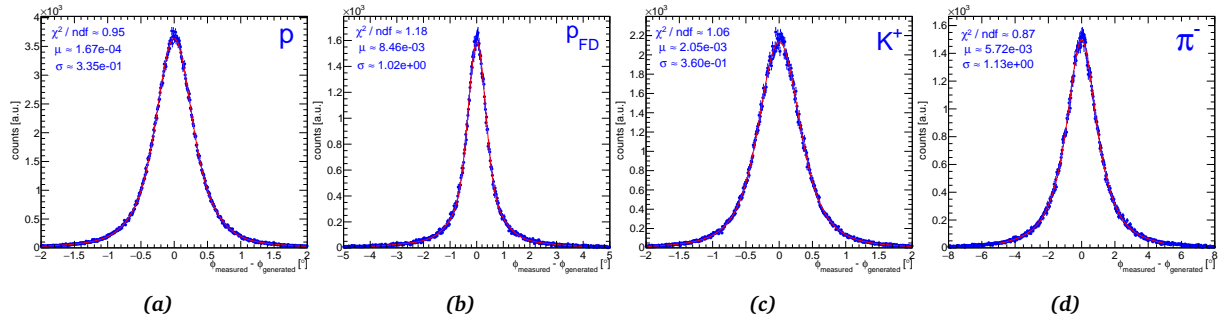


Figure 116: The resolution plots for the azimuthal angle (ϕ) (a) of protons detected in the main HADES detector setup, (b) of protons detected in the FD, (c) kaons and (d) pions.

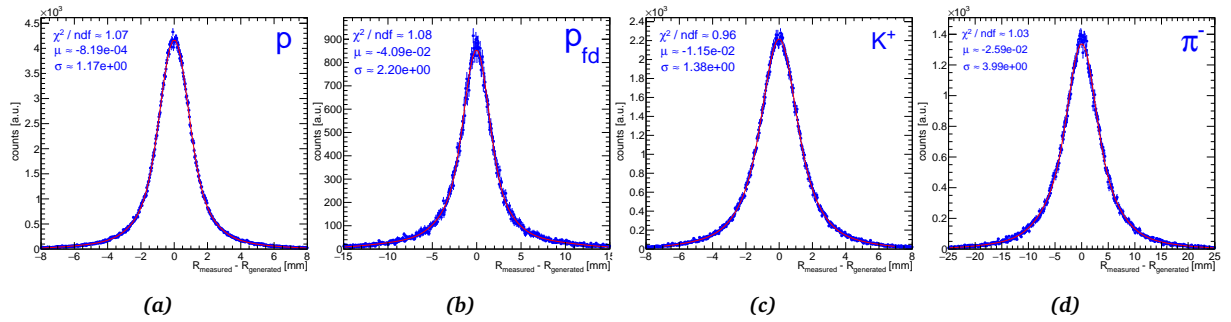


Figure 117: The resolution plots for the DCA between the track and the beam axis (R) (a) of protons detected in the main HADES detector setup, (b) of protons detected in the FD, (c) kaons and (d) pions.

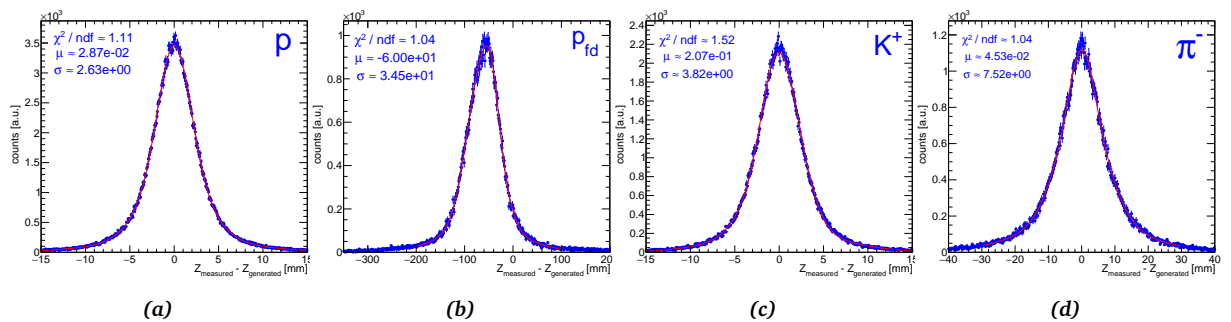


Figure 118: The resolution plots for the z -coordinate of the PCA between the track and the beam axis (z) (a) of protons detected in the main HADES detector setup, (b) of protons detected in the FD, (c) kaons and (d) pions.

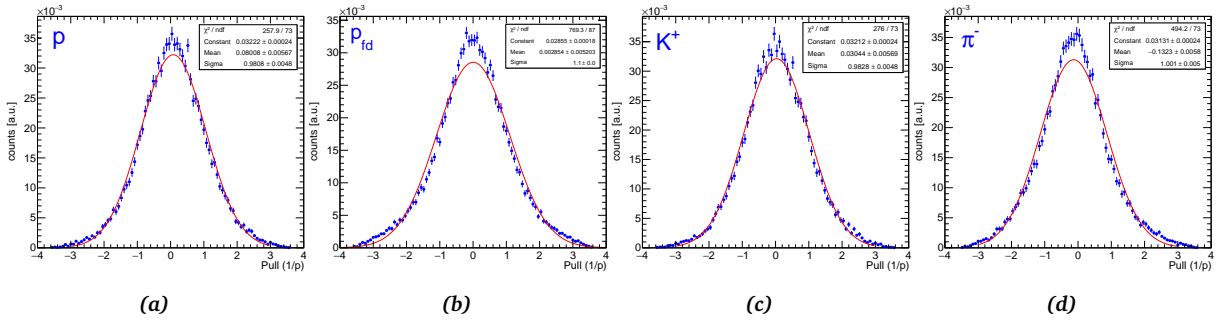


Figure 119: The pull distributions for the absolute momentum inverse ($1/p$) (a) of protons detected in the main HADES detector setup, (b) of protons detected in the FD, (c) kaons and (d) pions. Each distribution has been fit by a Gaussian distribution and the fit parameters are stated in the inset.

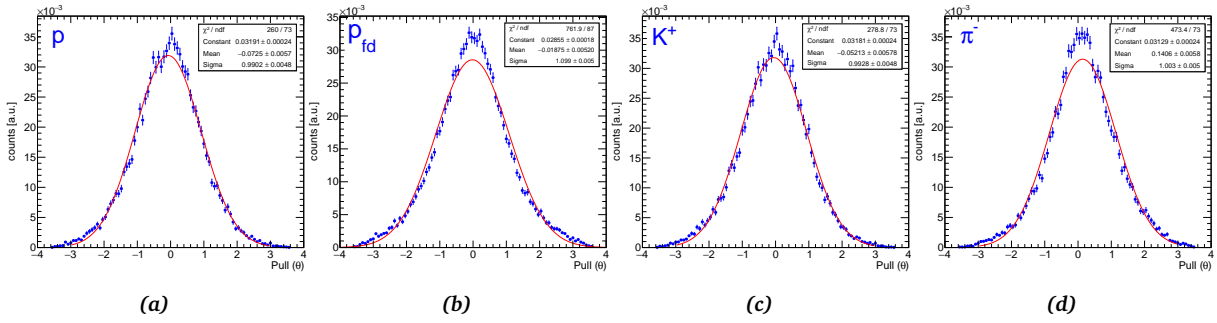


Figure 120: The pull distributions for the polar angle (θ) (a) of protons detected in the main HADES detector setup, (b) of protons detected in the FD, (c) kaons and (d) pions.

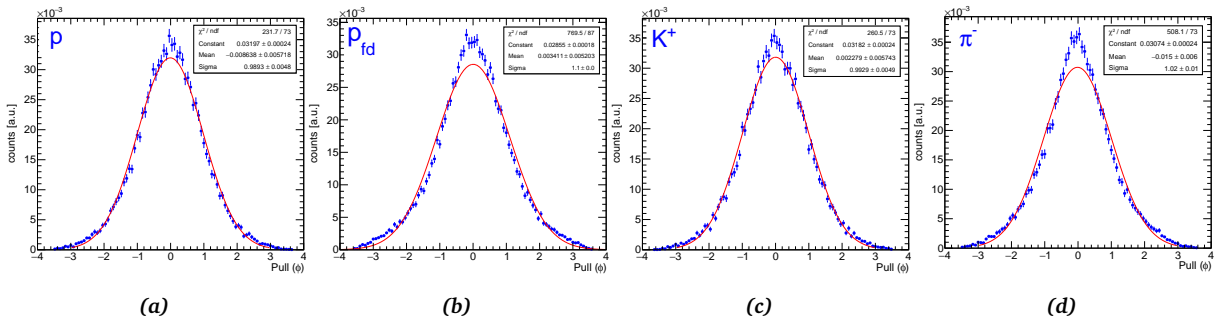


Figure 121: The pull distributions for the azimuthal angle (ϕ) (a) of protons detected in the main HADES detector setup, (b) of protons detected in the FD, (c) kaons and (d) pions.

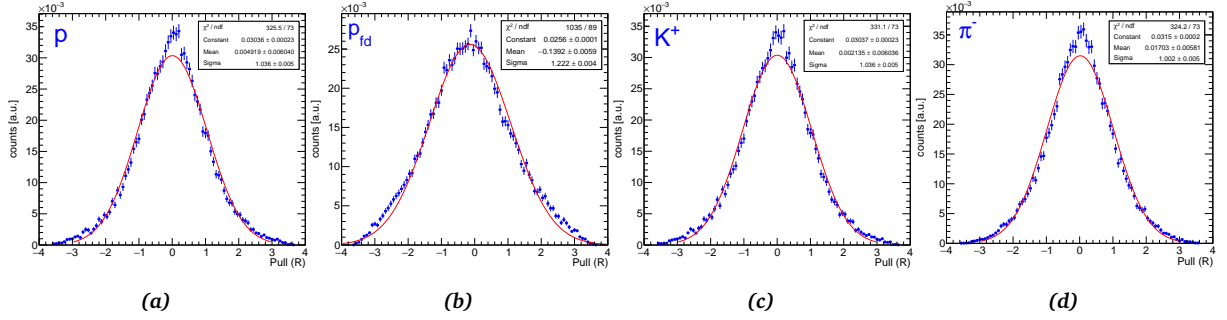


Figure 122: The pull distributions for the DCA between the track and the beam axis (R) (a) of protons detected in the main HADES detector setup, (b) of protons detected in the FD, (c) kaons and (d) pions.

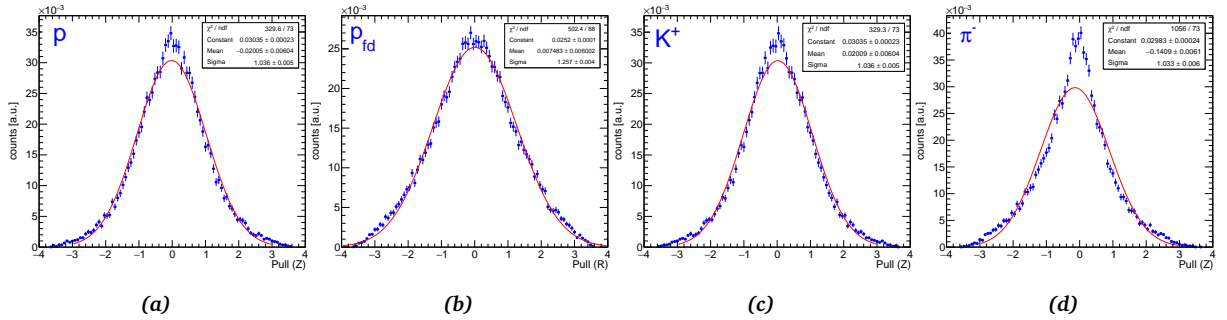


Figure 123: The pull distributions for the z-coordinate of the PCA between the track and the beam axis (z) (a) of protons detected in the main HADES detector setup, (b) of protons detected in the FD, (c) kaons and (d) pions.

PARTIAL WAVE ANALYSIS: BACKGROUND ESTIMATION

The main background channel contributing to the signal region is the $pp \rightarrow pK^+\Lambda$, its contributions was estimated to be 14%. First a mass window $1.090 < MM(pK^+)[\text{GeV}/c^2] < 1.150$ has been applied to select the Λ -like events as shown in Fig. 124. In total 6607 Λ events were selected.

Because the PWA method works on an event-by-event basis, it is important to identify whether a particular event belongs to the signal or the background. Therefore, it was necessary to model the Λ kinematics as accurately as possible. To achieve this, the PWA method explained in chapter 4 has been applied to the selected Λ events.

The Λ production has been studied extensively by HADES by the PWA technique [15]. The different solutions published in [15] has been tried out and the solution No. 8/1 was found to be the best solution in describing the experimental data (log-likelihood value $\mathcal{L} = -1469.8$) by including p-p initial waves 1S_0 , 3P_0 , 3P_1 and 1D_2 .

p-p Initial State	non-resonant $pK^+\Lambda$	$N^*(1650)$	$N^*(1710)$	$N^*(1720)$	$N^*(1900)$
1S_0	24.73	27.82	00.26	00.61	00.12
3P_0	03.44	01.60	00.06	03.00	06.51
3P_1	21.57	14.76	00.09	10.23	05.00
1D_2	08.73	13.69	07.20	14.36	23.41

Table 17: Partial wave contributions to the total $pK^+\Lambda$ production.

The transition waves with the different contributions of intermediate states to the $pK^+\Lambda$ production are listed in Tab. 17. This solution gives a good description of the experimental data, as shown in Fig. 125 and Fig. 126 for different kinematic observables and angular distributions, respectively. The agreement between the PWA solution and experimental the data is quantified by a reduced χ^2 value (see Eq. 40) calculated for each observable (average $\chi^2 \approx 1.86$). The PWA solution has been applied to the 4π phase

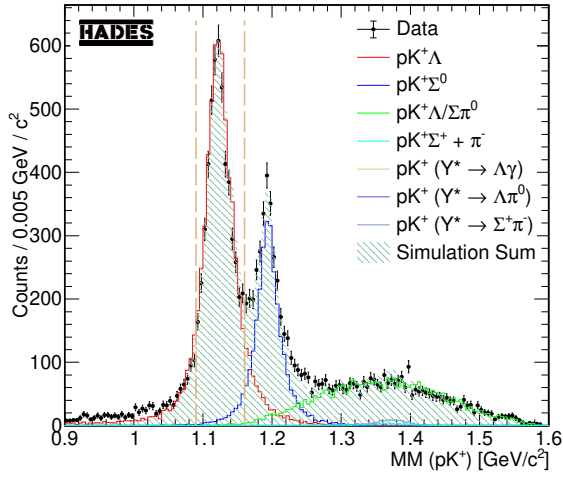


Figure 124: The missing mass distribution of the primary proton and the kaon for the sum of the HADES and the FWall data-sets. The vertical dashed lines indicates the mass window applied in order to select Λ events.

space simulations and then these events are filtered through the full simulation and analysis chain.

After reconstructing the $pK^+\Lambda$ events that have been assigned a PWA weight, the missing mass $MM(pK^+)$ spectrum was investigated and the $pK^+\Lambda$ contribution in the signal region ($1.170 < MM(pK^+)[\text{GeV}/c^2] < 1.220$) was determined to be 292 events. Those events are then added to signal list with a negative weight.

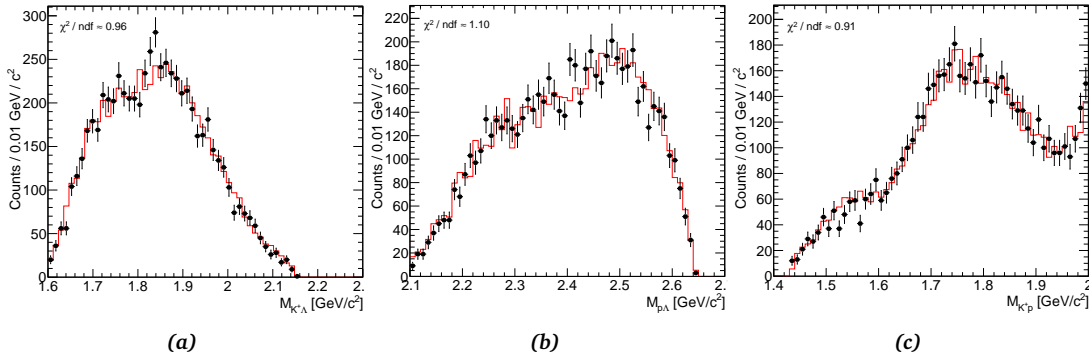


Figure 125: A comparison between the experimental data (black points) for which $1.090 < MM(pK^+)[\text{GeV}/c^2] < 1.150$ and the PWA solution (red histogram) listed in Tab. 17 for (a) the $K^+\Lambda$ invariant mass, (b) the $p\Lambda$ invariant mass and (c) the K^+p invariant mass distributions.

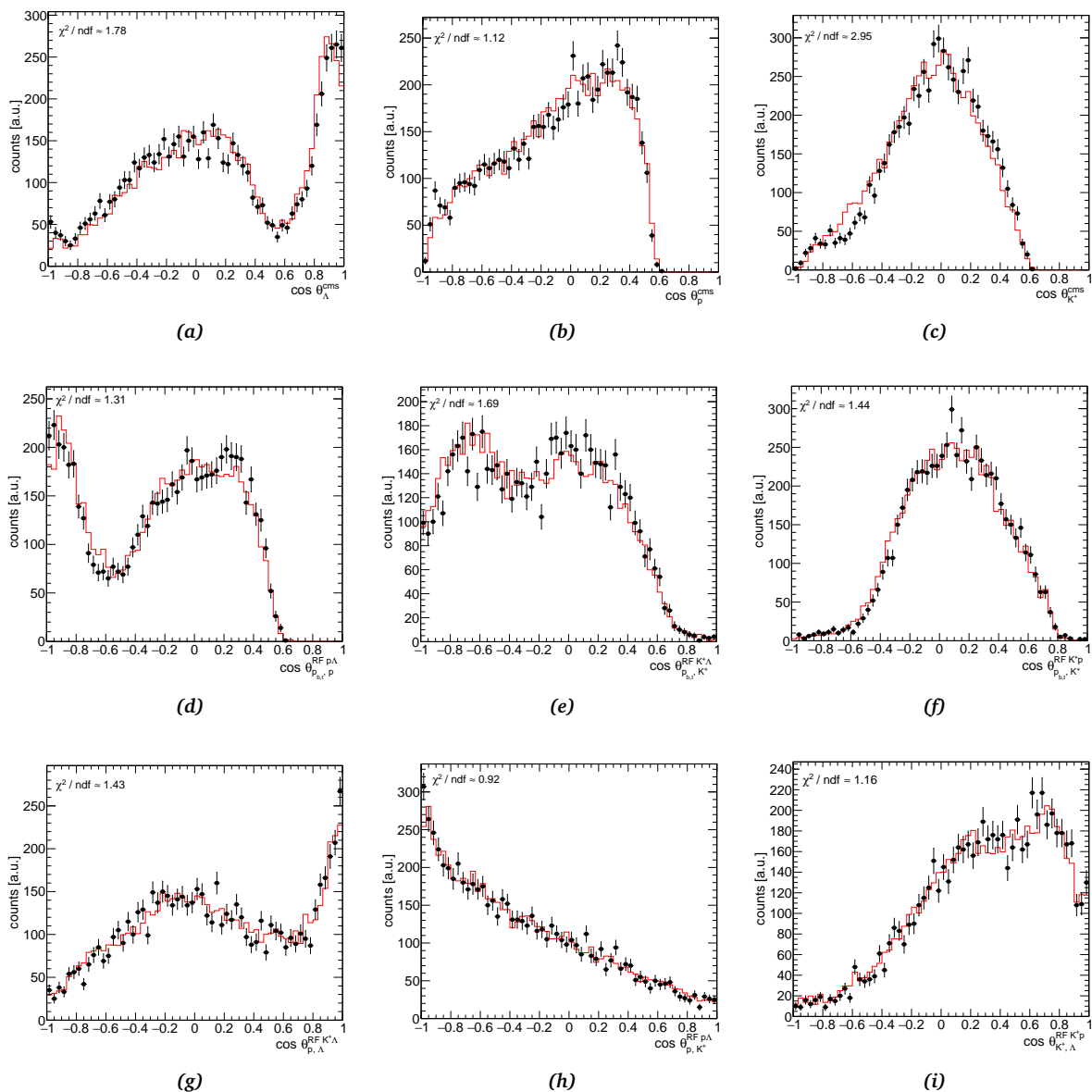


Figure 126: A comparison between the experimental data (black points) for which $1.090 < MM(pK^+) [\text{GeV}/c^2] < 1.150$ and the PWA solution (red histogram) listed in Tab. 17. The upper row shows the CMS angular distributions, the middle row shows the G-J angular distributions and the bottom row shows the helicity angular distributions.

BIBLIOGRAPHY

- [1] \bar{P} ANDA. URL: <https://panda.gsi.de/>.
- [2] Georges Aad et al. “Observation of a new particle in the search for the Standard Model Higgs boson with the ATLAS detector at the LHC”. In: *Phys. Lett. B* 716 (2012), pp. 1–29. DOI: [10.1016/j.physletb.2012.08.020](https://doi.org/10.1016/j.physletb.2012.08.020). arXiv: [1207.7214](https://arxiv.org/abs/1207.7214) [hep-ex].
- [3] Roel Aaij et al. “Observation of $J/\psi p$ Resonances Consistent with Pentaquark States in $\Lambda_b^0 \rightarrow J/\psi K^- p$ Decays”. In: *Phys. Rev. Lett.* 115 (2015), p. 072001. DOI: [10.1103/PhysRevLett.115.072001](https://doi.org/10.1103/PhysRevLett.115.072001). arXiv: [1507.03414](https://arxiv.org/abs/1507.03414) [hep-ex].
- [4] Roel Aaij et al. “Observation of New Resonances Decaying to $J/\psi K^+ +$ and $J/\psi \phi$ ”. In: *Phys. Rev. Lett.* 127.8 (2021), p. 082001. DOI: [10.1103/PhysRevLett.127.082001](https://doi.org/10.1103/PhysRevLett.127.082001). arXiv: [2103.01803](https://arxiv.org/abs/2103.01803) [hep-ex].
- [5] M. Abdel-Bary et al. “Production of Λ and Σ^0 hyperons in proton-proton collisions”. In: *Eur. Phys. J. A* 46 (2010). [Erratum: *Eur.Phys.J.A* 46, 435–436 (2010)], pp. 27–44. DOI: [10.1140/epja/i2010-11023-0](https://doi.org/10.1140/epja/i2010-11023-0). arXiv: [1008.4287](https://arxiv.org/abs/1008.4287) [nucl-ex].
- [6] J. Adamczewski-Musch et al. “ Σ^0 production in proton nucleus collisions near threshold”. In: *Phys. Lett. B* 781 (2018), pp. 735–740. DOI: [10.1016/j.physletb.2018.02.043](https://doi.org/10.1016/j.physletb.2018.02.043). arXiv: [1711.05559](https://arxiv.org/abs/1711.05559) [nucl-ex].
- [7] J. Adamczewski-Musch et al. “ $\Delta(1232)$ Dalitz decay in proton-proton collisions at $T=1.25$ GeV measured with HADES at GSI”. In: *Phys. Rev. C* 95.6 (2017), p. 065205. DOI: [10.1103/PhysRevC.95.065205](https://doi.org/10.1103/PhysRevC.95.065205). arXiv: [1703.07840](https://arxiv.org/abs/1703.07840) [nucl-ex].
- [8] J. Adamczewski-Musch et al. “Inclusive Λ production in proton-proton collisions at 3.5 GeV”. In: *Phys. Rev. C* 95.1 (2017), p. 015207. DOI: [10.1103/PhysRevC.95.015207](https://doi.org/10.1103/PhysRevC.95.015207). arXiv: [1611.01040](https://arxiv.org/abs/1611.01040) [nucl-ex].
- [9] J. Adamczewski-Musch et al. “Production and electromagnetic decay of hyperons: a feasibility study with HADES as a phase-0 experiment at FAIR”. In: *Eur. Phys. J. A* 57.4 (2021), p. 138. DOI: [10.1140/epja/s10050-021-00388-w](https://doi.org/10.1140/epja/s10050-021-00388-w). arXiv: [2010.06961](https://arxiv.org/abs/2010.06961) [nucl-ex].
- [10] Tim Adye. “Unfolding algorithms and tests using RooUnfold”. In: *PHYSTAT 2011*. Geneva: CERN, May 2011. DOI: [10.5170/CERN-2011-006.313](https://doi.org/10.5170/CERN-2011-006.313). arXiv: [1105.1160](https://arxiv.org/abs/1105.1160) [physics.data-an].

- [11] G. Agakishiev et al. “Baryonic resonances close to the $\bar{K}N$ threshold: The Case of $\Sigma(1385)^+$ in pp collisions”. In: *Phys. Rev. C* 85 (2012), p. 035203. DOI: [10.1103/PhysRevC.85.035203](https://doi.org/10.1103/PhysRevC.85.035203). arXiv: [1109.6806](https://arxiv.org/abs/1109.6806) [nucl-ex].
- [12] G. Agakishiev et al. “Baryonic resonances close to the $\bar{K}N$ threshold: the case of $\Lambda(1405)$ in pp collisions”. In: *Phys. Rev. C* 87 (2013), p. 025201. DOI: [10.1103/PhysRevC.87.025201](https://doi.org/10.1103/PhysRevC.87.025201). arXiv: [1208.0205](https://arxiv.org/abs/1208.0205) [nucl-ex].
- [13] G. Agakishiev et al. “Inclusive dielectron spectra in $p+p$ collisions at 3.5 GeV”. In: *Eur. Phys. J. A* 48 (2012), p. 64. DOI: [10.1140/epja/i2012-12064-y](https://doi.org/10.1140/epja/i2012-12064-y). arXiv: [1112.3607](https://arxiv.org/abs/1112.3607) [nucl-ex].
- [14] G. Agakishiev et al. “Lambda hyperon production and polarization in collisions of $p(3.5\text{ GeV})+\text{Nb}$ ”. In: *Eur. Phys. J. A* 50 (2014), p. 81. DOI: [10.1140/epja/i2014-14081-2](https://doi.org/10.1140/epja/i2014-14081-2). arXiv: [1404.3014](https://arxiv.org/abs/1404.3014) [nucl-ex].
- [15] G. Agakishiev et al. “Partial Wave Analysis of the Reaction $p(3.5\text{ GeV})+p\rightarrow pK^+\Lambda$ to Search for the “ ppK^- ” Bound State”. In: *Phys. Lett. B* 742 (2015), pp. 242–248. DOI: [10.1016/j.physletb.2015.01.032](https://doi.org/10.1016/j.physletb.2015.01.032). arXiv: [1410.8188](https://arxiv.org/abs/1410.8188) [nucl-ex].
- [16] G. Agakishiev et al. “The High-Acceptance Dielectron Spectrometer HADES”. In: *Eur. Phys. J. A* 41 (2009), pp. 243–277. DOI: [10.1140/epja/i2009-10807-5](https://doi.org/10.1140/epja/i2009-10807-5). arXiv: [0902.3478](https://arxiv.org/abs/0902.3478) [nucl-ex].
- [17] S. Agostinelli et al. “GEANT4—a simulation toolkit”. In: *Nucl. Instrum. Meth. A* 506 (2003), pp. 250–303. DOI: [10.1016/S0168-9002\(03\)01368-8](https://doi.org/10.1016/S0168-9002(03)01368-8).
- [18] Saad Albawi et al. “Understanding of a convolutional neural network”. In: *2017 International Conference on Engineering and Technology (ICET)*. 2017, pp. 1–6. DOI: [10.1109/ICEngTechnol.2017.8308186](https://doi.org/10.1109/ICEngTechnol.2017.8308186).
- [19] Walter Ikegami Andersson. “Exploring the Merits and Challenges of Hyperon Physics with \bar{P} ANDA at FAIR”. PhD thesis. Uppsala University, 2020.
- [20] A. Anisovich et al. “Partial wave decomposition of pion and photoproduction amplitudes”. In: *Eur. Phys. J. A* 24 (2005), pp. 111–128. DOI: [10.1140/epja/i2004-10125-6](https://doi.org/10.1140/epja/i2004-10125-6). arXiv: [hep-ph/0407211](https://arxiv.org/abs/hep-ph/0407211).
- [21] A. V. Anisovich and A. V. Sarantsev. “Partial decay widths of baryons in the spin-momentum operator expansion method”. In: *Eur. Phys. J. A* 30 (2006), pp. 427–441. DOI: [10.1140/epja/i2006-10102-1](https://doi.org/10.1140/epja/i2006-10102-1). arXiv: [hep-ph/0605135](https://arxiv.org/abs/hep-ph/0605135).
- [22] I. Antcheva et al. “ROOT — A C++ framework for petabyte data storage, statistical analysis and visualization”. In: *Computer Physics Communications* 180.12 (2009), pp. 2499–2512. ISSN: 0010-4655. DOI: <https://doi.org/10.1016/j.cpc.2009.08.005>.
- [23] J. T Balewski et al. “ Λ -hyperon production via the $pp\rightarrow pK^+\Lambda$ reaction 2-MeV above threshold”. In: *Phys. Lett. B* 388 (1996), pp. 859–865. DOI: [10.1016/S0370-2693\(96\)01360-3](https://doi.org/10.1016/S0370-2693(96)01360-3).

- [24] Dmitriy Baranov et al. “The Particle Track Reconstruction based on deep Neural networks”. In: *EPJ Web Conf.* 214 (2019). Ed. by A. Forti et al., p. 06018. DOI: [10.1051/epjconf/201921406018](https://doi.org/10.1051/epjconf/201921406018). arXiv: [1812.03859](https://arxiv.org/abs/1812.03859) [cs.LG].
- [25] V. E. Barnes et al. “Observation of a Hyperon with Strangeness Minus Three”. In: *Phys. Rev. Lett.* 12 (1964), pp. 204–206. DOI: [10.1103/PhysRevLett.12.204](https://doi.org/10.1103/PhysRevLett.12.204).
- [26] G. Barucca et al. “PANDA Phase One”. In: *Eur. Phys. J. A* 57.6 (2021), p. 184. DOI: [10.1140/epja/s10050-021-00475-y](https://doi.org/10.1140/epja/s10050-021-00475-y). arXiv: [2101.11877](https://arxiv.org/abs/2101.11877) [hep-ex].
- [27] F. Beaujean et al. “p-values for model evaluation”. In: *Phys. Rev. D* 83 (2011), p. 012004. DOI: [10.1103/PhysRevD.83.012004](https://doi.org/10.1103/PhysRevD.83.012004). arXiv: [1011.1674](https://arxiv.org/abs/1011.1674) [physics.data-an].
- [28] Olaf Behnke et al., eds. *Data analysis in high energy physics: A practical guide to statistical methods*. Weinheim, Germany: Wiley-VCH, 2013. ISBN: 978-3-527-41058-3, 978-3-527-65344-7, 978-3-527-65343-0.
- [29] Jia-Chii Berger-Chen. “The Production of K^0 in p+p Reactions at 3.5 GeV”. PhD thesis. Technischen Universität München, 2015.
- [30] Jacek Biernat. “Measuring di-electron Dalitz decays of baryon resonances with HADES and PANDA”. PhD thesis. Jagiellonian U. (main), 2017.
- [31] R. Bijker et al. “Algebraic models of hadron structure. 2. Strange baryons”. In: *Annals Phys.* 284 (2000), pp. 89–133. DOI: [10.1006/aphy.2000.6064](https://doi.org/10.1006/aphy.2000.6064). arXiv: [nucl-th/0004034](https://arxiv.org/abs/nuc1-th/0004034).
- [32] Michael M. Bronstein et al. “Geometric Deep Learning: Going beyond Euclidean data”. In: *IEEE Signal Processing Magazine* 34.4 (2017), pp. 18–42. DOI: [10.1109/MSP.2017.2693418](https://doi.org/10.1109/MSP.2017.2693418).
- [33] G. E. Brown et al. “Kaon production from hot and dense matter formed in heavy ion collisions”. In: *Phys. Rev. C* 43 (1991), pp. 1881–1892. DOI: [10.1103/PhysRevC.43.1881](https://doi.org/10.1103/PhysRevC.43.1881).
- [34] René Brun et al. “GEANT Detector Description and Simulation Tool”. In: (Oct. 1994). DOI: [10.17181/CERN.MUHF.DMJ1](https://doi.org/10.17181/CERN.MUHF.DMJ1).
- [35] W. E. Burcham and M. Jobes. *Nuclear and particle physics*. 1995.
- [36] Malcolm N. Butler et al. “Strong and electromagnetic decays of the baryon decuplet”. In: *Nucl. Phys. B* 399 (1993), pp. 69–88. DOI: [10.1016/0550-3213\(93\)90617-X](https://doi.org/10.1016/0550-3213(93)90617-X). arXiv: [hep-ph/9211247](https://arxiv.org/abs/hep-ph/9211247).
- [37] Eero Byckling and K. Kajantie. *Particle Kinematics: (Chapters I-VI, X)*. Jyvaskyla, Finland: University of Jyvaskyla, 1971.
- [38] Serguei Chatrchyan et al. “Observation of a New Boson at a Mass of 125 GeV with the CMS Experiment at the LHC”. In: *Phys. Lett. B* 716 (2012), pp. 30–61. DOI: [10.1016/j.physletb.2012.08.021](https://doi.org/10.1016/j.physletb.2012.08.021). arXiv: [1207.7235](https://arxiv.org/abs/1207.7235) [hep-ex].

- [39] A. K. Chaudhuri. *A short course on Relativistic Heavy Ion Collisions*. IOPP, Sept. 2014. ISBN: 978-0-7503-1061-1, 978-0-7503-1060-4. DOI: [10.1088/978-0-7503-1060-4](https://doi.org/10.1088/978-0-7503-1060-4). arXiv: [1207.7028 \[nucl-th\]](https://arxiv.org/abs/1207.7028).
- [40] G. F. Chew and F. E. Low. “Unstable particles as targets in scattering experiments”. In: *Phys. Rev.* 113 (1959), pp. 1640–1648. DOI: [10.1103/PhysRev.113.1640](https://doi.org/10.1103/PhysRev.113.1640).
- [41] Kyunghyun Cho et al. “Learning Phrase Representations using RNN Encoder–Decoder for Statistical Machine Translation”. In: *Proceedings of the 2014 Conference on Empirical Methods in Natural Language Processing (EMNLP)*. Doha, Qatar: Association for Computational Linguistics, 2014, pp. 1724–1734. DOI: [10.3115/v1/D14-1179](https://doi.org/10.3115/v1/D14-1179).
- [42] S. K. Choi et al. “Observation of a narrow charmonium - like state in exclusive $B^{+-} \rightarrow K^{+-} \pi^+ \pi^- J / \psi$ decays”. In: *Phys. Rev. Lett.* 91 (2003), p. 262001. DOI: [10.1103/PhysRevLett.91.262001](https://doi.org/10.1103/PhysRevLett.91.262001). arXiv: [hep-ex/0309032](https://arxiv.org/abs/hep-ex/0309032).
- [43] G. Cowan. *Statistical data analysis*. 1998. ISBN: 978-0-19-850156-5.
- [44] G. D’Agostini. “A Multidimensional unfolding method based on Bayes’ theorem”. In: *Nucl. Instrum. Meth. A* 362 (1995), pp. 487–498. DOI: [10.1016/0168-9002\(95\)00274-X](https://doi.org/10.1016/0168-9002(95)00274-X).
- [45] Jurij W. Darewych et al. “The Photon Decays of Baryons with Strangeness”. In: *Phys. Rev. D* 28 (1983), p. 1125. DOI: [10.1103/PhysRevD.28.1125](https://doi.org/10.1103/PhysRevD.28.1125).
- [46] Narsingh Deo. *Graph Theory with Applications to Engineering and Computer Science (Prentice Hall Series in Automatic Computation)*. USA: Prentice-Hall, Inc., 1974. ISBN: 0133634736.
- [47] Carl Doersch. “Tutorial on Variational Autoencoders”. In: (2016). arXiv: [2103.06995 \[hep-ex\]](https://arxiv.org/abs/2103.06995).
- [48] E. Kaxiras et al. “Hyperon radiative decay”. In: *Phys. Rev. D* 32.695 (1985).
- [49] K. N. Ermakov et al. “The study of the proton-proton collisions at the beam momentum 1628 MeV/c”. In: *Eur. Phys. J. A* 47 (2011), p. 159. DOI: [10.1140/epja/i2011-11159-3](https://doi.org/10.1140/epja/i2011-11159-3). arXiv: [1109.1111 \[hep-ex\]](https://arxiv.org/abs/1109.1111).
- [50] W. Esmail et al. “Machine Learning for Track Finding at PANDA”. In: *Connecting the Dots and Workshop on Intelligent Trackers*. Oct. 2019. arXiv: [1910.07191 \[physics.ins-det\]](https://arxiv.org/abs/1910.07191).
- [51] Martin Ester et al. “A Density-Based Algorithm for Discovering Clusters in Large Spatial Databases with Noise”. In: *Proc. of 2nd International Conference on Knowledge Discovery and.* 1996, pp. 226–231.
- [52] Laura Fabbietti. “Study of the e^+e^- pair acceptance in the dilepton spectrometer HADES”. PhD thesis. Technischen Universität München, 2003.
- [53] FAIR. URL: <https://www.gsi.de/en/researchaccelerators/fair>.

- [54] Steven Farrell et al. “Novel deep learning methods for track reconstruction”. In: *4th International Workshop Connecting The Dots 2018*. Oct. 2018. arXiv: [1810.06111](https://arxiv.org/abs/1810.06111) [hep-ex].
- [55] Steven Farrell et al. “The HEP.TrkX Project: deep neural networks for HL-LHC online and offline tracking”. In: *EPJ Web Conf.* 150 (2017). Ed. by C. Germain et al., p. 00003. DOI: [10.1051/epjconf/201715000003](https://doi.org/10.1051/epjconf/201715000003).
- [56] E. Ferrari and S. Serio. “Three-Body Associated Production in Proton-Proton Collisions and the One-Boson-Exchange Model”. In: *Phys. Rev.* 167 (5 Mar. 1968), pp. 1298–1308. DOI: [10.1103/PhysRev.167.1298](https://doi.org/10.1103/PhysRev.167.1298).
- [57] V. Flaminio et al. “Compilation of Cross-sections. 3. P and \bar{P} Induced Reactions”. In: (Apr. 1984).
- [58] A.G. Frodesen et al. *Probability and Statistics in Particle Physics*. Bergen, Norway: Universitetsforlaget, 1979. ISBN: 978-82-00-01906-0.
- [59] I. Fröhlich et al. “Pluto: A Monte Carlo Simulation Tool for Hadronic Physics”. In: *PoS ACAT* (2007), p. 076. DOI: [10.22323/1.050.0076](https://doi.org/10.22323/1.050.0076). arXiv: [0708.2382](https://arxiv.org/abs/0708.2382) [nucl-ex].
- [60] R. Fruhwirth. “Application of Kalman filtering to track and vertex fitting”. In: *Nucl. Instrum. Meth. A* 262 (1987), pp. 444–450. DOI: [10.1016/0168-9002\(87\)90887-4](https://doi.org/10.1016/0168-9002(87)90887-4).
- [61] R. Frühwirth and R. K. Bock. *Data analysis techniques for high-energy physics experiments*. Ed. by H. Grote, D. Notz, and M. Regler. Vol. 11. Cambridge University Press, 2000. ISBN: 978-0-521-63548-6, 978-1-139-14219-9.
- [62] Yarin Gal and Zoubin Ghahramani. “Dropout as a Bayesian Approximation: Representing Model Uncertainty in Deep Learning”. In: *Proceedings of The 33rd International Conference on Machine Learning*. Ed. by Maria Florina Balcan and Kilian Q. Weinberger. Vol. 48. Proceedings of Machine Learning Research. New York, New York, USA: PMLR, 20–22 Jun 2016, pp. 1050–1059.
- [63] Murray Gell-Mann. “A Schematic Model of Baryons and Mesons”. In: *Phys. Lett.* 8 (1964), pp. 214–215. DOI: [10.1016/S0031-9163\(64\)92001-3](https://doi.org/10.1016/S0031-9163(64)92001-3).
- [64] A. Gil et al. “Front-end electronics development for the new resistive plate chamber detector of HADES”. In: *JINST* 2 (2007), T11001. DOI: [10.1088/1748-0221/2/11/T11001](https://doi.org/10.1088/1748-0221/2/11/T11001).
- [65] Justin Gilmer et al. “Neural Message Passing for Quantum Chemistry”. In: *Proceedings of the 34th International Conference on Machine Learning*. Ed. by Doina Precup and Yee Whye Teh. Vol. 70. Proceedings of Machine Learning Research. PMLR, June 2017, pp. 1263–1272.
- [66] N. K. Glendenning. “Neutron stars are giant hypernuclei ?” In: *APJ* 293 (June 1985), pp. 470–493. DOI: [10.1086/163253](https://doi.org/10.1086/163253).

- [67] K. Gottfried and John David Jackson. “On the Connection between production mechanism and decay of resonances at high-energies”. In: *Nuovo Cim.* 33 (1964), pp. 309–330. DOI: [10.1007/BF02750195](https://doi.org/10.1007/BF02750195).
- [68] David J Griffiths. *Introduction to elementary particles; 2nd rev. version*. Physics textbook. New York, NY: Wiley, 2008.
- [69] D. Grzonka et al. “InnerTOF - a Trigger Scintillator for HADES”. In: *IKP Annual Report 2020* (2021).
- [70] Rajan Gupta. “Introduction to lattice QCD: Course”. In: *Les Houches Summer School in Theoretical Physics, Session 68: Probing the Standard Model of Particle Interactions*. July 1997. arXiv: [hep-lat/9807028](https://arxiv.org/abs/hep-lat/9807028).
- [71] Jonathan M. M. Hall et al. “Lattice QCD Evidence that the $\Lambda(1405)$ Resonance is an Antikaon-Nucleon Molecule”. In: *Phys. Rev. Lett.* 114.13 (2015), p. 132002. DOI: [10.1103/PhysRevLett.114.132002](https://doi.org/10.1103/PhysRevLett.114.132002). arXiv: [1411.3402](https://arxiv.org/abs/1411.3402) [hep-lat].
- [72] Andreas Herten. “GPU-based Online Track Reconstruction for \bar{P} ANDA and Application to the Analysis of $D \rightarrow K\pi\pi$ ”. PhD thesis. Ruhr-Universität Bochum, 2015.
- [73] Sepp Hochreiter and Jürgen Schmidhuber. “Long short-term memory”. In: *Neural computation* 9.8 (1997), pp. 1735–1780.
- [74] Andreas Hocker and Vakhtang Kartvelishvili. “SVD approach to data unfolding”. In: *Nucl. Instrum. Meth. A* 372 (1996), pp. 469–481. DOI: [10.1016/0168-9002\(95\)01478-0](https://doi.org/10.1016/0168-9002(95)01478-0). arXiv: [hep-ph/9509307](https://arxiv.org/abs/hep-ph/9509307).
- [75] Kurt Hornik et al. “Multilayer feedforward networks are universal approximators”. In: *Neural Networks* 2.5 (1989), pp. 359–366. ISSN: 0893-6080. DOI: [https://doi.org/10.1016/0893-6080\(89\)90020-8](https://doi.org/10.1016/0893-6080(89)90020-8).
- [76] *Hydra*. URL: <https://hades.gsi.de/?q=computing>.
- [77] Nathan Isgur and Gabriel Karl. “P Wave Baryons in the Quark Model”. In: *Phys. Rev. D* 18 (1978), p. 4187. DOI: [10.1103/PhysRevD.18.4187](https://doi.org/10.1103/PhysRevD.18.4187).
- [78] Xiangyang Ju et al. “Physics and Computing Performance of the Exa.TrkX TrackML Pipeline”. In: (Mar. 2021). arXiv: [2103.06995](https://arxiv.org/abs/2103.06995) [hep-ex].
- [79] Martin Jurkovic et al. “Dielectron production in Ar+KCl collisions at $E(\text{kin}) = 1.76\text{-AGeV}$ ”. In: *PoS BORMIO2010* (2010). Ed. by Wolfgang Kuhn, p. 051. DOI: [10.22323/1.103.0051](https://doi.org/10.22323/1.103.0051).
- [80] V. Kartvelishvili. “Unfolding with Singular Value Decomposition”. In: *PHYSTAT 2011*. Geneva: CERN, Jan. 2011. DOI: [10.5170/CERN-2011-006.264](https://doi.org/10.5170/CERN-2011-006.264).
- [81] Moritz Kiehn et al. “The TrackML high-energy physics tracking challenge on Kaggle”. In: *EPJ Web Conf.* 214 (2019). Ed. by A. Forti et al., p. 06037. DOI: [10.1051/epjconf/201921406037](https://doi.org/10.1051/epjconf/201921406037).

- [82] Durk P Kingma et al. “Semi-supervised Learning with Deep Generative Models”. In: *Advances in Neural Information Processing Systems*. Ed. by Z. Ghahramani et al. Vol. 27. Curran Associates, Inc., 2014.
- [83] P. Koch et al. “Strangeness in Relativistic Heavy Ion Collisions”. In: *Phys. Rept.* 142 (1986), pp. 167–262. DOI: [10.1016/0370-1573\(86\)90096-7](https://doi.org/10.1016/0370-1573(86)90096-7).
- [84] Roman Koniuk and Nathan Isgur. “Baryon Decays in a Quark Model with Chromodynamics”. In: *Phys. Rev. D* 21 (1980). [Erratum: *Phys.Rev.D* 23, 818 (1981)], p. 1868. DOI: [10.1103/PhysRevD.21.1868](https://doi.org/10.1103/PhysRevD.21.1868).
- [85] P. Kowina et al. “Energy dependence of the Lambda / Sigma0 production cross-section ratio in p p interactions”. In: *Eur. Phys. J. A* 22 (2004), pp. 293–299. DOI: [10.1140/epja/i2003-10236-6](https://doi.org/10.1140/epja/i2003-10236-6). arXiv: [nucl-ex/0402008](https://arxiv.org/abs/nucl-ex/0402008).
- [86] D. Lazer et al. “Life in the network: The coming age of computational social science: Science”. In: 2009.
- [87] Maxim Mai. “Review of the $\Lambda(1405)$: A curious case of a strange-ness resonance”. In: (Sept. 2020). arXiv: [2010.00056](https://arxiv.org/abs/2010.00056) [[nucl-th](#)].
- [88] M. A. Mandelkern. “Production of K mesons in three-body states in proton-proton interactions at 6 BeV/c”. PhD thesis. Calif. U. Berkeley, 1967.
- [89] McCulloch et al. “A logical calculus of the ideas immanent in nervous activity”. In: *The bulletin of mathematical biophysics* 5.4 (Dec. 1943), pp. 115–133. ISSN: 1522-9602. DOI: [10.1007/BF02478259](https://doi.org/10.1007/BF02478259).
- [90] Tom M. Mitchell. *Machine Learning*. New York: McGraw-Hill, 1997. ISBN: 978-0-07-042807-2.
- [91] R. Münzer et al. “Determination of N^* amplitudes from associated strangeness production in p+p collisions”. In: *Phys. Lett. B* 785 (2018), pp. 574–580. DOI: [10.1016/j.physletb.2018.08.068](https://doi.org/10.1016/j.physletb.2018.08.068). arXiv: [1703.01978](https://arxiv.org/abs/1703.01978) [[nucl-ex](#)].
- [92] Takato Nishijima. “Universal Approximation Theorem for Neural Networks”. In: *CoRR* abs/2102.10993 (2021). arXiv: [2102.10993](https://arxiv.org/abs/2102.10993).
- [93] Alessia Palmese et al. “Strangeness production in heavy-ion collisions”. In: *PoS CPOD2014* (2015), p. 069. DOI: [10.22323/1.217.0069](https://doi.org/10.22323/1.217.0069). arXiv: [1506.04653](https://arxiv.org/abs/1506.04653) [[hep-ph](#)].
- [94] Adam Paszke et al. “PyTorch: An Imperative Style, High-Performance Deep Learning Library”. In: *Advances in Neural Information Processing Systems* 32. Ed. by H. Wallach et al. Curran Associates, Inc., 2019, pp. 8024–8035.
- [95] Santanu Pattanayak. *Pro Deep Learning with TensorFlow: A Mathematical Approach to Advanced Artificial Intelligence in Python*. 1st. USA: Apress, 2017. ISBN: 1484230957.

- [96] Attilio Tarantola Pelsoni. “Dielectron analysis in p-p collisions at 3.5 GeV with the HADES spectrometer: ω meson line shape and a new electronics readout for the Multi-wire Drift Chambers”. PhD thesis. Johann Wolfgang Goethe-Universität, 2010.
- [97] A. Pich. “Introduction to chiral perturbation theory”. In: *AIP Conf. Proc.* 317 (1994). Ed. by J. L. Lucio Martinez and M. Vargas, pp. 95–140. DOI: [10.1063/1.46859](https://doi.org/10.1063/1.46859). arXiv: [hep-ph/9308351](https://arxiv.org/abs/hep-ph/9308351).
- [98] Joaquin Quiñonero-Candela et al. *Dataset Shift in Machine Learning*. The MIT Press, Dec. 2008. ISBN: 9780262255103. DOI: [10.7551/mitpress/9780262170055.001.0001](https://doi.org/10.7551/mitpress/9780262170055.001.0001).
- [99] G. Ramalho and K. Tsushima. “What is the role of the meson cloud in the $\Sigma^* \rightarrow \gamma\Lambda$ and $\Sigma^0 \rightarrow \gamma\Sigma$ decays?” In: *Phys. Rev. D.* 88.5, 053002 (Sept. 2013), p. 053002. DOI: [10.1103/PhysRevD.88.053002](https://doi.org/10.1103/PhysRevD.88.053002). arXiv: [1307.6840 \[hep-ph\]](https://arxiv.org/abs/1307.6840).
- [100] Johannes Rauch and Tobias Schlüter. “GENFIT — a Generic Track-Fitting Toolkit”. In: *J. Phys. Conf. Ser.* 608.1 (2015). Ed. by L. Fiala, M. Lokajicek, and N. Tumorova, p. 012042. DOI: [10.1088/1742-6596/608/1/012042](https://doi.org/10.1088/1742-6596/608/1/012042). arXiv: [1410.3698 \[physics.ins-det\]](https://arxiv.org/abs/1410.3698).
- [101] Giorgia Rauco. “Search for New Physics in All-Hadronic Final States with the CMS Experiment”. PhD thesis. Universität Zürich, 2019.
- [102] James Ritman. “Strange Hadron Production in Strongly Interacting Systems”. PhD thesis. Justus Liebig Universität Gießen, 2000.
- [103] F. Rosenblatt. “The perceptron: a probabilistic model for information storage and organization in the brain.” In: *Psychological review* 65 6 (1958), pp. 386–408.
- [104] David E. Rumelhart and James L. McClelland. “Learning Internal Representations by Error Propagation”. In: *Parallel Distributed Processing: Explorations in the Microstructure of Cognition: Foundations*. 1987, pp. 318–362.
- [105] Anar Rustamov. “Exclusive η Meson Reconstruction in Proton-Proton Collisions at 2.2 GeV with the HADES Spectrometer and High Resolution Tracking”. PhD thesis. Technischen Universität Darmstadt, 2006.
- [106] Anders Ryd et al. “EvtGen: A Monte Carlo Generator for B-Physics”. In: (May 2005).
- [107] Salabura, Piotr et al. “Exploring time like tranistions in pp, πp and AA reactions with HADES”. In: *EPJ Web Conf.* 241 (2020), p. 01013. DOI: [10.1051/epjconf/202024101013](https://doi.org/10.1051/epjconf/202024101013).
- [108] Nora Salone and Stefan Leupold. “Electromagnetic transition form factors and Dalitz decays of hyperons”. In: *Eur. Phys. J. A* 57.6 (2021), p. 183. DOI: [10.1140/epja/s10050-021-00493-w](https://doi.org/10.1140/epja/s10050-021-00493-w). arXiv: [2104.05675 \[hep-ph\]](https://arxiv.org/abs/2104.05675).

- [109] A. V. Sarantsev et al. “Decays of baryon resonances into Lambda K+, Sigma0 K+ and Sigma+ K0”. In: *Eur. Phys. J. A* 25 (2005), pp. 441–453. DOI: [10.1140/epja/i2005-10121-4](https://doi.org/10.1140/epja/i2005-10121-4). arXiv: [hep-ex/0506011](https://arxiv.org/abs/hep-ex/0506011).
- [110] A. Sibirtsev et al. “Phenomenology of the Λ/Σ^0 production ratio in p p collisions”. In: *The European physical journal / A* 29 (2006), pp. 363–367. ISSN: 1434-6001. DOI: [10.1140/epja/i2006-10097-5](https://doi.org/10.1140/epja/i2006-10097-5). arXiv: [oai:arXiv.org:hep-ph/0608098](https://arxiv.org/abs/oai:arXiv.org:hep-ph/0608098).
- [111] A. Sibirtsev et al. “Resonances and final state interactions in the reaction $pp \rightarrow pK^+\Lambda$ ”. In: *Eur. Phys. J. A* 27.3 (2006), pp. 269–285. DOI: [10.1140/epja/i2005-10268-x](https://doi.org/10.1140/epja/i2005-10268-x). arXiv: [nuc1-th/0512059](https://arxiv.org/abs/nuc1-th/0512059).
- [112] Johannes Siebenson et al. “Strange baryon resonances in pp collisions measured with HADES”. In: *Hyperfine Interact.* 213.1-3 (2012), pp. 63–70. DOI: [10.1007/s10751-011-0388-3](https://doi.org/10.1007/s10751-011-0388-3).
- [113] Johannes Stephan Siebenson. “Strange baryonic resonances below the $\bar{K}N$ threshold - Results from p + p reactions at the HADES experiment”. PhD thesis. Technischen Universität München, 2013.
- [114] B. Singh et al. “Technical Design Report for the PANDA Forward Spectrometer Calorimeter”. In: (Apr. 2017). arXiv: [1704.02713](https://arxiv.org/abs/1704.02713) [[physics.ins-det](https://arxiv.org/abs/1704.02713)].
- [115] J. Smyrski et al. “Design of the forward straw tube tracker for the PANDA experiment”. In: *Journal of Instrumentation* 12.06 (June 2017), pp. C06032–C06032. DOI: [10.1088/1748-0221/12/06/c06032](https://doi.org/10.1088/1748-0221/12/06/c06032).
- [116] J. Smyrski et al. “Pressure stabilized straw tube modules for the PANDA Forward Tracker”. In: *Journal of Instrumentation* 13.06 (June 2018), P06009–P06009. DOI: [10.1088/1748-0221/13/06/p06009](https://doi.org/10.1088/1748-0221/13/06/p06009).
- [117] V. Sola et al. “First FBK production of 50 μm ultra-fast silicon detectors”. In: *Nuclear Instruments and Methods in Physics Research Section A: Accelerators, Spectrometers, Detectors and Associated Equipment* 924 (2019), pp. 360–368. DOI: <https://doi.org/10.1016/j.nima.2018.07.060>.
- [118] Nitish Srivastava et al. “Dropout: A Simple Way to Prevent Neural Networks from Overfitting”. In: *Journal of Machine Learning Research* 15.56 (2014), pp. 1929–1958. URL: <http://jmlr.org/papers/v15/srivastava14a.html>.
- [119] O. Svoboda et al. “Electromagnetic calorimeter for the HADES@FAIR experiment”. In: *JINST* 9 (2014). Ed. by Pietro Govoni et al., p. C05002. DOI: [10.1088/1748-0221/9/05/C05002](https://doi.org/10.1088/1748-0221/9/05/C05002).
- [120] Katarzyna Szymanska. “Production of Double Hypernuclei with antiprotons at PANDA”. In: *34th International Conference on High Energy Physics*. Oct. 2008. arXiv: [0810.2663](https://arxiv.org/abs/0810.2663) [[hep-ex](https://arxiv.org/abs/0810.2663)].
- [121] M. Tanabashi et al. “Review of Particle Physics”. In: *Phys. Rev. D* 98.3 (2018), p. 030001. DOI: [10.1103/PhysRevD.98.030001](https://doi.org/10.1103/PhysRevD.98.030001).

- [122] S. Taylor et al. “Radiative decays of the Sigma0(1385) and Lambda(1520) hyperons”. In: *Phys. Rev. C* 71 (2005), p. 054609. DOI: [10.1103/PhysRevC.71.054609](https://doi.org/10.1103/PhysRevC.71.054609). arXiv: [hep-ex/0503014](https://arxiv.org/abs/hep-ex/0503014).
- [123] The pandas development team. *pandas-dev/pandas: Pandas*. Version latest. Feb. 2020. DOI: [10.5281/zenodo.3509134](https://doi.org/10.5281/zenodo.3509134).
- [124] Mark Thomson. *Modern Particle Physics*. Cambridge University Press, 2013. DOI: [10.1017/CB09781139525367](https://doi.org/10.1017/CB09781139525367).
- [125] Jeroen Ashwin Niels van Tilburg. “DTrack simulation and reconstruction in LHCb”. PhD thesis. VRIJE UNIVERSITEIT, 2005.
- [126] Mohammad Al-Turany and Florian Uhlig. “FairRoot framework”. In: *PoS ACAT08* (2008). Ed. by Thomas Speer, Federico Carminati, and Monique Werlen, p. 048. DOI: [10.22323/1.070.0048](https://doi.org/10.22323/1.070.0048).
- [127] Jake VanderPlas. *Python Data Science Handbook: Essential Tools for Working with Data*. 1st. O’Reilly Media, Inc., 2016. ISBN: 1491912057.
- [128] Fjodor van Veen. *Neural Networks Chart*. 2016. URL: <https://www.asimovinstitute.org/neural-network-zoo/>.
- [129] M. Warns, W. Pfeil, and H. Rollnik. “Electromagnetic properties of hyperons in a relativized quark model”. In: *Phys. Lett. B* 258 (1991), pp. 431–440. DOI: [10.1016/0370-2693\(91\)91113-A](https://doi.org/10.1016/0370-2693(91)91113-A).
- [130] Zonghan Wu et al. “A Comprehensive Survey on Graph Neural Networks”. In: *IEEE Transactions on Neural Networks and Learning Systems* 32.1 (2021), pp. 4–24. DOI: [10.1109/TNNLS.2020.2978386](https://doi.org/10.1109/TNNLS.2020.2978386).
- [131] Jie Zhou et al. “Graph Neural Networks: A Review of Methods and Applications”. In: *AI Open* 1 (2020), pp. 57–81. ISSN: 2666-6510. DOI: <https://doi.org/10.1016/j.aiopen.2021.01.001>.
- [132] Xiaojin Zhu and Andrew B. Goldberg. “Introduction to Semi-Supervised Learning”. In: *Synthesis Lectures on Artificial Intelligence and Machine Learning* 3.1 (2009), pp. 1–130. DOI: [10.2200/S00196ED1V01Y200906AIM006](https://doi.org/10.2200/S00196ED1V01Y200906AIM006).
- [133] Iris Zimmermann. “Feasibility studies for the measurement of the time-like electromagnetic proton form factors at the PANDA experiment.” PhD thesis. Johannes–Gutenberg–Universität in Mainz, 2018.

ACKNOWLEDGMENT

This thesis would not have been possible without the support of many people. Firstly, I would like to express my sincere gratitude to my advisor Prof. James Ritman (IKP-Jülich Forschungszentrum) for giving me the opportunity to join his group and for his continuous support, for his patience, motivation, and immense knowledge. Your guidance helped me in all the time of research and writing of this thesis. I could not have imagined having a better advisor and mentor.

I want to express my grateful to my advisor Dr. Tobias Stockmanns (IKP-Jülich Forschungszentrum) for his continual patience, outstanding guidance, invaluable discussions, support in software related questions, sharing expertise. Your encouraging words and thoughtful, detailed feedback have been very important to me.

My sincere thanks go to my colleagues at the IKP, Dr. Peter Wintz, Dr. Yong Zhou, Dr. Jennifer Pütz, Dr. Huagen Xu, Jakapat Kannika, Anna Alicke, Gabriela Perez, Ashish Thampi, thank you all for your support and the invaluable discussions. Special thanks to Kevin Luckas for proofreading the abstract and for the fruitful discussions. I would like to express another thanks to my former colleague and my dear friend Dr. Tamer Tolba for encouraging and guiding me during my PhD.

I am extremely thankful to Prof. Piotr Salabura for hosting me at the Jagiellonian University and for his valuable inputs and suggestions throughout this thesis. Special thanks to Dr. Rafał Lalik (Jagiellonian University) for his time, patience and the detailed answers to all of my questions. Special thanks also go to Krzysztof Nowakowski (Jagiellonian University) for his time and support, I really enjoyed our discussions.

I am also thankful to Prof. Karin Schönning, Dr. Michael Papenbrock, Jenny Regina, Adeel Akram and Jana Rieger at Uppsala University, Sweden for the fruitful collaboration.

I also would like to say special thank you to Dr. Ralf Kliemt (GSI) and Dr. Jochen Markert (GSI) for their continuous help and guidance in the software related questions.

I gratefully recognize the help of Dr. Andrey Sibirtsev (Bonn University), thank you for providing the partial wave analysis software and the assistance in running and understanding the code.

Many thanks to my dear wife, for her support and endless patience, I am indebted to you for your unconditional love and care, and helping me in writing my thesis.

Last but not the least, I would like to thank my family, for supporting me spiritually throughout writing this thesis and my life in general.

LEBENS LAUF

Persönliche Informationen

Name	Waleed Ahmed Mohammed Esmail
Adresse	Wiesenstr. 6G, 52428 Jülich
Email	waleed.physics@gmail.com
Geburtstag	16.06.1986
Geburtsort	Kairo, Ägypten
Nationalität	Ägyptisch

Education

- 2018 – 2021 **Doktorand**, Fakultät für Physik und Astronomie, Ruhr-Universität Bochum, Deutschland
Thema der Dissertation: *Deep Learning for Track Finding and the Reconstruction of Excited Hyperons in Proton Induced Reactions.*, IKP-1, Forschungszentrum Jülich GmbH.
- 01 – 04/2016 **Forscher**, Physikabteilung, Universität Bari, Italien.
- 2013 – 2016 **M.Sc.**, Fakultät für Naturwissenschaften, Universität Helwan, Ägypten.
Thema der Dissertation: *GEM Performance Studies in CMS Experiment with Four Muons Final State.*
- 2011 – 2012 **Diplom**, Fakultät für Naturwissenschaften, Universität Helwan, Ägypten.
- 2005 – 2009 **B.Sc.**, Fakultät für Naturwissenschaften, Universität Helwan, Ägypten.

CURRICULUM VITAE

Personal information

Name	Waleed Ahmed Mohammed Esmail
Address	Wiesenstr. 6G, 52428 Jülich
Email	waleed.physics@gmail.com
Birthday	16.06.1986
Birthplace	Cairo, Egypt
Nationality	Egyptian

Education

2018 – 2021	Ph.D. , Faculty of Physics and Astronomy, Ruhr University Bochum, Germany. Thesis title: <i>Deep Learning for Track Finding and the Reconstruction of Excited Hyperons in Proton Induced Reactions.</i> , Juelich Research Center.
01 – 04/2016	Physicist , Physics Department, Bari University, Italy.
2013 – 2016	M.Sc. , Faculty of Science, Helwan University, Egypt. Thesis title: <i>GEM Performance Studies in CMS Experiment with Four Muons Final State.</i>
2011 – 2012	Pre-Master , Faculty of Science, Helwan University, Egypt.
2005 – 2009	B.Sc. , Faculty of Science, Helwan University, Egypt.

